Glacier-Ocean interaction at Store Glacier (West Greenland)

Nolwenn Chauché

A thesis submitted in fulfilment of the requirements for the degree of Doctor of Philosophy

February 9, 2016

Aberystwyth University

Supervisors: Dr Alun Hubbard, Dr Mark Neal,

Dr Jean-Claude Gascard (Uni. of Pierre et Marie Curie),

Dr Richard Bates (Uni. of St Andrews)

Declaration and statements

Declaration

This work has not previously been accepted in substance for any degree and is not being concurrently submitted in candidature for any degree.

Signed ..... Date 09 February 2016

Statement 1

This thesis is the result of my own investigations except where otherwise stated. Other sources are acknowledged giving explicit references. A bibliography is appended.

Signed ..... Date 09 February 2016

Statement 2

I hereby give consent for my thesis, if accepted, to be available for photocopying and for inter-library loan, and for the title and summary to be made available to outside organisations.

Signed ..... Date 09 February 2016

Acknowledgements

I would like to thank Alun Hubbard for the opportunity to undertake this investigation using S/V *Gambo* and for his guidance over the years. I also thank my secondary supervisor, Mark Neal, for his invaluable advice and support. I am indebted to Jean Claude Gascard for his supervision regarding all the oceanographic sections of this work, and to Richard Bates for his help and input regarding the use of the Bathyswath system. I am grateful for advice on GPS processing from Sam Doyle. I would also like to thank Jason Box, Poul Christoffersen, Marion Bougamont and many others, who helped me during this project.

For assistance in the field I am indebted to the tireless crew of S/V *Gambo* and particularly, Grant Redvers, Max Deneuville, James Killingbeck, Mathieu Depoorter, Pascaline Bourgain, Ludovic Mocochain, Dave Chandler, Pauline de Gesnais, Jean Noël Dory, Dave Burton and the inevitable people I have inadvertently overlooked. I thank Dave Kelly at Aberystwyth University for technical advice. I also thank Michael Field for advice and careful listening during this last year as well as Denis and Ann Bates for hosting me in Aberystwyth.

I would like to thank the grateful support to my project I have received in Greenland, particularly the Uummannaq Polar Institute and Children's Home, Pierre Auzias, Annie Kerouedan, Lars Therkelsen, Hans and Suffi Gronvold.

The fieldwork undertaken in this thesis was funded by the UK Natural Environment Research Council (NERC) Grant NE/G010595/1, the Aberystwyth University Research Fund and the Royal Geographical Society for the 2009-2010 field work. I also would like to thank the BBC Operation Iceberg series which funded the field work of the summer 2012, and the European ACCESS project which funded a part of the field work of the summer 2013. I acknowledge the support of an Aberystwyth University doctoral scholarship.

Finally I thanks my friend, family and colleagues for their support over the last three years.

Abstract

Accurate forecasting of the Greenland Ice Sheet's contribution to global sea-level rise requires detailed knowledge of the processes in action at marine-terminating glaciers and their sensitivity to the controls that govern them. Both ice velocities and supraglacial-melt have increased significantly over the last decade, while recent research suggests that the dynamic ice-loss can be attributed to oceanic rather than atmospheric forcing. Warm, subtropical-originating Atlantic water has been identified as a primary driver of mass loss across the marine sectors of the Greenland Ice Sheet. Subglacial drainage networks inject fresh-water at depth producing a buoyant upwelling at the glacier front, renewing the Atlantic water in contact with the ice and thus enhancing the submarine-melt. To investigate these processes, their mutual forcing, and seasonal variability, a time-series of oceanographic, glaciological, and atmospheric measurements was collected at the front of Store Glacier, a major marine terminating outlet in Uummannaq bay (West Greenland). These data revealed a submarine-melt rate of $1.9\pm0.5\,\mathrm{m\,d^{-1}}$ during winter months, which is five times larger than previous assumptions, and is attributed to the year-round contribution of basal-melt to the subglacial discharge of fresh water. A novel method using repeated 3D scanning of the submerged part of the glacier front permitted us for the first time to directly measure a summer submarine-melt rate of $3.4\pm0.7\,\mathrm{m\,d^{-1}}$. Together, summer and winter submarine-melt contributed to 14% of the annual frontal ablation and up to 25% during summer months. Measurements from inside two upwelling plumes provided insight to their physical characteristics as well as their impact on the entire glacier front. These results highlight the need to reconsider the assumptions used in current model parametrisations of the ocean-glacier interface when evaluating the response of the Greenland-ice sheet to a warmer climate.

Contents

Table of contents ix

List of figures xvii

List of tables xxi

Authors contributions **xxiii**

1 Introduction **1**

1.1 Greenland Ice Sheet 1

1.2 Characteristics of Greenland fjords 3

1.2.1 Glacier front dynamics 3

1.2.2 Fjord circulation 7

1.3 Ocean-Glacier interaction processes 9

1.3.1 Quantification of submarine-melting 10

1.3.2 Subglacial fresh water discharge 11

1.4 Background methods 14

1.4.1 Processes identification 15

1.4.2 Processes quantification 20

1.5 Aims and objectives 33

1.6 Structure of thesis 33

2 Field site and survey platform **35**

2.1 Bathymetric survey of Store Fjord 38

2.1.1 Method 40

2.1.2 Results 43

2.2 *Gambo*: the survey platform 47

2.2.1 Summer setting 47

2.2.2 Winter setting 48

3 Ocean-glacier processes: identification and variability at Store and Rink glaciers **53**

3.1 Summary 53

3.2 Introduction and background 54

3.3 Field site 56

3.4 Methods 59

3.4.1 Data collection 59

3.4.2 Water-body identification 60

3.4.3 Identification of interaction processes 61

3.4.4 Interpolation of oceanic measurements 62

3.4.5 Runoff discharge estimation 62

3.5 Results 63

3.5.1 Water types present at the glacier front 63

3.5.2 Mixed water masses and inferred processes 67

3.5.3 SgFW discharge estimation 68

3.5.4 Turbidity analysis and plume observation 69

3.6 Discussion 71

3.6.1 Ocean–glacier interaction 71

3.6.2 SgFW-driven upwelling: spatial spreading and glacier impact 77
3.6.3 Oceanic and bathymetric influence on glacier front behaviour 78
3.7 Conclusions 79

4 Vigorous submarine-melt sustained throughout winter months at Store Glacier 81

4.1 Summary 81
4.2 Introduction and background 82
4.3 Field site and data collection 85
4.4 Methods 88
4.4.1 Oceanographic measurements 88
4.4.2 Circulation induced by the ocean-glacier interaction 89
4.4.3 Models 90
4.4.4 Bathymetry cross-section 100
4.5 Results 101
4.5.1 Water characteristics 101
4.5.2 Current 102
4.5.3 Runoff and Submarine-melt discharges 103
4.5.4 Gade model intermediate results 103
4.5.5 Motyka model intermediate results 105
4.5.6 Model uncertainties 106
4.6 Discussion 106
4.6.1 Comparison with previous studies 106
4.6.2 Runoff regime impact 108
4.6.3 Consequences for Store Glacier and the Greenland Ice Sheet 111
4.7 Conclusion 112

5 Plume-induced surface circulation and evolution 115

5.1 Summary . . . 115

5.2 Introduction and background . . . 116

5.3 Field site . . . 118

5.4 Methods . . . 118

5.4.1 Georeferencing . . . 120

5.4.2 Plume area . . . 120

5.4.3 Iceberg velocity field . . . 121

5.4.4 Air temperature forcing on plume dynamics . . . 122

5.5 Results . . . 123

5.5.1 General weather conditions . . . 123

5.5.2 Plume area . . . 123

5.5.3 Fjord horizontal circulation . . . 126

5.6 Discussion . . . 126

5.6.1 Plume impact on the glacier front . . . 126

5.6.2 Limitation of the feature-tracking method . . . 130

5.6.3 Air temperature forcing on plume dynamics . . . 130

5.7 Conclusion . . . 135

6 Characterisation of upwelling plumes 137

6.1 Summary . . . 137

6.2 Introduction and background . . . 138

6.3 Experiment . . . 142

6.4 Method . . . 142

6.4.1 Instruments . . . 142

6.4.2 ADCP and CTD transects . . . 144

6.5 Results . . . 145
6.5.1 General condition . . . 145
6.5.2 Circulation and Turbidity transect . . . 145
6.5.3 Water characteristics . . . 148
6.6 Discussion . . . 148
6.6.1 Plume location . . . 148
6.6.2 Plume impact on the glacier front in contact with the rising plume . . . 150
6.7 Conclusion . . . 154

7 Submarine melt impact estimated from recently calved iceberg 155
7.1 Summary . . . 155
7.2 Introduction and background . . . 156
7.3 Method . . . 158
7.3.1 Structure-from-motion . . . 158
7.4 Results . . . 159
7.4.1 Calving event description . . . 159
7.4.2 Iceberg reconstruction . . . 160
7.4.3 Iceberg scale . . . 160
7.4.4 Iceberg shape . . . 162
7.5 Discussion . . . 163
7.5.1 Submarine melt impact . . . 163
7.5.2 Vertical runnels . . . 165
7.6 Conclusion . . . 166

8 Direct measurement of submarine melting from repeated side-scan sonar surveys **169**

8.1 Summary . . . 169

8.2 Introduction and background . . . 170

8.3 Method . . . 172

8.3.1 Instruments . . . 172

8.3.2 Glacier coordinate system and gridding . . . 177

8.3.3 Glacier front area . . . 178

8.3.4 Glacier front dynamics . . . 179

8.3.5 Glacier velocity estimation . . . 179

8.3.6 Correction of the glacier velocity . . . 182

8.3.7 Front ablation processes . . . 182

8.3.8 Uncertainty evaluation . . . 183

8.4 Results . . . 185

8.4.1 Repeated scan . . . 185

8.4.2 Glacier description . . . 186

8.4.3 Glacier Velocity . . . 188

8.4.4 Submarine melting . . . 190

8.5 Discussion . . . 192

8.5.1 Velocity profile . . . 192

8.5.2 Submarine melting . . . 193

8.6 Conclusion . . . 194

9 Synthesis **197**

9.1 The state of knowledge before 2011 . . . 197

9.2 Progress between 2011 and 2014 . . . 198

9.2.1 ocean-glacier interaction processes 198
9.2.2 Submarine melting: rate and seasonal evolution 200
9.2.3 Impact of the upwelling plume on the glacier front 202
9.3 Direction for future research 204

10 General conclusions **209**

Reference **212**

Appendix **226**

A Publication **227**

List of Figures

1.1 Greenland surface thinning 2
1.2 Schematic of ocean circulation around Greenland 4
1.3 Greenland's main tidewater glaciers and bathymetry 6
1.4 Schematic of the different fjord circulations 7
1.5 Schematic of the Motyka model 8
1.6 Impact of submarine-melt and runoff on fjord ambient water 11
1.7 Upwelling plume structure 12
1.8 Gade meltwater line (Gade, 1979) 16
1.9 Meltwater line from Jenkins (1999) 18
1.10 Meltwater and runoff mixing lines from Straneo and others (2011) . 19
1.11 Fjord circulation from Straneo and others (2011) 20
1.12 Simplified Ocean-Glacier model from Motyka and others (2003) . . 21
1.13 Motyka model applied to Torsukatak Glacier by Rignot and others (2010) 24
1.14 Motyka model applied to Store glacier by Xu and others (2013) . . 25
1.15 Plume model from Jenkins (2011) 26
1.16 Plume model from O'Leary (2011) 27
1.17 Fjord model from Sole and others (2012) 28

1.18 Fjord model circulation from Sole and others (2012) 29
1.19 Fjord model from Sciascia and others (2013) 29
1.20 Fjord model from Xu and others (2012) 31
1.21 Plume high resolution 3D model from Xu and others (2013) 32
1.22 Plume high resolution 3D model from Kimura and others (2014) . . 32

2.1 Map of the study area 36
2.2 Store Glacier 37
2.3 West Greenland flow speed 39
2.4 IBCAO source of data 43
2.5 Data sets used in bathymetry interpolation 44
2.6 Bathymetry of Store and Lille fjords 45
2.7 Bathymetry near Store glacier front 45
2.8 Differences between IBCAO and Interpolated bathymetry 46
2.9 Hydrographic profiler setting 48
2.10 ADCP and Sonar summer setting 49
2.11 *Gambo* during the winter 50
2.12 Instrumentation setting in winter 51

3.1 Map of Rink and Store measurements 58
3.2 Water characteristics at Rink and Store 64
3.3 Temperature-Salinity diagram 65
3.4 Temperature along the fjord 70
3.5 Temperature across the fjord 71
3.6 Turbidity section in plume 72
3.7 Schematic of ocean-glacier interaction pattern 74
3.8 Photography of the plume at Store 75

3.9 Photographs of Store and Rink glacier 76

4.1 Air-temperature and rain events near Store in 2012-2013 86
4.2 Map of the winter experiment 87
4.3 Temperature-salinity diagram during the winter 93
4.4 Bathymetry cross section 101
4.5 Raw data from the oceanographic measurements 102
4.6 Gade and Motyka models results for each period 104
4.7 Flux of the water resulting of each process 105

5.1 Map of the plume evolution experiment 119
5.2 Time-series of plume characteristics 125
5.3 Velocity fields of the surface circulation 127
5.4 Schematic of the plume circulation 129
5.5 air temperature at Summit camp versus observed area of the plume 132
5.6 air temperature at Store front versus the residual plume area 133
5.7 Plume area reconstruction 134

6.1 Plume schematic dynamic 139
6.2 Map of transects in plumes 143
6.3 Transect along plume flow 146
6.4 Transect parallel to the glacier front 147
6.5 Water characteristics in and around the plumes 149
6.6 Schematic of the plume circulation 152

7.1 Time-lapse of the calving event 160
7.2 Iceberg reconstruction mesh 161
7.3 Fully reconstructed iceberg 162

7.4 Schematic of runnels formation 164
7.5 Melt runnels observed on icebergs 165

8.1 Principle of the Bathyswath system 173
8.2 Principle of the interferometry used in the Bathyswath 174
8.3 Ping coordinate system filtering 175
8.4 Map of the study area 178
8.5 3D Position of Store Glacier front 187
8.6 Glacier front positions and velocity 189
8.7 Submarine melt rate distribution 191
8.8 3D view of submarine melt measurements 192

List of Tables

3.1 Profiler specifications 60
3.2 Characteristics of the fjord waters 66

4.1 Variables used in the Gade and Motyka models 94
4.2 Summary of melt-rate and subglacial runoff discharge estimates . . 107
4.3 Partitioning of forcing on submarine-melt 110

6.1 Summary of plume characteristics 153

Authors contributions

Several authors contributed to the research presented in these chapters. Jason E. Box produced the supraglacial runoff estimation discussed in Chapter 3, Andrew Sole, Henry Patton, Richard Bates and Michele Koppes advised and commented on the writing of Chapter 3 which was published in The Cryosphere (Chauché and others, 2014). Marion Bougamont has produced the basal-melting estimation in Chapter 4.

Chapter 1

Introduction

The overall aim of this thesis is to gain insight into the processes in play at the interface between tidewater-glaciers and the ocean. It is motivated by the need to better understand the ocean-glacier interface and the interaction between them. It specifically addresses the need for quantification, based on observation, of the annual submarine-melting occurring at the glacier front, and of the impact of buoyant-upwelling induced by the injection at depth of subglacial runoff.

1.1 Greenland Ice Sheet

The Greenland Ice Sheet (GrIS) contains 2.85 million gigatonnes of ice, which if melted completely would raise global sea levels by 7.36 m (Bamber and others, 2013). The GrIS is currently losing mass and it has been estimated that over the last two decades, the GrIS has contributed 7.8±2.8 mm of sea level rise, which is approximately double of the contribution of the larger Antarctic ice-sheet (Shep-

herd and others, 2012). Moreover, from 1992 to 2011, the contribution of the GrIS to sea level rise has quadrupled and during the period 2005-2010 reached up to $0.9\,\mathrm{mm.yr^{-1}}$ (Shepherd and others, 2012). Concomitantly several large outlet glaciers accelerated (Holland and others, 2008; Joughin and Smith, 2013; Moon and others, 2012; Rignot, 2006) and thinned significantly (Figure 1.1, (Pritchard and others, 2009; Stearns and Hamilton, 2007)) highlighting the dynamic response of the GrIS. Using satellite gravimetry and modelled surface-mass-balance it has been estimated that the GrIS's mass loss is equally split between mass-balance processes (runoff and precipitation) and ice dynamics (van den Broeke and others, 2009).

Figure 1.1: Rate of change of surface elevation for Greenland over the period 2003-2007. After Pritchard and others (2009).

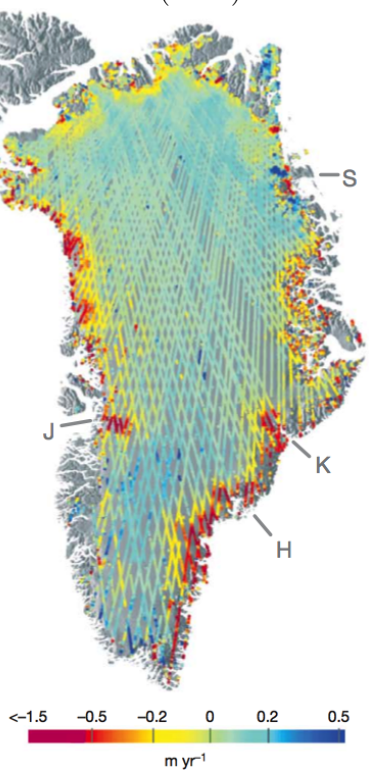

1.2 Characteristics of Greenland fjords

In NW Greenland, two distinct phases of dynamic ice loss (1985–1990 and 2005–2010) across the Melville Coast have been attributed to oceanic rather than atmospheric forcing (Kjær and others, 2012).

Glacier acceleration and thinning result from either (i) loss of buttressing at marine termini, through enhanced calving of icebergs, submarine-melt or the disintegration of ice shelves, or (ii) surface melt induced acceleration (Thomas, 2004).

1.2.1 Glacier front dynamics

At the front of a grounded marine-terminating glacier, the terminus position is in equilibrium with submarine-melt, advection and iceberg calving (Enderlin and Howat, 2013; Straneo and others, 2013). Calving is influenced by ice-mélange which buttresses the glacier front and impedes iceberg rotation and calving (Amundson and others, 2010). While advection is mostly related to glacier dynamics, through driving stress, basal drag, and lateral drag (Nick and others, 2010b), iceberg calving can reduce the basal and lateral drag of the glacier front hence potentially increase its velocity (Nick and others, 2010a; Todd and Christoffersen, 2014). Submarine-melting directly impacts the glacier front by ablation (Rignot and others, 2010; Straneo and Heimbach, 2013). The resulting undercut glacier front is thus thought to favour the calving of the overhanging ice (O'Leary and Christoffersen, 2013).

The outlet glaciers of the GrIS are connected to the surrounding ocean through long (50100 km), narrow (510 km) and deep fjords (hundreds of meters), often

characterised by one or more sills (Figures 1.2 and 1.3, Straneo and Cenedese, 2013) with depths vary considerably but typically of hundreds of meters for the large fjords (Johnson and Munchow, 2011; Rignot and others, 2010; Straneo and Cenedese, 2013; Straneo and others, 2012). Sill depth has been shown to have a significant impact on the fjord circulation and the water-masses found at the glacier front (Mortensen and others, 2011; Straneo and others, 2011, 2010).

Figure 1.2: Schematic ocean circulation around Greenland with the presence of warm, salty Atlantic Water (red to yellow) and cold, fresh Polar Water (blue). After Straneo and Cenedese (2013).

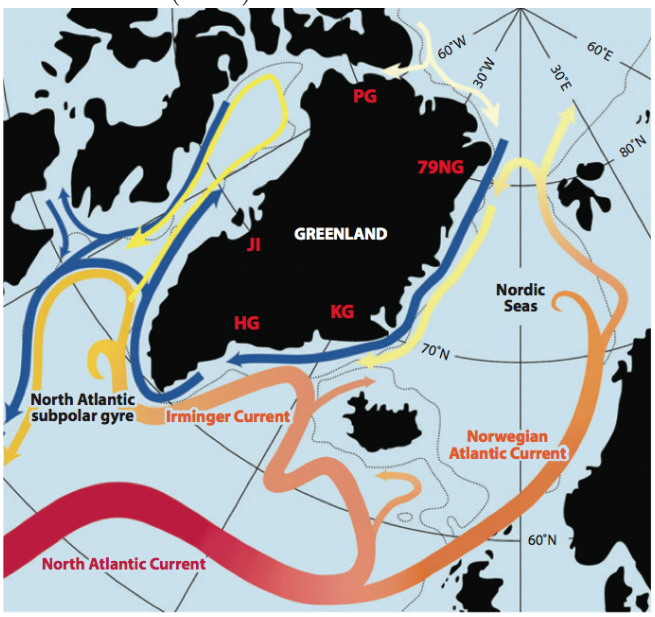

The waters found inside fjords usually correspond to those present on the nearby continental shelf, with the cold and relatively fresh Polar Water (PW) originating from the Arctic Ocean, advected around Greenland by the East and West Greenland currents (Myers and others, 2007; Straneo and Heimbach, 2013; Sutherland and Pickart, 2008), overlying the warm and salty Atlantic water (AW) with temperatures up to 10°C on the south-east coast, and cooling as it flows westward around

the south tip of Greenland (Figure 1.2, Holland and others, 2008; Mortensen and others, 2011; Straneo and Cenedese, 2013; Straneo and Heimbach, 2013; Straneo and others, 2012; Xu and others, 2013).

In addition, water-masses resulting from submarine-melting of the glacier and from mixing with subglacial runoff from glacier have been observed inside fjords (Johnson and Munchow, 2011; Mortensen and others, 2011; Straneo and others, 2011, 2012; Sutherland, 2012).

The advection of the warm AW around the south coast of Greenland transfers large fluxes of thermal energy of a subtropical origin into this sensitive polar environment (Christoffersen and others, 2012; Holland and others, 2008; Kjær and others, 2012; Mortensen and others, 2011; Ribergaard, 2009; Sutherland and others, 2013).

The frontal dynamics of tidewater outlet glaciers draining the GrIS can be profoundly influenced by AW, which has the potential to directly access their calving fronts via over-deepened glacial troughs cut through the continental shelf (Hanna and others, 2008; Pfeffer, 2007; Rignot and others, 2010). For example, in west Greenland the observed sustained attrition of Jakobshavn Isbræ, since 1998 (Joughin and others, 2012), has been attributed to the warming of subsurface water in Disko Bay and adjacent coastal seas (Holland and others, 2008). Similarly, AW was identified circulating within Sermilik and Kangerdlugssuaq fjords in east Greenland and is thought to be implicated in the retreat of Helheim and Kangerdlugssuaq glaciers over the last decade (Straneo and others, 2011, 2010).

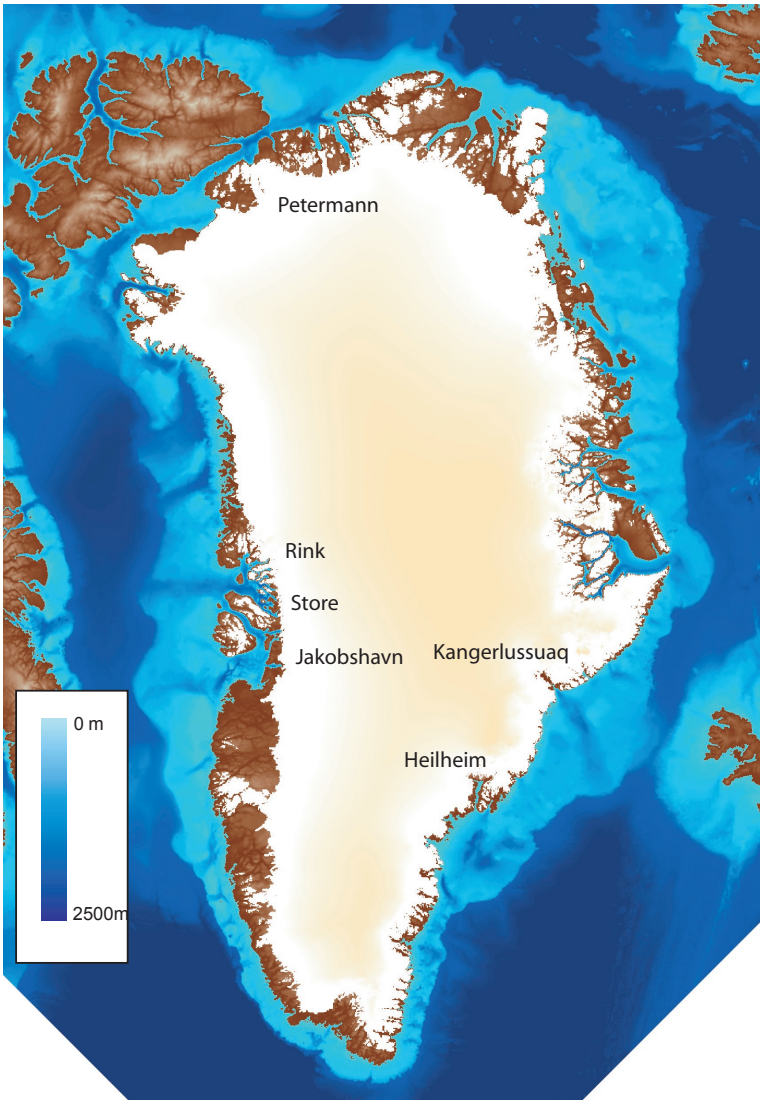

Figure 1.3: Greenland main tidewater glaciers and the IBCAO bathymetry (Jakobsson and others, 2012). Note the presence of troughs across the continental shelf for most major outlet glaciers.

1.2.2 Fjord circulation

In general, along-fjord circulation tends to dominate over across-fjord circulation, consistent with the fact that many fjords are too narrow for the circulation to be influenced by Earth's rotation (Jackson and Sutherland, 2014; Sciascia and others, 2014; Straneo and Cenedese, 2013; Sutherland, 2012). It is emerging that the along-fjord circulation in Greenland's deep fjords is more complex than the single convective cell (estuarine-like) circulation (Figure 1.5) that has been previously assumed in energy-mass balance calculations (Motyka and others, 2003; Rignot and others, 2010). For instance, a vertical superposition of convective cells was observed (Jackson and Sutherland, 2014; Straneo and others, 2011, 2012) and more recently modelled (Sciascia and others, 2013, 2014; Sole and others, 2012) within deep fjords in east Greenland (Figure 1.4).

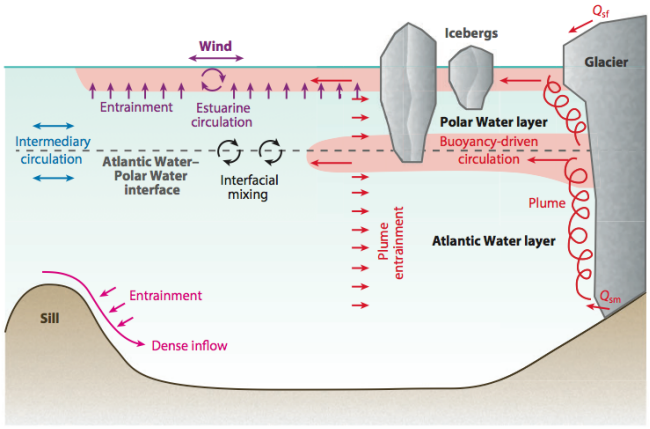

Figure 1.4: Schematic representation of the different circulations in a Greenland glacial fjord. Red indicates the buoyancy-driven circulation resulting from the submarine-melting and subglacial discharge; purple the estuarine circulation resulting from surface runoff only; blue the intermediary baroclinic circulation; and pink the circulation generated by the dense inflow over the sill. From Straneo and Cenedese (2013).

The presence of oscillating circulations forced by wind events on the nearby continental shelf (hereafter, intermediate circulation) has been demonstrated to be a major factor controlling the circulation and water masses present inside fjords, and therefore on the interaction with the glacier front (Jackson and Sutherland, 2014; Sciascia and others, 2014; Straneo and Cenedese, 2013).

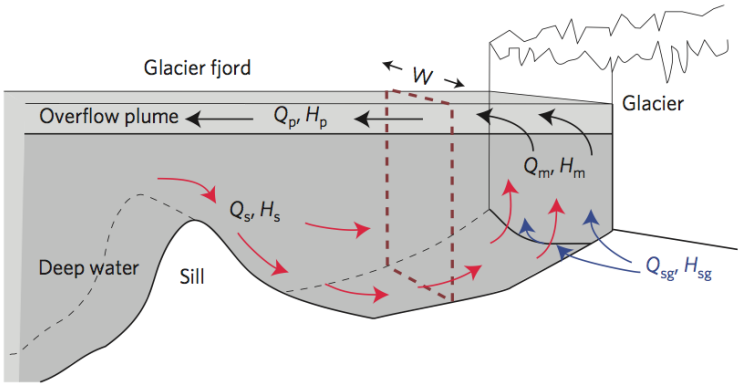

Figure 1.5: A simplified two-layer model of forced convective flow in a glacier fjord. Deep-water access is guarded by a sill and terminated by a calving front. The incoming mass flux from the deep ocean, Q_s, and from subglacial water, Q_{sg}, is balanced by the mass flux from the overflow plume, Q_p, and the submarine meltwater, Q_m The incoming deep-ocean heat flux, H_s, and subglacial water heat flux, H_sg, melt submarine ice with a heat flux, H_m, to yield an overflow plume with a heat flux, H_p The overflow plume is not homogeneous in velocity structure. After Rignot and others (2010).

1.3 Ocean-Glacier interaction processes

Several processes of interaction between the fjord water-masses and marine-terminating glacier fronts have been observed, modelled and/or speculated upon, including:

- Submarine-melting of the ice-face driven by warm AW present at the base of the glacier front.

- Discharge of subglacial fresh water at depth inducing a buoyancy driven convection and enhanced melting of the glacier front (Jenkins, 2011; Kimura and others, 2014; Mugford and Dowdeswell, 2011; Salcedo-Castro and others, 2011; Sciascia and others, 2013; Sole and others, 2012; Xu and others, 2013, 2012).

- Enhanced iceberg calving due to submarine undercutting of the glacier front (O'Leary and Christoffersen, 2013; Todd and Christoffersen, 2014).

All these processes are impacting or impacted by the submarine-melting of the glacier front. Moreover, ninety percent of the GrIS drains into the ocean (Rignot, 2006) and many of the outlet glaciers have deep (hundreds of metres) ice fronts (Straneo and Cenedese, 2013; Straneo and others, 2012) exposing a large area of the glacier front to the ocean. However, to date only limited observation and estimation of the submarine-melt rate have been made (Mortensen and others, 2011; Rignot and others, 2010; Sutherland, 2012; Xu and others, 2013), thus motivating the need to better understand submarine-melting, the specific controls governing it, and the potential impact on the glacier stability.

1.3.1 Quantification of submarine-melting

The most commonly discussed model for estimating the submarine-melt impact on the glacier front was developed from observation by Motyka and others (2003) for Alaskan glaciers. It is based on a heat, salt, and volume budget of the fjord water (Figure 1.5). The application of the Motyka model to Greenland glaciers has produced summer submarine-melt rate estimates of $0.7-4\,\mathrm{m\,d^{-1}}$ (Rignot and others, 2010; Sutherland, 2012; Xu and others, 2013), which are of the same order of magnitude as the typical front advection rates(Ahn and Box, 2010; Moon and others, 2012; Rignot, 2006; Ryan and others, 2014).

Similarly, numerical simulations of the ocean-glacier interface provides submarine-melt estimates of $2-6\,\mathrm{m\,d^{-1}}$ (Kimura and others, 2014; O'Leary, 2011; Sciascia and others, 2013; Xu and others, 2013). Moreover, modelling tests have suggested that submarine-melt rate is a function of the water temperature and the subglacial-runoff discharge.

Identification of the fjord water mass resulting from melting of the glacier front (hereafter Melt-water - MW) has been possible using a specific relation between the freshening and the cooling of the AW (Gade, 1979; Jenkins, 1999; Straneo and Cenedese, 2013; Straneo and others, 2011). Melt-water was observed in various fjords around Greenland (Johnson and Munchow, 2011; Mortensen and others, 2013; Straneo and others, 2011, 2012) suggesting that submarine-melt occurs at most marine-terminating glaciers around Greenland.

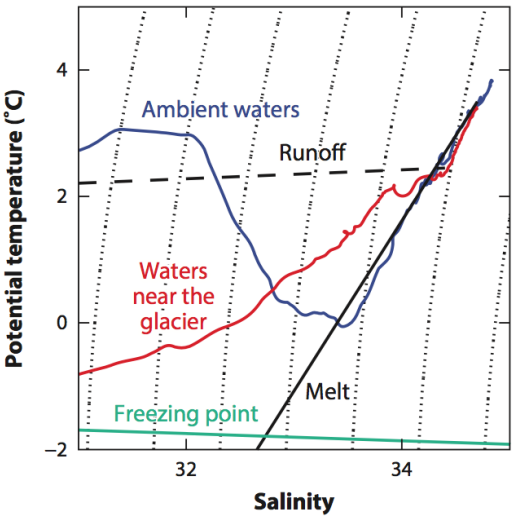

Figure 1.6: Potential temperature versus salinity (θ/S) plot at the mouth (blue) of Sermilik Fjord and near Helheim glacier (red) for August 2009. Overlaid are the submarine-melt line (solid black), runoff-mixing line (dashed black), freezing-point line (solid green), and isopycnals (dotted curves). This θ/S plots shows the transformation of ambient waters found near the mouth into a water column containing glacially modified waters found near the glacier. In summer, the glacially modified water contains both melt-water and subglacial fresh water (i.e. in θ/S space, its properties are within a triangle enclosed by the submarine-melting and runoff-mixing lines). From Straneo and Cenedese (2013); Straneo and others (2011)

1.3.2 Subglacial fresh water discharge

Subglacial discharge is a combination of many sources, which are drained through englacial and subglacial drainage networks to the glacier front (Bartholomew and others, 2011; Chandler and others, 2013; Cowton and others, 2013): (i) surface-melting ice and snow due to atmospheric forcing (hereafter, supraglacial runoff), (ii) basal melting of the glacier by friction against the bed rock and geothermal flux from the Earth (hereafter basal runoff), and (iii) rain events.

Refreezing and englacial/subglacial reservoirs can retain a portion of the supraglacial and basal runoff (Rennermalm and others, 2013), however the remainder reaches the glacier front where it is injected at depth into fjords producing a buoyant upwelling of sediment laden water, called a plume (Greisman, 1979; Jenkins, 2011; Kimura and others, 2014; Mugford and Dowdeswell, 2011; Salcedo-Castro and others, 2011; Sciascia and others, 2013; Sole and others, 2012; Xu and others, 2013, 2012). Some of the upwelling plume reaches the surface and hence can be observed and documented using the sediment concentration and extent (Chu and others, 2009; Hudson and others, 2014).

It was suggested that the internal dynamics of a plume can be divided into four sections (Figure 1.7, Kimura and others, 2014; Powell, 1990; Salcedo-Castro and others, 2011; Syvitski, 1989; Xu and others, 2013, 2012):

Figure 1.7: Sketches of upwelling plumes resulting from injection of subglacial fresh water at depth. Most commonly, subglacial discharge forms a jet that rises to the fjord surface (b and c) prior to outflow at the surface (c) or at depth (b). Some jets never reach the surface, and outflow directly at depth (a). ZFE: zone of jet flow establishment, VBP: vertical buoyant plume, HBP: horizontal buoyant plume. Adapted from Powell (1990)

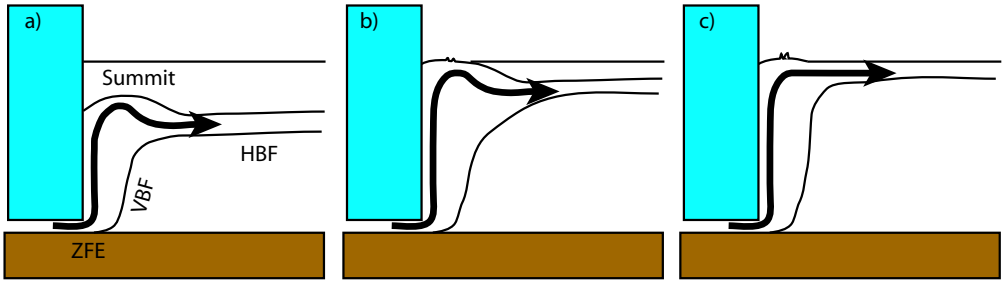

Injection at depth: The runoff water is injected at depth through subglacial or englacial conduits (Jenkins, 2011; Kimura and others, 2014; Rignot and

others, 2010; Xu and others, 2013) and thus mixes with the ambient water, initiating the buoyant plume water.

Vertical Plume: The buoyant plume water rises through the water column and along the ice face enhancing the submarine-melting of the glacier with an intensity function of the runoff discharge (Jenkins, 2011; Kimura and others, 2014; O'Leary, 2011; Xu and others, 2013) and the conduit shape (Kimura and others, 2014; Xu and others, 2013).

Summit: The plume reaches its shallowest point in the water column, or summit, when no more vertical kinetic energy is available, which in some case is at the surface of the fjord (Salcedo-Castro and others, 2011; Xu and others, 2013, 2012).

Horizontal Plume: Plume outflow occurs at its depth of hydrostatic equilibrium, which can be at the surface or at depth (Salcedo-Castro and others, 2011; Sciascia and others, 2013; Xu and others, 2012).

The identification of plume water resulting from the mixing of ambient water with subglacial fresh water is possible by distinguishing the specific relation between the freshening and the cooling of fjord water (Figure 1.6, Mortensen and others, 2013; Straneo and others, 2011, 2012).

It is understood that the circulation induced by the plume water enhances submarine-melting by renewing the water in contact with the glacier front as well as increasing the turbulent thermal and salinity transfer at the ice interface (Kimura and others, 2014; Sciascia and others, 2013; Xu and others, 2013, 2012). Numerical simulation suggests that the submarine-melt rate increases as the square or cubic-root of the subglacial runoff discharge (Sciascia and others, 2013; Xu and others, 2013).

Summer submarine-melting rates of $1-6\,\mathrm{m\,d^{-1}}$ (Rignot and others, 2010; Sciascia and others, 2013; Sole and others, 2012; Xu and others, 2013, 2012), which have been estimated for several glaciers around Greenland are thought to be attributable to the significant subglacial runoff discharge during the summer months (Chandler and others, 2013; Cowton and others, 2013). However, negative air-temperatures during the winter largely halts the generation of supraglacial-melt which should impede the submarine-melt rate. Numerical simulations have suggested that the free-forced (runoff-free) submarine-melting should be one order of magnitude smaller than in summer (Sciascia and others, 2013; Xu and others, 2013, 2012). Hence, in models evaluating the Greenland Ice Sheet response to ocean forcing, winter submarine-melt is neglected (Nick and others, 2013; Sciascia and others, 2013; Sole and others, 2012; Todd and Christoffersen, 2014). Nevertheless, Christoffersen and others (2012) have suggested that during winter months basal melting of the glacier contributes to the subglacial runoff discharge and could potentially double the winter free-forced submarine-melt rate.

1.4 Background methods

Due to this thesis being structured as short chapters which could be submitted independently in peer reviewed journals, this background section intend to give a general overview on the methods used and developed prior to this work (i.e. before 2012).

The section is divided into two sub-sections, the first discussing the identification methods of ocean-glacier interaction processes, and the second discussing the

methods developed to quantify these processes with a particular focus on the quantification of submarine melt.

1.4.1 Processes identification

The impact of submarine melt, on the potential temperature (θ) and salinity (S) of the surrounding ocean, was theoretically evaluated by Gade (1979). This study evaluate the idealized situation of an infinite horizontal ice slab sustaining melt as to represent the condition occurring at the base of the Antarctica ice shelf. Assuming homogenous properties both in the ocean and in the ice, negligible impact of thermodynamic effects of mixing different waters, of the limited range of water density involved, and of thermal diffusivity equal to the diffusivity of salt, the relation $\frac{d\theta}{dS}$ (fig. 1.8) take the form of:

$$\frac{d\theta}{dS} = S_{sw}^{-1}[\theta - \theta_f + \frac{C_i(\theta_f - \theta_i) + L_i}{C_{sw}}] \tag{1.1}$$

where θ_{f} is the pressure-corrected melting point of ice, L_{i} is the latent heat of fusion of fresh water ice, C_{i} and C_{sw} are the specific heat capacities of ice and seawater, respectively. It appear from eq. (1.1) that the slope $\frac{d\theta}{dS}$ is mostly governed by the intrinsic properties of ice and seawater and particularly the ratio $\frac{L_i}{C_{sw}}$ with a limited variation ($\sim 10\%$) due to the initial temperature of the ice (θ_i), the temperature and salinity of the surrounding water, θ_{sw} and S_{sw}, respectively, and the depth at which the melt occurs.

Jenkins (1999) has later enlarge the scope of Gade (1979) melt induced oceanic variation to a broader number of conservative common properties, χ of ice and seawater but that impart distinctive characteristics, such as: isotopically ratio of

Figure 1.8: Temperature and Salinity diagram of the Muir Inlet, Alaska, oceanographic survey 1967 (square) with Gade's meltwater line superimposed Gade (1979)-Fig. 5.

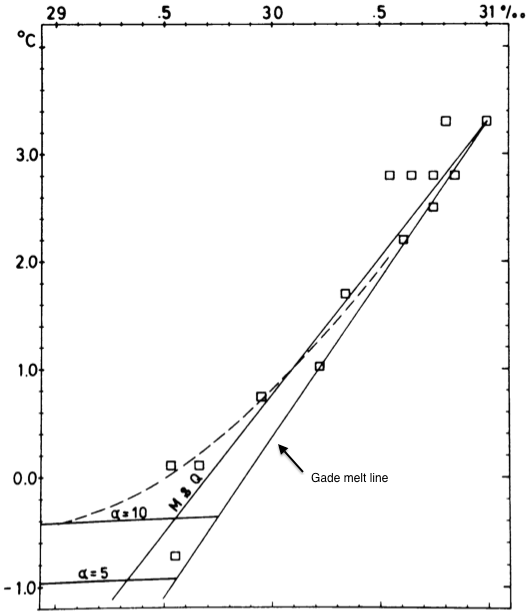

heavy forms of water or dissolved gases, salinity or heat content. Those characteristics, being conservative the mixing ratio of melted-ice within seawater can be determined by the mass of ice, Q_i, and of water, Q_w, that contribute to the mixture as follow:

$$Q\chi = Q_w\chi_w + Q_i\chi_i \tag{1.2}$$

where $Q = Q_i + Q_w$ is the total mass of the mixture.

To facilitate the comparison of variation of heat content to the other conservative properties, for an oceanographic point of view, Jenkins (1999) propose the usage of an effective potential temperature, θ_{eff}. This θ_{eff} is evaluated from the same energy budget as proposed by Gade (1979) in eq. (1.1), which includes an ocean

heat transfert to the ice by three distinctive processes: 1) warming of the ice from its in situ temperature to the freezing point θ_f, 2) absorption of latent heat during the phase change, and 3) mixing of the resulting melted-ice water with the ambient seawater.

θ_{eff} can thus be evaluated as follow:

$$\theta_{\mathrm{eff}} = \theta_{\mathrm{f}} - \frac{L_{\mathrm{i}} - C_{\mathrm{i}}(\theta_{\mathrm{f}} - \theta_{\mathrm{i}})}{C_{\mathrm{sw}}}, \tag{1.3}$$

Note that, θ_{eff} can take value as low as $\sim$-90°C, although this value do not reflect any real measurable temperature.

Therefore, if the seawater can be assumed to be uniform and knowing the initial salinity and temperature of both the seawater and the melting ice it is possible to identify a water mass that has been involved in submarine melting of ice as it will fall, in a temperature and salinity (TS) diagram (fig. 1.9), along a line with slope:

$$\frac{\theta_{sw} - \theta_{eff}}{S_{sw} - S_i} \tag{1.4}$$

where S_{sw} is the salinity of seawater melting the ice, S_i the salinity of ice, θ_{sw} the potential temperature of seawater, and θ_{eff} the effective temperature as estimated from eq. (1.3).

Later, Straneo and others (2011) has extended the meltwater identification method from Jenkins (1999) to the mixing of runoff water with the ambient seawater. Indeed, it was observed, in a TS diagram, that in Sermilik Fjord (East Greenland),

Figure 1.9: The meltwater mixing line as proposed by Jenkins (1999)-Fig. 5. The dashed lines represent approximations to the ambient trend in the main thermocline (bold) and a meltwater mixing line passing through the deepest waters, while dash-dotted lines are contours of meltwater fraction

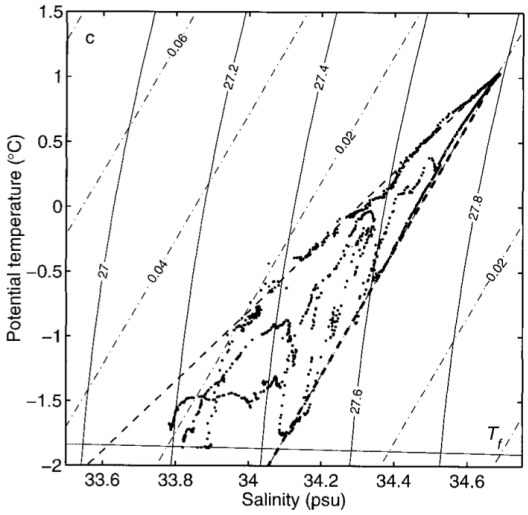

the meltwater depart from the the mixing line of the same name at a depth shallower than 300 m. It was thus supposed that an additional mixing with runoff water (originating from the glacier) is likely to occur (fig. 1.10). This mixing will follow a mixing line such as:

$$\frac{\theta_{sw} - \theta_{rw}}{S_{sw} - S_{rw}} \tag{1.5}$$

where S_{sw} is the salinity of seawater, S_i the salinity of ice, θ_{sw} the potential temperature of seawater, and θ_{eff} the effective temperature.

In all these studies the assumed temperature and salinity of the runoff water was assumed to be that of the fresh water freezing point (i.e. θ=0, S=0), which appears to be the most reasonable assumption since no direct measurement of the runoff water have been possible to date at the subglacial outlet.

Figure 1.10: The meltwater and runoff mixing lines as proposed by (Straneo and others, 2011)-Fig. 4. Potential temperature/salinity profiles at Sermilik fjord (Helheim Glacier), from August 2009, at various across section ranging from 20 – 40 km from the glacier front. Overlaid are the meltwater line (black solid; uses the densest warm water as an end point) and the runoff mixing line (black dashed; uses properties at 300 m as an end point).

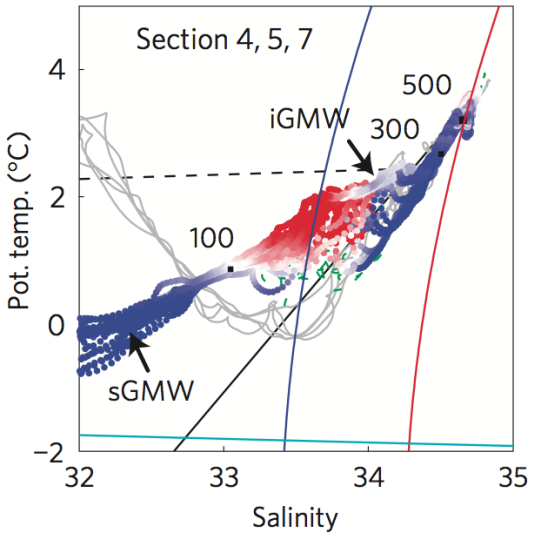

Comparing the temperature and salinity in the water column from a transect 60 km down the fjord with the water nearer the glacier front, Straneo and others (2011) shows that it is possible to identify the impact of the ocean-glacier interaction on the water column. The temperature and Salinity anomaly also permit to infer the fjord circulation induced by the outflow of runoff and meltwater (fig. 1.11).

These identification methods are first used in this thesis in chapter 3 in order to evaluate which processes are taking place at the front of Store Glacier and later modified in chapter 4 to develop a new quantification method of the submarine melt estimation from hydrographic survey.

Figure 1.11: Along fjord temperature (e and f) and salinity (g and h) anomaly in Sermilik fjord. The inferred circulation is marked with the black arrows (Straneo and others, 2011)-Fig. 3.

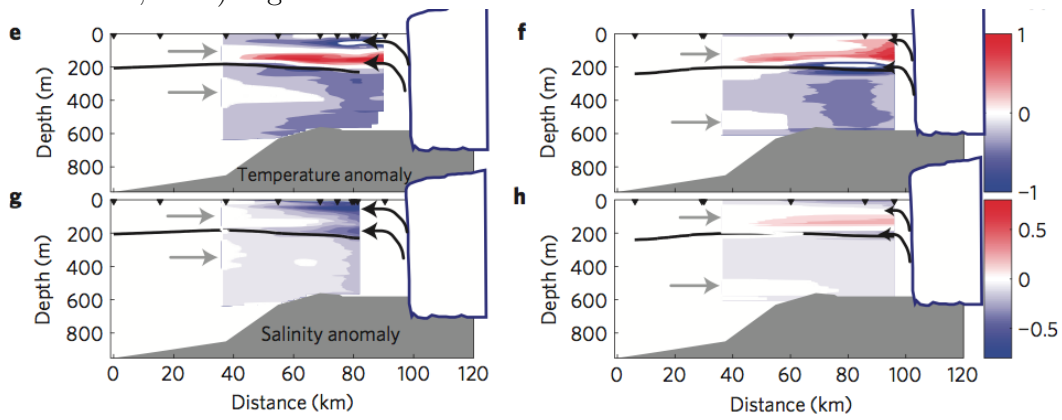

1.4.2 Processes quantification

In order to evaluate the total submarine melt sustained by Le Comte Glacier (Alaska) during a summer survey, Motyka and others (2003) developed a simplified model of the fjord circulation and interaction. This model is based on the conservation of salt, volume, and heat throughout the fjord such that by determining the characteristics of the water (i.e. temperature, salt, current) through a cross section of the fjord it is possible to evaluate the average submarine melting occurring on the glacier. It assume a negligible heat transfer from the atmosphere to the ocean and the absence of other source of salt than the ocean. In this model the introduction of subglacial runoff water at depth drives a convective flow along the ice face, drawing deep and warm water toward the ice producing submarine melt of the glacier. The buoyant meltwater rise in a turbulent plume; which outflow near the surface (fig. 1.12). In order to estimate the meltwater discharge, it is a two steps process: First a volumetric flux estimation is made on a cross section down fjord which as a net outflow of plume water, Q_p, due to the influx of

Figure 1.12: Model of forced convective flow in proglacial fjord from Motyka and others (2003)-Fig. 5. Subglacial discharge, Q_{sq}, carrying heat, H_{sq}, drives convection, drawing deep saline water (Q_s, H_s) toward terminus where the two components mix and turbulently rise along the ice face. The ascending waters melt ice along the face (Q_m, H_m), which adds to convection. The turbulent plume reaches the water surface then flows away from the terminus in over- flow plume (Q_p, H_p).

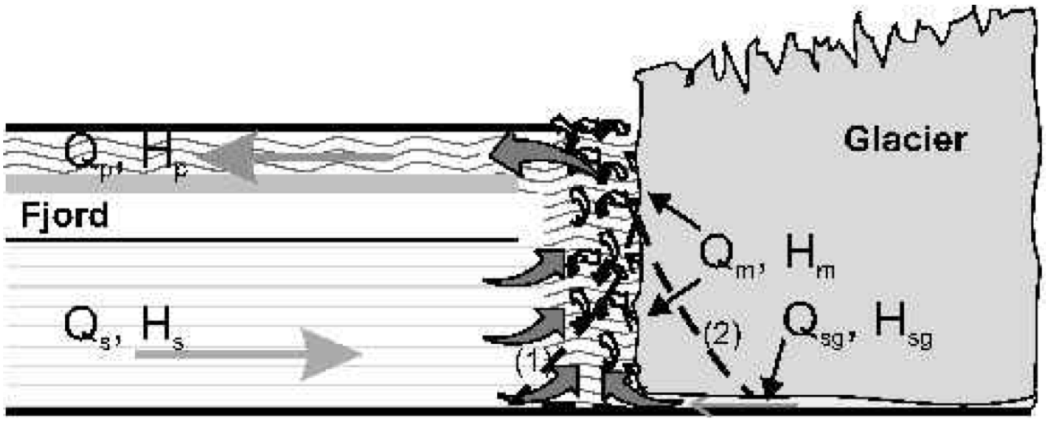

subglacial runoff in the fjord, Q_{sg}, and the production of meltwater, Q_m such as:

$$Q_p = Q_s + Q_{sg} + Q_m \tag{1.6}$$

where Q_s is the influx of seawater at depth.

Secondly, from the conservation of energy, assuming the ice and subglacial runoff water to be at 0°C, and taking $H_s^{T=0°C}$ as a reference state, the heat budget can

be written:

$$H_s + H_{sg} - H_p - H_m = 0 \tag{1.7}$$

$$H_s - H_p - H_m = 0 \tag{1.8}$$

$$H_m = H_s - H_p \tag{1.9}$$

where H_m is the latent heat lost to melting ice. It is thus assumed that at first order H_s and H_p are isothermal and isohaline therefore their values can be estimated as follow:

$$H_s = \rho_s Q_s C_s T_s \tag{1.10}$$

$$H_p = \rho_p Q_p C_p T_p \tag{1.11}$$

Assuming the ice and the surrounding water to be at the melting point, the discharge of meltwater can thus be deduced from:

$$Q_m = \frac{H_s - H_p}{L_i} \tag{1.12}$$

Similar calculation can be integrated from discrete layers of the water column if $Q(z)$, $\theta(z)$, and $S(z)$ are known.

It is subsequently possible to evaluate the subglacial runoff discharge $Q_s g$ from the salt budget. Indeed, the salt budget, integrated over the cross section of the fjord, is assumed to be null (i.e. no external source of salt) allowing to evaluate the net

fresh water budget (i.e. $Q_m + Q_{sg}$) using eq. (1.6) as follow:

$$\begin{aligned} Q_s S_s - Q_p S_p &= 0 \\ Q_s(S_s - S_p) - (Q_{sg} + Q_m) S_p &= 0 \\ Q_{sg} &= \frac{Q_s(S_s - S_p)}{S_p} - Q_m \end{aligned} \tag{1.13}$$

where S_p and S_s are the salinity of the plume and the seawater, respectively.

In the case where the fjord volumetric budget is not perfectly known, a compensative seawater discharge Q_s^{comp} can be evaluated in order to close the salt budget which as to be null. It follows:

$$Q_s S_s - Q_p S_p + Q_s^{comp} S_s = 0 \tag{1.14}$$

$$Q_s^{comp} = \frac{Q_p S_p - Q_s S_s}{S_s} \tag{1.15}$$

and eq. (1.10) becomes:

$$H_s + H_s^{comp} - H_p - H_m = 0 \tag{1.16}$$

$$H_m = H_s + H_s^{comp} - H_p \tag{1.17}$$

and then from eq. (1.12) it turns that the submarine meltwater discharge becomes:

$$Q_m = \frac{H_s + H_s^{comp} - H_p}{L_i} \tag{1.18}$$

Rignot and others (2010) applied the Motyka and others (2003) model to Greenland's glacier investigating Torsukatak, Eqip, and Kangilerngata glaciated fjords of Disko bay (West Greenland -fig. 1.13). In this survey, the current was estimated from a 5 min average at 1.5 m interval in the top 50 m and 15 m interval below 50 m. Tidal currents was not corrected. Temperature and salinity was recorded both during the descent and ascent of the hydrographic profiler. One convective cell circulation was assumed as for Motyka and others (2003) to close the volumetric budget.

Figure 1.13: Temperature, salinity and current cross sections from Torsukatak Glacier used in the Motyka model by Rignot and others (2010)-Fig. 3. The position and depth of the hydrographic profiles are shown by the white line. The horizontal distance is from North to south in km.

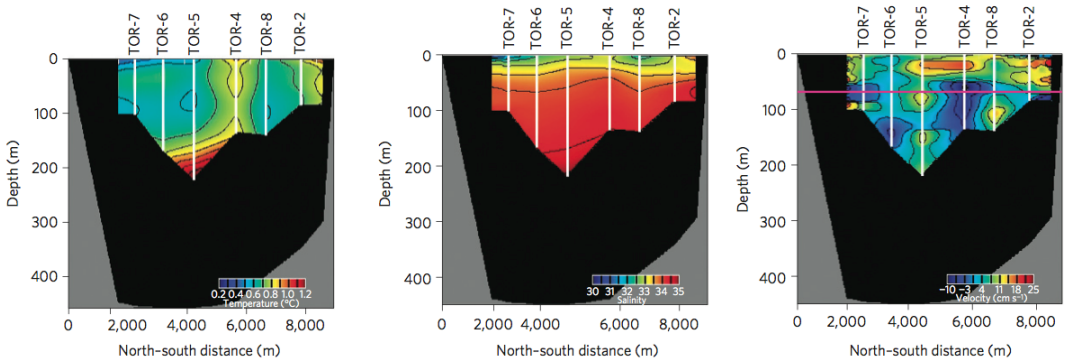

Later, Motyka and others (2003) model was applied at Store glacier by Xu and others (2013)from a hydrographic survey (temperature, salinity and current versus depth) from August 2010 in Store Fjord collected on a cross section about 1 km away from the ice front (fig. 1.14). In this estimation the upper 20 m of the water column is excluded for two reasons: 1) the high temperature and low salinity of this layer are primarily supposed to be due to solar heating and melting of calved ice debris, and therefore, do not provide useful information about submarine melting; and (2) the relatively fresh, warm, and therefore stable surface waters do not

participate in the melting of ice below the surface. An estimating of the error from omitting the upper layer is added in the error budget. Temperature, salinity, and velocity are interpolated and extrapolated across the entire hydrographic section. For velocity, it is assumed by Xu and others (2013) a zero velocity along the sidewalls of the fjord. Finally the missing velocity data at depth are estimated closing the salinity budget of Motyka and others (2003) model.

Figure 1.14: Temperature cross section from Store Glacier used in the Motyka model by Xu and others (2013)-Fig. 1. The position and depth of the hydrographic profiles are shown by the dashed line. The horizontal distance is from North to south in km.

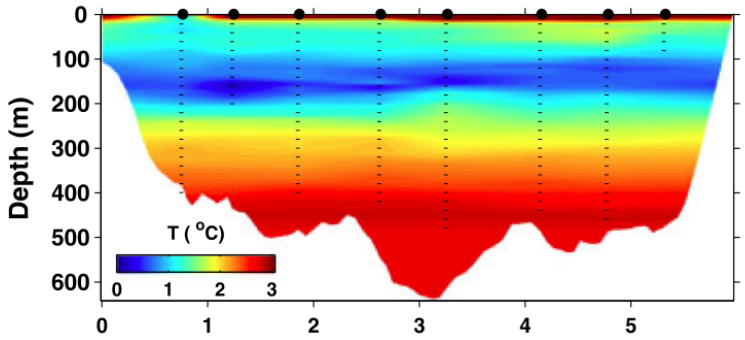

In order to estimate the spatial distribution of submarine melt, induced fjord circulation, and impact of the subglacial discharge on these latter, one-dimensional model have been developed by Jenkins (2011) and later modified by O'Leary (2011).

The model developed by Jenkins (2011) is based on the theory of buoyant plumes (Jenkins, 1991) and intend to account for observation of melting near the grounding lines of glaciers both of ice shelves and vertical calving front. The model is steady in time, uniform in the across-flow direction, follow the distance from the grounding line, and its four differential equations conserve the fluxes of mass, momentum,

heat and salt. The model considers that the same physical approach can be used for an ice-ocean interface ranging from near horizontal (e.g. ice shelf) to vertical (e.g. tidewater glacier) and only the angle of the ice face in respect to the vertical is to be taken into account (fig. 1.15).

The one dimensional model also assume limited impact of the Coriolis effect particularly on a vertical wall, and horizontal homogeneity (i.e. the discharge outlets of subglacial runoff are spread along the whole grounding line).

Figure 1.15: One dimensional model of plume driven flow on an ice-ocean interface from Jenkins (2011)-Fig. 1. One dimensional model of plume driven flow and submarine melt on an ice-ocean interface. The model assumes that a similar approach can be taken for a vertical tidewater glacier and an ice shelf where only the angle of the ice-ocean interface is different.

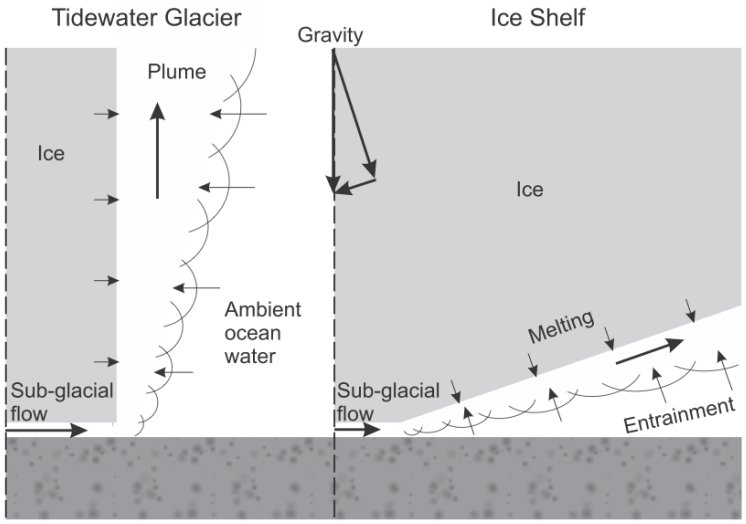

This model intend to focus on the near grounding line melt rate and the flux of fresh water as well as the angle of the ice-ocean interface can be adjusted.

To take into account the buoyant plume variability of shapes in the horizontal plane, O'Leary (2011) has modified the model from Jenkins (1991, 2011) and added a geometry factor, to take into account the potentially localised or spread subglacial

runoff portal(s), leading a plume shape varying from semi-conic to prism-like, respectively (fig. 1.16).

Figure 1.16: One dimensional model of plume driven flow on an ice-ocean interface with a shape factor α from O'Leary (2011)-Fig. 2.1.

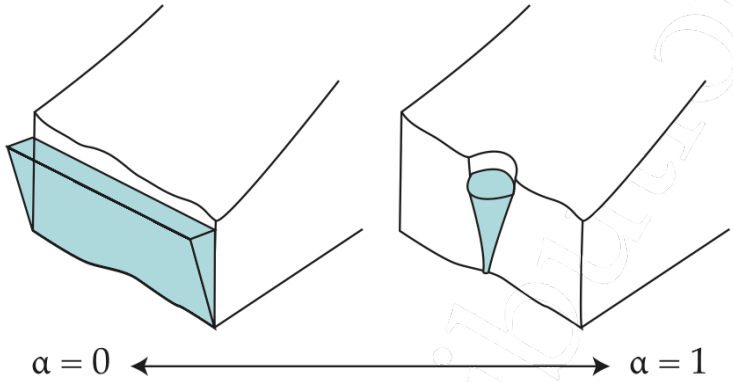

Multi-dimensional numerical simulation approach have been used to get a better understanding of the circulation, submarine melt rate, and impact of the subglacial discharge on these latter. Although this work was produced during the span of this thesis, a resume of their methods will be indicated here in order to give a better understanding of the methods underlaying their results. Detailed comparison of the results will be given in the respective chapters.

Sole and others (2012), used a 2-D model spreading along the center line of the Kangerdlugssuaq Fjord (East Greenland) and originating on the glacier side at the plume outlet. Physically the model is based on the Bergen Ocean Model with σ-coordinate (bathymetry following). This model assumes Boussinesq and hydrostatic approximations and allows to vary the driving influence of: discharge and depth of entrance of the subglacial runoff, tidal forcing, wind forcing (fig. 1.17). The subglacial forcing is estimated from the catchment area and an estimation of the aerial melting occurring on the glacier. An added discharge is considered for

the production of runoff water from basal friction. The time-series of subglacial forcing is shown in fig. 1.17. During the winter months (i.e. September to May, included) no subglacial runoff discharge is considered. This model tends to create

Figure 1.17: Two dimensional model of fjord circulation in a glaciated fjord from Sole and others (2012)-Fig. 3. a-c) time-serie showing the external forcing (i.e. subglacial runoff discharge, tide, and wind) of the model during a year long experiments. d) The model domain with the relaxation zone (FRSZ) at the fjord mouth.

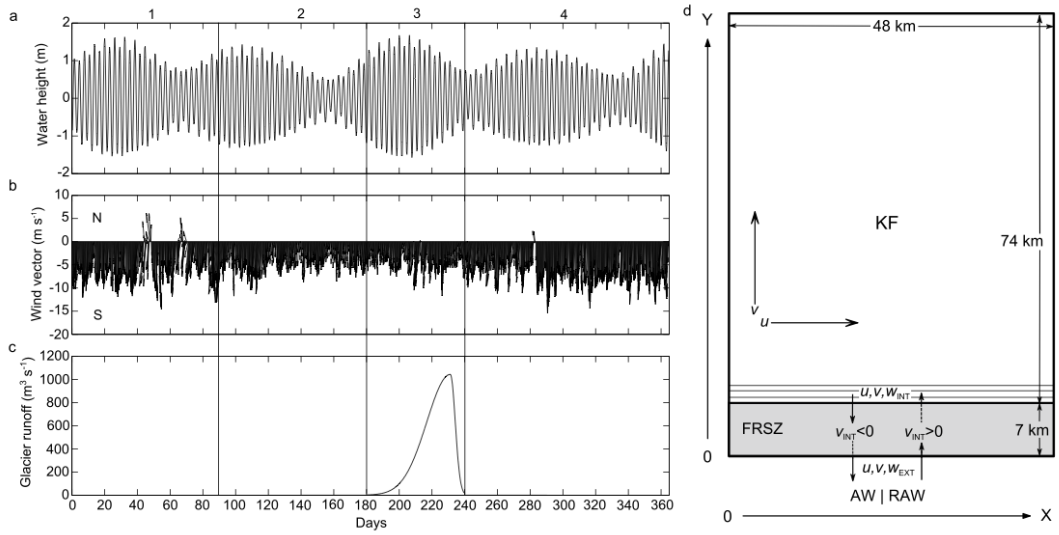

a double convective cell fjord circulation (fig. 1.18) contrarily to the simpler one convective cell fjord circulation assumed by Motyka and others (2003)-fig. 1.12.

Simultaneously,Sciascia and others (2013, 2014) has used a high resolution 2-D model for similar simulations that Sole and others (2012) but for Sermilik Fjord (Helheim Glacier - East Greenland). The physics of the model is based on the MITgcm which assumes Boussinesq and non-hydrostatic conditions. The domain has a curvilinear grid with finite-volume discretisation on an horizontal Arakawa C-grid, and with vertical z-levels, following the along fjord center line of the fjord.The

Figure 1.18: Schematic fjord circulation generated by the two dimensional model from Sole and others (2012)-Fig. 9.

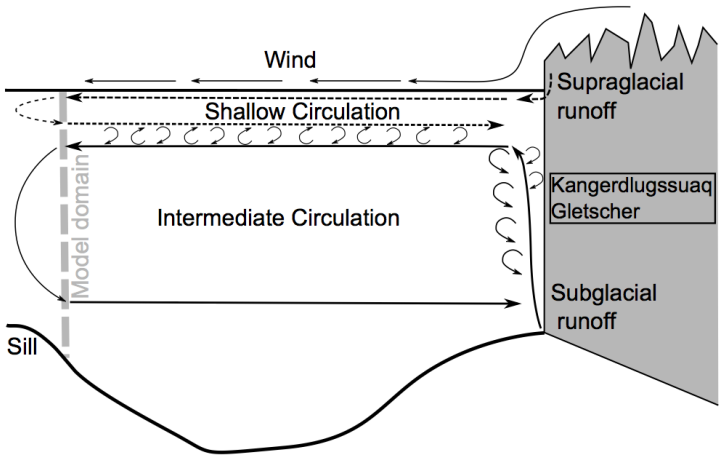

horizontal and vertical resolution at the glacier front are 10 m. At the glacier front the model assumes the injection of subglacial runoff discharge, confined to the lowest two cells near the bottom (fig. 1.19).

Figure 1.19: Two dimensional fjord model domain from Sciascia and others (2013)-Fig. 1. The two main forcing layers: Polar water and Atlantic water and their physical characteristics are labeled on the figure.

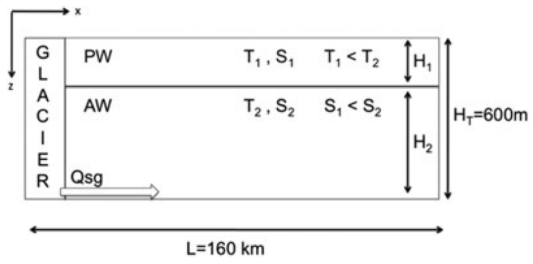

According to Sciascia and others (2013), the domain is sufficiently long (i.e. 160 km) for the simulations to reach a steady state before the open boundary conditions influence the circulation at the glacier front.

The parameterisation of the turbulent heat and salt transfert adopt a functional dependence on water velocities. The ocean initial condition are simplified using a two layers stratification based on temperature and salinity survey from both winter and summer. Winter experiments are run without subglacial discharge. Summer experiment contain a continuous discharge of subglacial runoff. The discharge is evaluated from an overall aerial melt on the glacier catchment (Andersen and others, 2010) and consider two scenarios: 1) the subglacial discharge is uniformly distributed along the entire base of the ice front; 2) the entire subglacial discharge occurs in a single opening 200 m wide.

At Store Glacier, Xu and others (2012) used also the MITgcm 2-D model with similar assumption that Sciascia and others (2013). The model resolution as a 20 m horizontal grid spacing (fig. 1.20). The fjord temperature and salinity used as initial conditions and the estimated depth of the ice front were collected in August 2010. To determine the subglacial runoff discharge, Xu and others (2012) uses the surface runoff estimate from the Regional Climate Model (RACMO) as a proxy. It is thus assumed that: a) all glacier surface meltwater collects at the glacier bed upstream of the glacier terminus and b) subglacial meltwater channels are expected to merge into a few large channels before reaching the terminus, as is commonly observed at land terminating glaciers. The subglacial runoff rate is considered to vary from 500 $m^3 s^{-1}$ in summer to near-zero in winter.

The size of the subglacial portal at the base of the ice front is evaluated from the assumption of a balanced rate of opening from melting the inner face and closure caused by ice deformation. The channel is thus assumed to have a cross section of 50-100 m^2, which are then test with rectangular shape of size of: 2.5×10 m, 5×10 m, and 10×10 m. The same model that Xu and others (2012) was later

Figure 1.20: Two dimensional fjord model domain for Store Glacier and the fjord initial conditions (i.e. temperature and salinity) from Xu and others (2012)-Fig. 1.

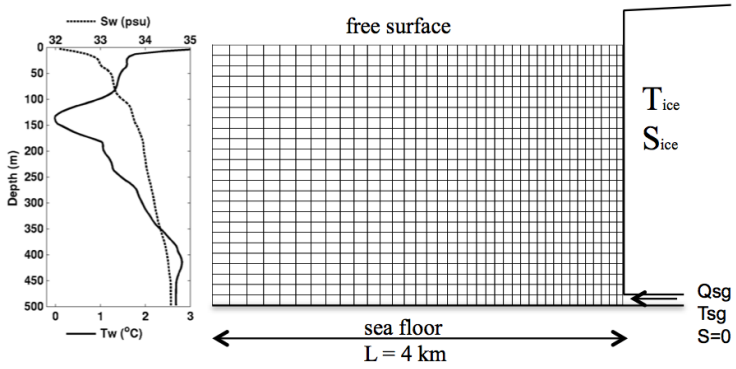

developed by Xu and others (2013) for high resolution 3-D simulations of the region of the subglacial forced plume of Store Glacier. The model domain has a uniform sea floor at 500 m depth and the fjord is rectangular in shape with a simulation section of the vertical ice face 150 m in width and extends 500 m from the ice face. The horizontal and vertical grid spacing is 1 m near the glacier front and increase horizontally to 5 m near the open ocean boundary. Similar estimation that Xu and others (2012) are used to force the model with subglacial discharge, temperature and salinity. Subglacial discharge portals are estimated to have a size from 0 to 90 m and are 1/, high.

Theoretical plume circulation model and associated melt rate have also been evaluated from a 3-D model by Kimura and others (2014). This model is based on the Fluidity-ICOM model which was first applied on ice shelf (Kimura and others, 2013) to evaluate circulation and melt rate. It uses the non-rotating Boussinesq and non-hydrostatic equations in a Cartesian coordinate system with a finite-element grid. The model has been extended to simulate not only the melting but also frazil ice formation and deposition to better represent the potential freezing

Figure 1.21: Three dimensional plume induced circulation for Store Glacier and the salinity impact for 3 different configuration of the subglacial discharge, after Xu and others (2013)-Fig. 1.

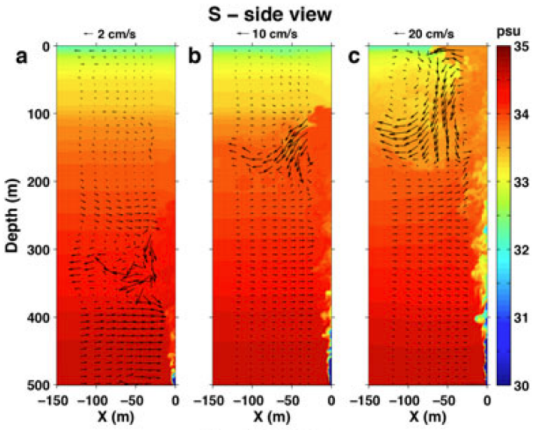

process. These experiments intend particularly to evaluate the geometry of the rising plume in the presence or absence of an ice wall and particularly to determine if the plume is in contact with the ice front during its ascent. Various configuration of number and size of the subglacial outlet are tested with a base case scenario with a channel 10×10 m in width and height. The subglacial discharge is varied from 30-150 $m^3 s^{-1}$.

Figure 1.22: Three dimensional simulation of a plume induced circulation and temperature establishing on a vertical ice wall after 300 s (a), 700 s (b), and 1300 s (c), from Kimura and others (2014)-Fig. 4.

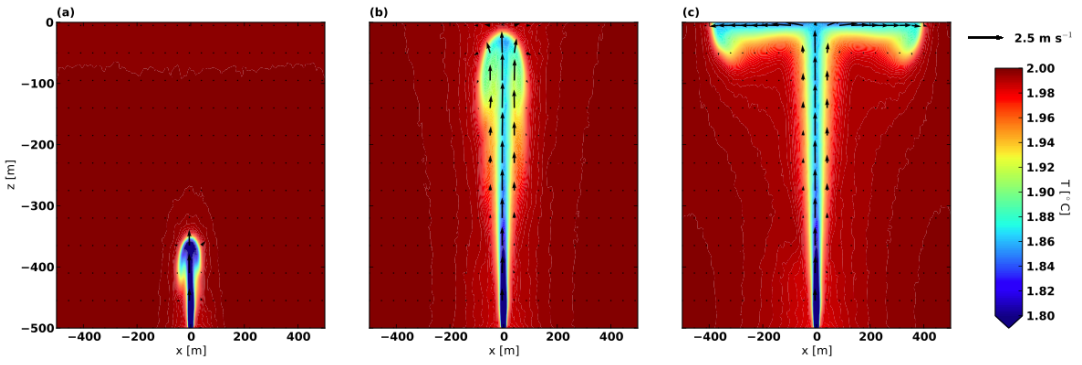

1.5 Aims and objectives

The aim of this thesis is to further our knowledge of the processes in action at the ocean-glacier interface and their seasonal evolution. This thesis particularly focuses on in-situ measurements to identify and quantify the controls that govern submarine-melting and subglacial discharge impacts on the glacier front. It is hoped that the insights gained will contribute to our collective understanding of the interdependent behaviour of marine-terminating margins of the Greenland Ice Sheet and the adjacent ocean.

Within these broad aims the following specific objectives have been identified:

1. Identify the spatial and temporal pattern of submarine-melting and subglacial discharge at marine-terminating glaciers.
2. Quantify the impacts of the submarine-melting on the glacier front during the summer and winter months.
3. Develop robust and innovative methods to quantify the submarine-melting.
4. Evaluate the structure of the upwelling plume and its impact on the glacier front, internal and external to the plume itself.
5. Develop a method to quantify the plume characteristics and their evolution.

1.6 Structure of thesis

This thesis is structured into 10 chapters. Chapter 1 has introduced the Greenland Ice Sheet and the interaction with the oceans that border it. Chapter 2

introduces the field site and the survey platform. Chapters 3 to 8 take the form of standalone experiments: Chapter 3 identifies the spatial and temporal patterns of ocean-glacier interaction processes between two major outlet glacier fronts; Chapter 4 estimates the submarine-melt rate during the winter 2012-2013 using two independent models based on oceanographic measurements; Chapter 5 quantifies the horizontal circulation induced by the plume along the whole glacier front and discusses the plume response to two atmospherically-driven extreme-melt events during the summer 2012; Chapter 6 observes the internal structure of two buoyancy driven upwelling plumes, their forcing and impact on the glacier front; Chapter 7 observes the impact of submarine-melting on a recently calved iceberg; and Chapter 8 develops a novel method to directly measure the submarine-melt rate of the glacier and discusses the spatial impact of the submarine-melt during the summer 2012. Chapter 9 discusses the results presented in Chapters 3 to 8 and places them into a broader context,and identifies directions for future research. Finally Chapter 10 presents the main conclusions of this thesis.

Chapter 2

Field site and survey platform

Uummannaq Bay is unique on the west coast of Greenland insofar as it has an over-deepened glacial trough to at least $\sim 450\,\mathrm{m}$ depth, which extends uninterrupted to the continental shelf break (Jakobsson and others, 2012) (Figure 2.1). The trough provides a direct route for the warm Atlantic water from Baffin Bay to enter the inner fjord basins and access over a dozen marine-terminating outlet glaciers which drain this sector of the GrIS (Figure 2.1). The existence of many large marine-terminating outlet glaciers draining into Uummannaq Bay, makes it a useful target to identify, isolate and quantify oceanic forcing on the glacier fronts.

Store and Rink glaciers are, after Jakobshavn Isbræ (Figure 2.1), the second and third fastest and biggest contributors to ice discharge from the west sector of the Greenland Ice Sheet, (Moon and others, 2012; Rignot, 2006).

This thesis will focus mostly on Store Glacier because it offered the possibility to be monitored during the winter months. Moreover, summer observations of warm Atlantic water at depth within Store fjord (Xu and others, 2013) and seasonal

Figure 2.1: Map of the study area with the three main glaciers of West Greenland: Jakobshavn, Rink, and Store. In this thesis we will focus mostly on Store Glacier. Bathymetry is extracted from IBCAO-v3 (Jakobsson and others, 2012).

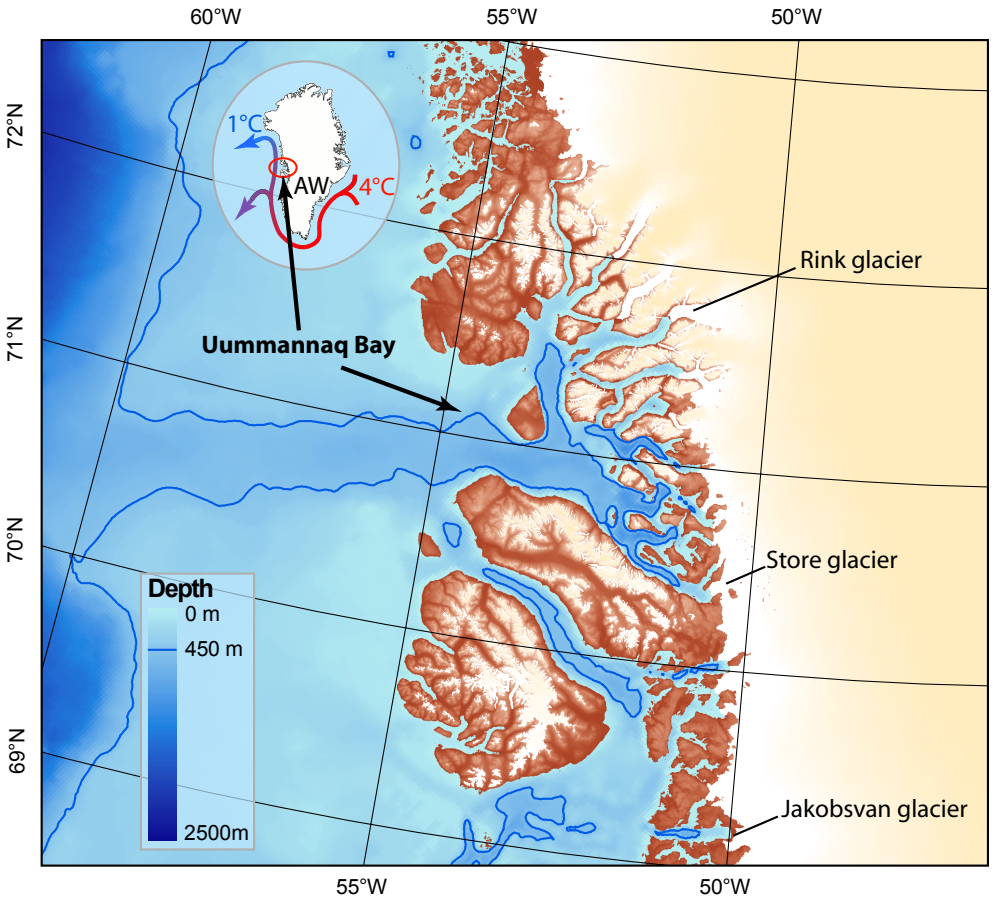

seaice cover render this tidewater glacier a good target for investigating winter and summer ice-ocean processes and associated circulation that are relevant to other major marine-terminating outlets.

Store Glacier is located at 70° N, 50° W and has an estimated ice discharge of $11-18\,\mathrm{km^3\,yr^{-1}}$ (Ryan and others, 2014; Weidick and Bennike, 2007) with near-terminus flow speeds of $\sim 14-16\,\mathrm{m\,d^{-1}}$ (Ahlstrøm and others, 2013; Ahn and Box,

2010; Ryan and others, 2014). This corresponds to 8% of the total annual discharge for the western GrIS (Rignot, 2006).

The glacier terminus is over 5 km wide and ~500 m deep, with a catchment sizes of 34 000 km^2 (Rignot, 2006). A 100 km long fjord connects the glacier front to Baffin Bay via a trough, with a minimal depth of 450 m, across the continental shelf, allowing water shallower than 450 m to enter the fjord uninterupted (Figure 2.1).

Figure 2.2: Store Glacier terminus in July 2012, view from its north flank

From 2005 to 2010 Store Glacier's front has been steadily speeding up by as much as 12% yr^{-1} (Figure 2.3, Ahlstrøm and others, 2013; Moon and others, 2012). Despite this acceleration, its front position remained relatively steady from 2000 to 2009

(Joughin and others, 2010; McFadden and others, 2011; Moon and others, 2012) implying that Store Glacier is at a stable position (Benn and others, 2007).

2.1 Bathymetric survey of Store Fjord

The bathymetry of the fjord and particularly the presence and depth of inner sills have a strong influence on the water-masses circulation in the fjord and present at the glacier front (Mortensen and others, 2011; Straneo and Cenedese, 2013). Around Greenland, most fjords have over-deepened inner basins (Jakobsson and others, 2012; Mortensen and others, 2011; Straneo and Cenedese, 2013), but the lack of exact bathymetry prevents an assessment of whether water-masses are able to penetrate fjords to the glacier fronts. It has been shown that shallow sills, while preventing deep water from entering the fjord, can produce dense warm water filling the inner basin and reaching the glacier front (Mortensen and others, 2011).

Bathymetric chart of the continental shelf of Greenland are widely available (Jakobsson and others, 2012), yet little is known of the inner part of most of the coastline. In Rink Fjord and in the outer part of Uummannaq Bay, a multibeam survey was conducted in 2009 (Dowdeswell and others, 2014) and located a transverse sill ~ 60 km from the ice front with a minimum depth of ~ 400 m. However, no bathymetry data are available at Store Glacier.

Here we present the results of a dense single beam bathymetric survey of Store Fjord, revealing the presence of an inner basin more than 50 km long with depths greater than 900 m and the absence of inner sill.

Figure 2.3: West Greenland flow speeds for 2005/06 (left) and change in speed from 2000/01 to 2005/06 displayed over a 2000/01 SAR mosaic (grayscale (©CSA, 2001)) (right). Speed is indicated by color and white 250 m.a^1 contours (v<1000 m.a^1) and black 1000 m.a^1 contours (v≥1000 m.a^1). Speed differences are shown with color (saturation is reduced where speed-up or slowdown is <20 m.a^1) and 500 m.a^1 black (speed-up) and white (slowdown) contours. Blue and red dots indicate retreat (red) and advance (blue). From Joughin and others (2010).

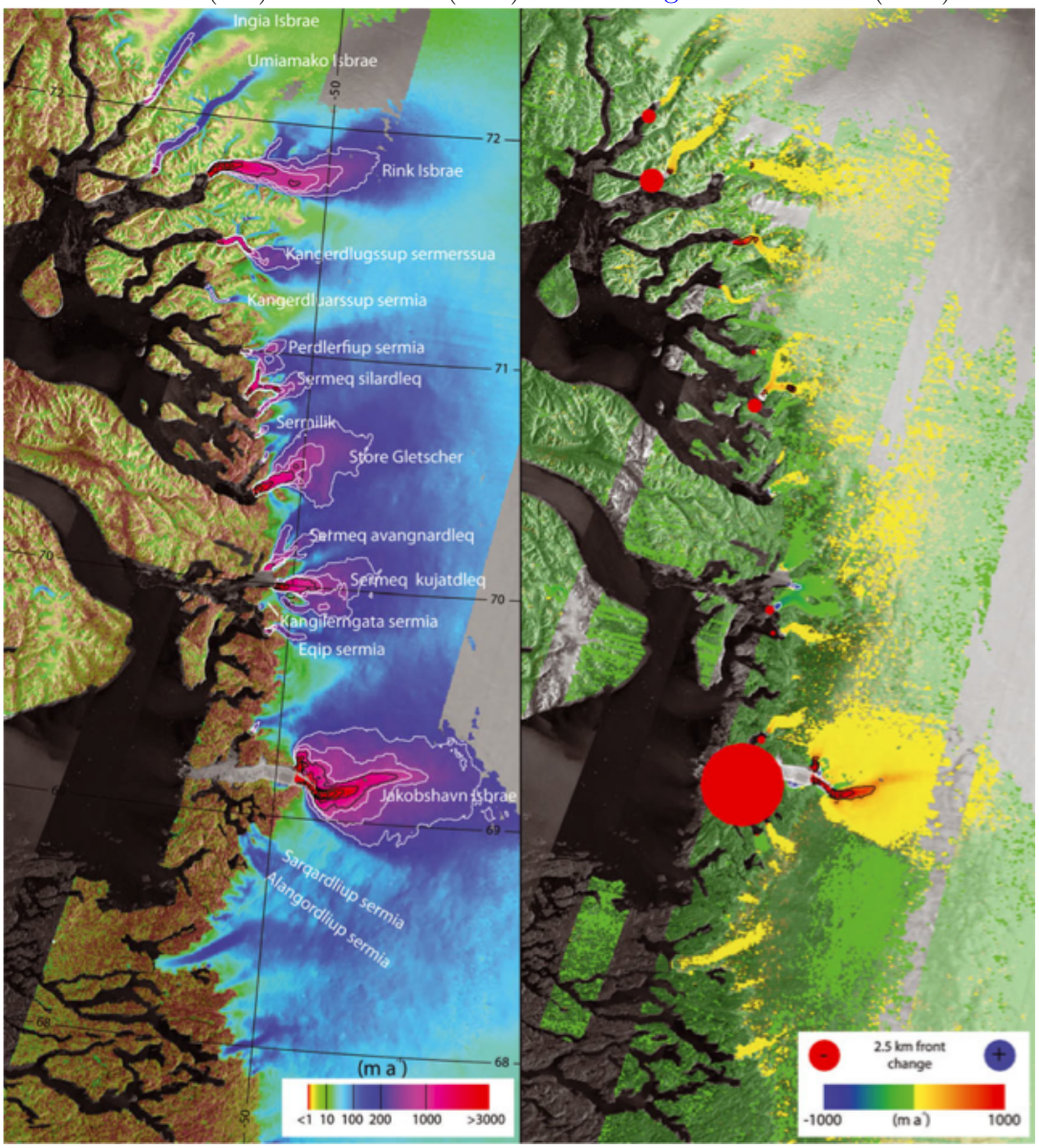

2.1.1 Method

In situ data

Single beam bathymetry data from Store Fjord and at the glacier front were obtained between 2009 and 2013 using a Raymarine 50 – 200 kHz, 1 kW depth sounder installed on the hull of the research sailing vessel Gambo (Figure 2.5). Georeferencing of the bathymetry survey was performed using a single frequency GPS receiver with an horizontal error of approximately 5 m. Due to the strong pycnocline found in glaciated fjords (Straneo and others, 2012), the echo sounder occasionally interpreted the pycnocline at ∼100 m depth as the fjord bottom required the data to be manually filtered.

Multiple source of depth uncertainty are present in this in-situ bathymetry survey, from which the most important are: tide, roll, speed of sound, pulse duration.

Tide ranges 1 – 2 m in Store Fjord as it has been recorded on a tide gauge near Store Glacier terminus. Due to the elongated shape of the fjord, a single tide gauge cannot be used for correcting the bathymetry measurements at a distance up to 60 km from the tide reference. An alternative would be the use of Padman and Erofeeva (2004) Arctic tide model, which has a spatial resolution of 5 km. However, when comparing the recorded tide with the prediction a significant phase difference and tide pattern was observed. This difference is likely due to the unreliable IBCAO bathymetry inside the fjords which is used in the barotropic tide model Padman and Erofeeva (2004). Therefore, the tide was not corrected from the bathymetry survey, thus leading to an uncertainty of ±1 m on the depth measured.

Roll of the survey platform has a significant impact on the distance to the seabed. Indeed a roll of 5°would result of an uncertainty of ∼4‰. The roll of the survey platform was not measured during the survey and thus cannot be corrected for, however the measurements were collected when the fjord was very calm and the boat's roll can be confidently estimated to be <5°thus an uncertainty <4‰.

Speed of sound varies with temperature and salinity and thus would affect the depth estimated from the time of travel. In the typical hydrographic condition the speed of sound varied by $sim3$‰.

Pulse duration constrain the resolution of the single beam. Due to the great depth of the Store Fjord (i.e. ∼900 m) and the presence of mud at the bottom, the pulse duration was set to its maximum value to yield a stronger return signal. The vertical resolution is thus equivalent to 8 m.

As all these sources of uncertainty being independent the total uncertainty can be summed to the quadrature yielding for a depth of 900 m an uncertainty of ±10 m of 1%, which is largely suffisant to gain the general shape of the inner bassin and the depth of potential sill.

A 3D survey was conducted near the front of Store glacier in July and August 2012 using a 117 kHz sidescan interferometer from Bathyswath. This survey produced a high resolution map (i.e. 5 m horizontal resolution) of the seabed for the innermost kilometre of the fjord. Chapter 8, discusses in more detail the method used to collect the bathyswath data.

Coast line

To constrain the interpolation of the bathymetry observations, the vectorial coast line of the Global Self-consistent, Hierarchical, High-resolution Geography (GSHHG) with a nominal resolution of 50 – 500 m (Wessel and Smith, 1996) was used. The coast line at the glacier front was removed as it was overlying the actual bathyswath survey.

Other bathymetry

Gaps between the single beam and bathyswath surveys were filled using the IBCAO-v3 (Figure 2.4). For the inner part of the fjord, significant differences of depth (>500 m) were observed between the in-situ and IBCAO data. Therefore, all IBCAO's grid points within 1 km of any in-situ measurement were removed. Similarly, all IBCAO data above 30 m depth were removed.

Interpolation

The three datasets (Figure 2.5) were converted to universal transverse mercator (UTM) coordinates based on the zone 22W and combined before being interpolated using a linear interpolation on a Delaunay triangulation.

Figure 2.4: IBCAO source of data. Note the dense survey at the mouth of Uummannaq bay where the trough is crossing the continental shelf, yet the lack of data inside Uummannaq bay. After Jakobsson and others (2012)

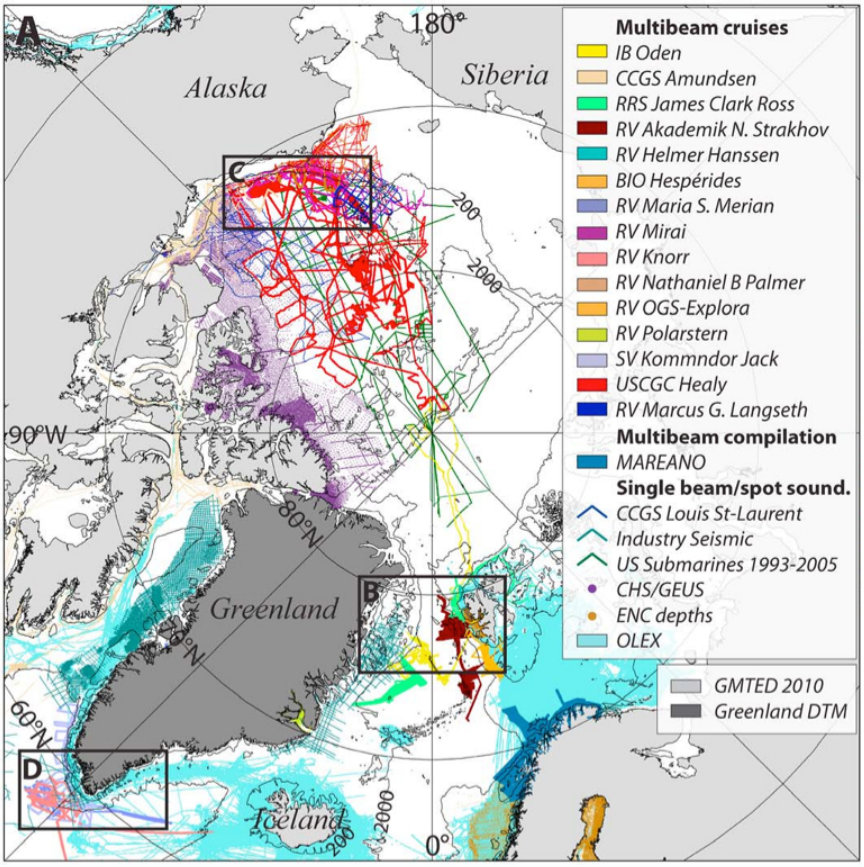

2.1.2 Results

Basins and sills

The bathymetry of Store Fjord shows a deep inner basin exceeding ~900 m depth, with no obstruction from Uummannaq Island (60 km away from the glacier) to the ice front. The only shallow feature present in Store Fjord is the 450 m deep, 100 km long and 30 km large trough across the continental shelf (Figure 2.1). A

Figure 2.5: Data sets used in the interpolation of the fjord bathymetry.

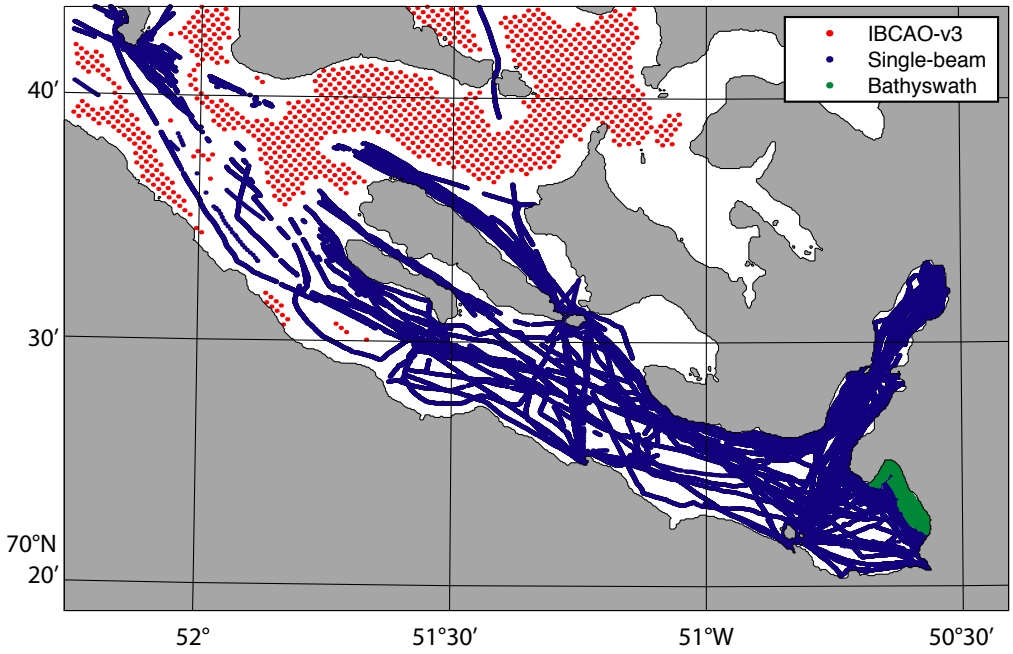

sea mount, 300 m high, was discovered ∼30 km from the glacier front although it does not impede the passage of the fjord water.

Store Glacier front

Near the glacier front, the fjord gradually shallows up to 400 m depth while a channel at 600 m depth is visible near the middle of the terminus. The center part of the glacier front displays a steep slope from 600 m to 400 m and a large plateau approximately 2 km wide where the terminus was located at the time of the surveys (Figure 2.7).

The submerged area of Store front is estimated as 1.8 km^2 with a maximum depth of 500 m which is 35% less than previous estimates of 2.7 km^2 and 650 m, (Xu and others, 2013) derived from a single transect of single beam bathymetry at ∼500 m

Figure 2.6: Bathymetry of Store and Lille fjords after incorporation of the single beam and Bathyswath surveys. Note the absence of sills in Store Fjord and the deep water of ∼800 m near the glacier front.

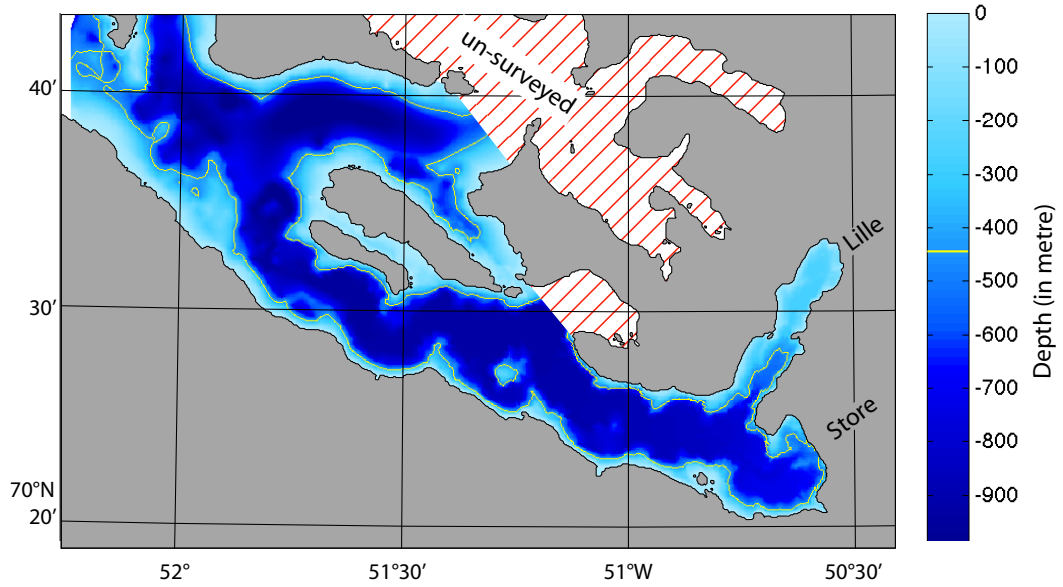

Figure 2.7: Oblique view of the bathymetry near Store glacier front. Black represent the lack of data. The glacier front was removed from the view to highlight the seabed shape at the terminus. Note the trough at 600 m depth reaching the glacier front.

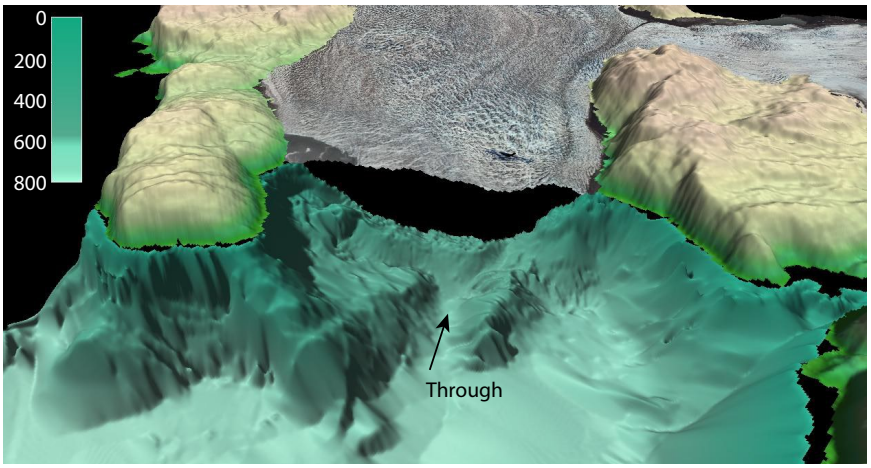

of the terminus. The higher frontal area estimate of Xu and others (2013) can be explained by the steep deepening slope on the middle section of the glacier terminus which would have resulted of the deeper result collected only 500 m away from the terminus, while the bathyswath survey was measuring the depth at the glacier toes itself.

We observe a significant difference of depth between the IBCAO-v3 bathymetry and the interpolated bathymetry Figure 2.8. This difference reaches up to ∼500 m at the glacier front, stressing the importance of surveys in the inner part of glacier fjords.

Figure 2.8: Differences (in m) between the IBCAO-v3 (Jakobsson and others, 2012) and the new bathymetry collected as part of the project. Positive values mean that IBCAO underestimates the actual depth. Note the significant difference, up to 500 m, for most of the inner basin.

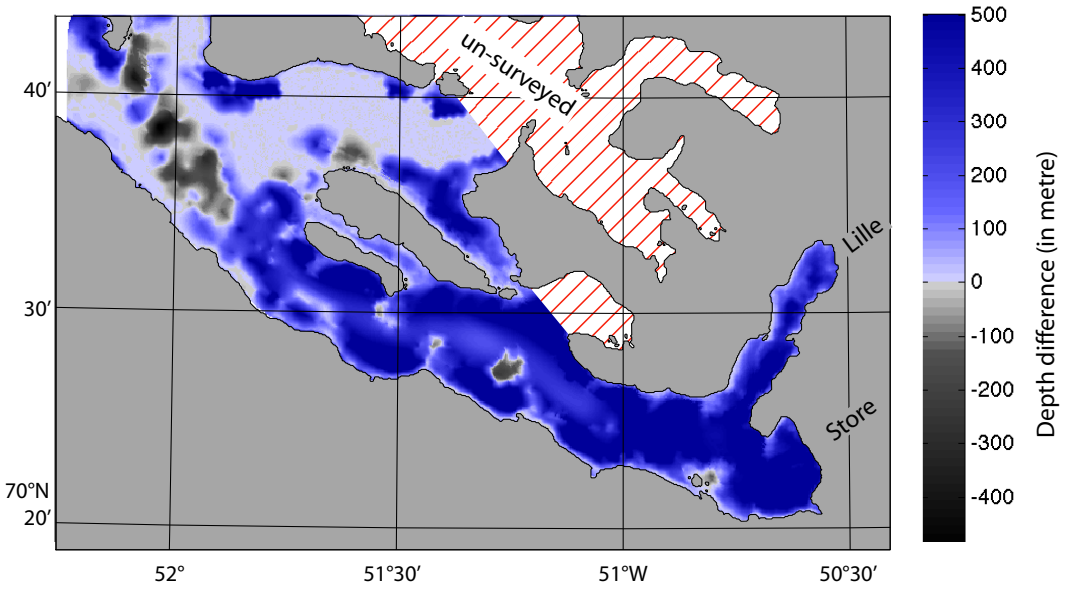

The shallowest obstruction from Baffin Bay into Store Fjord is the 450 m trough across the continental shelf, meaning that the water present in the deep inner

basin will mostly reflect the characteristics of the water present in Baffin Bay at 400 – 450 m depth. Because the 900 m-deep inner basin contains a large volume of water entering at the sill level and reaches the glacier front, the characteristics of this water and particularly its temperature may have a significant impact on the glacier front.

2.2 *Gambo*: the survey platform

During all the field campaigns the surveys were conducted from the 50', steel hull, sailing vessel *Gambo* owned by Dr Alun Hubbard. This low cost yet efficient logistical platform for conducting long term research has proved itself reliable through many expedition in Alaska, Antarctica, South Georgia and Greenland. From 2009 to 2013, Nolwenn Chauché was the skipper of *Gambo* as well as the technical and logistical manager. During the expedition "The long night survey 2012–2013" which included an overwinter with the ship intentionally frozen in the sea ice, N. Chauché was the expedition leader as well as the former status.

2.2.1 Summer setting

During the summer the hydrographic profile were collected from *Gambo* using a fishing 12 V electric winch with 1500 m of dynema line (Figure 2.9). The winch was modified by N. Chauché to be able to measure the distance of line taken out as well as control automatically the profiling velocity.

The acoustic doppler current profile (ADCP) and Bathyswath sonar were individually attached to the side of the boat on steel frames designed and built by

N. Chauché which allowed them to be swung out of the water when not collecting data, in order to avoid risk of collision with bergy bits during the navigation (Figure 2.10).

2.2.2 Winter setting

During the winter, *Gambo* was intentionally let to free in the sea ice in a sheltered bay of Lille Fjord (70°27.8' N 50°41.0' W – Figure 2.11). During this period *Gambo* was used as the logistical platform for N. Chauché and two assistants. Displacement inside the fjord were conducted using a snow-mobile towing a sledge with

Figure 2.9: Setting of the electric winch (orange box) lowering the hydrographic profiler during the summer measurements (line hanging from the black block on the ship's gantry).

Figure 2.10: Setting of the ADCP (white vertical tube in the foreground) and Bathyswath (black rectangle transceiver hanging upside-down. Both instrument are currently out of the water for navigation and can be swung underwater when measurements are taken.

the equipment. During the start and the end of frozen-in period, two individual size hovercrafts allowed to reconnaissance the fjord and test the strength of the sea ice before the snow-mobile would follow.

Measurements were conducted from the sea ice after drilled four holes with an ice auger of ∼30 cm diameter (Figure 2.12). The holes were drilled at each corner of a square and in order than the edges of two neighbor holes will be joined. The remaining center part was removed using a "Tuk" (i.e. Greenlandic word for a kind of ice chisel). The ice chips due to the drilling were removed using a metallic

Figure 2.11: The sailing vessel *Gambo* intentionally frozen in the sea ice during the winter measurements. Note the snow mobile and the two hovercraft kept by the side of *Gambo* in the sea ice.

sieve. This shape allowed the four transceivers of the ADCP to be lowered through the ice.

The hydrographic profiler was lowered and raised through the hole using the same electric winch than during the summer but attached to the sledge. The winch was powered with a 50 AH 12 V battery which was simultaneously recharged with a Honda i1000 generator and a 110 V–12 V charger. A horizontal tube 4 in diameter and was 2 m in length was attached to the top part of the ADCP, allowing for its easy transportation (i.e. the ADCP weight $\sim$ 80 km dry) and ultimately to hold the ADCP on the sea ice while recording.

Figure 2.12: Instrumentation setting during the winter measurements with: the electric winch (orange) attached to the sledge and the ADCP (blue circle in the ice hole) with the tube holding it across the hole.

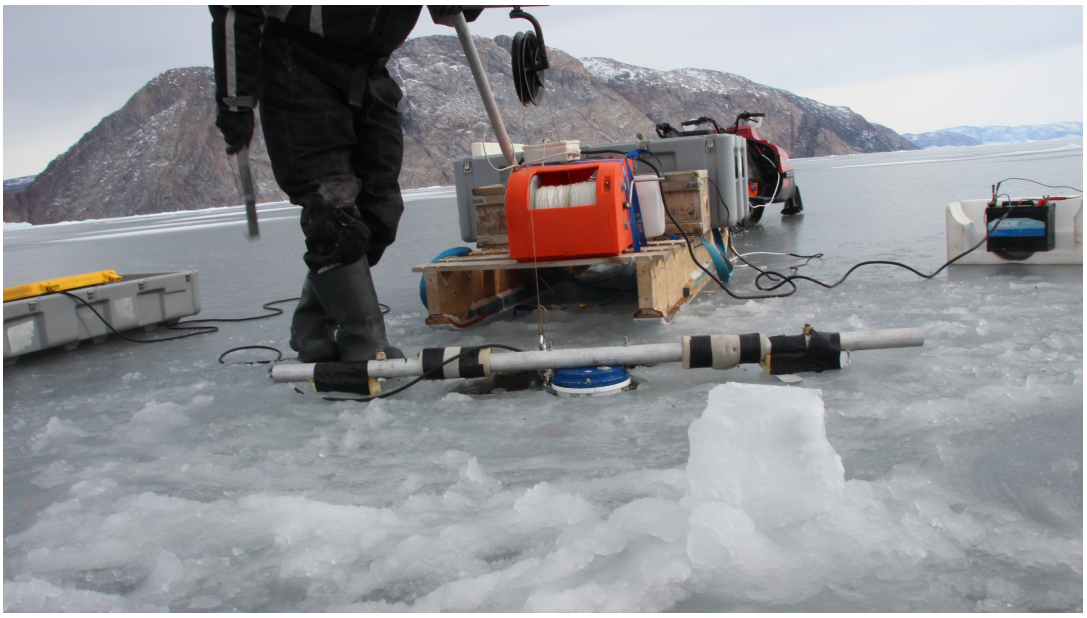

Sonar survey could not be conducted during the winter due to the presence of thick and unstable ice-mélange extending 10 km from the Store Glacier terminus.

Chapter 3

Ocean-glacier processes: identification and variability at Store and Rink glaciers

3.1 Summary

This chapter evaluates the difference of pattern of the ocean-glacier interaction processes at Store and Rink glaciers for two contrasting summers. Warm, subtropical-originating Atlantic water (AW) has been identified as a primary driver of mass loss across the marine sectors of the Greenland Ice Sheet (GrIS), yet the specific processes by which this water mass interacts with and erodes the calving fronts of tidewater glaciers, while frequently modelled and much speculated upon, remains largely unobserved. In this chapter we present a suite of fjord hydrographic observations (salinity, temperature, turbidity versus depth casts) along with glacial

runoff estimates from Rink and Store glaciers, two major marine outlets draining the western sector of the GrIS during 2009 and 2010. We characterise the main water bodies present and interpret their interaction with their respective calving fronts. We identify two distinct processes of ice–ocean interaction which have distinct spatial and temporal footprints: (1) homogenous free convective melting which occurs across the calving front where AW is in direct contact with the ice mass, and (2) localised upwelling-driven melt caused by turbulent subglacial runoff-mixing with fjord water which occurs at distinct injection points across the calving front. Throughout the study, AW at $2.8 \pm 0.2\,^{\circ}\mathrm{C}$ was consistently observed in contact with both glaciers below 450 m depth, yielding homogenous, free convective submarine-melting up to ~ 200 m depth. Above this bottom layer, multiple interactions are identified, primarily controlled by the rate of subglacial fresh-water discharge which results in localised and discrete upwelling plumes. In the record melt year of 2010, the Store Glacier calving face was dominated by these runoff-driven plumes which led to a highly crenellated frontal geometry characterised by large embayments at the subglacial portals separated by headlands which are dominated by calving. Rink Glacier, which is significantly deeper than Store has a larger proportion of its submerged calving face exposed to AW, which results in a uniform, relatively flat overall frontal geometry.

3.2 Introduction and background

The West Greenland current advects deep (> 400 m), warm ($> 3\,^{\circ}\mathrm{C}$) and saline (> 34.8 PSU – practical salinity units) Atlantic Water (AW) around the south coast of Greenland, transferring large fluxes of thermal energy of a subtropical origin

into this sensitive polar environment (Christoffersen and others, 2012; Holland and others, 2008; Kjær and others, 2012; Mortensen and others, 2011; Ribergaard, 2009; Sutherland and others, 2013). The frontal dynamics of tidewater outlet glaciers draining the Greenland Ice Sheet (GrIS) can be profoundly influenced by AW, which has the potential to directly access their calving fronts via over-deepened glacial troughs cut through the continental shelf, thereby controlling their energy and mass balance (Hanna and others, 2008; Pfeffer, 2007; Rignot and others, 2010). For example, in west Greenland the observed sustained attrition of Jakobshavn Isbræ, observed since 1998 (Joughin and others, 2012) has been attributed to warming of subsurface water in Disko Bay and adjacent coastal seas (Holland and others, 2008). Similarly, AW was identified circulating within Sermilik and Kangerdlugssuaq fjords in east Greenland and is implicated in the retreat of Helheim and Kangerdlugssuaq glaciers over the last decade (Straneo and others, 2011, 2010). In NW Greenland, two distinct phases of dynamic ice loss (1985–1990 and 2005–2010) across the Melville Coast have been attributed to oceanic rather than atmospheric forcing (Kjær and others, 2012). An implicit assumption in these studies is that warm AW comes into direct contact with the marine termini of large tidewater outlet glaciers draining the ice sheet (Holland and others, 2008; Kjær and others, 2012; Motyka and others, 2011; Rignot and others, 2010; Straneo and others, 2012). Yet to date few observational studies have been focused on the actual ice–ocean interface, in particular on the specific controls governing submarine-melt rates and the concomitant mass and energy exchanges which determine outlet glacier and fjord dynamics alike (Hubbard, 2011).

To date, several processes of interaction between fjord water and tidewater calving fronts have been observed, modelled and/or speculated upon including forced

convection caused by buoyant subglacial fresh water (SgFW) discharged at depth and entraining AW as it rises (Jenkins, 2011; Mugford and Dowdeswell, 2011; Salcedo-Castro and others, 2011; Sciascia and others, 2013; Sole and others, 2012; Xu and others, 2013, 2012) as well as wind stress and tide-driven fjord circulation (Mortensen and others, 2011; Sole and others, 2012; Straneo and others, 2010; Sutherland, 2012). Furthermore, it is emerging that circulation in Greenland's deep fjords is more complex than the single convective cell (estuarine-like) circulation model that has been assumed previously in energy-mass balance calculations (Motyka and others, 2003; Rignot and others, 2010). For instance, a vertical superposition of convective cells was observed (Straneo and others, 2011; Sutherland, 2012) and more recently modelled (Sciascia and others, 2013; Sole and others, 2012) within fjords in east Greenland.

In this study we observe and document the interaction between fjord waters and the calving front at two major outlets – Rink and Store – that drain the western GrIS over two successive, but contrasting, melt seasons (August 2009 and 2010). The processes of AW-driven submarine-melting and subglacial fresh-water-driven upwelling plumes are observed in both fjords. Differences and similarities in the spatial and temporal patterns of these processes are identified and highlighted, demonstrating significant impact and control of subglacial fresh-water runoff and discharge on calving front dynamics and geometry.

3.3 Field site

Uummannaq Bay is unique on the west coast of Greenland insofar as it has an over-deepened glacial trough to at least 450 m depth, which extends uninterrupted

to the continental shelf break (Jakobsson and others, 2012). It thereby provides a direct route for AW from Baffin Bay to enter its inner fjord basins and access over a dozen marine-terminating outlet glaciers which drain this sector of the GrIS (Figure 3.1). The existence of two large marine-terminating outlet glaciers, Rink and Store, which drain this sector into Uummannaq Bay, make it a useful target to isolate and compare individual tidewater glacier responses to similar atmospheric and oceanic forcing but with contrasting bed, fjord and frontal geometries and geological controls. Rink and Store glaciers are the second and third largest outlets in west Greenland after Jakobshavn Isbræ, with an estimated discharge of 11 – 17 $\mathrm{km^3\,year^{-1}}$ and 14 – 18 $\mathrm{km^3\,year^{-1}}$ respectively (Weidick and Bennike, 2007). This corresponds to 7 and 8 % of the total annual discharge for the western GrIS (Rignot et al., 2008). A recent aerial study of Store Glacier's terminus estimates the mass flux through the calving front to be 11.5 $\mathrm{km^3\,year^{-1}}$ (Ryan and others, 2014). Both glaciers and fjords are over 5 km wide and at least 100 km, long with catchment sizes of 45 000 $\mathrm{km^2}$ for Rink and 34 000 $\mathrm{km^2}$ for Store (Rignot et al., 2008). Store has a larger ablation area due to its lower-lying hypsometric profile. Bathymetric mapping reveals that both fjords have an inner basin deeper than 900 m and that the maximum depth of the calving front of Rink Glacier is $\sim$ 750 m, and Store Glacier is $\sim$ 450 m. In Rink Fjord a transverse sill is located 50 km from the ice front with a minimum depth of approximately 400 m (Dowdeswell and others, 2014) while Store Fjord has no such sill or obstruction to the outer trough (Figure 3.1).

Figure 3.1: Map of the study area. The yellow and black dots represent the CTD sections in 2009 and 2010 respectively. In the International Bathymetry Chart of the Arctic Ocean (IBCAO), the 450 m contour has been highlighted in blue to indicate the trough across the continental shelf allowing the AW to enter the fjord. Bathymetry of the centre line of Store and Rink fjords are shown for each fjord and correspond approximately to the purple line on the maps. Position of the shallowest sill in Rink Fjord is shown as a thick black line. Orange dots show the position of Store 2010 profiles inside and outside the surface plume. A false colour Landsat mosaic from August 2010 is used for the inset maps, superimposed over land and glaciers. Topography (brown shade) and ice mask (off-white) are taken from Greenland Ice Map Project (Howat and others, 2014).

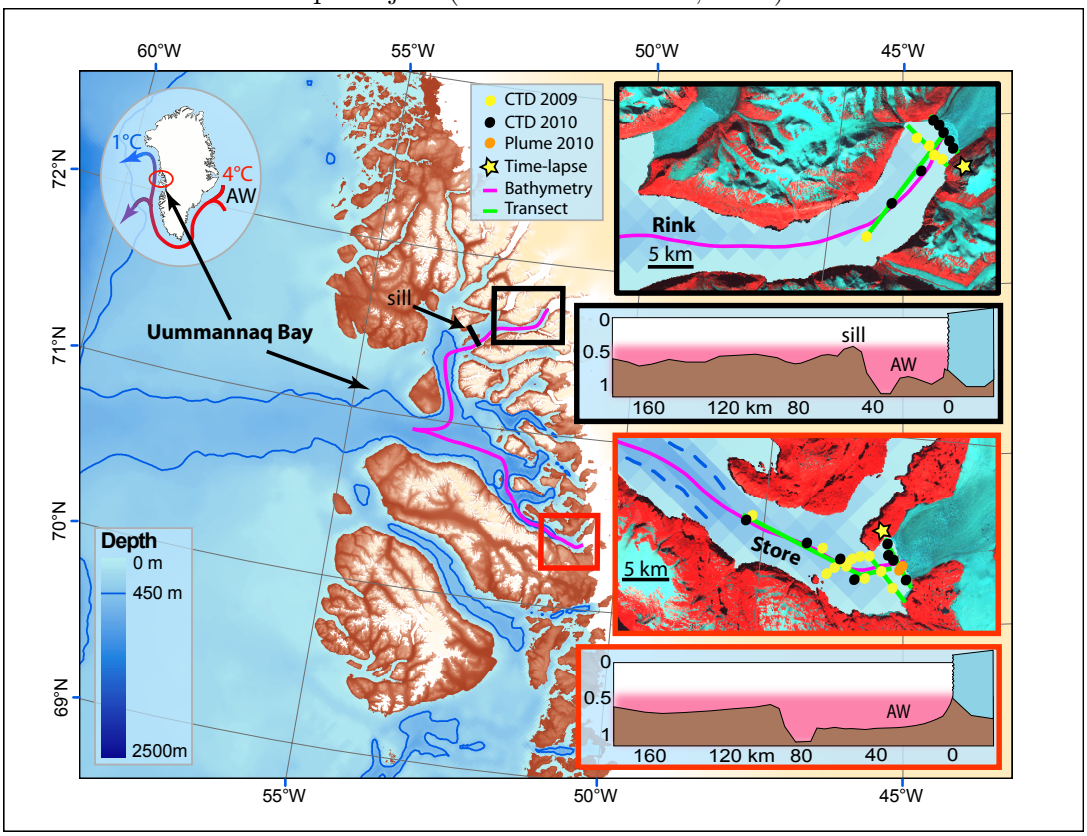

3.4 Methods

3.4.1 Data collection

Hydrographic surveys were conducted in August 2009 and 2010 comprising of 5 and 7 conductivity, temperature, turbidity and depth (hereafter called CTD) casts at Rink Fjord and 12 and 11 casts at Store Fjord, respectively. The CTD casts were taken along and across each fjord, at a distance of between 200 m and 20 km from their respective calving fronts (Figure 3.1) and to a maximum depth of 750 m. A MIDAS Valeport 2000 conductivity–temperature–depth profiler, equipped with a Seapoint turbidity sensor was used (Table 3.1). The profiler was calibrated before the survey in 2009. Measurements were logged at a sampling rate of 4 Hz with a descent rate of 1–2 $\mathrm{m\,s^{-1}}$, yielding 10 to 20 samples for every 5 m of vertical profile. The instrument also logged on recovery, which at a slower ascent rate of 0.3–0.5 $\mathrm{m\,s^{-1}}$ provided $\sim$40 samples per 5 m vertical interval. Data were filtered by removing points of more than one standard deviation from the unweighted moving average window ($n = 16$) to yield a statistically significant result. The filtered data were then averaged into 5 m vertical bins. Both the ascending and descending data were used to improve error estimation. The standard deviation provides an indication of measurement uncertainty and corresponds to $\pm$0.023 °C for potential temperature, $\pm$0.025 PSU for salinity and $\pm$1.4 nephelometric turbidity unit (NTU) for the turbidity. Potential temperature (θ) and salinity (S) were calculated according to the equations of state of seawater published by UNESCO 1983 (Fofonoff and Millard, 1983) and used to identify specific water bodies and mixing processes.

Table 3.1: Profiler's sensors (CTD) specifications, MIDAS Valeport 2000.

Sensor	Type	Accuracy
Pressure	Strain gauge	0.2 bar
Conductivity	Valeport inductive coils	0.01 mS cm^{-1}
Temperature	Fast-response platinum thermometer	0.01 °C
Turbidity	Seapoint	15 NTU

The turbidity in the fjord was used to trace the sediment-loaded subglacial fresh water (Bartholomew and others, 2011; Chu and others, 2009; Hudson and others, 2014; Motyka and others, 2003). Turbidity estimates are, however, based on backscattering of light, depending on both sediment concentration and type (lithology and size) of particles, which can vary from one fjord to another. To compare the extent of fresh-water-induced buoyant upwelling plumes in the two fjords, we expressed the turbidity as a percentage of the maximum value recorded in each fjord (i.e. within the plumes).

3.4.2 Water-body identification

When plotted in potential temperature–salinity (θ–S) space, two types of water body can be differentiated:

Water types are defined by thick, homogenous layers, in excess of 50 m within the water profile, which share similar temperature and salinity ($\Delta\theta < 0.2$ °C and ΔS<0.2 PSU). Such water types can be identified by dense clustering on a θ–S diagrams

Mixed water masses are defined as a layer within the water column combining two water types and are characterised by the line joining the two water types on the θ–S diagram. We define a mixed water mass when its thickness

exceeds 50 m, its $\delta\theta/\delta S$ gradient is constant and when there is sufficient difference ($\Delta\theta > 0.5\,^{\circ}$C and/or ΔS>0.5 PSU) between the top and the bottom of the layer.

3.4.3 Identification of interaction processes

To isolate which water body is driving subaqueous melt, we calculate the temperature and salinity loss due to the melting of glacier ice with reference to the Gade-slope (Gade, 1979; Holland and Jenkins, 1999; Mortensen and others, 2013; Straneo and Cenedese, 2013; Straneo and others, 2011). Given a potential temperature for glacier ice (θ_{i}) at the front, we define an effective potential temperature (θ_{eff}) of the corresponding virtual water type by calculating the energy required to melt a unit weight of ice as follows:

$$\theta_{\mathrm{eff}} = \theta_{\mathrm{f}} - \frac{L_{\mathrm{i}} - C_{\mathrm{i}}(\theta_{\mathrm{f}} - \theta_{\mathrm{i}})}{C_{\mathrm{sw}}}, \tag{3.1}$$

where θ_{f} is the pressure-corrected melting point of ice, L_{i} (337 kJ kg^{-1}) is the latent heat of fusion, C_{i} (2.1 kJ kg^{-1} K^{-1}) the specific heat capacity of ice and C_{sw} (3.9 kJ kg^{-1} K^{-1}) the specific heat capacity of seawater. In the θ–S diagram, the mixed water mass resulting from submarine-melting of the glacier will fall on the Gade-slope joining the water, driving the melt and the virtual water type with characteristics $\theta = \theta_{\mathrm{eff}}$ and $S = 0$ A similar identification procedure can be applied to track runoff-mixing and resulting mixed water mass as it will follow a line joining the ambient water and the fresh runoff water ($\theta = 0\,^{\circ}$C; $S = 0\,^{\circ}$C) (Mortensen and others, 2013; Straneo and others, 2011; Straneo and Heimbach, 2013) (hereafter called the runoff-slope). If both submarine-melting and runoff-mixing are affecting the same water parcel, the resulting mixed water mass will have a $\theta - S$ gradi-

ent proportional to the theoretical slope of each process (Mortensen and others, 2013).

3.4.4 Interpolation of oceanic measurements

Temperature, salinity and turbidity were interpolated across and along Rink and Store fjords. The cross profile was interpolated immediately adjacent to each ice front ($\sim$200 m) and the long-profile section tracks the midpoint of each fjord (Figure 3.1).

3.4.5 Runoff discharge estimation

In addition to synoptic meteorological conditions, surface glacier meltwater runoff is dependent upon the ablation area, its hypsometry and the seasonal distribution of snow/ice and its concomitant albedo. Monthly mean values of surface melt for each glacier were estimated following Box (2013) using a positive degree-day/melt-rate model applied to glacier catchment. The catchment of each glacier was determined from the GIMP digital elevation model of the ice sheet (Bamber and others, 2013; Howat and others, 2014). For the purposes of this study we assume an efficient, fully developed drainage system as would be expected in the latter half of the melt season where the bulk of surface meltwater runoff drains and is discharged directly into the fjord as subglacial fresh water (Chandler and others, 2013; Schoof, 2010).

3.5 Results

3.5.1 Water types present at the glacier front

Compiled θ–S plots reveal that the distinct water bodies observed within both Rink and Store fjords (Figures 3.2 and 3.3 and table 3.1) interact with their respective calving fronts (Section 3.5.2). Except for polar water (PW) described below, all the other observed water bodies were directly adjacent ($\sim 200\,\mathrm{m}$) to each glacier and can be assumed to be in direct contact with the submerged calving face. Four distinct water types were observed:

Surface water (SW) is the uppermost layer of the fjord and is strongly affected by solar insolation, atmospheric forcing, brash-ice melt as well other external processes including river runoff and vertical mixing (Mortensen and others, 2011). In this study, the pycnocline at the lower interface of the SW appears to act as a barrier to buoyant upwelling waters (Section 3.5.4) often constraining them below the SW. Throughout our surveys, SW was limited to the upper 15 m of the water column with temperatures ranging from 0 to 10 °C and salinity from 28 to 33 PSU. We define the limit of the SW by its density ($\sigma_\theta < 26.5\,\mathrm{kg\,m^{-3}}$) as it is above this value that most of the variability appears.

Atlantic water (AW) (Straneo and others, 2012), also known as subpolar mode water (Mortensen and others, 2011) or intermediate Irminger water (Ribergaard, 2009), is the deepest and warmest water body present in the fjord. This water type is advected along the coast by the West Greenland Current (Mortensen and others, 2013, 2011; Ribergaard, 2009; Straneo and Heimbach,

Figure 3.2: Potential temperature, salinity and turbidity vs. depth for all profiles. On the right-hand side panel, each water-body vertical extent is represented for each survey. The estimated maximal depth of each glacier front is shown with a continuous horizontal black line. The depth of Uummannaq Trough and Rink Sill are shown as horizontal red lines. The turbidity has been converted to a percentage of the maximum value measured inside the plume of each fjord. For Store in 2010, the profile inside the plume (ST 16) is shown in purple.

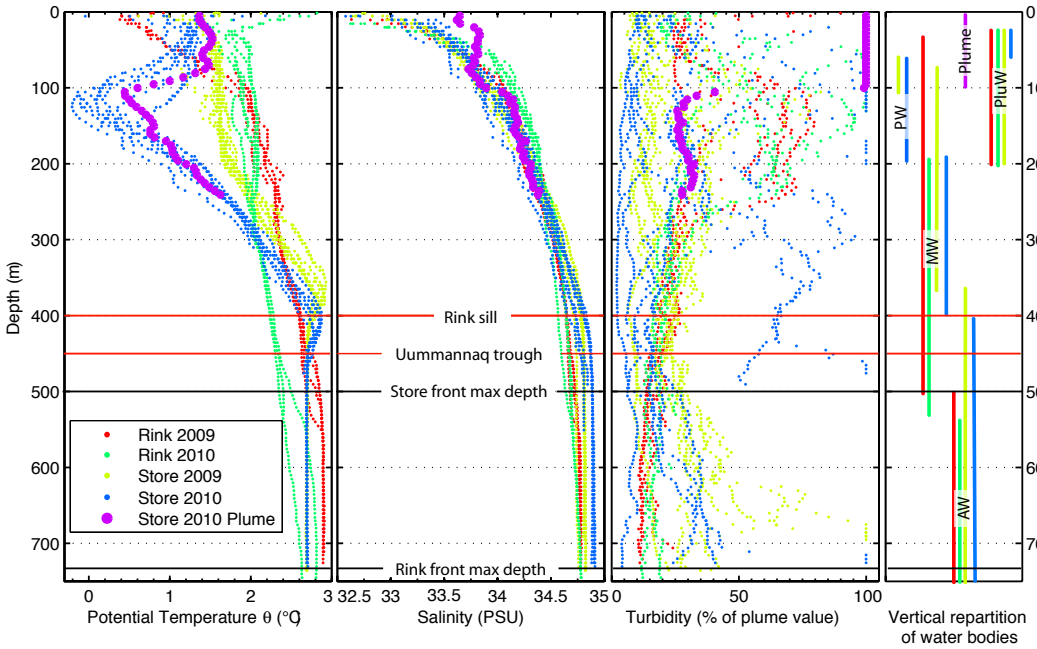

2013; Straneo and others, 2012), entering the fjord via the Uummannaq Bay trough carved across the continental shelf. Throughout our surveys, AW was always present below 400 to 500 m depth and had highly consistent temperature and salinity characteristics ($\theta = 2.8 \pm 0.2\,^{\circ}\mathrm{C}$ and $S = 34.8 \pm 0.1\,\mathrm{PSU}$) for both fjords over both years.

Polar water (PW), which was only observed in Store Fjord, is the coldest water body (Figures 3.2 and 3.3). PW originates from the Arctic Ocean (Hopkins, 1991) and is present along the west coast of Greenland at 50 to 150 m depth

Figure 3.3: Potential temperature–salinity diagram of the CTD stations in 2009 and 2010 for Rink and Store fjords. The distal (∼20–30 km) and proximal (∼0.2–1 km) profiles are in black and red, respectively. The labels and the depth of the water types are outlined in red whilst the mixed water masses are in blue. Isopycnals are in black with $\sigma = 26.5\,\mathrm{kg\,m^{-3}}$ highlighted in bold to represent the lower limit of the surface water. Green continuous and blue dashed lines represent the theoretical Gade-slope and runoff slope, respectively.

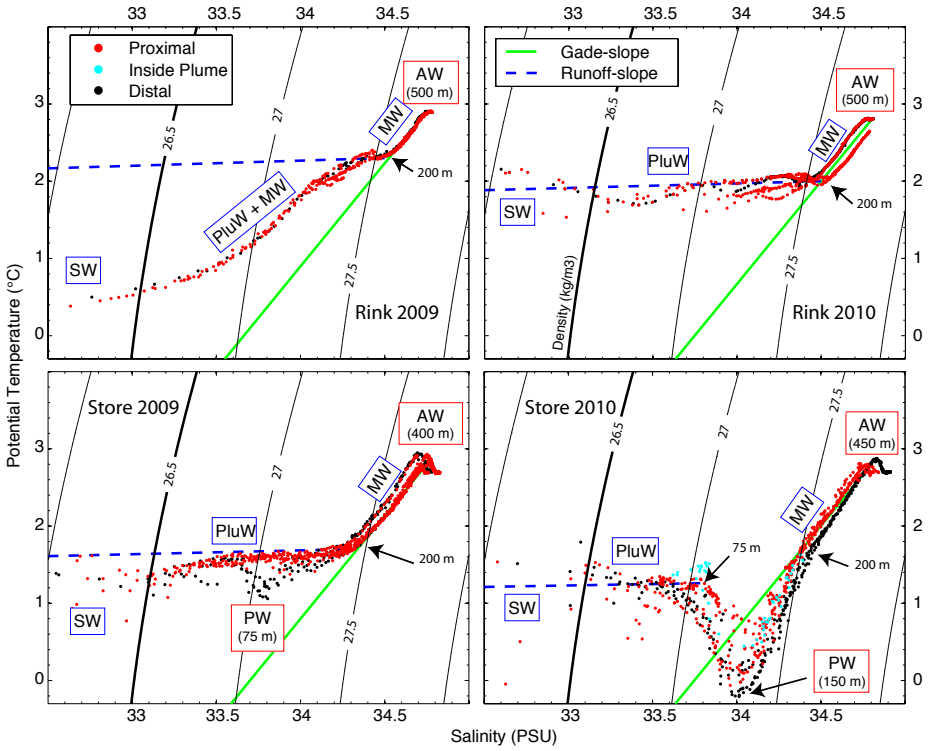

(Ribergaard, 2009) where it would be able to advect into Uummannaq Bay. In 2010 at Store, PW was observed at 50 to 200 m depth, separating SW and AW, and had a minimum temperature of $\theta \approx 0\,^{\circ}\mathrm{C}$ and S=34 PSU at ∼150 m depth. At Store in 2009, remnant traces of PW were visible for the most distal CTD cast (∼ 10 km from the glacier), but were not observed in direct contact with the calving front (Figure 3.4). In Rink Fjord, PW was not observed in either year.

Subglacial fresh water (SgFW) includes runoff of basal and surface-meltwater and is injected into the fjords at depth through conduit in the calving front. SgFW is very difficult to measure in its original state (i.e. unmixed) due to the vigorous mixing which occurs on its injection from the portal (Mugford and Dowdeswell, 2011; Salcedo-Castro and others, 2011; Xu and others, 2013, 2012). Hence, SgFW is reasonably assumed to have the basic characteristics of $\theta = 0\,°\mathrm{C}$ and $S = 0\,\mathrm{PSU}$ (Mortensen and others, 2013; Motyka and others, 2013; Rignot and others, 2010; Straneo and others, 2012).

Table 3.2: Characteristics of the water types and mixed waters observed during the surveys.

	$[\theta(°\mathrm{C});S(\mathrm{PSU})]$ or $(\delta(°\mathrm{C})/\delta S(\mathrm{PSU}))$	Origin	Transport	Depth Range
AW	[2.8; 34.8]	Subpolar gyre	Advected by WGC	400 m bottom
PW	[0;34]	Arctic Ocean	Advected by WGC	$\sim$ 50–200 m
SgFW	[0;0]	Surface/basal glacier melt	$\sim$ 500 m (Store) $\sim$ 750 m (Rink)	
MW	(2.5)	Result from submarine-melting	Local formation	200–$\sim$ 400 m
PluW	(0.05)	Result of runoff-mixing	Local formation	15–200 m or 15-75 m
SW	*NA*	River mixing, solar insulation	Local formation	0-15 m

3.5.2 Mixed water masses and inferred processes

Submarine-melting

Applying Equation (3.1) and assuming a temperature for glacier ice of $\theta_i = -10\,^\circ\mathrm{C}$ (taken from Jakobshavn Isbræ; Thomas (2004)) and a salinity (S_i) of 0 PSU at the base of Store calving front yields a virtual water-type temperature of $\theta_{eff} = -89.8\,^\circ\mathrm{C}$. Note that θ_{eff} is not sensitive to the assumed values of θ_i Hence, meltwater (MW) driven by AW ($S = 34.8$ PSU and $\theta = 2.8\,^\circ\mathrm{C}$) will follow a Gade-slope of $\sim 2.7\,^\circ\mathrm{C\,PSU^{-1}}$ MW was found in all surveys above the AW and below SW (or PW if present). The gradient derived from our observations of MW of $\sim 2.5\,^\circ\mathrm{C\,PSU^{-1}}$ is in good agreement with the theoretical Gade-slope (Fig. 3). MW was observed at a depth of 100 to 250 m from the base of the calving front up to 200 m from the surface (Figure 3.2). Rink Fjord in 2009 was an exception when MW was present along with plume water (see below) from 200 m to 15 m depth (Figure 3.3). The presence of MW below the outer sill depth at Rink Fjord (Figure 3.2) indicates that it is formed locally by interaction with the calving front and is not merely advected in from Baffin Bay.

Runoff-mixing

Following Straneo and others (2011, 2012), the horizontal inflection in the θ–S diagram is used to define the second apex of the runoff slope (Figure 3.3) and gives a theoretical value of $\sim 0.05\,^\circ\mathrm{C\,PSU^{-1}}$ and $0.04\,^\circ\mathrm{C\,PSU^{-1}}$, respectively. Plume water (PluW) is produced by the mixing of SgFW with ambient fjord water at depth and is sometimes referred to as subglacial water (Mortensen and others, 2011). In our surveys, PluW has a runoff slope of $\sim 0.07\,^\circ\mathrm{C\,PSU^{-1}}$ (Figure 3.3)

and was found below the SW and above a depth of either 200 m (Rink 2009–2010 and Store 2009) or 75 m (Store 2010).

Mixing of MW and PluW with similar proportions to each other was only observed in 2009 at Rink within the upper layer.

Due to the lack of direct observation of plume processes (within tens of metres of the ice front), the inflection in the θ–S diagram (Figure 3.3) reflects the depth at which the PluW outflows horizontally and not the depth of injection of the SgFW into the fjord.

3.5.3 SgFW discharge estimation

The surveys were conducted in August of 2009 and 2010 during two contrasting melt seasons with very different glacier meltwater runoff characteristics. In 2009, air temperatures and glacial melt were normal and close to the 2000 to 2010 mean, whereas temperature, extent and magnitude of surface melt were record-setting in 2010 (van As and others, 2012; Tedesco and others, 2011). In the absence of precipitation during both sets of surveys we assume that the monthly variations in the discharge of SgFW are predominantly driven by glacier surface melt. Surface melt runoff modelling, performed by J. Box, yields a predicted SgFW discharge at Rink of $1000 \pm 300\,\mathrm{m^3\,s^{-1}}$ in 2009 and $1500 \pm 450\,\mathrm{m^3\,s^{-1}}$ in 2010. At Store, the SgFW discharge is estimated at $1500 \pm 450\,\mathrm{m^3\,s^{-1}}$ in 2009 and $2000 \pm 600\,\mathrm{m^3\,s^{-1}}$ in 2010. Uncertainties are defined by the 30 % standard error derived from comparisons between modelled (Box, 2013) and measured (van de Wal and others, 2012) runoff at the Kangerlussuaq transect, some 300 km to the south of our study site. Given that Rink and Store catchments are within the same fjord system, it can

be noted that any bias in the runoff model should affect both glaciers consistently and hence the relative variation in discharge of SgFW for the two glaciers can be compared directly. The SgFW discharge of Store Glacier in 2009 was $\sim 50\,\%$ greater than that for Rink, due to the latter's smaller ablation area. SgFW discharge at both glaciers is amplified by $\sim 50\,\%$ compared to 2009, driven by very high air temperatures in August 2010.

3.5.4 Turbidity analysis and plume observation

At Store, a variable turbid plume was visible at the water surface adjacent to the calving front in time-lapse imagery acquired in July 2009 (http://vimeo.com/2638166) (Ahn and Box, 2010), but was not visible in August. In contrast, in August 2010, a large, dominant turbid plume extended $\sim 1\,\mathrm{km}$ away from the ice front. Logging of the time-lapse imagery indicates that the forced convection associated with the plume was reaching the surface from June until the end of August 2010. Horizontal surface outflow from this plume attained speeds up to $\sim 1.5\,\mathrm{m\,s^{-1}}$, sufficient to force brash ice or mélange out from the embayment (Figure 3.8). A distinct boundary was observed at the outer limit of the plume, visible by a marked change in water turbidity (Figure 3.8). The outflow of PluW is observed at 50–100 m depth (Figure 3.5) and extends up to 3 km away from the front (Figure 3.4). A layer of intense turbidity was also observed from 300 m depth to the bottom (Figures 3.4 to 3.6) at Store in 2010 (Figure 3.5). Turbidity measurements within and just outside of the surface plume (visually defined by the contrast in water colour), indicate that PluW sinks below the pycnocline of the SW after attaining the surface (Figure 3.6), an observation that is in agreement with plume modelling at Store (Xu et al., 2013).

Figure 3.4: Potential temperature along fjord section (parallel to the fjord main axis), with the glacier front to the left and the open ocean to the right. Dashed areas show waters resulting from submarine-melting (blue) and runoff-mixing (red). The brown dashed area corresponds to a turbidity $> 80\,\%$ of the maximum recorded in the plume. The estimated bottom profile is depicted as a solid brown area.

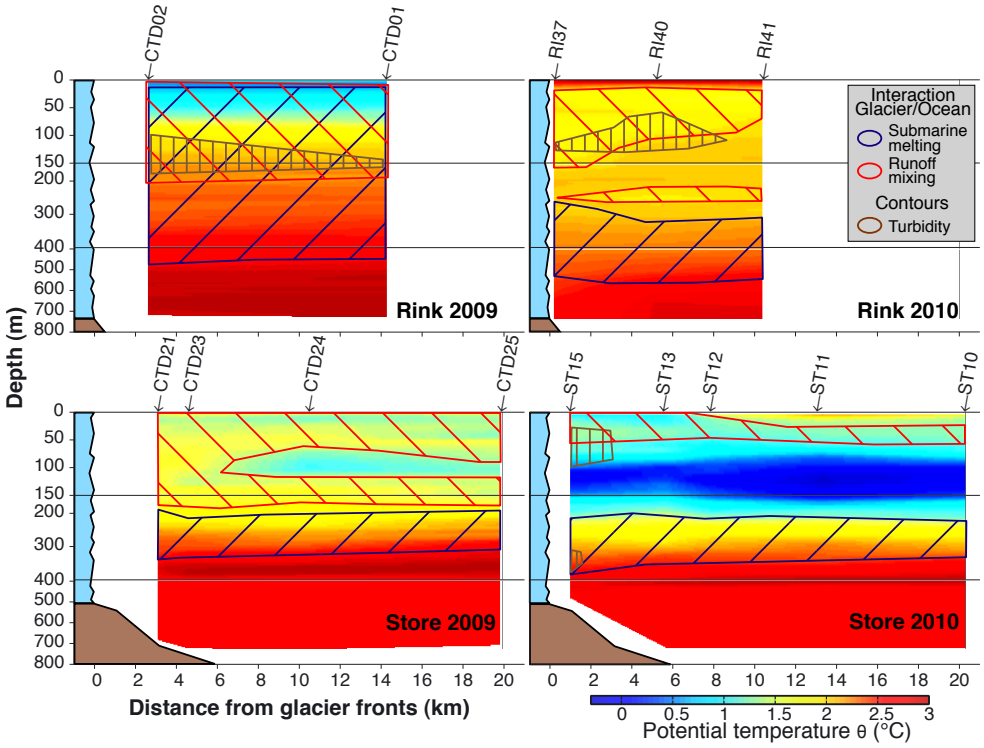

In contrast to Store, there was very little surface plume activity observed at Rink. Logging of time-lapse photography of Rink (http://vimeo.com/6038577) (Ahn and Box, 2010) reveals just one surface plume on its southern margin in July 2009 and 2010, which had, however, disappeared completely by early August. Despite this apparent absence of surface plume activity, turbid waters were observed just below the SW, suggesting that the plume was still present but was not attaining the surface. In August 2009, a submarine turbid water jet was present in the middle of the cross section between 100 and 200 m depth and spreading up to

10 km down the fjord (Figure 3.4). In August 2010, two turbid jets are present, one along the north side of the fjord and one along the south side with the strongest jet measured beneath the pycnocline of the SW at 15 m depth (Figure 3.5).

Figure 3.5: Same as Figure 3.4, but with the across-fjord section (parallel to the front at ∼200–1000 m distance). The north side of the fjord is on the left and it is facing the ice front.

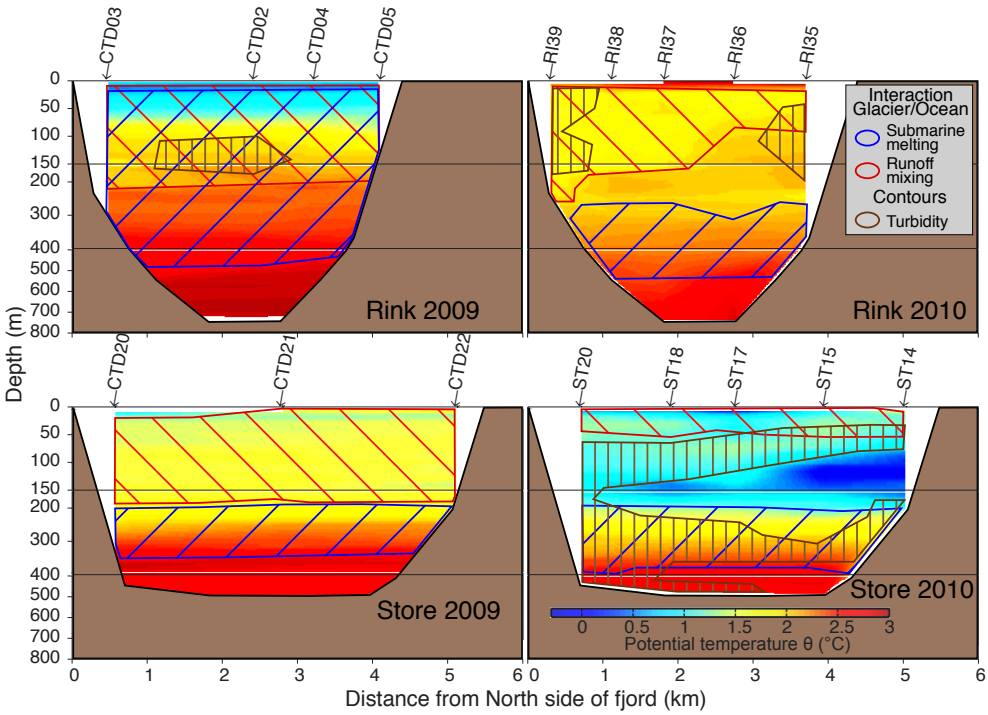

3.6 Discussion

3.6.1 Ocean–glacier interaction

The hydrographic surveys at Rink and Store provide four snapshots of glacier–ocean interaction during the latter half of the melt season when SgFW discharge

Figure 3.6: Turbidity section across the boundary of the surface plume at Store in 2010 (Fig. 8). The turbidity is shown as a percentage of the maximum turbidity recorded in the plume. The profile ST15 was done ∼200 m outside the turbid plume where the surface of the sea was a normal blue colour and no significant surface current was observed. The profile ST16 was done ∼100 m inside the surface plume, the colour of the surface was dark brown and a strong turbulent current flowing away from the glacier was observed. ST16 was not lowered to the bottom of the fjord for safety reasons, therefore interpolation below 250 m is not realistic. The arrows show a schematics circulation in the plume with SgFW in blue, AW in red and PluW in brown.

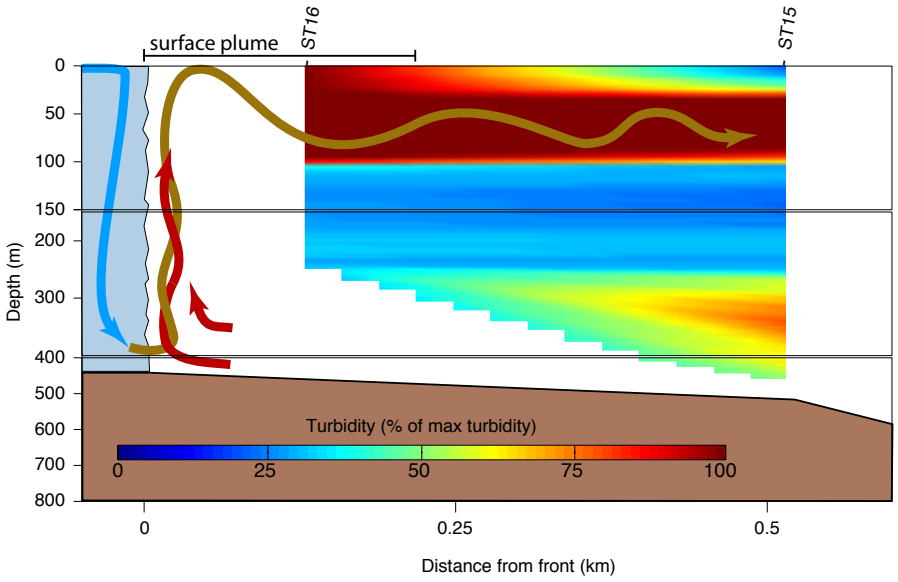

should be most pronounced. Direct observation of these interactions and their repartitioning within the water column shows marked similarities and differences between both years and fjords from which we identify key suites of processes significantly and simultaneously impacting a water parcel (hereafter called states). Below 200 m depth, free convective submarine melting is the only process which is consistently identified (Figures 3.4 and 3.5), whereas three different states can be distinguished within the upper layers of the water column (0–200 m depth):

state 1: submarine-melting interlaced with runoff-mixing both of similar magnitude (Rink 2009)

state 2: significant runoff-mixing alone (Store 2009 and Rink 2010)

state 3: similar to state 2 but with a shallower (<75 m) outflow (Store 2010).

Comparison of these observed states with calculated SgFW discharge suggests that the interaction processes in the upper layer are potentially influenced by glacier meltwater runoff rates. Indeed, when the SgFW discharge increases at Store, the PluW outflow becomes shallower and evolves from state 2 to state 3 (Figure 3.7), an observation which resonates with recent modelling (Sciascia and others, 2013; Xu and others, 2013).

At Rink, in 2009, both PluW and MW were observed in similar proportions in the upper layer (state 1). By contrast, in 2010 PluW was the only water to contribute significantly to the upper layer (state 2). As both the temperature and depth of the AW as well as the vertical extent of submarine-melting remained the same in the 2009 and 2010 surveys, we infer that the 50 % stronger SgFW discharge in 2010 is responsible for a more pronounced runoff-mixing and hence explain the evolution from state 1 to state 2.

A simplified schematic of the three observed states of ocean–glacier interaction and the associated circulation patterns is presented in Figure 3.7. Excluded from this schematic are the impact of external factors such as wind-driven circulation (Sciascia and others, 2014; Straneo and others, 2010; Sutherland, 2012), tides (Mortensen and others, 2011; Sole and others, 2012) and seasonality of the forcing cycle (Mortensen and others, 2013), all of which will influence the circulation patterns as well.

Figure 3.7: Simplified schematic of the three states of interaction identified (Section 3.6.1), the associated SgFW discharge and the circulation induced at the glacier front. The arrow thicknesses represent an approximate magnitude, and the colours represent the different processes of interaction with the following: SgFW (blue), runoff mixing (brown) and submarine-melting (orange). The upper and bottom layers are represented above and below 200 m depth. Each water body observed in the water column is labelled as in the text (Sections 3.5.1 and 3.5.2).

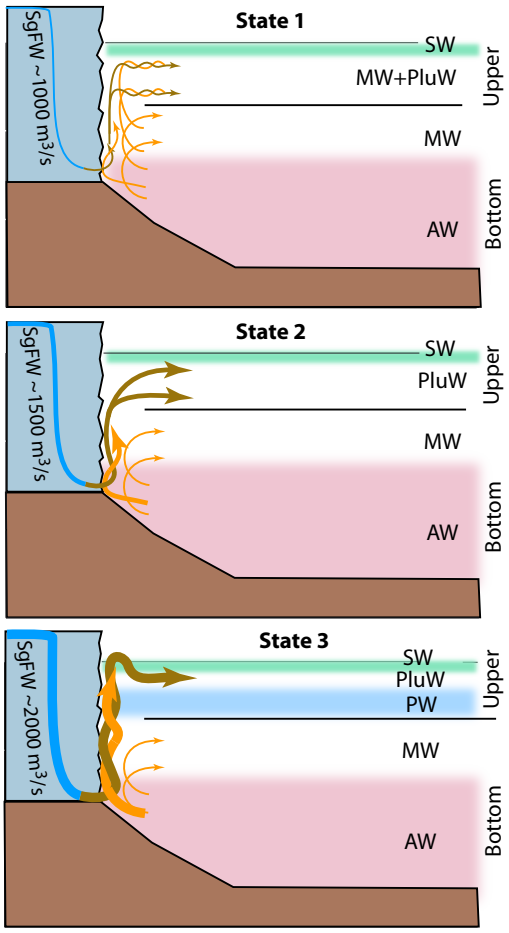

Figure 3.8: Picture taken from the southern side of Store Glacier in 2012 (looking north). The red line shows the boundary of the turbid surface plume observed from June to September and its approximate extent.

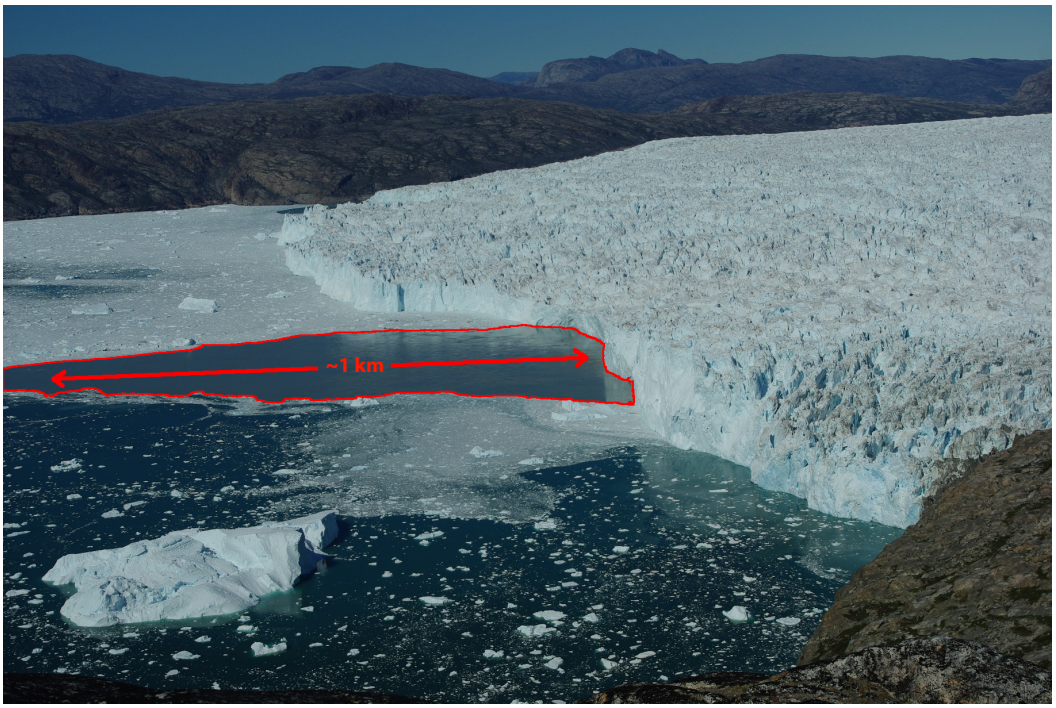

Despite these limitations, the circulation induced by the runoff-mixing and submarine-melting, and its evolution, must significantly contribute to the general circulation across and along the glacier front. Indeed, both processes produce vertical entrainment of ambient AW in direct contact with the ice front, which is a major driver of enhanced melting at the calving front (Jenkins, 1991, 2011; Josberger and Martin, 1981; Kimura and others, 2014; Xu and others, 2013, 2012).

Figure 3.9: Time-lapse photographs of Store and Rink glacier termini in August 2010. The general shape and position of each glacier front for the winter preceding each survey and the summer of the survey have been outlined in orange (winter 2009), green (summer 2009), red (winter 2010) and blue (summer 2010).

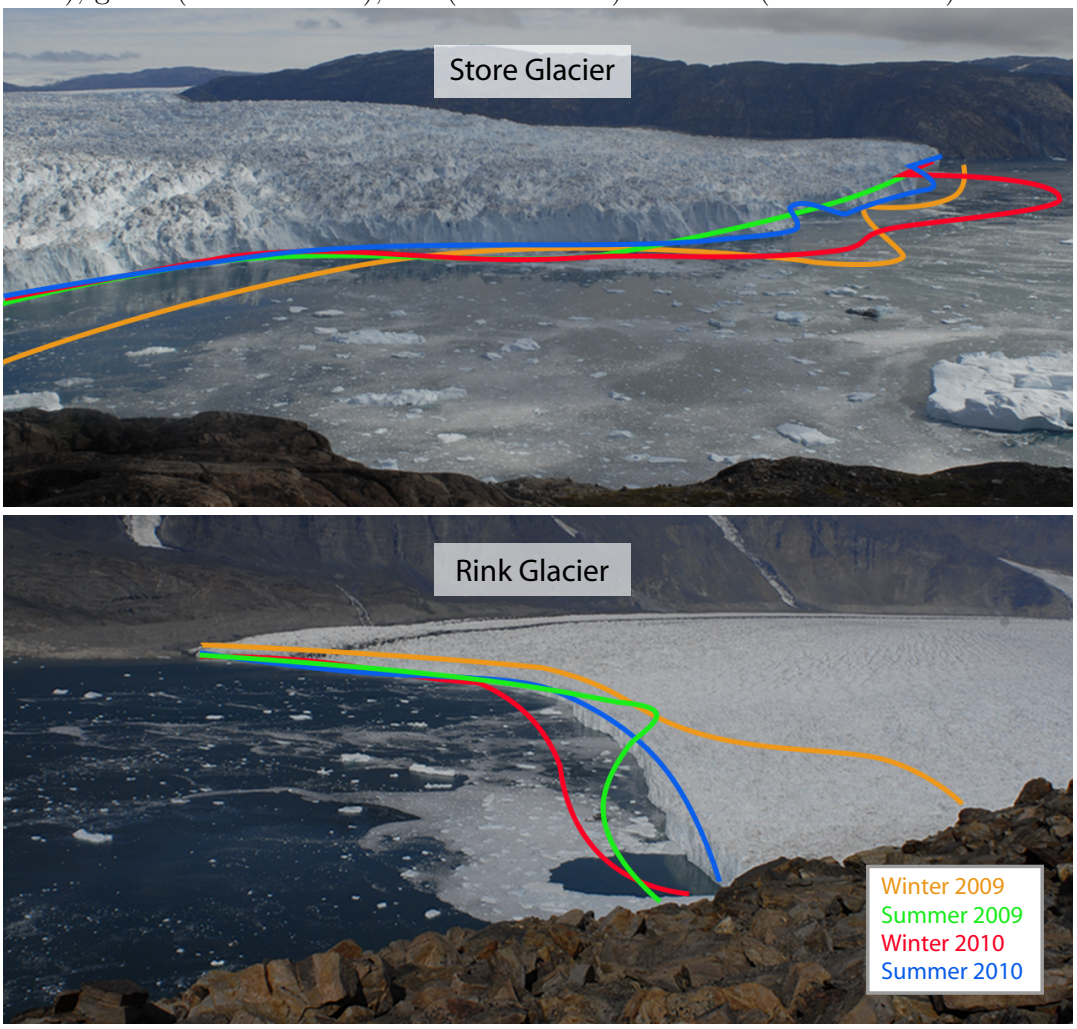

3.6.2 SgFW-driven upwelling: spatial spreading and glacier impact

Buoyant upwelling plumes, producing PluW, are commonly associated with enhanced submarine-melting through the entrainment of warm water along the ice front (Jenkins, 2011; Kimura and others, 2014; Motyka and others, 2003, 2011; Rignot and others, 2010; Sciascia and others, 2013; Sole and others, 2012; Xu and others, 2013, 2012). The scale of the subglacial channels allowing SgFW to enter the fjord is, to date, not well defined (Jenkins, 2011; Kimura and others, 2014; Sciascia and others, 2013; Xu and others, 2013). It has been hypothesised that emerging SgFW is channelised and hence injected through discrete portals (Jenkins, 2011; Mugford and Dowdeswell, 2011) rather than being evenly injected all along the front (Sciascia and others, 2013; Sole and others, 2012; Straneo and others, 2012; Xu and others, 2012). This is in agreement with the well-defined surface plume observed at Store (Figure 3.8) and elsewhere (Mortensen and others, 2013; Motyka and others, 2003; Rignot and others, 2010; Xu and others, 2013), which indicates a point source injection at depth, and with the presence of turbid jets at Rink (Figure 3.5) which also have a distinct spatial footprint. In all surveys, the layer of PluW was, nevertheless, present uniformly across the fjord near the glacier and fading downstream (Figures 3.4 and 3.5), suggesting that despite the potential localised injection point, PluW rapidly spreads across as well as along the fjord at its hydrostatic equilibrium depth and can potentially have an indirect impact on the glacier front.

3.6.3 Oceanic and bathymetric influence on glacier front behaviour

The presence of sills in Uummannaq Bay has a strong impact on how water is transported into the deeper fjords and toward each of the glacier calving fronts. The trough on the continental shelf near the entrance to Uummannaq Bay provides access for all water above 450 m to penetrate as far as Store Glacier. At Rink, the presence of an additional sill at 400 m depth and 50 km down the fjord (Dowdeswell and others, 2014) further affects the temperature of water found at Rink's calving front. Indeed, we found the bottom water at Rink to have the characteristics of the AW found at Store at 400 m depth (i.e. the depth of Rink sill) showing that Rinks inner basin is filled with the water present outside the fjord at the same depth of its sill (Figure 3.2). Rink's sill is approximately at the depth of the AW maximum of temperature, thus the water present at Rink ice front has even more melting potential than for Store fjord.

At Rink Glacier, mass loss (i.e. calving and submarine-melt combined), logged by time-lapse photography, appears to be relatively homogeneous across the entire ice front with maximum losses at the central sector, coincident with the deepest part of the fjord and fastest ice flow. At Store Glacier, frontal mass loss during both summers is greater on the southern flank, where a large embayment between two headlands coincides with an upwelling plume visible at the surface. These observations suggest that in addition to the fjord geometrical control on the glacier calving processes (McFadden and others, 2011; Schild, 2013), the presence of warm, subpolar-originating water bodies at the glacier front, along with the presence of sills and inner basins in the fjord, also has a considerable impact on the calving

dynamics, and thus on the shape of the calving front. We hypothesise that deep tidewater glaciers, such as Rink (~ 750 m), which are exposed to warm AW at their base (~ 75 % at Rink), will be influenced by widespread, submarine-melting, which would favour a relatively flat calving face (Figure 3.9). For glaciers such as Store, which have a shallower ice front (< 500 m), the impact of SgFW discharge on the upper layer (0–200 m) may be the primary factor driving frontal geometry and dynamics. We suggest that notch cutting and the resulting headlands along the ice front are related to the presence of localised plume-induced melting of the ice front where SgFW is released from subglacial portals (Figures 3.8 and 3.9). The local undercutting of the calving face will, in this case, create a crenulated ice front characterised by a series of embayments and separated by headlands where calving processes will dominate.

3.7 Conclusions

Hydrographic surveys in Uummannaq Bay in August 2009 and 2010 reveal that warm (2.8 ± 0.2 °C) and deep Atlantic water (AW) was present below 450 m and driving free convective submarine-melting of Rink and Store, two fast-flowing outlets of west Greenland. Subglacial fresh water (SgFW) injected at depth was also observed to force buoyant plumes where runoff-mixing is the main process involved, yielding a turbid outflow of plume water (PluW). Turbidity transects across the upwelling plumes show that, after reaching the surface, the plumes sink below surface water (SW) and replace any water present at its level of outflow along and across the fjord. The plumes do not necessarily surface in the fjords, as revealed by jets of turbid water, observed at depths of 50 to 100 m. Two layers can be distin-

guished in the fjord structure. The upper layer (0–200 m) experiences the greatest variability in between the fjords and surveys, with three different states of interaction observed: submarine-melting and runoff-mixing (state 1), runoff-mixing alone (state 2) and runoff-mixing alone at shallower depth (75 m) (state 3). The evolution of the upper layer structure from state 1 to state 3 is hypothesised to be primarily controlled by the increase of SgFW discharge. The bottom layer below 200 m depth has similar characteristics in all surveys, with free convective submarine-melting being the only process involved. At Rink Glacier, which is 750 m deep, $\sim 75\,\%$ of the ice front is affected by submarine melting which favours a relatively flat calving front. In contrast, at Store, which is up to 500 m deep, SgFW discharge and buoyancy-driven plumes affect over 40 % of the calving front, leading to a crenulated terminus characterised by a series of notches separated by headlands which are exposed to mechanical failure and calving.

Chapter 4

Vigorous submarine-melt sustained throughout winter months at Store Glacier

4.1 Summary

The influx of warm Atlantic Water around Greenland is argued to be one of the main drivers of the on-going retreat and dynamic thinning of the many tidewater outlet glaciers that drain the ice sheet (Box and others, 2012; Holland and others, 2008; Pritchard and others, 2009; Rignot, 2006). Recent studies show that in summer, wind and tidal driven fjord circulation and glacial meltwater runoff drives enhanced submarine-melting across the calving front which is a significant component, of total mass loss (Rignot and others, 2010; Sutherland, 2012; van de Wal and others, 2008; Xu and others, 2013). Nevertheless, little is known about winter

conditions and it is often assumed that submarine-melt is retarded by reduced supraglacial melt runoff and fjordal capping by sea-ice, which by limiting the impact of the wind on the surface water would limit the overturning fjord circulation. This chapter presents oceanographic measurements (temperature, salinity and current) from November 2012 to May 2013 adjacent to Store Glacier. A mean winter submarine-melt rate of $1.9\pm0.5\,\mathrm{m\,d^{-1}}$ across the calving front was determined by two methods, which is approximately five times larger than previously assumed for similar glaciers around Greenland (Christoffersen and others, 2012; Sciascia and others, 2013; Sole and others, 2012; Xu and others, 2013) and of same order of magnitude than summer submarine-melt (Enderlin and Howat, 2013; Rignot and others, 2010; Sciascia and others, 2013; Sutherland and others, 2013; Xu and others, 2013, 2012). Such vigorous submarine-melting is fuelled by deep, saline Atlantic Water within the fjord at a temperature of 2.8 ± 0.1°C and which is actively circulated across the calving front throughout winter by sustained subglacial discharge of $36\pm22\,\mathrm{m^3\,s^{-1}}$, which we infer is derived from frictional melting of the glacier bed. On an annual timescale submarine-melting amounts to $\sim1.5\,\mathrm{Gt\,yr^{-1}}$ or ~14% of the total ice discharge of Store Glacier, an amount which is comparable to summer surface ablation.

4.2 Introduction and background

Ninety percent of the Greenland ice sheet is drained through marine terminating glaciers (Rignot and Mouginot, 2012) thus, understanding the ocean interaction with them is crucial to evaluating the mass balance and dynamics of the GrIS and its impact on future sea-level rise. Recent ice thickness measurements and basal

topographic inversions reveal that the ice sheet is underlain by major troughs on the scale of the Grand Canyon (Bamber and others, 2013) which drain into the heart of the ice sheet thereby rendering it much more susceptible and vulnerable to ocean forcing and destabilisation than previously thought (Bamber and others, 2013) The influx of warm Atlantic Water around Greenland is argued to be one of the main drivers of the on-going retreat and dynamic thinning of the many tidewater outlet glaciers that drain the ice sheet (Box and others, 2012; Holland and others, 2008; Pritchard and others, 2009; Rignot, 2006).

Summer oceanographic observations around Greenland reveal submarine-melt rates at the calving fronts of large outlets glacier to be of $1-4\,\mathrm{m\,d^{-1}}$ (Rignot and others, 2010; Sutherland, 2012; Xu and others, 2013). These high rates of submarine-melting are associated with fjord circulation induced by the presence of subglacial runoff along with wind and tidal effects. Despite this, little is known of winter conditions and it is assumed that submarine-melt is repressed by reduced supraglacial-melt and fjordal capping by sea-ice.

Subglacial runoff enters the fjord at depth via portals on the ice front, mixes with deep ambient water which yields a buoyant upwelling along the calving-face resulting in enhanced, sustained submarine-melt (Jenkins, 2011; Motyka and others, 2013, 2003; O'Leary, 2011; Salcedo-Castro and others, 2011; Sole and others, 2012; Straneo and others, 2010; Sutherland, 2012; Xu and others, 2013, 2012).

Three contributors to the subglacial-runoff are generally identified as: 1) supraglacial-melt (hereafter, supraglacial-runoff) routed to the glacier base via crevasses and moulins (Chandler and others, 2013; Cowton and others, 2013); 2) basal-melt of the glacier (hereafter, basal-runoff) induced by the frictional heat resulting from the sliding of the glacier over bedrock and the geothermal heat flux (Bougamont

and others, 2011); and, 3) rainfall (Motyka and others, 2003). Tides or wind in and near the fjord causes currents alternatively flowing inward and outward (internal waves or seiche effects) modifying the fjord circulation (Sole and others, 2012; Straneo and others, 2010; Sutherland, 2012). The presence of sills within the fjords provides a primary control on the advection of the deep warm Atlantic Water toward the glacier front (Mortensen and others, 2011; Straneo and others, 2012) and promotes deep mixing (Mortensen and others, 2013, 2011).

Supraglacial-runoff is largest from June to August (Christoffersen and others, 2012; Sole and others, 2012) with values up to $1000\,\mathrm{m^3\,s^{-1}}$ (Rignot and others, 2010; Xu and others, 2013) and negligible during the remainder of the year (Christoffersen and others, 2012; Sole and others, 2012). In summer, the west coast of Greenland has a surface water temperature ranging from $0-10°\mathrm{C}$, which decreases rapidly with depth (Mortensen and others, 2011; Rignot and others, 2010; Straneo and others, 2012; Xu and others, 2013) down to 150 m. Between 150 m and 450 m depth the Melt Water (MW) resulting from submarine-melting is found with a temperature increasing steadily with depth. Below 450 m depth is the Atlantic Water (AW), the warmest water present (excluding the surface), with a temperature of $2-5°\mathrm{C}$ and thickness in excess of 400 m (Azetsu-Scott and others, 2012; Straneo and others, 2012; Xu and others, 2013). In winter, the surface layer reaches a temperature near its freezing point (i.e. -1.8°C) (Mortensen and others, 2013, 2011; Straneo and others, 2010, 2012) which characterises the Polar Water (Hopkins, 1991). To date, no observation has assessed and quantified the winter ocean-glacier interaction processes. In Uummannaq Bay, the presence, in summer and potentially all year round, of the warm AW in contact with major outlet glaciers (Xu and others, 2013), as well as sea-ice cover (i.e. limiting the

ocean/atmosphere interaction) from January to June, make this area of particular interest for quantifying the impact of submarine-melting on the glacier front when the supraglacial-runoff discharge is negligible.

The along-fjord circulation induced by ocean-glacier interaction inside deep fjords is expected to be comprised of two convective cells stacked vertically with intensity and direction oscillating as a result of external forcing such as wind-events on the continental shelf (Jackson and Sutherland, 2014; Sciascia and others, 2013, 2014; Sole and others, 2012; Straneo and Cenedese, 2013; Straneo and others, 2011; Sutherland, 2012). Such patterns are usually refereed to as an intermediate circulation (Sciascia and others, 2014; Sutherland, 2012) and can have periods varying on the order of hours to days (Arneborg and Liljebladh, 2001; Jackson and Sutherland, 2014; Sciascia and others, 2014; Sutherland, 2012).

4.3 Field site and data collection

During the winter 2012 – 2013, we recorded the water conditions within the fjord of the marine terminating Store Glacier in Uummannaq Bay. Store is the 6th fastest glacier in Greenland and the 3rd largest contributor to the drainage of the western flank of the Greenland ice sheet (Rignot and Mouginot, 2012). Every month (hereafter referred to as a period), from November 2012 to May 2013, 4 – 7 stations were completed between 10 and 15 km from the glacier front (Figure 4.2). For each station, we deployed through the sea-ice a Conductivity, Temperature, and Depth (CTD) profiler (SeaBird 19plus) and an Acoustic Doppler Current Profiler (ADCP) (RDI Workhorse long ranger 117 kHz). Measurements were taken from the surface to ∼750 m depth. Bathymetry of the fjord was collected between the summers of

2009 and 2013 using a single-beam echo-sounder (Raymarine DSM300 200 – 50 kHz, 1 kW). Sea-ice up to ∼40 cm thickness covered the entire Store Fjord and part of Uummannaq Bay from February to late April. Air temperatures during the same period ranged from -30°C to +8°C, with an average of -8°C (Figure 4.1).

Figure 4.1: Air-temperature and rain events near Store in 2012-2013, as measured every 15 minutes. A weather station was placed on an island ∼8 km from the glacier front. Red vertical lines show the timing of each period of measurements. Note that rain-events of mid-March and May are artefacts due to the melting of the snow that had collected inside the rain gauge.

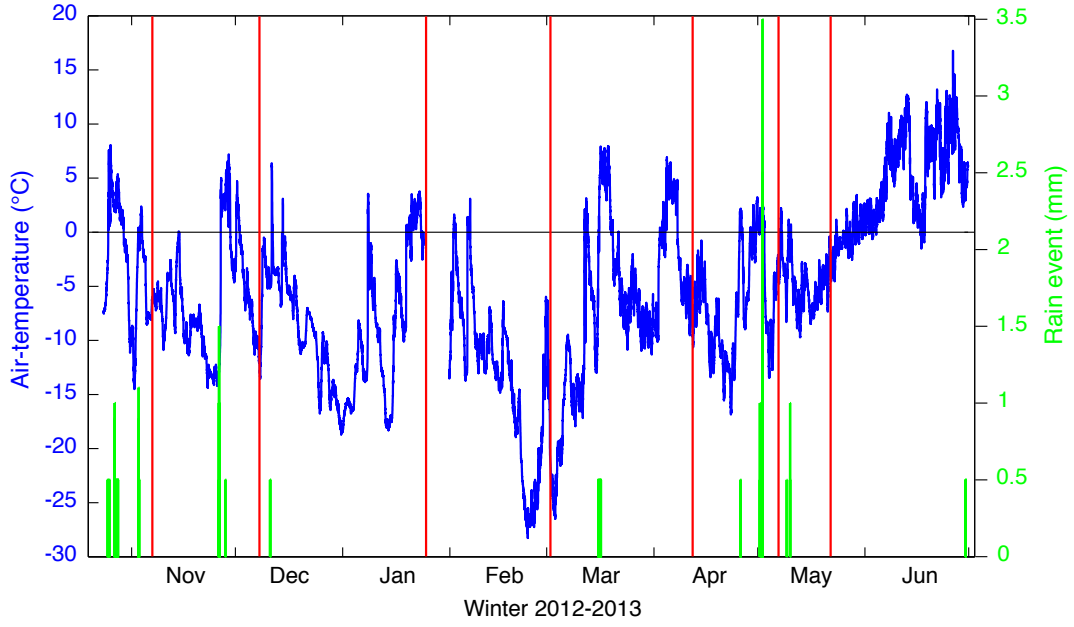

Figure 4.2: Map of the study area. a) Schematic of the different sources of water to the subglacial-runoff discharge and the induced circulation at the glacier front. Bathymetry of Store Fjord along the center profile (b–purple line) is displayed to exhibit the possibility for the warm Atlantic water to reach the glacier front. b) Location of the stations collected during the winter 2012–2013. Stations are color-coded according to the period of the measurement with repeated stations divided to display each period of measurement. The 450 m depth contour has been plotted in orange to show the possibility for the AW to penetrate to the glacier front. The green line shows the position of the cross section of the fjord used in the models for constraining the advection of water through the fjord.

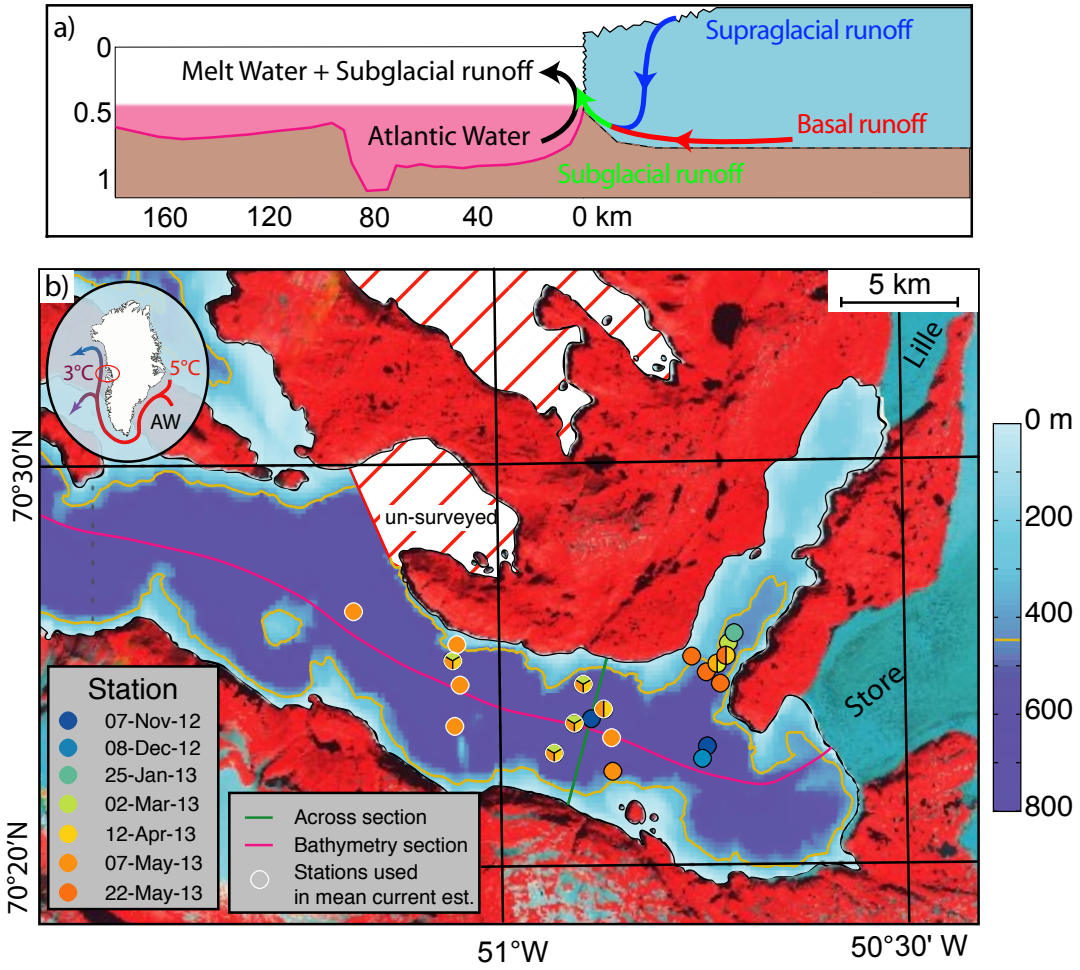

4.4 Methods

4.4.1 Oceanographic measurements

CTD data

The CTD is lowered and raised using an electrical winch in the fjord at a controlled speed of $1\,\mathrm{m\,s^{-1}}$ Each profile of temperature and salinity is vertically averaged into spatial bins of 1 m that include data from both the descent and ascent of the probe. Data from the first 10 m of the descent are omitted due to a bias created by the thermal shock between the air ($\sim$ -15°C) and the water (-1.5°C), even after 1 minute of thermal equilibration at the surface. The measurement uncertainty is 0.0025°C for temperature and 0.0013 PSU for salinity.

ADCP data

Each individual current profile is the time average of a continuous hour of measurement with the ADCP kept at the surface and pointing downward. Values deeper than 430 m depth are removed due to the low quality of the measurements obtained below that depth. A barotropic (i.e. identical for all depth) tidal current is estimated from a tide gauge, installed at $5-10\,\mathrm{km}$ from the ADCP stations (not shown), and subtracted for each current profiles. The maximum tidal current during spring tide is $<0.5\,\mathrm{cm\,s^{-1}}$ In the following section, all current are corrected for the tide.

4.4.2 Circulation induced by the ocean-glacier interaction

In order to estimate the monthly impact of the ocean on the glacier it is necessary to isolate the circulation induced by the ocean-glacier interaction from the intermediate circulation (Sciascia and others, 2014; Sutherland, 2012). The limited number of current profiles, both spatially and temporally, however prevents from performing a full time/spatial analysis (Sciascia and others, 2014; Sutherland, 2012). Hence for simplification, we assume:(1) the circulation induced by the ocean-glacier interaction is constant during the winter (i.e. from November to May); and (2) the intermediate circulations have on average no significant impact on the transport of heat. The first hypothesis is reinforced by the absence of significant variation in runoff discharge from November until May (i.e. no supraglacial-runoff and constant basal-runoff) (Christoffersen and others, 2012). Moreover, the lack of significant temperature and salinity changes of the water-masses below 100 m depth suggests that the impact of the glacier on the water column is relatively similar throughout the winter. The second hypothesis is strengthened by the oscillatory character of the intermediate circulation (Arneborg and Liljebladh, 2001; Jackson and Sutherland, 2014; Sciascia and others, 2014; Sutherland, 2012) which should thus have a null average transport. Moreover, only the current profiles near the centre of the fjord and concomitant with sea-ice cover in Uummannaq and Baffin bays, are used to limit both the coastal effect (Sutherland, 2012) on the measured current and the impact of the wind on the intermediate circulation.

Finally, to reduce the bias of the current flowing into Lille Fjord on Store Fjords circulation, the current profiles from Lille fjord mouth (i.e. January, February, and May) are discarded (Figure 4.2). The depth average of the 18 remaining

current profiles (hereafter: mean current) is thus expected to be representative of the circulation induced by the ocean-glacier interaction.

4.4.3 Models

To assess ocean-glacier interactions we applied two semi-independent approaches using the physical characteristics of the fjord water (temperature, salinity and current) to quantify the submarine-melting and runoff discharge.

The Gade model: first developed by Gade (1979) to identify a water-mass resulting from submarine-melting of ice by the specific salinity and temperature drop associated with this process; it has since been extended by Straneo and others (2011) to account for the subglacial runoff-mixing occurring on Arctic glaciers (Mortensen and others, 2013; Motyka and others, 2013, 2003; Rignot and others, 2010; Xu and others, 2013). We adapted the model to not only identify but also quantify the impact of each of these processes (see below). Another process was also added: the thermal cooling of a water mass independently from submarine-melting or runoff-mixing.

The Motyka model: first developed by Motyka and others (2003) for Alaskan glacier and subsequently applied in Greenlandic fjords (Johnson and Munchow, 2011; Motyka and others, 2013; Rignot and others, 2010; Sutherland, 2012), this model is based on the conservation of heat, salt and volume through a fjord cross section. It evaluates the submarine-melt rate by assuming that all heat lost is due to submarine-melting. The subglacial runoff discharge is deduced from the volume budget and the submarine-melt con-

tribution. A salt budget is used to balance the volume budget when velocity profiles are not known for the entire cross-section.

For each period, we assume a steady state and no spatial or temporal variability during the time needed (2 – 4 days) to take all the measurements (typically 4 – 7 profiles). All the temperature and salinity profiles for a period are averaged before being processed along with the mean current in each model. A cross section of the fjord bathymetry at 15 km from Store front (Figure 4.4) is used to control the advection of the water.

Gade model

The Gade model is based on the identification and the quantification of the processes having impacted a layer of the water column. Each process modifies the temperature and the salinity according to a relationship determined theoretically and proportionally to the magnitude of the impact (Gade, 1979; Jenkins, 1999; Straneo and Cenedese, 2013; Straneo and others, 2011). The identification of a process in a Temperature-Salinity (TS) diagram is thus possible by comparing a water body gradient and the slope determined theoretically for this process (Figure 4.3). Such an approach was developed to identify the melting of ice in the ocean (Gade, 1979; Jenkins, 1999) and for mixing of glacial runoff water with fjord water (Mortensen and others, 2013; Straneo and Cenedese, 2013; Straneo and others, 2012). To quantify a process impact sustained by a water-mass, we have adapted the Gade model to compare the observed variation of temperature and salinity with depth to an impact of reference. At Store Fjord, five processes have been identified as potentially impacting the fjord water during the winter months:

- Submarine-melting

- Runoff-mixing
- Thermal cooling
- Local sea-ice formation
- Mixing with water-mass from outside the fjord

The local sea-ice formation from November to April would have resulted in an increase of the water column salt content of $\sim$0.45 kg m^{-2} (i.e. estimated for the average ice thickness observed of $\sim$30 cm, and a residual salinity of $\sim$15 PSU in the ice –Aagaard and Carmack, 1981). In contrast an increase in salt content of approximately 14 kg m^{-2} is observed between the profiles of December and April (Figure 4.3). Thus, local sea-ice formation is considered to have a negligible impact on the water column structure and is neglected hereafter. Similarly, the relative similar structure of the water column from January to May suggests that no major mixing with water-masses from outside the fjord occured and that the changes observed between December and January are due to seasonal variability.

For a given impact δ, the theoretical temperature and salinity change related to each of the three processes and the corresponding TS–slope can be estimated as follow (refer to Table 4.1 for nomenclature and constant values).

Submarine-melting:

$$\begin{aligned}
\Delta T_{Gade} &= \delta V_{ice} \frac{C_{sw}\rho_{sw}(FP_{ice} - T_{sw}) - \rho_{ice}(C_{ice}(FP_{ice} - T_{ice}) + L)}{V + \delta V_{ice}} \\
\Delta S_{Gade} &= \frac{\delta V_{ice}(S_{ice} - S_{sw})}{V + \delta V_{ice}} \\
\text{Gade-slope} &= \frac{\Delta T_{Gade}}{\Delta S_{Gade}}
\end{aligned} \tag{4.1}$$

Figure 4.3: Mean temperature-salinity (TS) profiles color-coded by period. Submarine-melting (blue), runoff-mixing (Pink) and thermal cooling theoretical slopes used to identify the process in the Gade model are shown. Schematic (arrows) of the three sets of two processes, used in the Gade model, have been added. Isopycnal of 26.3 and 27.1 kg m^{-3} are marked with black lines. The blue and red grids correspond to the evolution that would follow a water parcel with starting characteristics of 35 PSU and temperature ranging from -1 to 12°C, if impacted by submarine-melt or runoff-mixing, respectively. Note that the rsunoff-slope and Gade-slope are dependent of the temperature and salinity.

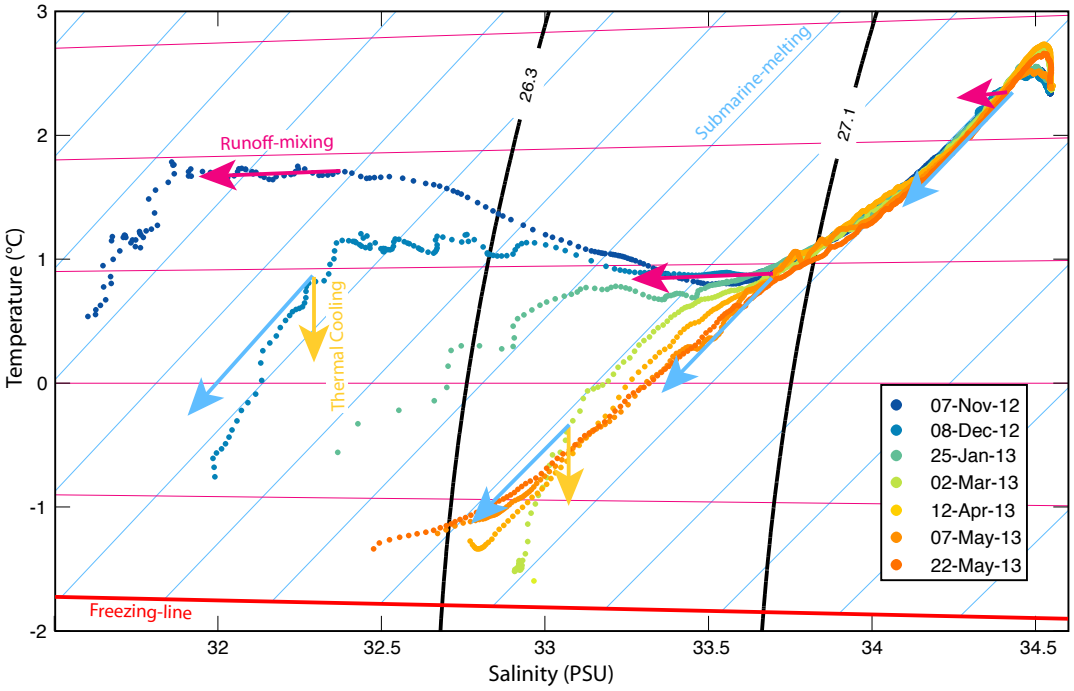

Runoff-mixing:

$$\Delta T_{runoff} = \frac{\delta V_{rw}(T_{rw} - T_{sw})}{V + \delta V_r w}$$
$$\Delta S_{runoff} = \frac{V_{rw}(S_{rw} - S_{sw})}{V + \delta V_{rw}} \tag{4.2}$$
$$\text{Runoff-slope} = \frac{\Delta T_{runoff}}{\Delta S_{runoff}}$$

Thermal cooling:

$$\begin{aligned} \Delta T_{ThC} &= \frac{\delta E_{ref} t}{\rho_{sw} V C_{sw}} \\ \Delta S_{ThC} &= 0 \\ \text{ThC-slope} &= \frac{\Delta T_{ThC}}{\Delta S_{ThC}} = +\infty \end{aligned} \tag{4.3}$$

Table 4.1: Variables used in the Gade and Motyka models. Values in orange are constants influencing the scaling of the results; purple values are assumed; blue values are extracted from the literature; green values are measured or calculated

Description	Variable	Value	Uncertainty	Units	Reference
Water parcel volume of reference	V	1000		litre	
Temperature of glacier ice	T	-20	±10	°C	Thomas et al. 2004
Salinity of glacier ice	S	0	±0	PSU	Rignot et al. 2010
Freezing-point of glacier ice	FP	-0,5	±0.5	°C	Rignot et al. 2010
Reference impact for submarine-melting	δ	0,1		litre	
Temperature of subglacial runoff water	T	0	±2	°C	Rignot et al. 2010
Salinity of subglacial runoff-water	S	0	±1	PSU	Rignot et al. 2010
Reference impact for runoff-mixing	δ	0,1		litre	
Reference energy for thermal cooling	E	-100		W/m	
Reference time	t	86400		second	
Latent heat of fusion	L	334000		J/kg	
Heat capacity of ice	C	2100		J/kg/°C	
Density of ice	ρ	0,9		kg/m	
Depth	z	Measured		m	
Heat capacity of seawater	C	Calculated		J/kg/°C	
Temperature of seawater	T	Measured	Calculated	°C	
Salinity of seawater	S	Measured	Calculated	PSU	
Density of seawater	ρ	Calculated		kg/m	
Along-fjord velocity	U	Measured	Calculated	cm/s	
Heat budget	ΔH	Calculated	Calculated	J	

Because only two independent parameters are known for a water parcel (i.e. temperature and salinity), only two processes can be quantified at once. Comparison of the TS gradient of each layer and the slope of each process for all profiles indicates that three main situations are identified (Figure 4.3):

- TS gradient $\geq$ Runoff-slope, and TS gradient $\leq$ Gade-slope
- TS gradient $>$ Gade-slope, and TS gradient $\leq$ ThC-slope
- TS gradient $<$ Runoff-slope

In most situations the TS profile is significantly affected by one process and slightly modified by another (Figure 4.3). Hence for each situation identified above we associate two processes as follow:

- Runoff-mixing and submarine-melting
- Submarine-melting and thermal cooling
- Runoff-mixing alone

The impact of a process within a layer is determined by comparing the impact of reference for this process with the temperature and salinity difference, between the observed layer and the layer immediately below. Indeed, for the runoff-mixing and submarine-melting, the resulting water is more buoyant than the original water. Similarly, the atmospheric cooling propagates downward in the water column from the surface and therefore the energy lost by a layer can be compared to the energy of the layer immediately below.

As the processes observed in this study engender either a buoyant water (i.e. submarine-melt and runoff-mixing) or has an impact decreasing with depth (i.e. thermal cooling from ocean-atmospheric exchanges), thus the impact sustained locally by a fjord layer can be determined by comparing this layer to the layer immediately below.

Moreover, the modification dT and dS, sustained by a layer, under the local impact i_n, of two processes n is proportional to the impact of reference ΔT_n and ΔS_n as

follow:

$$\begin{cases} dT(z) = i_1(z)\Delta T_1(z) + i_2(z)\Delta T_2(z) \\ dS(z) = i_1(z)\Delta S_1(z) + i_2(z)\Delta S_2(z) \end{cases} \tag{4.4}$$

Due to the buoyancy resulting of the submarine-melt and runoff-mixing, the modified water parcel can interact again with the glacier at a shallower depth, hence be modified again. In order to obtain the total submarine-melt and runoff-mixing contribution for a given layer, it is necessary to integrate the local impact measured in each deeper layers through to the glacier bottom. Analogously, the total thermal-cooling sustained by a water parcel is the cumulative sum of all the local cooling measured for the layer below.

Thus, the total contribution of each process I at a given depth is evaluated from the local impact i (Equation (4.4)) as follows:

$$I_n(z) = \sum_{p=bottom}^{z} i_n(p) \tag{4.5}$$

Finally, the vertical profile of cumulated impact I for each process n is advected through the fjord using the mean current profile $U(z)$ to quantify the total ocean-glacier interaction at Store:

$$Q_n(z) = I_n(z)W(z)U(z) \tag{4.6}$$

where $W(z)$ is the width of the fjord at a certain depth z

Uncertainty estimation: Estimation of the uncertainty is achieved by propagation of the measured uncertainty (i.e. temperature, salinity, current) and subjectively assumed error on the hypothesis (i.e. ice temperature, in-situ freezing point) (Table 4.1), through the equations. All the uncertainties associated with each parameter are supposedly independent thus in the estimation of the model uncertainty the measured and assumed error are summed in quadrature.

Limitation: The necessity to cumulate the local impact of the processes upward is a significant source of uncertainty for the upper layers as in Equation (4.5) each layer cumulates the uncertainty from the layers below. Tests were performed applying Equation (4.5) with one or two layers to evaluate the impact of the two stacked convective cell (Sciascia and others, 2013; Straneo and others, 2011; Sutherland, 2012). When varying the depth of the two layers interface, a variation <10% in the model results was obtained.

Another limitation of the model is the inability to differentiate more than two processes at once without resorting to assumptions. Although, the assumptions made here are relatively robust, access to other independent variables would improve the differentiation and quantification of multiple intricated processes.

Motyka model

The Motyka model (Motyka and others, 2003) is based on the heat, volume, and salt budgets through a fjord cross-section.

When the volume budget through a fjord section is not perfectly known, an evaluation of the unknown volume and heat discharge has to be determined apriori to

assess the total volume and heat budget. This is evaluated by assuming that the only source of salt in the water column is the ocean (Motyka and others, 2013; Rignot and others, 2010; Xu and others, 2013). Thus, if the current U at any point of the fjord was known perfectly, the salt budget Q_{salt} defined as follows should be balanced:

$$Q_{salt} = \sum_{z} S(z)U(z)W(z).dz \tag{4.7}$$

where $S(z)$ is the salinity and $W(z)$ the width of the fjord at a particular depth z.

The maximal range of the current profiler was 450 m, so is an unknown current below this depth. To balance the salinity budget (Equation (4.7)) a compensatory water discharge Q_{comp} and the resulting current U_{comp} is estimated between 450 m and the fjord bottom as follow:

$$\begin{aligned} Q_{comp} &= \frac{Q_{salt}}{S_{sw}(z = 450)} \\ U_{comp} &= \frac{Q_{comp}}{A_{comp}} \end{aligned} \tag{4.8}$$

where A_{comp} is the area of the fjord below 450 m depth. Note that the salinity below 450 m is very homogeneous, thus the depth z taken for $S_{sw}(z)$ has a negligible impact on the estimation of Q_{comp}

Then we can estimate the heat budget for the fjord cross section using Q_{comp} below 450 m:

$$\Delta H = C_{sw}(z = 450)Q_{comp}\rho_{sw}(z = 450) + \sum_{z} C(z)Q_{sw}(z)\rho(z) \tag{4.9}$$

where C_{sw} the thermal capacity ρ_{sw} the density of seawater, respectively.

The imbalance in the heat budget ΔH is thus assumed to be totally due to submarine-melting which can be estimated as follow:

$$Q_{sbm} = \frac{\Delta H}{L\rho_{ice} + (FP_{ice} - T_{ice})C_{ice}\rho_{ice}} \tag{4.10}$$

Because there are two external sources of water into the fjord (subglacial-runoff water and submarine-melt water), the volume budget is not balanced and a net outflow of water should occur. The volume budget can thus can be written as follow:

$$Q_{rw} + Q_{sbm} = Q_{sw} + Q_{comp} \tag{4.11}$$

where Q_{rw} and Q_{sbm} are the subglacial runoff-water and melt-water discharges, respectively.

The runoff Q_{rw} discharge can thus be deduced from Equations (4.8), (4.10) and (4.11) as follows:

$$Q_{rw} = Q_{sw} + Q_{comp} - Q_{sbm} \tag{4.12}$$

Uncertainty estimation: As for the Gade model, the uncertainty is estimated by propagation of the measured uncertainty through the equation.

Limitation: The Motyka model was used widely (Motyka and others, 2003; Rignot and others, 2010; Sutherland and others, 2013) to assess the submarine-melt

rate and runoff-mixing contribution around Greenland and Alaska. However, an important limitation is the assumption that no heat is gained or lost from ocean-atmospheric exchanges. This assumption has led the previous studies to ignore the upper 10-30 m which is strongly affected by the exchanges with the atmosphere (Rignot and others, 2010; Xu and others, 2013). Yet, the upper layer is also significantly affected by the runoff water and submarine-melt due to the interaction with the glacier.

Another source of limitation resides in the estimation of the subglacial runoff discharge. Due to the inference of the runoff discharge from the water budget (eq. 4.11) and the estimated submarine-melt discharge (eq. 4.10), the runoff discharge uncertainty is summing, to the quadrature, the absolute uncertainty in Q_{sw}, Q_{comp}, and Q_{sbm}, thus resulting of a large relative uncertainty in Q_{rw}

4.4.4 Bathymetry cross-section

The cross-section of the fjord used to advect water is at ∼15 km from the glacier front and has a maximum depth of 860 m and a width of 7 km at the surface. The total section is 4.3 km^2 (Figure 4.4). The submerged area of the glacier front is estimated to 1.8 km^2 (Chapter 2) with a maximum depth of 500 m and a maximal width of 5 km (Figure 4.4).

Figure 4.4: Bathymetry cross section of the glacier front (blue) and of the fjord (brown) 15 km down the fjord (Figure 4.2) used to estimated the submarine-melt rate and advection.

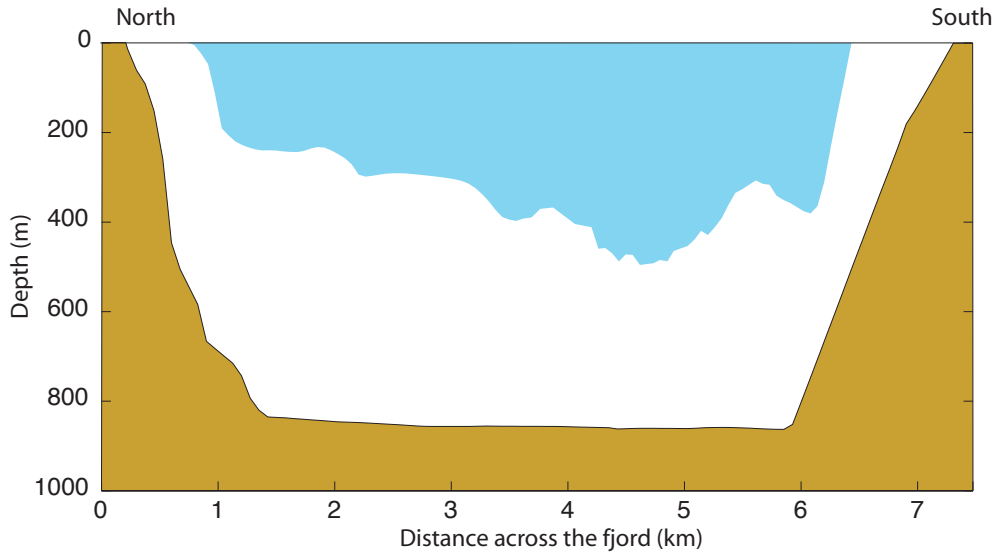

4.5 Results

4.5.1 Water characteristics

AW is observed throughout the winter below 450 m depth with a maximum temperature of 2.8±0.1°C and a salinity of 34.5 PSU. A gradual cooling and salinity increase is observed from November to January over the upper 150 m. Meanwhile, the variation of temperature and salinity, both spatially and temporally, is negligible from February to May over the rest of the water column (Figure 4.5).

Figure 4.5: Raw data from the oceanographic measurements. a) temperature and, b) salinity profiles, averaged per periods. In a) the main water bodies identified (black vertical lines) are labelled as in the text. c) All individual currents (grey) are used to estimate the mean current (blue line) and the uncertainty (shaded blue). Positive value is current going toward the glacier. The averaged compensatory current produced by the Motyka model is displayed below 450 m (dashed blue) for comparison.

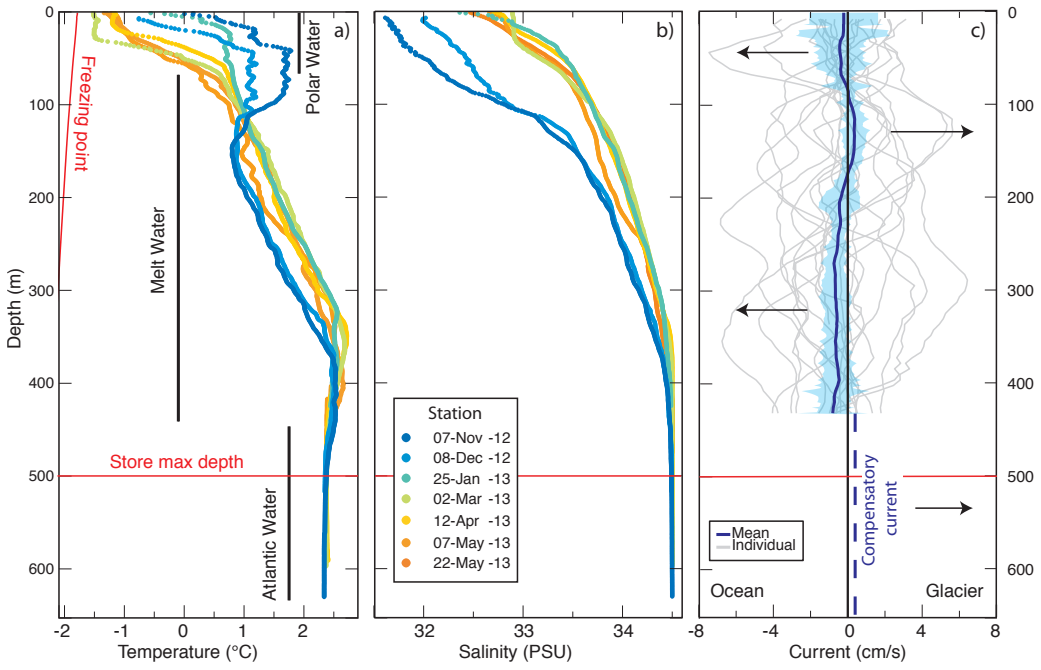

4.5.2 Current

The measured instantaneous currents are highly variable with oscillations up to $\pm 6\ \mathrm{cm\,s^{-1}}$, with no defined pattern.

The mean current is estimated using 18 current profiles (Figure 4.2) corrected for the tide and averaged per depth. The average velocity of the mean current is $\sim 0.9 \pm 0.4\ \mathrm{cm\,s^{-1}}$ (Figure 4.5) with two convective cells, stacked above each other, as previously observed for other deep Greenlandic fjords (Mortensen and others,

2011; Sole and others, 2012; Straneo and others, 2010; Sutherland, 2012; Xu and others, 2013). The first convective cell is located between 0-200 m and the second below 200 m depth. For both convective cell, the outflow is in the upper part, confirming a buoyancy driven circulation forced by the ocean-glacier interaction (Jenkins, 2011; Sciascia and others, 2013; Sole and others, 2012; Xu and others, 2013).

4.5.3 Runoff and Submarine-melt discharges

The Motyka and Gade models produced comparable estimates for both submarine-melt and runoff discharges, (Figure 4.6 and table 4.2). On average over the winter, the submarine-melting of Store front is 1.6±0.4 $\mathrm{m\,d^{-1}}$ for the Motyka model, 2.2±0.5 $\mathrm{m\,d^{-1}}$ for the Gade model, and 1.9±0.5 $\mathrm{m\,d^{-1}}$ for both models averaged. Runoff values average 49±23 $\mathrm{m^3\,s^{-1}}$, 22±21 $\mathrm{m^3\,s^{-1}}$, and 36±22 $\mathrm{m^3\,s^{-1}}$ respectively for Motyka and Gade models individually and combined. No significant temporal trend is discernable for the submarine-melting, however, the discharge of subglacial runoff displays a decrease from November through to January (Figure 4.6).

4.5.4 Gade model intermediate results

The Gade model permits us to estimate the flux of melt-water and runoff-water for each layer of the water column (Figure 4.7). As expected, the outflow of runoff-water is maximal near the surface of the fjord as well as just below the upper convective cell. The runoff-water flux pattern is relatively homogenous throughout the study period, but for November and December when the discharge is significantly greater over the upper 200 m. This increased runoff discharge at the

Figure 4.6: The Gade and Motyka models results for each period. Submarine-melting is estimated in $m^3\,s^{-1}$ and converted to the equivalent ablation of the submerged part of the glacier front ($m\,d^{-1}$ water equivalent).

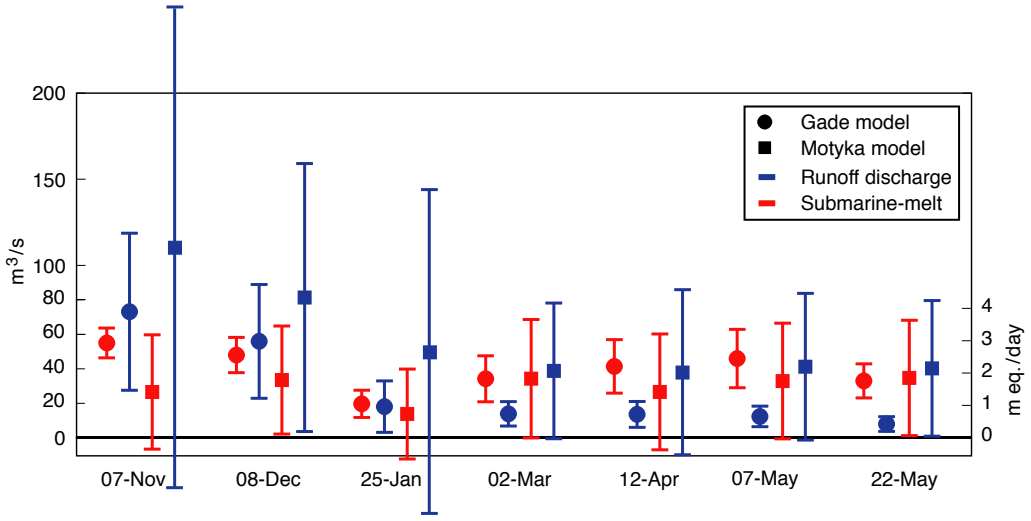

surface is in accordance with the observation of minor rainfall events associated with low pressure systems in November and December (Figure 4.1).

Submarine-melt water outflows begin ∼50 m above the glacier toe (at 450 m) and increase in intensity to 300 m depth. Between 300 m depth and the top of the lower convective cell (200 m depth) the submarine-outflow is relatively steady. On the upper convective cell an inflow of submarine-melt water between 100-200 m depth suggests mixing of the outflowing submarine-melt water with the inflowing layer, which is in agreement with previous work on the fjord circulation (Straneo and Cenedese, 2013).

The intensity of the thermal-cooling is maximal in March and reached a depth of ∼50 m (Figure 4.7) when the minimum of temperature (i.e. -28°C – Figure 4.1) was measured. In November and December while the fjord surface is not yet completely

covered with sea-ice, the thermal-cooling remains important but decreases rapidly with depth. From April to May the thermal-cooling decreases until it becomes negligible by the end of May.

Figure 4.7: Flux of the runoff and melt waters resulting of subglacial runoff-mixing and submarine-melting, respectively. Note that for the runoff-mixing, the seasonal evolution appears to have more impact than the fjord circulation.

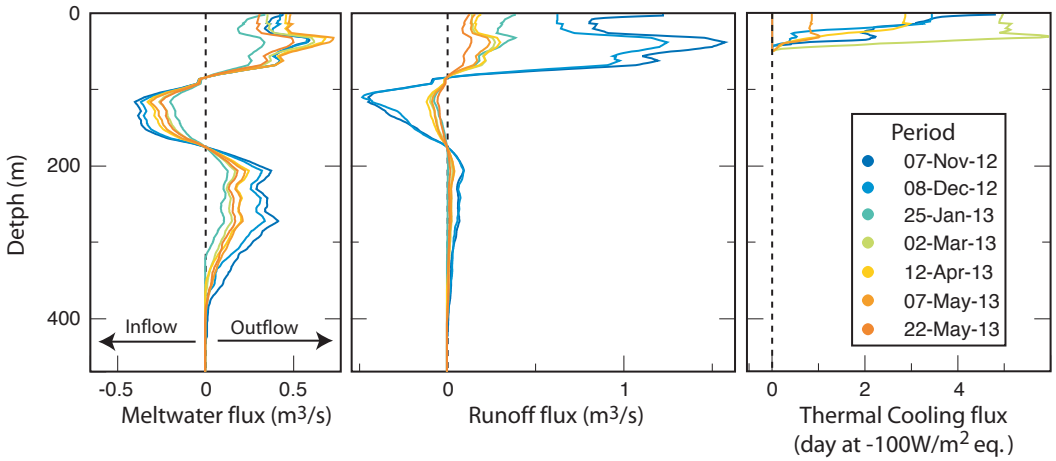

4.5.5 Motyka model intermediate results

To balance the salinity budget of the Motyka model an inflowing compensatory current of $0.4 \pm 0.1\,\mathrm{cm\,s^{-1}}$ between 430 m and the fjord bottom is necessary (Figure 4.5). This current is in agreement with the two convective cells structure and is consistent with the average velocity of the mean current (i.e. $0.9 \pm 0.4\,\mathrm{cm\,s^{-1}}$).

4.5.6 Model uncertainties

The largest source of error in calculating the submarine-melting in both models is the presence of intermediate circulations, which are oscillating and have an intensity an order of magnitude larger than the ocean-glacier interaction driven circulation (Jackson and Sutherland, 2014; Sciascia and others, 2014; Straneo and others, 2010; Sutherland, 2012). Another potential source of error is the presence of Lille Glacier upstream of our measurements, although, with a submerged area of $\sim$0.2 km^2 and a maximum depth of 170 m, hence not in contact with the AW, it is assumed to have a negligible impact.

4.6 Discussion

4.6.1 Comparison with previous studies

Previous studies have implemented numerical simulations to estimate the submarine-melting sustained by Store Glacier (O'Leary, 2011; Xu and others, 2013). O'Leary (2011) is a 1D upwelling model adapted from Jenkins (1999) and where a factor control the horizontal shape of the plume (i.e. flat or semi-circular) to evaluate the impact of distributed or channelised subglacial conduits (chapter 1). On the other hand, Xu and others (2013) use the 3D MITgcm model, with a free–surface, non–hydrostatic configuration and adapted to represent the freezing/melting occurring on a vertical ice face Xu and others (2012) to simulated an idealised representation of Store Glacier with a domaine 500 m high, 150 m wide, and extend 500 m from the ice face. The resolution is 1 m and 5 m, vertically and horizontally, respectively. Both model can be forced with individual discharge rate of subglacial runoff to

represent the effect of the plume. Their estimates range from 0.7 to 2 m d^{-1} with a subglacial runoff forcing ranging from 290 – 600 $m^3 s^{-1}$ and 0.4 m d^{-1} when no subglacial runoff forcing is applied (Table 4.2). Summer observations, at Store from August 2010, and using the Motyka model, yield an estimate of the submarine-melt rate as 4.5±1.5 m d^{-1} (i.e. 93±31 $m^3 s^{-1}$ over an ice front surface of 1.8 km^2), and the subglacial-runoff discharge as 246±45 $m^3 s^{-1}$ (Table 4.2, Xu and others, 2013). A numerical simulation at Helheim Glacier, in east Greenland, estimates the submarine-melting in winter as 1.5 m d^{-1} with a basal-runoff forcing and 0.7 m d^{-1} without (Table 4.2, Christoffersen and others, 2012).

Table 4.2: Summary of melt rate and subglacial runoff discharge values (Figure 4.6) for this study and comparison with other studies in Greenland. The numbers with an asterisk are used to estimate the impact of runoff regimes on submarine-melting (Table 4.3).

			Melt rate (m/d)	Runoff (m^3/s)	Period	Runoff regime	
Store Glacier	This study	Gade	2.2 ± 0.5	22 ± 21	Winter	Basal	Observation
		Motyka	1.6 ± 0.4	49 ± 23	Winter	Basal	
		Average	1.9 ± 0.5 *	36 ± 22	Winter	Basal	
	Xu et al. (2013)		4.5 ± 1.5 *	246 ± 45	Summer	Surface+Basal	
			2.0 ± 0.3	289	Summer	Surface	Simulation
			0.4 ± 0.1 *	0	Summer	Runoff-free	
	O'Leary (2011)		0.7 ± 0.5	60	Summer	Surface	
Helheim Glacier	Christofersen et al. (2012)		0.7	0	Winter	Runoff-free	
			1.5	30	Winter	Basal	

4.6.2 Runoff regime impact

Numerical simulations without subglacial discharge (hereafter, runoff-free regime) have been commonly supposed to represent the winter-like conditions (Sciascia and others, 2013; Sole and others, 2012; Xu and others, 2013, 2012). However, such simulations produce winter submarine-melt rates $3-5$ times smaller than the estimated winter submarine-melt rate of $1.9\pm0.5\,\mathrm{m\,d^{-1}}$ derived here, which in the same order of magnitude as summer submarine-melt forced by supraglacial-runoff (surface regime) (Table 4.2). Christoffersen and others (2012) suggest that the basal-runoff (i.e. from basal-melting of the glacier), which contributes throughout the year to the runoff discharge and becomes the principal contributor (basal-runoff regime) in winter, could enhanced by a factor of 2 the runoff-free submarine-melt during winter months (Table 4.2).

During the winter 2012-2013 at Store, basal-runoff is likely to be the only contributor to the estimated runoff using the Gade and Motyka models (Figure 4.6) as the negative air-temperature would have prevented supraglacial-melt of the glacier and only minor rainfall events occurred in November and December (Figure 4.1).

A basal-runoff estimate was produced by M. Bougamont, using the three dimensional community ice-sheet model (CISM) (Bindschadler and others, 2013; Bougamont and others, 2011; Price and others, 2011) to perform a numerical inversion of the winter 2005 surface velocity of Store Glacier, at 500 m resolution. The model inversion provides steady state fields of the ice velocity, temperature and basal traction (Beem and others, 2014; Christoffersen and others, 2014; Price and others, 2011). The associated basal melt distribution yields a total basal runoff of $22\,\mathrm{m^3\,s^{-1}}$ ($\sim0.7\,\mathrm{Gt\,yr^{-1}}$), which compares well with the estimated runoff of $36\pm22\,\mathrm{m^3\,s^{-1}}$

from the Motyka and Gade models. We thus hypothesise that the submarine-melt rate estimated for Store during the winter 2012-2013 corresponds to the impact of the basal-runoff regime.

To partition the impact of each different runoff regime on the submarine-melt rate and the annual glacier submarine ablation, we assume that the runoff regime evolves from runoff-free to basal and from basal to surface when incorporating the discharge of basal and surface runoff, respectively. This assumption is reinforced by the continuous presence of the warm Atlantic Water at the base of Store front (Figure 4.5 and chapters 3 and 8, Xu and others, 2013), hence the potential sustained impact of the runoff-free regime if no runoff discharge occurs. Similarly, as basal-runoff is a function of the glacier velocity, which is relatively constant throughout the year (Ahlstrøm and others, 2013), the basal-runoff regime would maintain its impact on the glacier front throughout the year, in the absence of supraglacial-runoff during summer months.

By subtracting the winter-like simulation (i.e. runoff-free regime) of $0.4\pm0.1\,\mathrm{m\,d^{-1}}$ (Xu and others, 2013) from the winter submarine-melting estimate of $1.9\pm0.5\,\mathrm{m\,d^{-1}}$ (i.e. basal-runoff regime), we deduce the basal-runoff regime to contribute to $1.5\pm0.5\,\mathrm{m\,d^{-1}}$ of submarine-melt, which increases the runoff-free regime by a factor of 5 (Table 4.3).

From June to August when the supraglacial-runoff becomes significant (Christoffersen and others, 2012; Sole and others, 2012) and enhances the basal-runoff on the driving the submarine-melting, the contribution of the surface regime is estimated by subtracting the winter estimate (basal regime) from the summer estimate of $4.5\pm1.5\,\mathrm{m\,d^{-1}}$ (Xu and others, 2013). Surface regime is therefore assumed to

contribute to the submarine-melt by $2.6 \pm 1.6\,\mathrm{m\,d^{-1}}$ (Table 4.3), which produces an increase from the basal regime by a factor of 2.4.

Table 4.3: Estimation of the impact of different forcing on submarine-melting from Table 4.2. Subglacial runoff discharge is given as a reference.

Forcing	Reference melt-rates	Assumed melt rate (m/d)	Runoff (m^3/s)	Assumed period (days)	Annual Submarine-melting (m/yr)	(Gt/yr)	
Free-convective	Runoff-free	0.4 ± 0.1	0	365	150 ± 40	0.2 ± 0.1	16%
Basal-runoff	Basal minus Runoff-free	1.5 ± 0.5	~35	365	550 ± 180	0.9 ± 0.2	59%
Surface-runoff	Surface+Basal minus Basal	2.6 ± 1.5	~200	90	230 ± 50	0.4 ± 0.1	25%
				Total	930 ± 230	1.5 ± 0.4	

Finally, on the annual cycle, the total submarine-melting ablation at Store is estimated to 930±230 m.yr^{-1} (1.5±0.4 Gt yr^{-1}), of which 16±4% is attributed to runoff-free submarine-melting, 25±5% to supraglacial-runoff and the majority, 59±20%, to basal-runoff (Table 4.3).

4.6.3 Consequences for Store Glacier and the Greenland Ice Sheet

Store Glaciers annual ice advection is ∼11-18 Gt yr^{-1} (Ryan and others, 2014; Weidick and Bennike, 2007), thus the estimate of the annual submarine-melting of 1.5±0.4 Gt yr^{-1} corresponds to 8-14% of the total annual discharge of the glacier. The remaining 86-92% are likely due to iceberg calving from the glacier front. Annual surface ablation is roughly estimated for Store as ∼1.9 Gt yr^{-1} (i.e. 250 m^3 s^{-1} (Xu and others, 2013) over 3 months) ranking the surface ablation and submarine-melting equally in terms of overall ablation of the glacier.

Quantification of the impact of submarine-melting on iceberg calving (O'Leary and Christoffersen, 2013) would potentially increases the relative partition of runoff and submarine-melt to the total ablation budget of the glacier.

This finding of persistently high, year-round submarine-melting at Store Glacier calls into question the validity of recent numerical modelling, both of Store Glacier and other major tidewater glaciers in Greenland, that implicitly assume negligible or absent submarine-melt in winter (Nick and others, 2013; Sciascia and others, 2013; Sole and others, 2012; Todd and Christoffersen, 2014). It is now clear that this common assumption of negligible winter submarine-melt, which was first questioned by Christoffersen and others (2012) when estimating that basal-runoff could

double the submarine-melt rate during winter months, is no longer valid. New parametrisations in the models of the submarine-melting, taking into account the year-round subglacial forcing, would radically alter recent conclusions that the GrIS will experience reduced long-term retreat and contribution to sea-level rise, or that the GrIS is insensitive to ocean forcing (Nick and others, 2013; Stocker and others, 2013).

Moreover, in situ subglacially-derived melt (i.e. basal runoff) is principally driven by frictional heat dissipation associated with fast-flow and basal motion at its bed (Christoffersen and others, 2012). Hence, reports of significant acceleration in Greenland's tidewater glaciers (Joughin and others, 2010; Moon and others, 2012; Rignot, 2006) will likely have resulted in increased basal-melt runoff, subglacial discharge, fjordal circulation, and finally submarine-melting across their respective ice fronts and particularly during winter months. Consequently, where AW was present at these calving fronts, higher submarine-melt rates would be experienced and sustained than by mechanical calving processes alone. Hence, the sustained thinning and retreat of these glacier commonly attributed to ice flow dynamics may partly be attributed to enhanced submarine-melting, which as discussed is likely to be effective throughout winter, when the supraglacial melting is absent.

4.7 Conclusion

In this chapter we adapted the Gade model based on the identification of the specific impact of a interacting process on the water column, to quantify the submarine-melt, runoff-mixing, and thermal-cooling.

Along with the Motyka model, we estimated from oceanographic observation the submarine-melt and subglacial-runoff discharge at the front of Store Glacier during the winter 2012-2013. Inferred submarine-melt of $1.9\pm0.5\,\mathrm{m\,d^{-1}}$ was on the same order of magnitude than previous summer observation.

This important winter submarine-melt, which was $3-5$ times more important than numerical simulation, which invalidate the common assumption of negligible submarine-melt during winter months, is supposed to be forced by limited yet continuous discharge of subglacial runoff originating from the basal-melt of the glacier.

Evaluation of the impact of each runoff regime on the submarine-melt rate exhibit that the discharge of basal-runoff increased the runoff-free submarine-melting by a factor of 5, while the presence of supraglacial-runoff during summer months increased the basal-runoff melt-rate by a factor of 2.4.

The annual submarine-melt ablation of Store Glacier is estimated to $930\pm230\,\mathrm{m.yr^{-1}}$ ($1.5\pm0.4\,\mathrm{Gt\,yr^{-1}}$), of which $16\pm4\%$ is attributed to runoff-free submarine-melting, $25\pm5\%$ to supraglacial-runoff and the majority, $59\pm20\%$, to basal-runoff.

The annual submarine-melting of $1.5\pm0.4\,\mathrm{Gt\,yr^{-1}}$ corresponds to 8-14% of the total annual discharge of the glacier, while the remaining 86-92% are likely to be related to iceberg calving.

Chapter 5

Plume-induced surface circulation and evolution

5.1 Summary

This chapter evaluates the characteristics of the surface fjord circulation induced by the upwelling plumes at the front of Store Glacier. The response of the plume and the induced circulation to two extreme-melt events are evaluated. Upwelling plumes are forced by the injection of subglacial fresh water at depth into the fjord, resulting in a buoyant flow at the ice face. This process, by renewing the water present at the glacier front, is thought to be a leading factor driving submarine melt at tidewater glacier fronts in the Arctic. However, the enhanced submarine melt is constrained to a relatively small section of glacier front. Here we present quantification of the fjord circulation using time-lapse imagery along the Store Glacier terminus at high spatial and temporal resolutions. A lateral circulation

of $5-10\,\mathrm{cm\,s^{-1}}$ induced by the upwelling on the whole glacier front is observed. Such plume-induced circulation would enhance the submarine melt rate outside the plume upwelling core and should be considered, when evaluating the plume overall impact on the glacier terminus.

The sub-daily response and 95% correlation between plume activity and surface air temperature during two extreme-melt events of the summer 2012 suggests that any surface-melt event, even on a daily timescale, will induce both a negative surface mass balance and an enhanced submarine melting on the whole glacier width.

5.2 Introduction and background

Understanding the upwelling-plumes present at the front of tide-water glaciers forced by discharge of subglacial runoff discharged at depth, is essential in order to quantify the interaction between the Greenland ice sheet and the adjacent ocean.

Several studies have shown that subglacially driven plumes induce a buoyant vertical circulation which renews the water present at the ice front (Greisman, 1979; Motyka and others, 2013; Rignot and others, 2010; Xu and others, 2013), thus enhancing submarine melt rates (Jenkins, 2011; Motyka and others, 2013; Rignot and others, 2010). Furthermore, modelling has estimated that the summer plume can induces a submarine melt rate of $6-8\,\mathrm{m\,d^{-1}}$ (Kimura and others, 2014; O'Leary, 2011; Xu and others, 2013, 2012). However, this impact is spatially limited to the part of the ice front situated above the subglacial injection point (Kimura and oth-

ers, 2014; Xu and others, 2013). It is commonly accepted that due to the elongated shape of the glaciated fjords the water circulation is mostly along the fjord axe, thus models are often limited to a 2D section extending from the glacier front, and within the plume, downstream along the center line of the fjord (Jenkins, 1991; Mugford and Dowdeswell, 2011; Salcedo-Castro and others, 2011; Sciascia and others, 2013, 2014; Sole and others, 2012; Xu and others, 2012). To estimate the circulation and submarine melt outside of the plume itself the former 2D model are run with a null subglacial discharge, which is supposed to be representative of the free-forced circulation. Free-forced circulation (i.e. no subglacial discharge) have been modelled and produce a submarine melt rate $<0.2\,\mathrm{m\,d^{-1}}$ (Sciascia and others, 2013; Sole and others, 2012; Xu and others, 2012) which is often considered as negligible. Despite the spatially limited size of the plume, to date, only one study has modelled in 3D the plume-induced circulation in a glaciated fjord (i.e. Store Glacier– Xu and others, 2013). However the width of the model's domain being limited to 150 m, no conclusion can be drawn on the circulation on the side of the plume.

Plumes formed by pro-glacial river are often visible at the surface of fjords from June to September and have an intensity (i.e. sediment concentration and extent area) proportional to the discharge of runoff water originating from surface melting of the glacier (Chu and others, 2009; Hudson and others, 2014). However, such plume are injected directly at the surface of the fjord and do not induce the vertical buoyant flow typical of subglacial discharge.

Understanding plume behaviour, and hence its impact on fjord circulation and submarine melt is necessary to better predict the intra-seasonal evolution of tidewater glaciers.

5.3 Field site

Store Glacier is over 5 km wide with a catchment area of 34000 km^2 (Rignot and Steffen, 2008). An upwelling plume is commonly observed at the surface of the fjord during the summer months with a width of approximately 1 km (Chapter 3 Xu and others, 2013). Bathymetric mapping reveals that Store Fjord has an inner basin deeper than 1000 m filled with 2.8 °C Atlantic Water (AW) below 450 m depth, corresponding to the maximum depth of the calving-front (Chapters 3, 4 and 8).

5.4 Methods

To characterise at high spatial and temporal resolutions the impact of the plume on the whole glacier front an experiment was developed using a time-lapse camera overlooking the ice-ocean interface of Store Glacier, when a major upwelling plume was active (Figure 5.1, Supplementary material – "Store Glacier_20120714-20120721.mov" and "Store Glacier_20120721-20120805.mov").

The time-lapse camera was installed on the edge of a cliff approximately 400 m above water level and took photographs continuously from 14th July to 5th August 2012 with an interval of 4 minutes.

Changes in plume extent and iceberg displacement are clearly visible in the time-lapse photographs. However, in order to quantify these changes, it is necessary to project and georeference these images in the Earth frame of reference.

Figure 5.1: Map of Store Glacier and the surrounding fjord. The time-lapse camera and its approximate field of view is marked on the south side of the fjord. The weather stations, AWS-Store and AWS-Summit, are identified with the yellow stars.

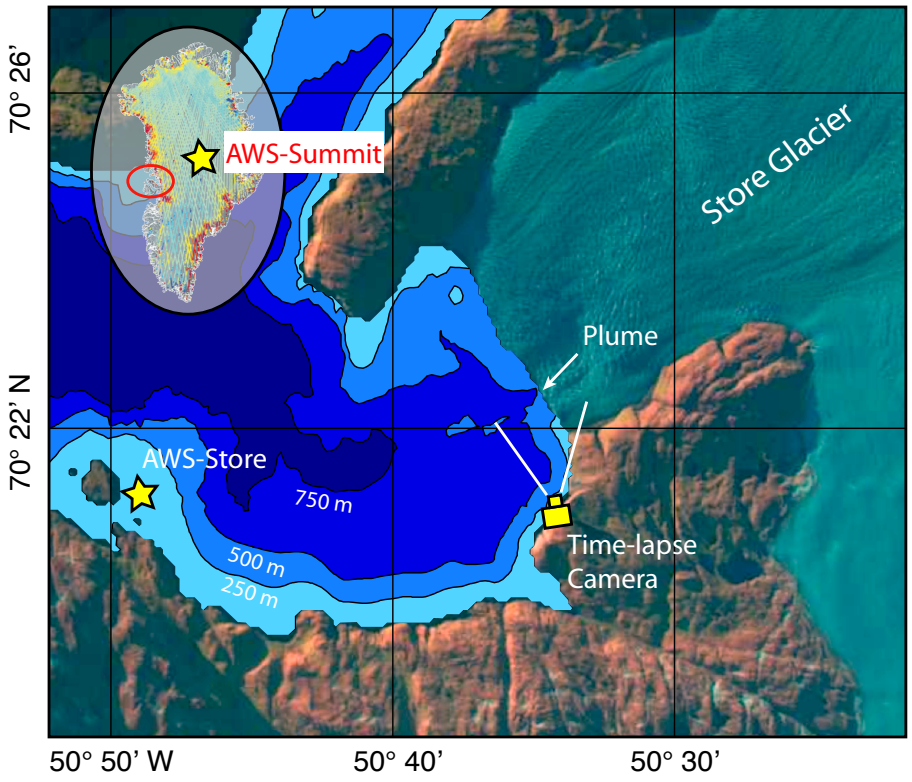

5.4.1 Georeferencing

The photographs are manually georeferenced by picking, from a clear day photograph, four ground control points (GCPs) on the coast line, which are also clearly identifiable on 7$^{\text{th}}$ April 2009 satellite image from Google Earth. An affine transformation matrix is established using the four GCPs, and allows to reprojection of each pixel to terrestrial coordinates. Slight motion (i.e. $1-3$ pixels) of the camera between different frames primarily due to wind gusts moving the tripod are assumed to be negligible compared to the iceberg displacement (i.e. $15-100$ pixels) and are therefore not corrected.

All photographs are projected onto the new coordinate system and are gridded into a 20×20 m grid, allowing for a uniform resolution across the entire width of the fjord. In the following sections, the term time-lapse photographs refers to the georeferenced and gridded images.

5.4.2 Plume area

When the plume is visible at the surface of the fjord, it is usually identifiable by a persistent, ice-free area of brown colored water spreading away from the glacier front. It has a clear outer boundary where brash-ice (i.e. small icebergs) accumulates.

The evolution of the plume region at the surface of the fjord is estimated, every hour, by manually tracing the position of the edge of the plume. In some cases, the western end of the plume extend out of the camera frame, thus the measured area underestimates the real size of the plume.

5.4.3 Iceberg velocity field

The displacement of small icebergs is used as a proxy for the horizontal fjord circulation close to the glacier front and near the plume boundary. In a wave-free environment the movement of icebergs at any given moment can be assumed to be due to the action of (1) wind on the aerial part, (2) currents on the underwater part, and, (3) the inertia of the iceberg (Bigg and others, 1997). In this experiment, inertia of the icebergs is neglected due to the relatively small sizes of the majority of the icebergs observed (i.e. <5 m). This hypothesis is validated by the observation of changes, between frames, of the path and velocity of icebergs even those with a size >100 m. Finally, as the wind is mostly calm during the period of the experiment (see discussion below), the movement of the icebergs at the ice front is assumed to depend of the fjord currents.

The displacement of the icebergs between two frames is determined by feature-tracking using the software Boujou (version 4 – www.vicon.com). The tracking is performed on the red channel of the photographs, because it increases the contrast of the images. The "small features" options and the highest sensitivity are chosen in the parameters of Boujou. Because the images were georeferenced prior to the feature-tracking, the East and North velocity components of a feature are deduced from the x and y displacement of this feature between two successive images. Finally, the icebergs horizontal velocity field at any given time is estimated by averaging the velocities of all features in a 200×200 m grid for the 25 images taken before and after that time.

It is not directly possible to extract the tracking, hence the velocity, uncertainty using Boujou as it is a commercial "black box". However since non-moving ob-

jects (e.g. coast line) have on average an associated velocity of $\pm 3\,\mathrm{cm\,s^{-1}}$ this value is assumed to correspond to the uncertainty in the velocity estimation. velocities $>250\,\mathrm{cm\,s^{-1}}$ are discarded because they are likely due to feature tracking blunders.

The simplified projection of the photographic pixels on the sea surface increases the footprint of any object with a significant height, in the same direction as the camera point of view. This will in turn bias the position associated with a feature detected on the highest part of an iceberg. However, because the vast majority of icebergs observed have a relatively limited height (i.e. $<2\,\mathrm{m}$) and due to the reduced final resolution (i.e. $200\,\mathrm{m}$), this bias is assumed to have a negligible impact on the final velocity field.

5.4.4 Air temperature forcing on plume dynamics

In order to test at first order the hypothesis of the forcing of air temperature induced supraglacial runoff on plume activity, the 2 m air temperature from two weather stations near the ice front on inland of the ice cap are compared with the plume area. A weather station located on an island 8.5 km down fjord from Store front (hereafter, AWS-Store Front) recorded the atmospheric condition near the glacier front at sea level. In the absence of weather station over Store Glacier catchment and to avoid potential local climate on weather stations situated in nearby glaciers, the weather station situated at the summit of the Greenland Ice Sheet (hereafter, AWS-Summit– Steffen and others, 1996) and $\sim$500 km inland from Store Glacier terminus was supposed representative of the temperature variation over Store Glacier catchment, at first order.

5.5 Results

5.5.1 General weather conditions

Concomitantly with the period of experiment, on the 29th July and the 5th of August 2012, the Greenland Ice Sheet has recorded surface melting over approximately 77% and 73% of the ice cap, respectively (Tedesco and others, 2013). These two events are the second and third most intense extreme melt events during the summer 2012 (Tedesco and others, 2013).

Similarly from July to August the region of Store Glacier underwent a positive temperature anomaly of 2.5 – 3.5°C between 1000-2000 m altitude, hence breaking a record in terms of surface ablation in 2012 (Tedesco and others, 2013).

The weather station measured an average temperature of 8.3±2.8 ° and -8.2±4.6°C between 13th July and 9th August 2012, with a maximum of 15°C on 27th July, and (∼0°C on 29th July) for AWS-Store Front and AWS-Summit, respectively (Figure 5.2).

It is to be noted that the weather condition at the end of July and begin of August 2012 were particularly warm and uncommon in Greenland (Nghiem and others, 2012).

5.5.2 Plume area

The area of the plume at the surface varied during the 21 days of observation between $0 - 18{\cdot}10^5\,m^2$ with an average area of $6.3{\cdot}10^5\,m^2$ (Figure 5.2). On 25th July, the plume disappeared completely from the surface of the fjord before reap-

pearing ∼500 m to the south a few hours later. From 01:00 UTC on 26th July the plume area significantly increased at a constant rate until 23:00 UTC on 27th July followed by a greater increase at a faster rate until 29th July, when it stabilised at a maximum area of $>18{\cdot}10^5\,m^2$ Note that the maximum area is underestimated because at that point the plume spread beyond the camera frame. Finally, on 30th July, the plume decreased and reached a minimum extent of $\sim 4 \cdot 10^5\,m^2$ in the late afternoon 31st July. On 2nd August, the area of the plume began to gradually grow again with a more intense rate after 3rd August 20:30 UTC, as a result of the rapid onset of a secondary plume touching the first plume and outflowing along the fjord wall.

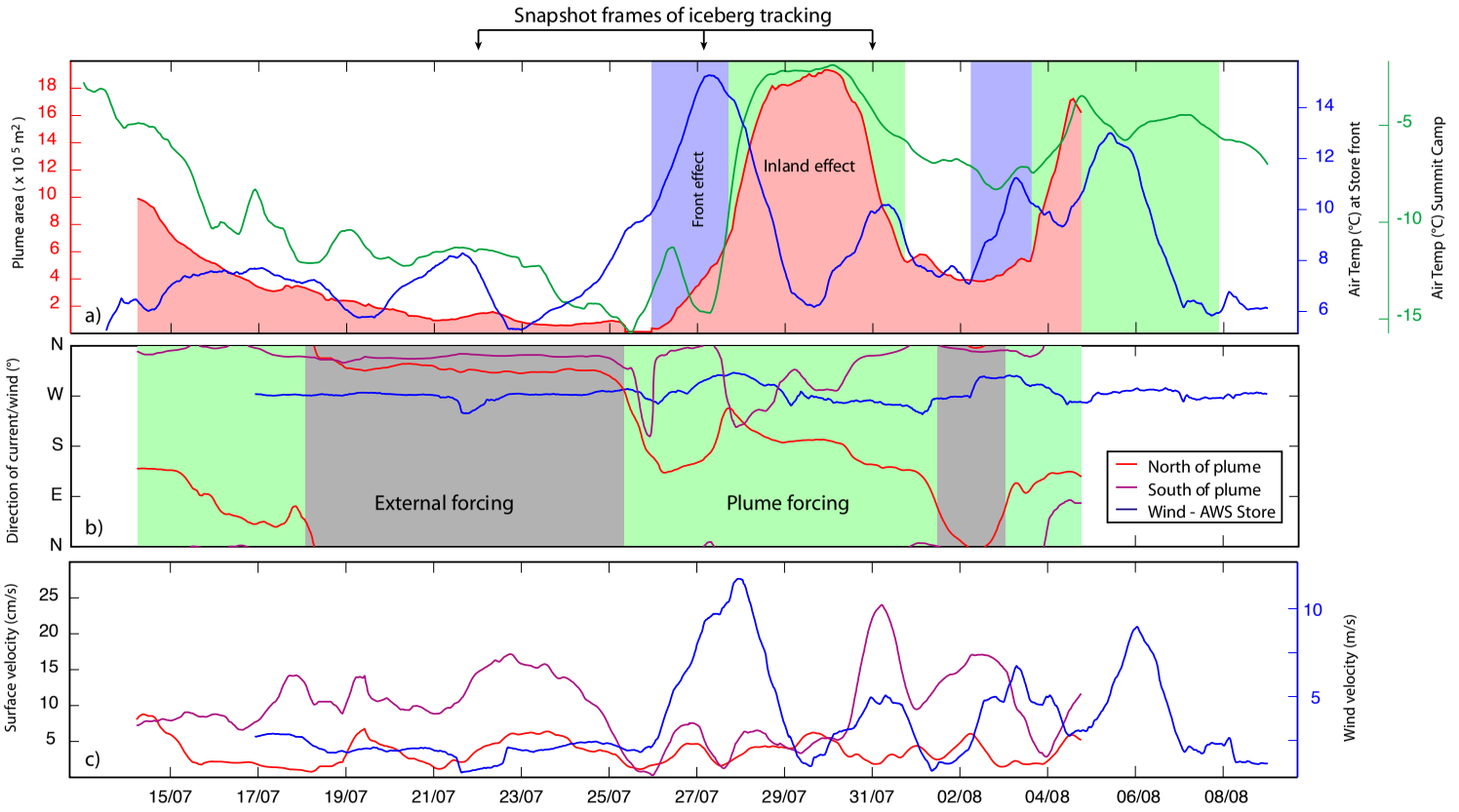

Figure 5.2: Time-series of the plume characteristics, impacts, and controls at Store Glacier during two extreme-melt events of 2012. Each parameter is smoothed using a 24 h-running average. a) Plume area (red region), air temperature at AWS-Summit (green) and at AWS-Store (blue). Vertical shades represent the periods when the air temperature at the front (blue) or at the summit (green) drives the plume area (see text). b) Direction of the surface current for the north (red) and south (purple) sections of the glacier front (Figure 5.3) compared to the wind (blue) from AWS-Store. Wind direction has been shifted by 180° to display its potential effect on moving the fjord surface. Vertical shades represent the two types of circulation observed: northwest-ward (grey) or converging from both side toward the plume (green). c) as for b) but for the velocity. Note the difference of scale for the current and wind velocity.

5.5.3 Fjord horizontal circulation

Two main states of fjord surface circulation are observed near Store Glacier (Figures 5.2 and 5.3): (1) currents flowing homogeneously across the whole glacier front, toward the north flank of the fjord, and (2) currents converging from the sides of the fjord toward the plume.

The currents observed in areas north and south of the plume range from 3 – 25 $\mathrm{cm\,s^{-1}}$ with an average of 7.4 $\mathrm{cm\,s^{-1}}$ and 10 $\mathrm{cm\,s^{-1}}$, respectively. Furthermore, when the currents are converging toward the plume, small icebergs (i.e. <2 m) tend to cluster at the edge of the plume (Figure 5.3, Supplementary material – "Store Glacier_20120714-20120721.mov"). It is also possible to observe the ejection of medium to large icebergs (>30 m) at high speed (i.e. >100 $\mathrm{cm\,s^{-1}}$) westward as they approach the sides of the plume. Some of these ejected icebergs are entrained backward toward the ice front by large eddies (diameter of 500 1000 m) on each side of the plume, and at a depth of approximately 50 – 100 m (i.e. the approximate keel depth of the big icebergs). Note that calving events can locally modify the surface circulation generating a current which diverges from the calved iceberg. These changes are, however, short-lived.

5.6 Discussion

5.6.1 Plume impact on the glacier front

Comparing the plume area and the fjord surface circulation, it is possible to infer that, at times the plume induces a cross-fjord (hereafter, lateral) circulation on

Figure 5.3: Velocity fields of the surface circulation extracted by iceberg tracking. The red arrows represent the estimated surface current and the brown shading the concomitantly observed plume area. Green rectangles are used to evaluate the current time-series from Figure 5.2. Panel a) correspond to the north-westward circulation when the plume has a limited area $< 4 \cdot 10^5\,\mathrm{m}^2$; b) the circulation starting to converge toward the plume when its area is $\sim 4 \cdot 10^5\,\mathrm{m}^2$; and c) the more intense converging circulation as the plume area is $> 8 \cdot 10^5\,\mathrm{m}^2$ The weather condition concomitant with these snapshots can be observed in Figure 5.2. Note that in panel c) the plume is extending beyond the camera frame, hence is larger than actually shown. The position of the time-lapse camera and the approximate picture angle of view is shown on the south side of the fjord.

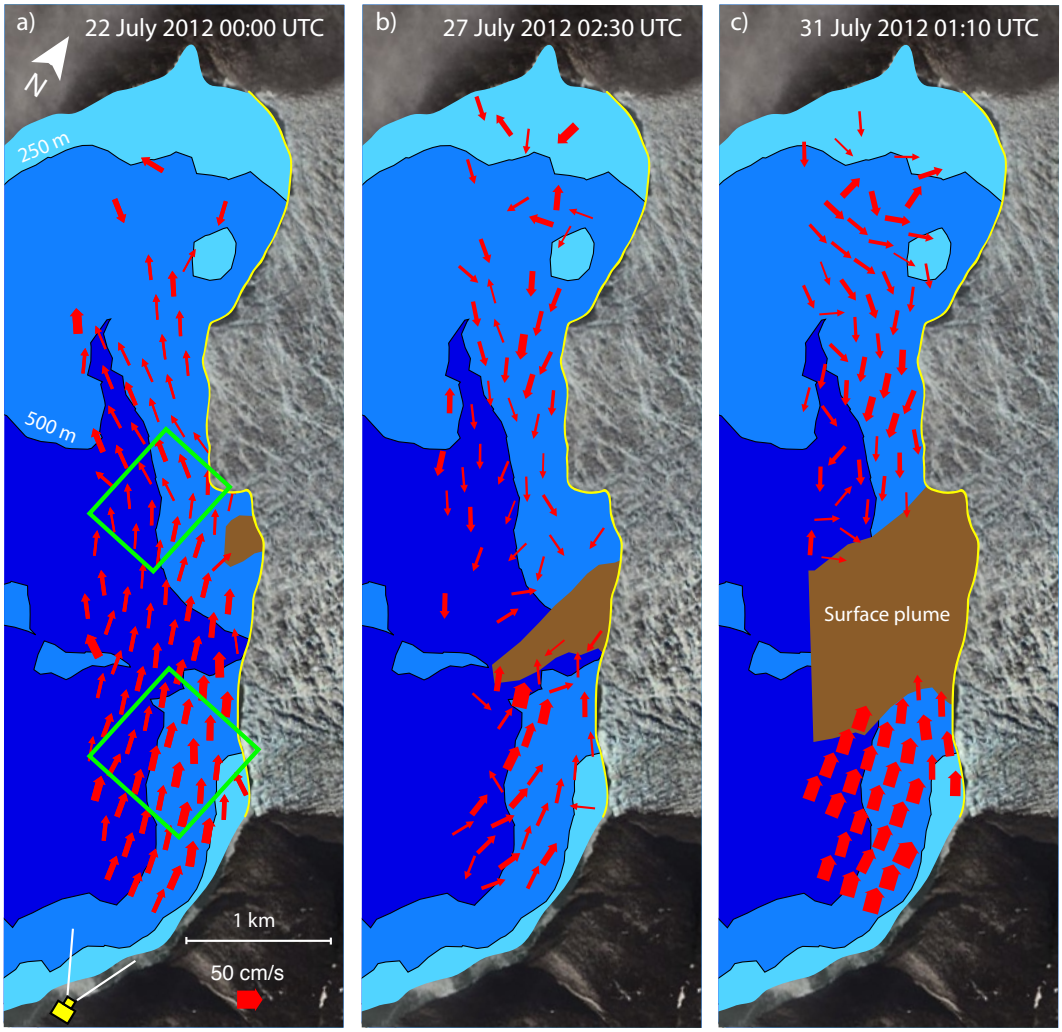

the glacier front external to the plume itself. Indeed, while the plume has an area $> 4 \cdot 10^5\,\mathrm{m}^2$, a surface current of $5-10\,\mathrm{cm\,s^{-1}}$ along the whole glacier front is converging from both sides toward the edge of the plume (Figure 5.3). This circulation persists even during a strong wind event on 27$^{\mathrm{th}}$ July.

In contrast, when the plume has an area $< 4 \cdot 10^5\,\mathrm{m}^2$, a circulation of $10-20\,\mathrm{cm\,s^{-1}}$ is observed flowing north-westward along the entire ice-front. This circulation exists regardless of the wind speed or direction (Figure 5.2), which suggests that other external factors such as the tide (Mortensen and others, 2011) or the intermediary circulation (Jackson and Sutherland, 2014; Mortensen and others, 2011; Sciascia and others, 2014; Straneo and others, 2010; Sutherland, 2012) might influence circulation at the ice front, during periods of less-vigorous plume activity.

The convergence of the surface water can be explained by the entrainment of the ambient surface water while the plume is sinking back to its hydrostatic depth of equilibrium (Chapter 6). Similarly, the large eddies observed on each side of the plume are probably due to outflowing of the plume water at depth associated with lateral drawing of ambient water along the ice face.

Circulation induced by the plume is key to the predicted high submarine melt rate ($6-8\,\mathrm{m\,d^{-1}}$) within the plume (Kimura and others, 2014; Sciascia and others, 2013; Xu and others, 2013). Yet, the overall impact of this process is rather limited due to narrowness of the plume core ($<$500 m) compared to the full glacier width (5 km).

However, as for vertical circulation within the plume, the lateral circulation would also enhance the submarine melt rate, even if smaller in magnitude, on the entire glacier front outside of the plumes boundaries (Figure 5.4). In fact, a subma-

Figure 5.4: Plan view schematic of the horizontal circulation (not to scale) induced by the upwelling plume at the surface, as previously understood (black), and observed during this study (red). Dashed line correspond to current at 50-100 m depth. Section of the glacier referred as internal and external to the plume are marked on the top graph.

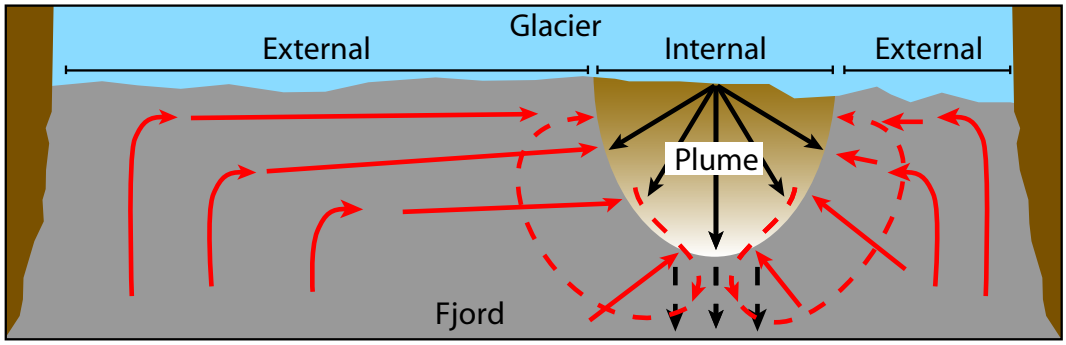

rine melt rate of only $\sim 1\,\mathrm{m\,d^{-1}}$ on the entire glacier front external to the plume would have the same impact as the $6-8\,\mathrm{m\,d^{-1}}$ submarine melt inside the plumes boundaries.

Therefore, to correctly predict the impacts of the plume on the glacier front, both internal and external, it is necessary to extend the model domain to the full glacier width of the front.

Such a model could potentially explain the difference between the measured submarine melt rate of $3.4 \pm 0.7\,\mathrm{m\,d^{-1}}$ (Chapter 8) on an area external to the plume, while the numerical simulations predict a melt $<1\,\mathrm{m\,d^{-1}}$ (Kimura and others, 2014; Xu and others, 2013).

As evaluated and modelled for the intermediary circulation (Jackson and Sutherland, 2014; Sciascia and others, 2014), the lateral circulation observed when plume is less vigorous (Figure 5.2), would also induce enhance submarine melting.

5.6.2 Limitation of the feature-tracking method

Two major limitations of the method to infer the fjord circulation are: (1) the necessity to have enough small icebergs throughout the field of view to evaluate the velocity field, and (2) a slow enough iceberg motion between two successive photographs to be successfully tracked by Boujou. For most of the area observed by the camera, the limited velocity of the lateral circulation and the regular calving of icebergs from the glacier front produced sufficient small icebergs to be tracked continuously. However, inside the area of the plume itself, the strong outflowing current of $\sim 1.5\,\mathrm{m\,s^{-1}}$ (Chapter 6) compared to the time-lapse interval (i.e. 4 minutes), as well as to the limited number of icebergs present, prevented the horizontal circulation inside the plume from being estimated.

5.6.3 Air temperature forcing on plume dynamics

The time-series of the plume characteristics (i.e. plume area and lateral circulation) was concomitant with two extreme melt events on the Greenland Ice Sheet (29$^{\mathrm{th}}$ July and 5$^{\mathrm{th}}$ August 2012, Nghiem and others, 2012; Tedesco and others, 2013). This rare short term and high amplitude events produced an unique opportunity to assess amplitude and timing response of the plume to the air temperature forcing.

Surface air temperature is one of the main factors controlling supraglacial ablation (Hock, 2005). However, the plume activity did not seems to respond to significantly to the variation of the air temperature at sea-level (i.e. AWS-Store Front). Meanwhile, the plume extent varied jointly with the air temperature observed at the Summit camp even if the weather station is more than $\sim 500\,\mathrm{km}$ from Store

Glacier terminus, (Figure 5.2). Looking more in details at the plume area, the first gradual increase of the plume area at the start of each event coincides with an increase of the air temperature near the glacier front, while the rapid increase of the plume area corresponds to the increase of the air temperature inland of the ice sheet (Figure 5.2).

A power law fit of the air temperature at AWS-Summit to the plume area explains 95% of the observed variance (Figure 5.5). Similarly, fitting the air temperature at AWS-Store on the residual explains another 1% of the variance (Figure 5.6), particularly during the start of the melt event on 29th July (Figure 5.7).

Although the derived power-law relation is likely not applicable for all ranges of temperatures, the response observed here is coherent with a heat-wave moving from the coast, where the small catchment limits the impact of the supraglacial-melting, to the ice-sheet interior where most of the catchment is affected, hence producing an extremely active upwelling plume at the glacier front. Note, that as the subglacial discharge increases, all other control being equal, the buoyancy of the plume increases (Sciascia and others, 2013; Xu and others, 2013, 2012). Over a certain subglacial discharge rate the PlW become more buoyant than the fjord surface water, thus outflows on the surface of the fjord. The plume extend will therefore increase more rapidly, for a similar increase in Subglacial discharge rate, than when the plume after reaching the surface sink to its hydrostatic level of equilibrium. Indeed, when the plume outflow on the surface, its extent it controlled by sedimentation and mixing and not by the dynamics of the plume itself.

Furthermore, the pulse-like character of the extreme-melt events show that the plume area responds rapidly (i.e. <6-12h) to the air temperature perturbation. The sub-daily response of the plume to a supraglacial-melt event is in agreement

Figure 5.5: air temperature at Summit camp versus observed area of the plume (blue dot) from 14th July to 5th August 2012. Red line corresponds to the least-square best fit of a power law function to the observations.

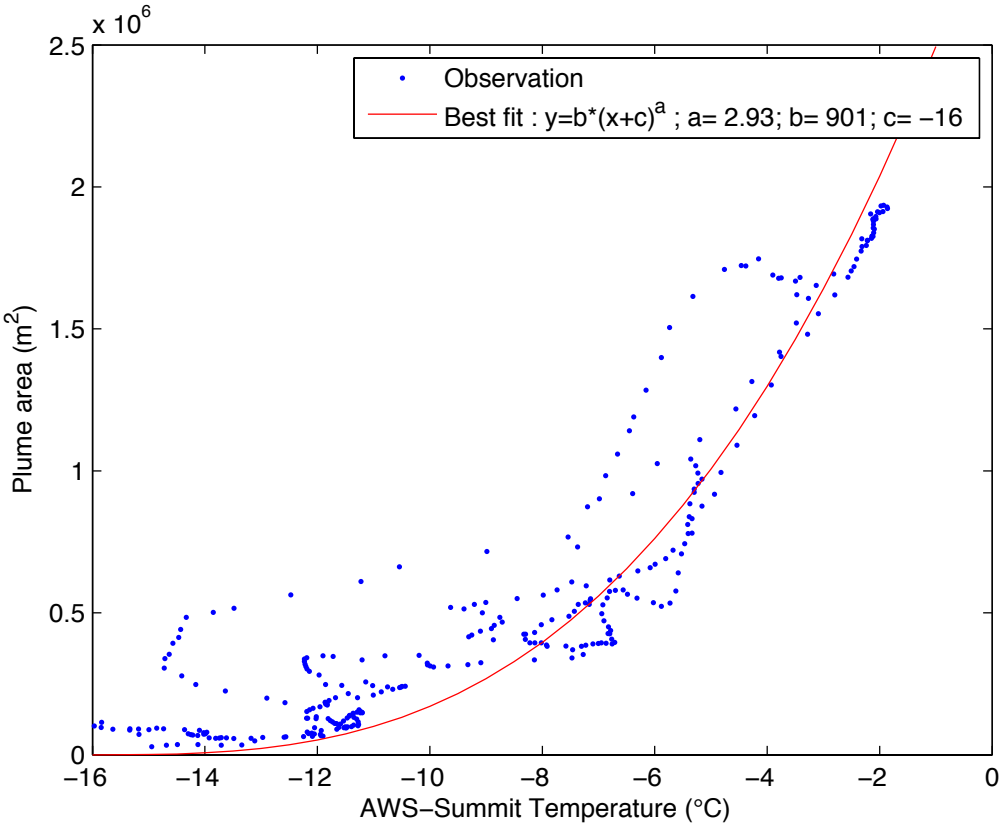

with an efficient, fully developed drainage network as previously observed for land terminating glaciers (Andersen and others, 2010; Chandler and others, 2013; Cowton and others, 2013).

Because the plume area responds significantly and rapidly to the variation of supraglacial-melting during summer months, the impact of the plume on the glacier front will vary accordingly. Therefore, any surface-melt event will not only produce a negative surface mass balance of the glacier but will also enhance frontal submarine melting. It is thus crucial to take into account daily variation of the subglacial

Figure 5.6: air temperature at Store front versus the residual plume area (blue dot) after the reconstruction based on the air temperature at Summit camp (Figure 5.7). Red line correspond to the least-square best fit of a power law function to the observation.

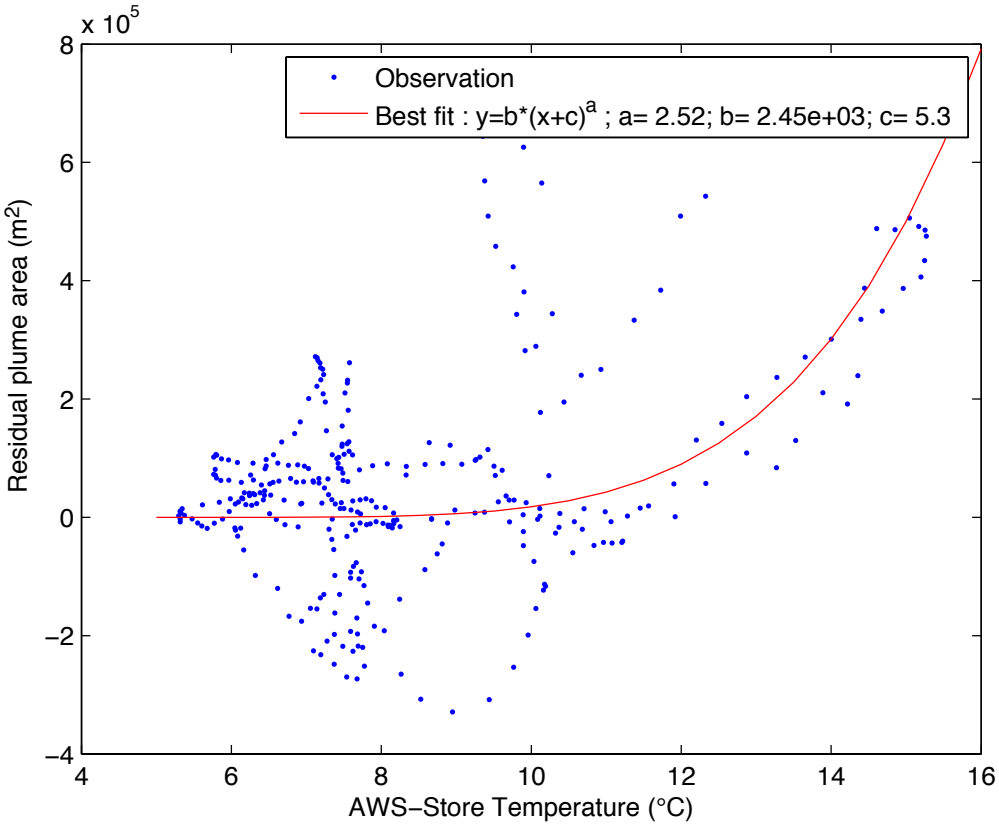

discharge in order to better predict the seasonal response of the marine-terminating glaciers dynamic and particularly the impact of submarine melt rate.

Although, the pattern of the horizontal circulation along the glacier front (i.e. convergent toward the plume, or to the northwest) appears to be related to the plume area with a threshold around $4 \cdot 10^5\,\mathrm{m}^2$, there is no obvious relation with the circulation velocity (Figure 5.2). Further research will be necessary to investigate the controls on the plume-induced circulation and the impact of submarine melt.

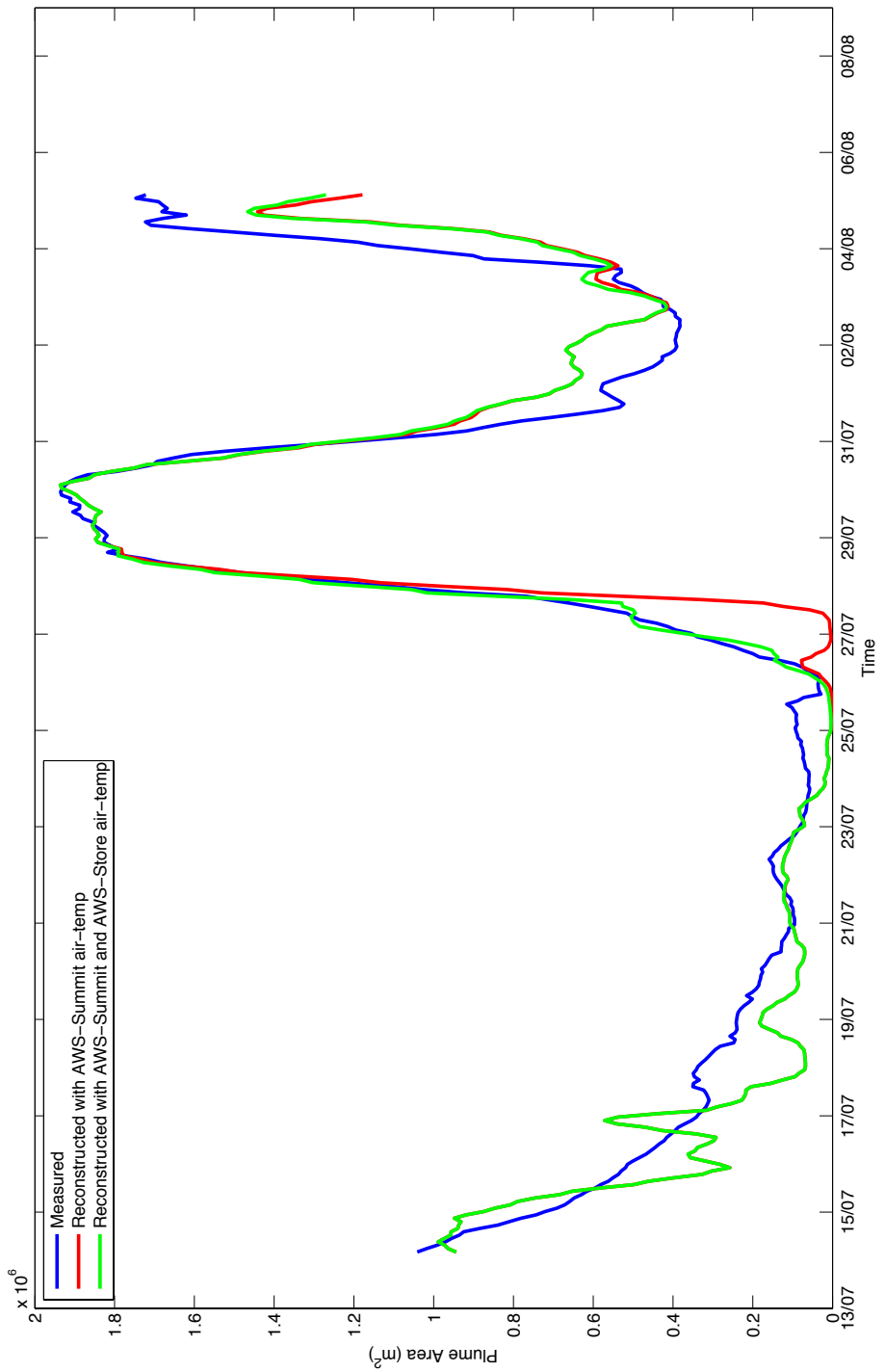

Figure 5.7: Plume area observation (blue) and reconstruction based on the air temperature at Summit camp only (red) and the air temperature at Summit camp plus the air temperature near Store front (green). Note how the use of the air temperature at Store front explain well the start of the plume area increase in 27th July.

5.7 Conclusion

In this chapter we developed a novel technique using iceberg-tracking from time-lapse photographs to quantify the fjord surface circulation at high spatial and temporal resolution.

Plume-induced circulation was observed on the entire glacier front, with a velocity of 10-15 $\mathrm{cm\,s^{-1}}$ when the surface plume had an area $> 4 \cdot 10^5\,\mathrm{m^2}$ Such external circulation would enhance the submarine melt rate on the entire glacier front and would easily exceed the impact of the submarine melt caused by the plume alone.

Sinking of the plume water after it reaches the surface generates an entrainment of the surface water resulting in a horizontal circulation converging toward the plume. Large eddies >1000 m in diameter on both sides of the plume recirculates the plume water toward the glacier front and back into the plume.

During the extreme melt events of 29$^{\mathrm{th}}$ July and 5$^{\mathrm{th}}$ August 2012, the plume area displayed a power law relation with the air temperature observed at the Summit of the Greenland Ice Sheet, explaining 95% of the observed variance in the plume area. The air temperature at sea-level near the glacier front also controls the plume area, although on a smaller scale.

The sub-daily (<6-12 h) response of the plume to the air temperature perturbation suggests an efficient englacial/subglacial drainage network.

Moreover, the relationship, between air temperatures, plume activity and the circulation induced at the glacier front suggest that any surface-melt event will produce a negative surface mass balance and enhanced submarine melting along the full glacier width.

Chapter 6

Characterisation of upwelling plumes

6.1 Summary

This chapter evaluates the characteristics of two upwelling plumes found at the front of a marine-terminating glacier. It describes the internal physical characteristics of the plume, as well as the forcing and induced impact on the glacier front. Upwelling plumes are forced by the injection of subglacial fresh water at depth into the fjord, resulting in a buoyant flow at the ice face. This process, which renews the water present at the glacier front is thought to be a leading factor driving submarine-melting of glacier fronts in the Arctic. Yet, the lack of field-based quantification of plume characteristics limits the potential for improving the numerical simulation of such processes. Here we present observations from within two major plumes at the front of Store Glacier during the summer 2012. The first

plume (main plume) reaches the surface of the fjord before it sinks and outflows at 50-100 m depth, while the second plume (deep plume) outflows directly at depths between 300-400 m. In the main plume a subglacial runoff discharge of $\sim 95\,m^3\,s^{-1}$ induces a submarine-melting of $\sim 100\,m^3\,s^{-1}$ (water equivalent). The plume entrains $\sim 16000\,m^3\,s^{-1}$ of warm Atlantic water as well as $\sim 6300\,m^3\,s^{-1}$ of cold Polar water. Similarly, in the deep plume, a subglacial discharge of $\sim 35\,m^3\,s^{-1}$ induces a submarine-melt of $\sim 20\,m^3\,s^{-1}$, which entrains $\sim 10000\,m^3\,s^{-1}$ of warm Atlantic water.

6.2 Introduction and background

Determining the characteristics of glacier upwelling-plumes and quantifying the exact forcing of runoff-water injected at depth on plume dynamics and submarine-melting is necessary to constrain the impact that this process has on the glacier terminus.

To date, several field observations have observed that runoff driven plumes inducing a buoyant vertical circulation are often present at the surface of glaciated fjords (Chauché and others, 2014; Greisman, 1979; Motyka and others, 2013, 2003; Rignot and others, 2010; Xu and others, 2013). Nevertheless, only limited hydrographic informations from the vicinity and within plumes are available (Chapter 3). However, to our knowledge, no direct field observation and quantification of the inner structure and dynamics of the plume have been made. Thus, the current understanding of plume dynamics is mostly derived from theoretical analysis and numerical modelling. It is considered that the upwelling plumes by outflowing near the surface of the fjord renew the water present at the ice front (Chauché

and others, 2014; Greisman, 1979; Motyka and others, 2013; Rignot and others, 2010; Xu and others, 2013), thus amplify the impact of submarine-melting (Jenkins, 2011; Motyka and others, 2013; Rignot and others, 2010). Note, that it is still debated whether the plume when rising in the water column is in contact with the icefront (Kimura and others, 2014; Mugford and Dowdeswell, 2011; O'Leary, 2011; Salcedo-Castro and others, 2011).

Numerical modelling has however suggested a square or cubic -root relation of submarine-melt to subglacial runoff discharge (Kimura and others, 2014; O'Leary, 2011; Xu and others, 2013, 2012). Despite this potential relation, no studies have directly measured the mixing ratio of subglacial runoff within a plume and evaluated the induced submarine melt inside a major upwelling plume.

Figure 6.1: Schematic of the four sections of the plume: (1) Injection of subglacial runoff-water at depth mixing with the ambient Atlantic water (AW); (2) Rising buoyant plume; (3) Summit of the plume ; (4) Horizontal outflow. Note, the summit is not always at the surface

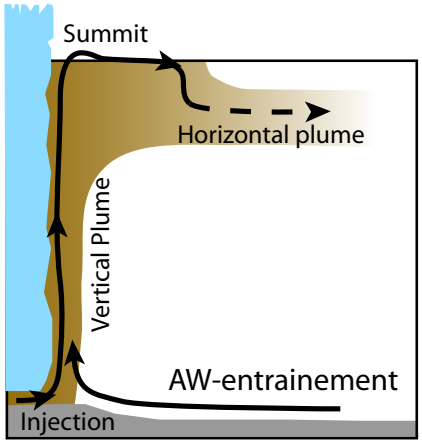

It has been suggested that the dynamics of the plume can be divided into four sections (Kimura and others, 2014; Powell, 1990; Salcedo-Castro and others, 2011; Syvitski, 1989; Xu and others, 2013, 2012) (Figure 6.1):

Injection at depth: The runoff water is injected at depth through subglacial or englacial conduits (Jenkins, 2011; Kimura and others, 2014; Rignot and others, 2010; Xu and others, 2013) and mixes with the ambient water at depth, producing buoyant plume water (PlW).

Vertical Plume: The buoyant PlW rises through the water column and along the ice face (Greisman, 1979; Jenkins, 2011; Kimura and others, 2014; Motyka and others, 2013; Powell, 1990; Sole and others, 2012; Syvitski, 1989; Xu and others, 2013, 2012), gaining kinetic energy (Kimura and others, 2014) and causing the renewal of the water in contact with the ice face (Jenkins, 2011; Motyka and others, 2013). During its ascent, the plume is in contact with the front (Jenkins, 2011; Kimura and others, 2014; Mugford and Dowdeswell, 2011; O'Leary, 2011; Salcedo-Castro and others, 2011; Xu and others, 2013), enhancing the submarine-melt of the glacier with an intensity function of the runoff discharge (Jenkins, 2011; Kimura and others, 2014; O'Leary, 2011; Xu and others, 2013) and the conduit shape (Kimura and others, 2014; Xu and others, 2013). The submarine-melt induced inside the plume will thus modify the PlW by cooling (due to the heat loss resulting of the melting) and by mixing with the resulting meltwater (MW) (Gade, 1979; Jenkins, 1991, 2011; Kimura and others, 2014; Straneo and others, 2011, 2012). Numerical simulation estimates the size of the vertical core of the plume to tens of meters in diameters and spreading sideway as it rises toward the surface (Kimura and others, 2014; Mugford and Dowdeswell, 2011; O'Leary, 2011; Salcedo-Castro and others, 2011; Xu and others, 2012).

Summit: Once the plume is shallower than its depth of hydrostatic equilibrium, the kinetic energy is converted into potential energy of gravity and reaches its

minimal depth, or summit, when no more kinetic energy is available (Salcedo-Castro and others, 2011; Xu and others, 2013, 2012). The summit may be at the surface of the fjord, although this is not always the case (Rignot and others, 2010; Sciascia and others, 2013; Xu and others, 2013, 2012). When the PlW reaching the surface is more buoyant than the ambient surface water, the plume outflows at the fjord surface extending over large areas and fading downstream (Chu and others, 2009). Otherwise, if the PlW reaching the surface is denser than the surface water, it sinks back to its depth of hydrostatic equilibrium (Xu and others, 2013, 2012). In such case, the area of the plume on the surface has clearly marked boundary with contrasting difference of color (Chapters 3 and 5).

Horizontal Plume: At the depth of hydrostatic equilibrium, the plume outflows horizontally oscillating vertically around this depth (Salcedo-Castro and others, 2011; Sciascia and others, 2013; Xu and others, 2012) and potentially altering the ambient water previously present at this depth (Bendtsen and others, 2014).

The difficulty of making measurements within tens of meters from an actively calving glacier front makes access observations inside of the plumes severely limited. In this chapter, we observe, the physical characteristics (i.e. runoff discharge, circulation, mixing ratio) of two major plumes of Store Glacier front and quantify the induced submarine-melting within the plume.

6.3 Experiment

Store Glacier has a quasi-permanent plume visible at the surface of the fjord during the summer months (Chapters 3 and 5, Xu and others, 2013). This plume is present on the south half of the terminus in front of a trough in the seabed (Figure 6.2).

In order to characterise the plume structure and impact on the glacier front, measurements of the fjord hydrography (temperature, salinity, turbidity, and current) were obtained along two transects intersecting with the surface plume (Figure 6.2). While the temperature, salinity, and current allow to estimate the forcing and impact of the plume, the turbidity helps to constrain the extent of the plume (Chapter 3).

6.4 Method

6.4.1 Instruments

The characteristics of the water masses (temperature, salinity, and turbidity) located in and near the plume were obtained from a SeaBird 19Plus conductivity-temperature-depth (CTD) profiler equipped with a Seapoint turbidity sensor. The instrument is lowered with an electric winch at a constant rate of $1\,\mathrm{m\,s^{-1}}$ and log at 4 Hz. The data are then averaged for each meter of the water column. Current measurements at depth were made using an acoustic Doppler current profiler (ADCP) WorkHorse Long Ranger 75 kHz. The ADCP was used in hull-mode (i.e. attached to the ship and pointing downward) and recorded a current profile ev-

Figure 6.2: Map of Store Glacier and the surrounding fjord. ADCP track along the front and across the plume are displayed in red and orange, respectively. CTD stations are marked as yellow point, with the CTD-ref (see text) before the confluence with an other glaciated fjord (north). The map inset shows the studied region (red oval).

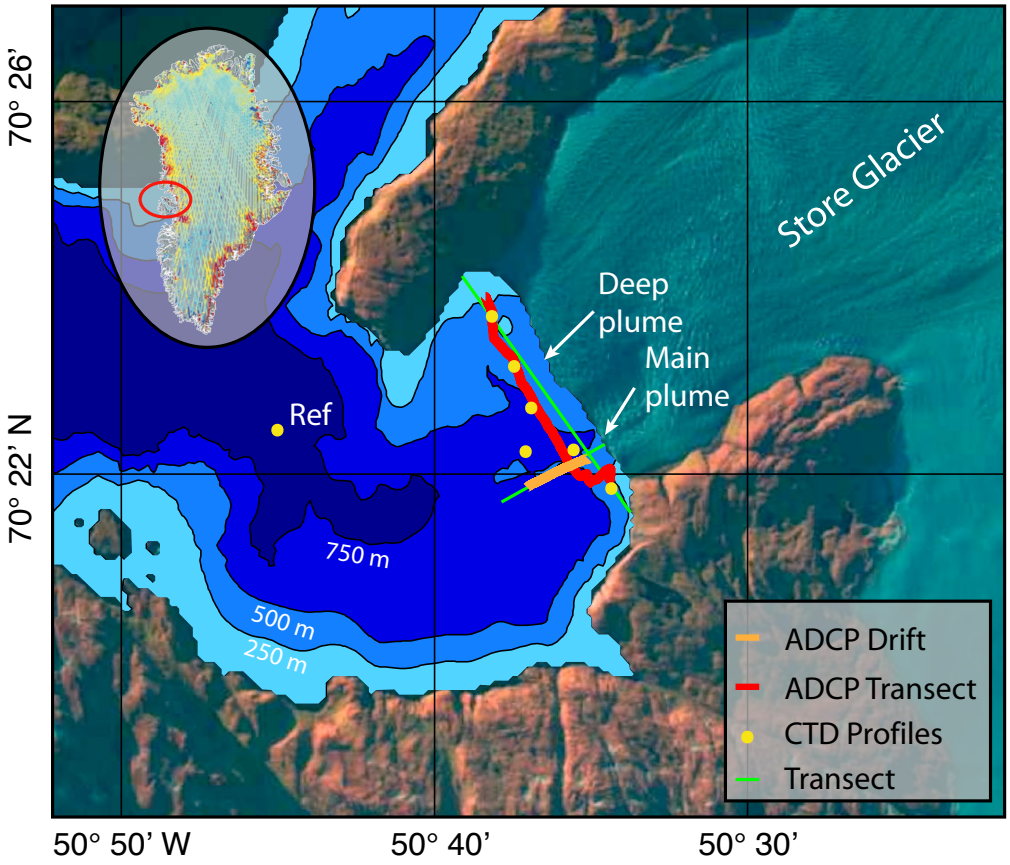

ery second. The ADCP was configured with 6 m bins, with the first bin being at 12 m depth, and the last at 750 m. Correcting the motion of the ship is performed using a post-processed Leica GPS 1200 and the heading information from a Crescent Vector II Hemisphere GPS. Rotation (i.e. roll and pitch) are automatically corrected using the build-in ADCP's motion reference unit.

6.4.2 ADCP and CTD transects

Two ADCP transects across and along the glacier front as well as through the plumes were obtained on 7$^{\text{th}}$ July 2012. The first transect was conducted parallel to the glacier front at a distance of ∼500 m and crosses the plume visible at the surface (hereafter, the main plume). The second transect was obtained by drifting within the main plume at approximately 1.5 m s^{-1} perpendicular to the glacier front. All vertical current profiles from each transect are averaged on a vertical transect section with 50×50 m grid. For the drifting transect inside the surface plume, the estimation of the horizontal current at the surface (i.e. 0-2 m depth) is made using the velocity of the ship inferred from GPS observations.

The CTD transect parallel to the glacier contains 5 profiles at ∼500 m from the ice front, including one inside the surface plume. A reference profile of the water attaining the glacier front was obtained 8.5 km from the glacier terminus. Similarly a profile was collected just outside of the surface plume. All CTD profiles are then interpolated linearly using the Delaunay triangulation method on the vertical section. For the transect parallel to the ice front, the north and south edges of the fjord are considered to have the same characteristics as the CTD profile nearest to each side.

6.5 Results

6.5.1 General condition

At the time of the experiments, (7^{th} of August 2012), the Greenland ice sheet was experiencing intense melting, with ∼73% of the ice cap undergoing supraglacial melt (Tedesco and others, 2013). The plume area at the time of the experiment was estimated to be 10-14·10^5 m^2 (Chapter 5).

6.5.2 Circulation and Turbidity transect

The circulation along the section parallel to the glacier front displays strong shear both in intensity and direction (Figure 6.4). The current is generally moving north-west roughly parallel to the ice front with vertical exchange from the near surface layers at ∼50 m depth to ∼200 m depth. Near the main plume and from the surface to 150 m depth, the currents converge toward the plume while outflowing westward at >100 $cm\,s^{-1}$ (Figure 6.6). In the surface plume the turbidity peaked at >600 Nephelometric turbidity units (NTU), and extended up to 100 m depth, while decreasing in intensity over a distance of more than 1 km on either side of the plume. Another area of high turbidity extended from the center of the fjord towards the northern flank along the bottom of the fjord.

The section across the plume outflow (Figure 6.3) shows the horizontal outflow of the plume between 0-50 m depth, with a velocity up to 150 $cm\,s^{-1}$ associated with a turbidity of >600 NTU, both decreasing away from the glacier. At a distance of 400-800 m from the front, the PlW outflows with a speed of 10-15 $cm\,s^{-1}$ while sinking gradually to a depth of 100-150 m where the largest turbidity. Below the

plume outflow, at depth of 100-400 m and at 600-800 m from the front, a sinking current orientated towards the glacier is observed with a velocity of 20-30 $\mathrm{cm\,s^{-1}}$ Furthermore, an inflowing current of 5 $\mathrm{cm\,s^{-1}}$ between 200-350 m depth is visible at 1600 to 1800 m from the ice front (Figure 6.6).

Figure 6.3: Transect of current (upper panel) and turbidity (lower panel) inside the main plume. Upper panel: Current profile, with current parallel to the transect represented by the red arrows, and the current perpendicular to the transect is represented by the color-coding with blue going southward (through the page) and black northward (out of the page). Lower panel: Turbidity transect using two CTD profiles one inside the main plume (ST12-23) and one outside (ST12-19). Suspected path of the PlW is represented by the brown arrow. The position of the glacier front was estimated using the georeferenced time-lapse imagery.

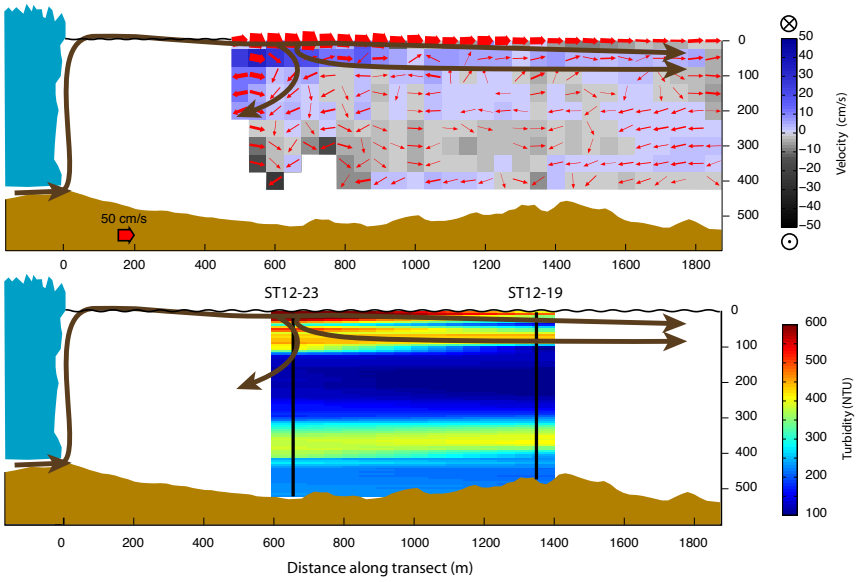

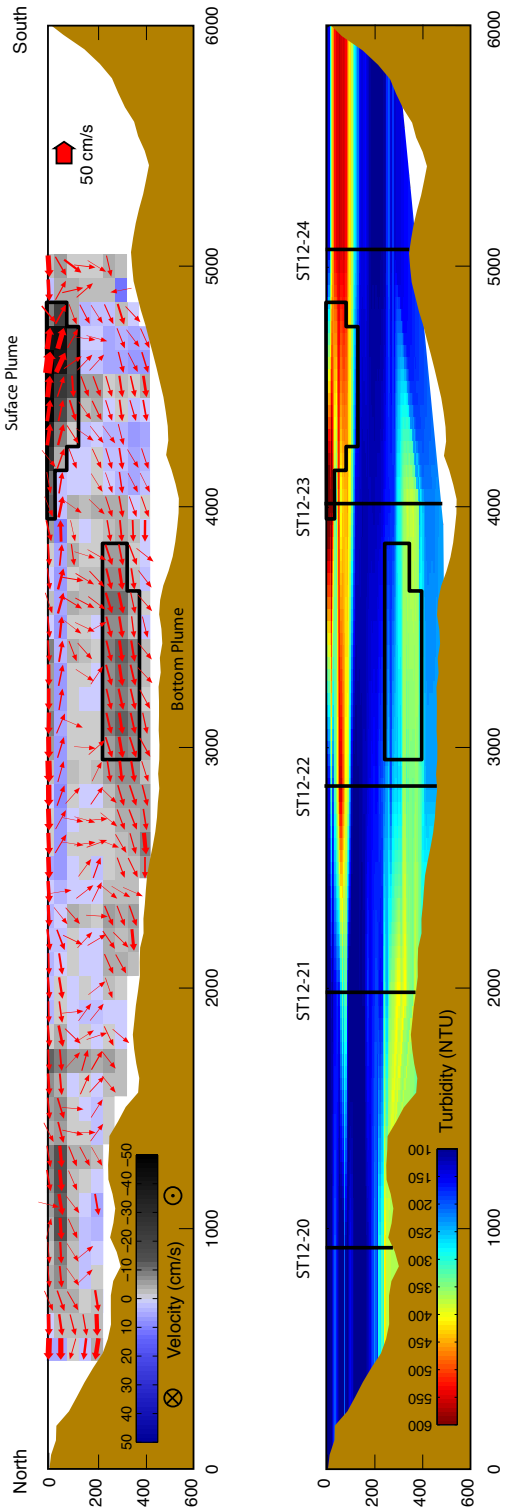

Figure 6.4: Same as Figure 6.3 but for the along glacier transect. Note the main plume and the deep plume areas used to estimate their total discharge (black contour).

6.5.3 Water characteristics

Comparing the ST12-26 profile collected 8 km downstream from the ice front (hereafter, CTD-ref) and the ST12-23 profile from inside the main plume (∼500 m from the ice front) we observe a significant difference in the temperature and salinity associated with a layer of high turbidity from the surface to 200 m depth (Figure 6.5). Inside the main surface plume, the salinity is relatively homogeneous with 34 PSU, which is up to 2-3 PSU higher than the surrounding waters (Figure 6.5) and the temperature is lower between 0-100 m and higher between 100-200 m than the CTD-ref.

Similarly, for the three deepest profiles near the glacier a peak of turbidity associated with a lower salinity (-0.1 PSU) and temperature (-0.2°C) than the CTD-ref is observed between 300-400 m.

6.6 Discussion

6.6.1 Plume location

Several plumes coexist at the front of Store Glacier, however only one plume appears on the surface most of the time. The presence of a layer in the water column, displaying a change in salinity and temperature associated with high turbidity (Figures 6.4 and 6.5) indicates that in addition to the main plume in the southern section of the front, a deep plume emerges in the central-north section. Similarly two plumes were observed next to each other during the extreme-melt event (Chapter 5).

Figure 6.5: Profiles of salinity, temperature and turbidity versus depth along the glacier front (ST12-20 to ST12-24, from North to South), inside the plume (ST12-23) and just outside (ST12-19) as well as the CTD-ref (ST12-26) used to estimate the presence of the plume. Profiles corresponding to the reference, main plume and deep plumes are in bold. In the temperature panel the vertical extend of the surface and deep plume have been marked with a red line.

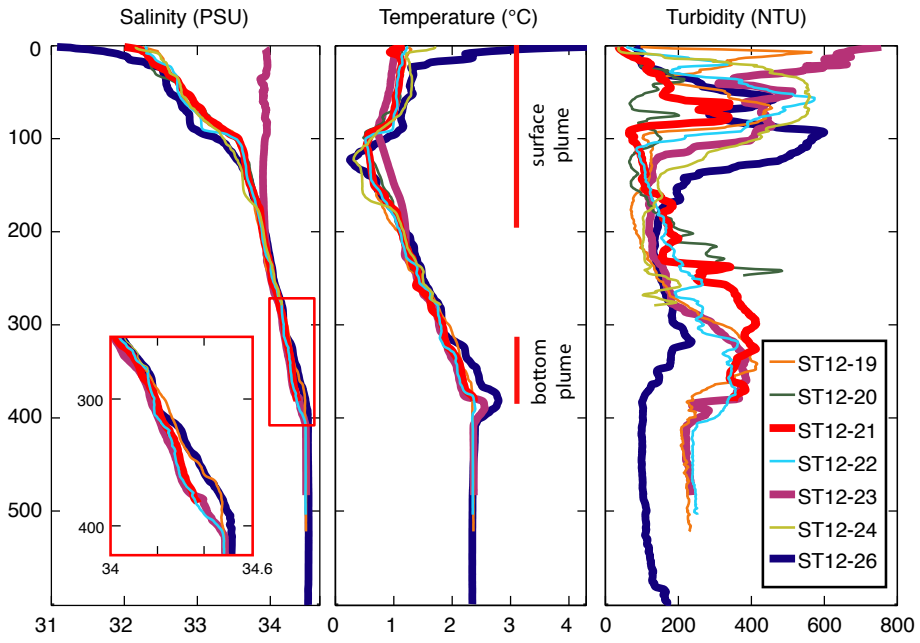

The spatially and temporally independent characteristics of each plume is consistent with the hypothesis that, in summer, the injection of runoff at depth occurs from individual conduits (Jenkins, 2011; Kimura and others, 2014; Xu and others, 2013). This implies that the impact of the plume on the glacier front is localised to the region of the plume outflow.

6.6.2 Plume impact on the glacier front in contact with the rising plume

The circulation induced by each plume is estimated by summing the outgoing current in the highly turbid area of strong outflow (Figure 6.4). This yields $\sim$22500 $m^3\,s^{-1}$ and $\sim$10000 $m^3\,s^{-1}$ for the main and deep plumes, respectively. Comparing the salinity of each plume with that at the base of the glacier (i.e. 470 m depth – where we assume the subglacial runoff-water to mix with the ambient water) shows the dilution of the ambient water by the fresh water (both subglacial runoff and submarine-melt water) to be $\sim$16.5‰ ($\sim$370 $m^3\,s^{-1}$) and $\sim$ 5.5‰ ($\sim$55 $m^3\,s^{-1}$) in the main and deep plume, respectively.

It is possible to partition the contribution of submarine-melt water and subglacial-runoff to the total fresh water estimated above, using the temperature drop associated the melting of the ice. Assuming an ice temperature of -20°C (Thomas, 2004) the temperature drop of the PlW ΔT_{sbm} resulting of the melting of a volume δV of ice (Gade, 1979) is:

$$\Delta T_{sbm} = \frac{L_i + (\theta_f - \theta_i)C_i}{C_{sw}}\rho\delta V \tag{6.1}$$

where L_i (337 $kJ.kg^{-1}$) the latent heat of fusion; C_i (2.2 $kJ.kg^{-1}\,K^{-1}$) the specific heat capacity of ice, C_{sw} (3.9 $kJ.kg^{-1}\,K^{-1}$) the specific heat capacity of seawater, ρ (0.9) the density of ice, and θ_f (-0.3°C) the pressure and salinity compensated fusion point of glacier ice.

Therefore, to account for the water-temperature drop between the base of the front and inside the plumes, the submarine-melt occurring in the plume should be

$\sim$275 $m^3 s^{-1}$ and $\sim$20 $m^3 s^{-1}$ and imply a subglacial runoff discharge of $\sim$95 $m^3 s^{-1}$ and $\sim$35 $m^3 s^{-1}$ for the main and deep plume, respectively. Note that these estimates are not very sensitive to the assumed depth of subglacial runoff mixing with ambient water.

In the case of the main plume, a submarine-melt of 275 $m^3 s^{-1}$ is extremely high. This would be equivalent to a submarine-melt rate of $\sim$45 $m\,d^{-1}$, over an area of the glacier front 500 m high and 1000 m wide (i.e. the likely greatest area of ice in contact with the plume). In comparison, Store Glacier has a frontal advection of 15-20 $m\,d^{-1}$ (Chapter 8, Ryan and others, 2014) and does not undergo any significant seasonal retreat (i.e. $<$500 m – Ahlstrøm and others, 2013; Ahn and Box, 2010; Moon and others, 2012). Hence, the submarine-melt rate estimated inside the main plume cannot exceed the advection rate. Furthermore, time-lapse imagery during the summer 2012 (Chapter 5) reveals that the section of the glacier front in contact with the plume did not calve any major icebergs or advance while the plume was active, implying that the submarine-melt rate inside the plume is likely to be equal to the advection rate.

Thus, assuming a maximal submarine-melt rate of 17$\pm$2 $m\,d^{-1}$ inside the main plume to match the advection (Chapter 8, Ryan and others, 2014), the MW discharge becomes $\sim$100 $m^3 s^{-1}$. Although, this assumption constrain the submarine-melt rate inside the main plume, it only partially explain the temperature drop of the PlW. A partition of the ambient mixing between the warm Atlantic water and a colder water can, however explain the low temperature of the main PlW (i.e. $\sim$1°C). A mixing with the coldest water found in the fjord at $\sim$150 m, which is the polar water (PW) (Chapters 3 and 4, Straneo and others, 2012; Xu and others, 2013), and at a ratio of $\sim$280‰ ($\sim$6300 $m^3 s^{-1}$) would indeed explain the observed

Figure 6.6: Schematic, not to scale, of the upwelling plume extent (brown shading) and induced circulation as previously understood (black) and observed during this study (red). Dashed line correspond to current at 50-100 m depth. Section of the glacier referred as internal and external to the plume are marked on the top graph. Note the diagram is not to scale. The down-view is extracted from Chapter 5.

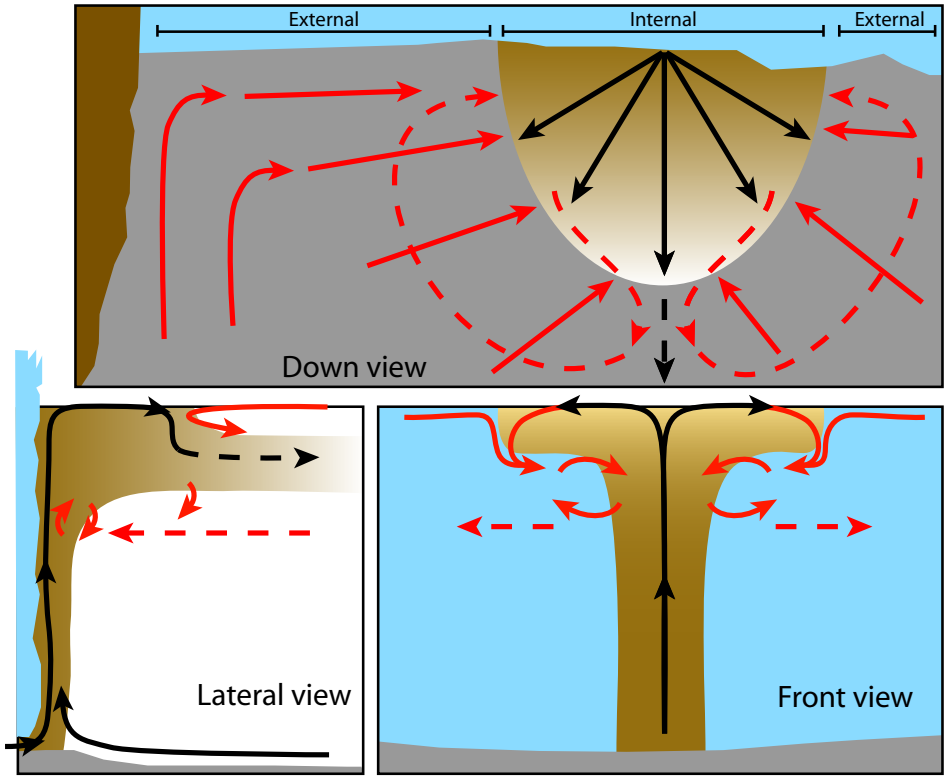

temperature and salinity in the main plume. Note that if the submarine-melt in the main plume is less than the assumed $17 \pm 2\,\mathrm{m\,d^{-1}}$, the contribution of cold Polar water to the PlW would increase accordingly.

The total estimated discharge of subglacial runoff water of $\sim 130\,\mathrm{m^3\,s^{-1}}$ during this experiment is more than one order of magnitude smaller than the previous estimate of 1500-2000 $\mathrm{m^3\,s^{-1}}$ (Chapter 3), similarly it is only half of the observation and modeling, at Store Glacier in August 2010, from Xu and others (2013) of

Table 6.1: Resume of water characteristics: Plume water (PlW), Atlantic water (AW), polar water (PW), subglacial runoff-water (RW) and melt-water (MW). Mixing ratio of the water forming the PlW with value measured (green), assumed (purple), and estimated (orange). Note in the main plume the assumption for the submarine-melt and the resulting mixing with the cold polar water.

	Main Plume					Deep Plume			
	Pl W	AW	PW	RW	MW	Pl W	AW	RW	MW
Temperature (°C)	1.2	2.37	0.25	-0.3	(eq 8.1)	2.17	2.37	-0.3	(eq 8.1)
Salinity (PSU)	33.93	34.49	33.55	0	0	34.30	34.49	0	0
Mixing ratio (‰)	1000	984	0	16.5		1000	995	5.5	
		710	280	4.2	4.4			3.5	2.0
Discharge (m3/s)	22500	22130	0	370		10000	9945	55	
		16000	6300	95	100			35	20

$246 \pm 45\,\mathrm{m^3\,s^{-1}}$ and $289\,\mathrm{m^3\,s^{-1}}$, respectively which should be emphasis by the fact that in August 2012 the GrIS experienced a higher supraglacial melt than usual (Tedesco and others, 2013) and time-lapse observation showed that the surface plume was more extended in August 2012 than 2010. This substantial difference of subglacial runoff discharge cannot be explained with the current data at hand.

The existence of the mixing between the PW and the PlW can potentially explain the presence of horizontal eddies suspected on both side of the plume at $\sim$100 m depth (Chapter 5). Indeed, if the PW is to mix with the PlW and thus outflow near the surface, a compensating inflow of PW should converge toward the plume which can generate the observed eddies. Similarly, the PlW temperature being warmer than the ambient water below 100 m depth and cooler above (Figure 6.5) can be explained by the mixing with the cold PW above 100 m depth. Such significant mixing of the PlW with ambient water at intermediate depth (Figure 6.6) also

appears on the high resolution 3D numerical simulation of Store plume (fig 2-c of Xu and others, 2013).

6.7 Conclusion

We have collected some of the first multi-dimensional physical observations (temperature, salinity, turbidity, and current) from within a major glacier upwelling plume emerging on the vertical face of a tide water glacier in Greenland. Two distinct plumes were observed simultaneously at Store Glacier. The main plume reaches the surface of the fjord before sinking to 100 m depth and outflowing at $>1\,\mathrm{m\,s^{-1}}$, while the deep plume outflows directly at depth between 300-400 depth. For each plume, the forcing of the subglacial runoff and the induced submarine-melt was estimated on 7^{th} August 2012. The main plume is driven by a subglacial discharge of $\sim 95\,\mathrm{m^3\,s^{-1}}$ which induces a submarine melting of $<100\,\mathrm{m^3\,s^{-1}}$ water equivalent. This entrains $\sim 16000\,\mathrm{m^3\,s^{-1}}$ of deep and warm Atlantic water as well as $>6300\,\mathrm{m^3\,s^{-1}}$ of cold polar water. The deep plume is driven by a subglacial runoff discharge of $\sim 35\,\mathrm{m^3\,s^{-1}}$ which induces $\sim 20\,\mathrm{m^3\,s^{-1}}$ w.e. of submarine-melting and entrains $\sim 10000\,\mathrm{m^3\,s^{-1}}$ of deep Atlantic water.

Chapter 7

Submarine melt impact estimated from recently calved iceberg

7.1 Summary

Evaluating the spatial impact of submarine melting on a vertical glacier front is crucial to understand the effect of undercutting on iceberg calving behaviour. In this chapter, we use a novel method based on the 3D reconstruction of recently calved iceberg to identify the effect of the submarine melting on the ice-front. We confirm the prediction, from numerical modelling, of a zone of maximum of melt near the mid-depth of the glacier front. The submarine melt rate between 100-300 m depth is estimated to be approximately $5\,\mathrm{m\,d^{-1}}$. Vertical runnels with a width of 0.5-10 m are also observed on the ice-front. Such features would, due to their fractal like pattern, increase significantly the surface of contact between the glacier and the ocean and hence potentially the submarine melt rate.

7.2 Introduction and background

The submarine melt rate of marine terminating glaciers and its spatial distribution is one of the key questions in understanding the impact of the ocean on the glaciers and particularly the effect of undercutting of the ice-front on calving behaviour (O'Leary and Christoffersen, 2013; Todd and Christoffersen, 2014). However, the extreme difficulty of measuring directly the submarine melt rate on an actively calving glacier front has hindered our understanding.

Numerical simulations of Store Glacier predict summer melt-rate of $2-6\,\mathrm{m\,d^{-1}}$ inside the plume with a vertical pattern having a maximal melting at mid-depth in the water column (O'Leary, 2011; Xu and others, 2013, 2012). This vertical pattern of melt-rate is also found in theoretical numerical simulation (Kimura and others, 2014).

In-situ oceanographic measurements (i.e. temperature, salinity and current) have been conducted near the ice-front of various glaciers and applying a model of conservation of heat, salt, and volume (Chapter 4, Motyka and others, 2003) estimated an average submarine melt rate of $1-4\,\mathrm{m\,d^{-1}}$ for Greenlandic glaciers with a vertical ice front (Chapter 4, Rignot and others, 2010; Sutherland, 2012; Xu and others, 2013). Such methods do not, however, give access to the spatial distribution of the submarine melt.

Remote sensing has also been able to estimate a submarine melting of $0.03-3\,\mathrm{m\,d^{-1}}$ on floating ice-tongues around Greenland (Dutrieux and others, 2014; Enderlin and Howat, 2013; Rignot, 1996; Rignot and Steffen, 2008). In particular, channelised melting was observed for Petermann Glacier in North-West Greenland (Dutrieux and others, 2014; Rignot and Steffen, 2008). Repeat phase sensitive radar surveys

of Petermann Glacier estimated the submarine melt to $0.01 - 0.04\,\mathrm{m\,d^{-1}}$ in 2003 (Dutrieux and others, 2014). However, such methods cannot be used on vertical ice faces (Enderlin and Howat, 2013), typical of Greenlandic glaciers.

Underwater scanning of the lower face of an ice-shelf in Antarctica showed flat terraces separated by step-like structures, which are thought to be result of the submarine melt (Dutrieux and others, 2014; Jenkins and others, 2010; Nicholls and others, 2006). Melting under this ice-shelf is supposed to be modulated by the geometry of the bottom of the ice-shelf: constant across each terrace, changing from one terrace to the next, and greatly enhanced on the inclined walls. However, to date no such survey have been conducted on a vertical ice-front.

Vertical runnels sub-meter wide spreading along ice face were observed on recently calved bergy bits. Similarly caves of meters size near the water level have been observed on vertical tidewater glacier front. Both of this features were associated to the melt induced by low discharge plume dominated by buoyancy forces and flowing along the ice front (Powell, 1990). Despite this small-scale observation, little is known of the general pattern of submarine melt over the whole ice front height.

In this chapter, we investigate the pattern of submarine melting using a 3D reconstruction of a recently calved iceberg. We infer from this observation a vertical profile of submarine melt rate, which are consistante with numerical simulation. We also observed vertical runnels present on the upper and lower third of the ice-front.

7.3 Method

Major outlet glaciers, like Store Glacier, regularly calve massive icebergs (>1000 m) of an entire section of the glacier front (Amundson and others, 2010; Todd and Christoffersen, 2014). Some of these icebergs rotate backward against the glacier exposing the previously ice-ocean interface on the its upper surface (Amundson and others, 2010).

A 3D reconstruction of the upper face of one of these icebergs can provide insight to the pattern of the submarine melt on the glacier front.

7.3.1 Structure-from-motion

To perform the 3D reconstruction of the iceberg, a method based on the structure-from-motion was performed using the PhotoScan software (`www.agisoft.com`) on a set of photographs taken from all around the iceberg. The software is based on the tracking of features from one image to another to yield the parallax effect. It is a three stage process:

Camera positioning: The software first deduces iteratively the probable 3D geometry of the scene comparing the features observed inside each photograph and the relative position (coordinates, orientation, focal length) of the camera for each scene. This process yield the relative position of each photograph. For the success of this step it is particularly important to have a significant distance between the foreground and the background, and sufficient overlap between each photograph. The simplified 3D-model contains

approximately 30 000 points and covers all the objects visible on the photographs.

Generation of the point cloud: A dense point cloud is produced for the region of interest (i.e. the iceberg) using refined parallax of all features identified on the images. This point cloud can comprise millions of points.

Meshing and texturising: The point cloud is meshed into Delaunay triangles and decimated to best represent the shape of the iceberg. In this process ∼300 000 triangles are in the mesh. Each face of a triangle is assigned the average colour of the object on the each images where it appears, therefore providing a texturised version of the 3D model.

Photoscan is able to reconstruct the scene even if no information is given on the position of the camera. However, in such case only a relative 3D model with no absolute scale is produced. It is necessary to either have the coordinates of the camera for some of the photographs or a set of position of known point (ground control points).

7.4 Results

7.4.1 Calving event description

On 17$^{\text{th}}$ July between 22:38 UTC and 22:42 UTC an iceberg approximately 500 m wide calved on the central section of Store Glacier. The iceberg tipped back toward the glacier, exposing the previous ice-ocean interface on the newly-formed upper

face (Figure 7.1). During the calving event most of the ice-ocean interface of the iceberg remained intact, as no sharp edges, due to ice breaking, were observed in the images.

Figure 7.1: Time-lapse photographs before and after the calving event. Notice the position of the waterline of the previous ice-front in the resulting iceberg

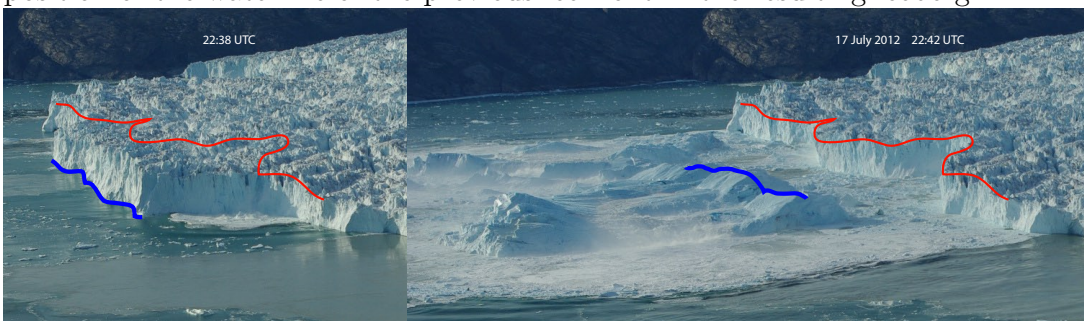

7.4.2 Iceberg reconstruction

The iceberg reconstruction used 46 high-resolution photographs from a hand-held camera, taken from a helicopter approximately 15 minutes after the calving event, from two laps around the iceberg (Figure 7.2). The 3D reconstruction first identified 32 235 points on all the scenes to determine the relative position of the photographs. A point cloud comprising 3 160 000 points was produced yielding a 3D meshed model with 337 000 faces (Figure 7.2).

7.4.3 Iceberg scale

Due to the lack of both absolute position of the camera and ground control points, the 3D model of the iceberg cannot be geo-referenced. However, a rescaling is performed assuming that the distance separating the groove left by the previous

Figure 7.2: Plan view of the iceberg reconstructed dense point cloud (purple) and the relative position of the camera for each of the 46 photographs (i.e. blue rectangles with their normal vector in black).

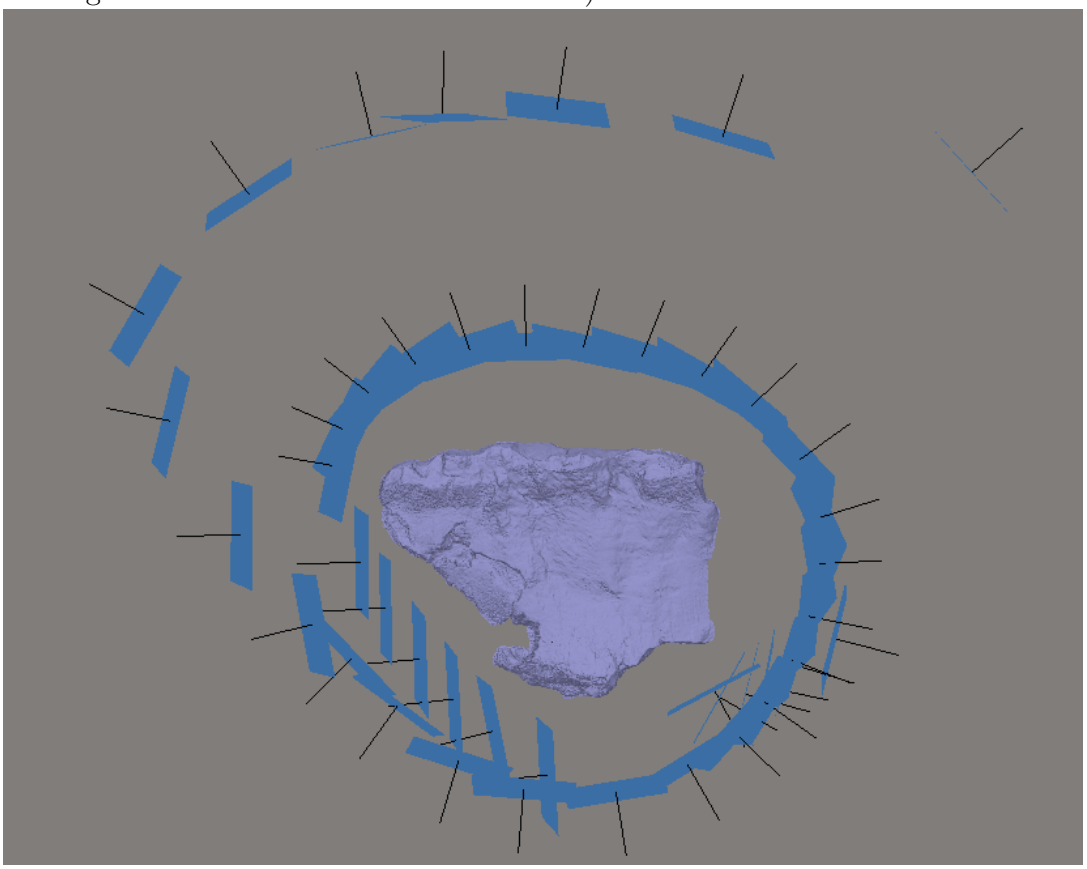

waterline and the distance to the foot of the iceberg to be 450 m, (i.e. the depth of the fjord at this section, Chapters 2 and 8).

The iceberg's upper surface which was previously the ice-ocean interface, is thus approximately 500 wide and 450 high. Moreover, based on the emerged volume of the iceberg, its overall volume is estimated to $70 \times 10^6\,\mathrm{m}^3$.

7.4.4 Iceberg shape

The general shape of the iceberg's face previously exposed to the ocean exhibits an indent 35 m inward the ice-front, between 70 – 250 m depth, gradually decreasing towards both the bottom and the surface (Figure 7.3). This pattern is relatively homogenous across the whole face visible on the iceberg (i.e. 500 m).

Vertical runnel-like channels (hereafter, runnels) with a width and incision depth on the order of several meters can be noted on different sections of the iceberg and particularly on the part corresponding to the foot of the glacier front and near the fjord surface (Figure 7.3).

Figure 7.3: Fully reconstructed and rescaled iceberg. a) Perspective view of the iceberg with the texture applied. The previous waterline is marked in blue and the zones with vertical runnels in red. b) Profile of the iceberg along the previous z-axis of the glacier front. The hatched areas on the top and bottom part of the profile represent the likely shape of the ice-front before the calving event. Similarly the supposed position of the seabed is marked in brown. c) One of the photograph used in the reconstruction, exhibiting the zones with vertical runnels. The photograph is looking from the foot of the glacier-front upward.

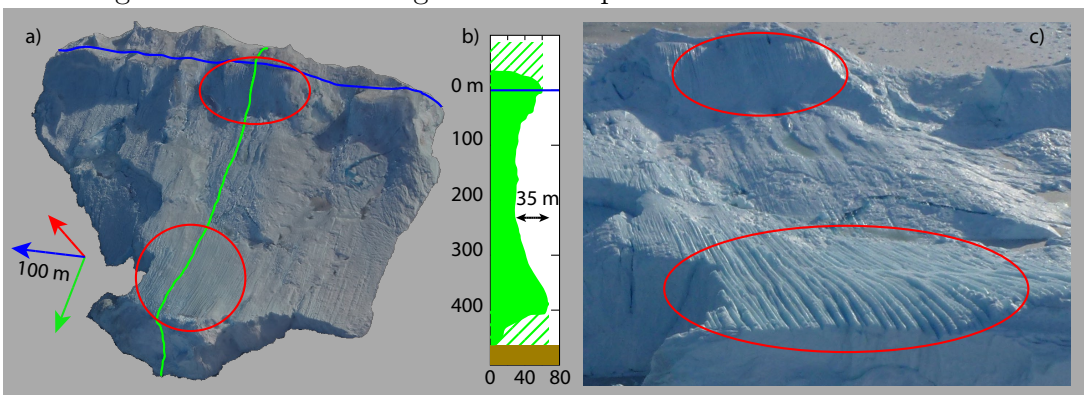

7.5 Discussion

7.5.1 Submarine melt impact

Between two calving events, the shape of ice-front will be affected by submarine melting and advection. If we assume the advection to be of plug flow (i.e. no variation of with depth – Rignot, 2006), then only the submarine melting will shape the vertical profile of the ice front. Photographs from a time-lapse camera overlooking the glacier front (not shown) show that the previous calving event occurred on 11th July at 02:30 UTC, which is approximately 7 days before the calving of the reconstructed iceberg. Thus, if we assume the bottom of the ice-front to have no melting, we can estimate a maximum submarine melt rate of approximately 5 m d^{-1} between 100-250 m depth (Figure 7.3). This melt-rate estimate compare well with the estimation of 4.5±1.5 m d^{-1} from observation at Store Glacier in August 2010 (Xu and others, 2013) and from further melt estimation produced at Store Glacier at the same period (Chapter 8).

The estimated submarine melt rate assumes that after the calving event of 11th July the glacier front was generally flat. There is no possibility with the data at hand to confirm this assumption. However, the vertical profile of submarine melt impact is in good agreement with the prediction from numerical models, which suggested an increasing melt-rate from the bottom of the ice-front to approximately 100 m above the seabed, then a relatively constant melt-rate along the middle section of the ice-front, before decreasing in the upper 100 m of the water column (Kimura and others, 2014; O'Leary, 2011; Xu and others, 2013, 2012). Hence we can considerer the vertical profile extracted from the iceberg and the maximum estimated

submarine melt, of $5\,\mathrm{m\,d^{-1}}$ between 100-250 m depth, to be a first approximation of the general impact of the submarine melting at Store Glacier.

This novel method has multiple advantage compared to the heat-flux methods described before (i.e. Motyka and Gade model – Chapters 4 and 6): 1) gives informations on the vertical distribution of the melt-rate, 2) can be reproduced at relatively low expense, particularly if using a remote controlled drone or high resolution satellite imagery, 3) can be conducted at any period of the year, as major calving event occurs throughout the winter, some of which might rotate backward. The main disadvantage of this method rely on the hypothesis that the ice front is relatively flat after a calving event.

Figure 7.4: Plan view schematic of the ocean-glacier interface illustrating a potential explanation for the runnel formation. 1) flat ice-front where the melting is relatively homogenous; 2) small runnels start to form as preferential melting occurs; 3) the small runnels merge into larger runnels; and 4) large runnels appear with smaller runnel on each of the faces.

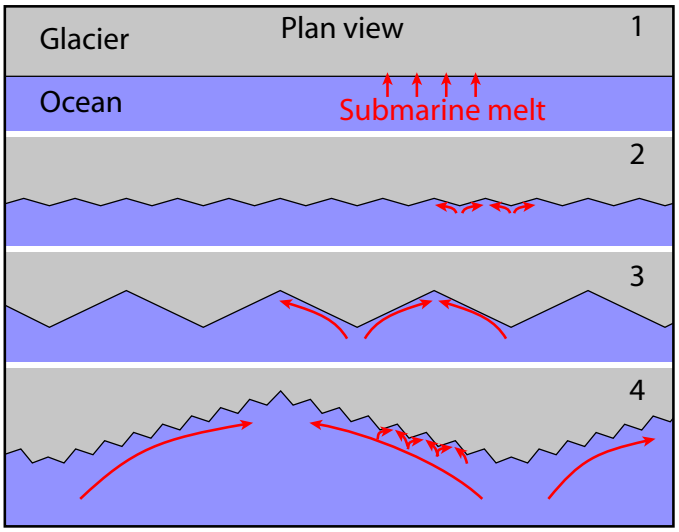

Figure 7.5: Icebergs observed in the fjord with similar runnels to those found on the iceberg that calved on the 17th of July. Approximate scale of the runnels is marked on each photograph. Note the fractal like pattern of the runnels on the top photograph (zoomed in red inset).

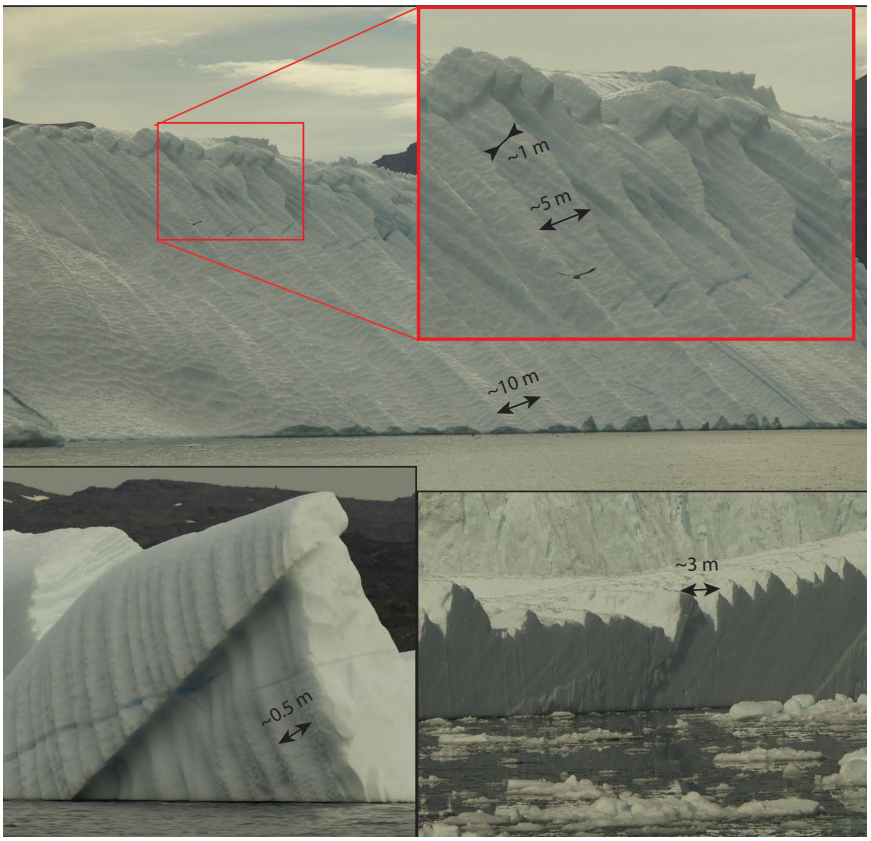

7.5.2 Vertical runnels

The vertical runnels observed at the foot and on the upper part of the glacier-front (Figure 7.3) have been suggested to result from the submarine melting of the ice face (Powell, 1990). At Store Glacier runnels were commonly observed on other icebergs with widths ranging from ∼0.5-10 m, and even fractal-like pattern with multiple nested scale runnels (Figure 7.5). A potential explanation for the formation of the runnels is that preferential melting occurs inside an initial indent

of the ice face, then the buoyancy driven circulation extends the indent into a vertical runnel. Small runnels grow as the water converges in the runnel and thus merge into larger ones. Finally, when large runnels form, small runnels appear on each of their faces producing the fractal like pattern observed (Figure 7.4). Such structure would significantly increase the surface area of contact between the glacier and the ocean, hence the submarine melting. Indeed, an equilateral triangular cross section runnel will double the surface area of ice prone to melt. In the case of a fractal-like structure of the 2^{nd} order it will triple the surface area. On the middle section of the glacier face where the melt rate is maximal, hence the free-forced upwelling, the runnels are less present, wider, and shallower. This relation between runnels presence and melt rate suggests a potential negative feedback between the water dynamics and the surface area exposed to melt. Therefore the more dynamics the water, the shallower the runnels, hence the smaller the surface area of ice prone to melt. There is an obvious minimal threshold to this feedback as the minimal surface area of the ice front is a flat plane. However, this also suggest that for slow water dynamic the melt rate is proportionally higher that what could be expected for similar condition but without runnels. This could potentially explain the high melt rate measured in winter time at Store Glacier (Chapter 4).

7.6 Conclusion

Applying the structure-from-motion method to reconstruct the 3D shape of a recently calved iceberg provided a way to evaluate the vertical and micro scale impacts of the submarine melting on a major glacier front.

The general vertical impact of the submarine melting is consistant with numerical simulation.

The submarine melt rate is estimated to be approximately $5\,\mathrm{m\,d^{-1}}$ between 100-300 m depth, decreasing toward both the surface and the glacier foot.

Vertical runnels observed on the glacier front are common features over the whole ice front. Due to their potential fractal like pattern the presence of runnels can significantly increase the surface area of contact between the glacier and the ocean, hence the impact of submarine melting. However, it appears that a negative feedback might occur such that the more dynamic the free-forced upwelling the less carved the runnels thus the less surface area of ice in contact with the ocean.

Chapter 8

Direct measurement of submarine melting from repeated side-scan sonar surveys

8.1 Summary

This chapter develops a cutting-edge technique to directly measure the spatial impact of submarine melting on a vertical glacier front. A minimal quantification of the submarine melt rate is estimated on a section of 2 km of the glacier front. The spatial distribution of submarine melt and its contribution to the ablation of Store Glacier front is discussed. Using repeat 3D underwater scanning of the glacier front, the first direct observations of submarine melting were achieved. melt rate are estimated to range from $0-4\,\mathrm{m\,d^{-1}}$ with a maximum between $100-400\,\mathrm{m}$ depth and decreasing both toward the bottom and surface of the fjord. The average

submarine melt rate of 3.4 ± 0.7, is consistent with previous estimates based on oceanographic measurements.

8.2 Introduction and background

The submarine melt rate of marine terminating glaciers is one of the key questions in understanding the impact of the ocean on the glaciers and particularly the effect of undercutting of the ice-front on calving behaviour (O'Leary and Christoffersen, 2013). However, the extreme difficulty of measuring directly the submarine melt rate on an actively calving glacier front has hindered our understanding. Different approaches to estimate submarine melt have been taken: Laboratory studies were conducted in order to evaluate the micro and meso-scale impact of submarine melt on a vertical ice-front in stratified water (Huppert and Josberger, 1980; Huppert and Turner, 1980; Josberger and Martin, 1981). Results showed that melting induces a circulation with multiple convective cells stacked upon each other and that the melt rate can vary with depth as a function of melt-induced convection.

In-situ oceanographic measurements (i.e. temperature, salinity and current) have been conducted near the ice-front of various glaciers and applying a model of conservation of heat, salt, and volume (Chapter 4, Motyka and others, 2003) estimated an average submarine melt rate of $1-4\,\mathrm{m\,d^{-1}}$ for Greenlandic glaciers with a vertical ice front (Chapter 4, Rignot and others, 2010; Sutherland, 2012; Xu and others, 2013). Such methods do not, however, give access to the spatial distribution of the submarine melt.

Remote sensing has also been able to estimate a submarine melting of $0.03-3\,\mathrm{m\,d^{-1}}$ on floating ice-tongues around Greenland (Enderlin and Howat, 2013; Rignot, 1996; Rignot and Steffen, 2008). In particular, channelised melting was observed for Petermann Glacier in North-West Greenland (Rignot and Steffen, 2008). However, this method cannot be used on vertical ice faces (Enderlin and Howat, 2013), typical of Greenlandic glaciers.

Numerical simulations, focusing on submarine melting inside the upwelling plume (Chapter 6), predict a melt rate of $2-6\,\mathrm{m\,d^{-1}}$ with a vertical pattern of minimal melting near the surface of the fjord and at the bottom of the ice face, while for the mid-depth section a relatively homogenous melting occurs (Kimura and others, 2014; O'Leary, 2011; Xu and others, 2013, 2012).

Three-dimensional (3D) surveys of the underwater interface of an Antarctic ice-shelf have been collected in order to observe the pattern of the submarine melting and found large horizontal terraces separated with stair-like steps (Dutrieux and others, 2014; Jenkins and others, 2010; Nicholls and others, 2006). Melting under this ice-shelf is supposed to be modulated by the geometry of the bottom of the ice-shelf: constant across each terrace, changing from one terrace to the next, and greatly enhanced on the inclined walls.

In this chapter, we present repeated 3D scans of the submarine section of Store Glacier front, allowing the direct evaluation of the submarine melt rate, its spatial pattern, and the total contribution to the frontal ablation.

8.3 Method

8.3.1 Instruments

Sonar data were collected using a Bathyswath-1-STD 117 kHz system, equipped with two transducers oriented parallel to the axis of the vessel at an angle of 36 ° and 102 ° of roll from the sea surface. The vessel roll, pitch, and heading were corrected using an Inertia Motion Unit-10 SMC and a Crescent Vector II Hemisphere GPS. Final georeferencing is performed using a post-processed Leica GPS 1200.

Each ping of the Bathyswath system collect a two dimensional vertical slice perpendicular to the transducers. The slices are then georeferenced and combined to form a 3D model of the glacier front and the seabed (Figure 8.1). Sonar measurements are collected by surveying parallel to the glacier front at a distance of $250-500$ m. The range of the instrument was adjusted between $300-700$ m resulting of a ping rate of $1-2.5$ Hz. During all the surveys the vessel was moving at a velocity $\leq 1\,\mathrm{m\,s^{-1}}$, and as much as the iceberg anti-collision navigation allowed, the heading of the vessel was kept constant.

Data filtering

Three levels of filtering are applied to the raw sonar measurements. The first is performed in the ping coordinate system, the second is a manual filter to remove residual noise. Finally the last filter creates a skin surface (i.e without thickness) of the ice-front.

Figure 8.1: Principle of the Bathyswath system. The geo-referencing of the 2D slices enable the reconstruction of a 3D model of the glacier front

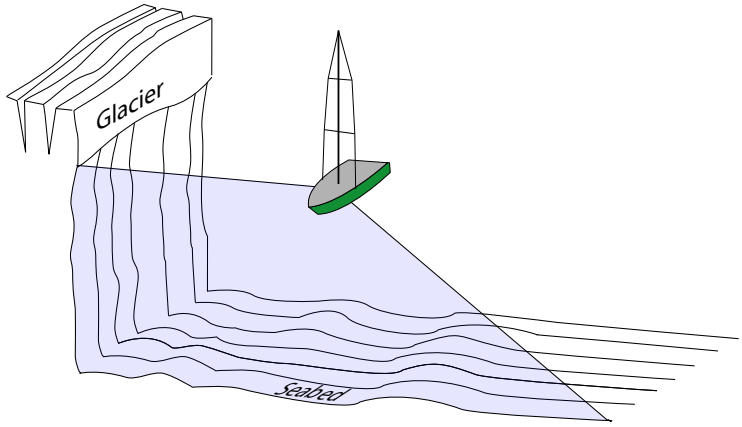

Ping coordinate system filtering: The Bathyswath sonar uses a principle of interferometry to determine not only the range between the glacier and the receiver, but also the angle between the antenna and a return signal (Figure 8.2 – Bathyswath, user manual). Thus, for a single ping, the system can collect up to 8000 points (Bathyswath, user manual) positioning them by range and angle inside a 2D slice perpendicular to the axis of the transducers. In order to compare the points inside a slice, each range and angle is parsed into a 2 m and 0.01° grid (i.e. ∼4 m of vertical resolution at the middle of the glacier face).

A portion of the recorded points is noise removed through post-processing filtering. Insofar as the ping is not able to penetrate through solid matter, we assume that for a given ping, only a single value of range must be associated to each given angle, the other being considered as noise. In addition to the range and angle, auxiliary informations such as return signal amplitude or phase confidence (Bathyswath, user manual) allow the Bathyswath pro-

Figure 8.2: Measurement of the angle existing between a return signal and the transducer using the interferometry principle. After Bathyswath, user manual

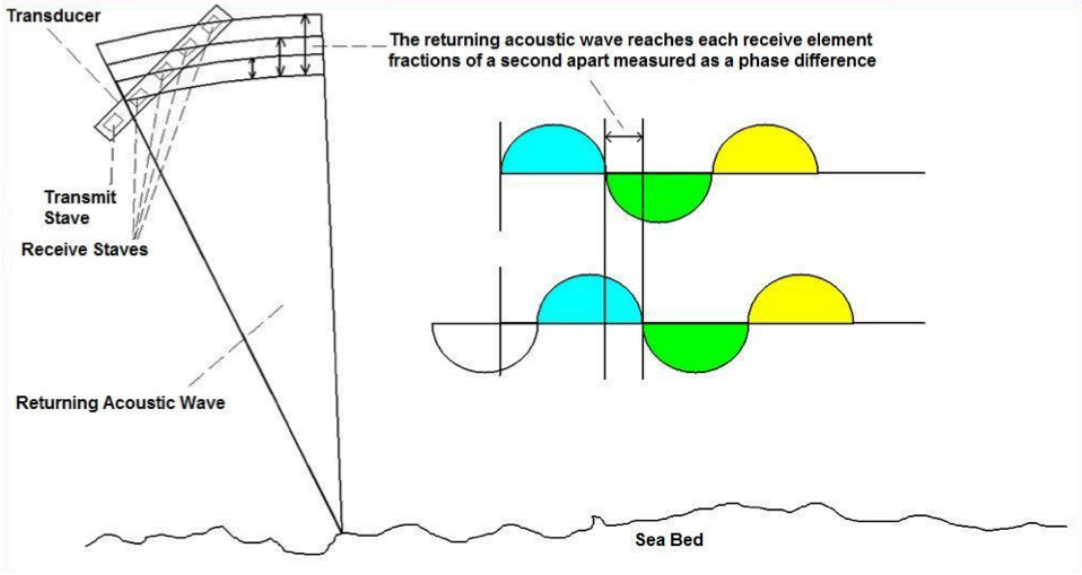

cessing software to determine a quality estimate (from 0 = bad to 1 = good) associated to each point. When the raw data are gridded the quality of each raw point contained in one grid bin are summed. Discarded points are either due to particles in the water column or electromagnetic noise that generate a false return signal. In both cases, the random character of the noise can be discerned from the relatively persistent position of the bottom or glacier returns. Hence, tolerating only a small change of range between a given grid point and the neighbouring points, both in time and angle filters out the remaining noise. Only the points that successively pass the three following tests are considered good and kept for further processing (Figure 8.3):

1. has the maximum quality of all the points within an angle bin

2. has a quality $> Q_{min}$

3. has a range difference (compared to the averaged range of the 5 nearest angle bins and to the 5 previous pings) $< \Delta R_{max}$

The value of Q_{min} and ΔR_{max} are adjusted manually during the post-processing of a dataset to maximise the efficiency of the filter. Typical values of Q_{min} and ΔR_{max} are 0.7-3 and 20-60 m, respectively.

Figure 8.3: Ping coordinate system filtering. Raw data are in grey and the result of the three successive tests: highest quality for each angle (green); threshold quality (red); proximity (black). All black points are considered as good. The black circle corresponds to the maximum range of the instrument, at 750 m. Note the noise near the transducers due to turbidity in the water column.

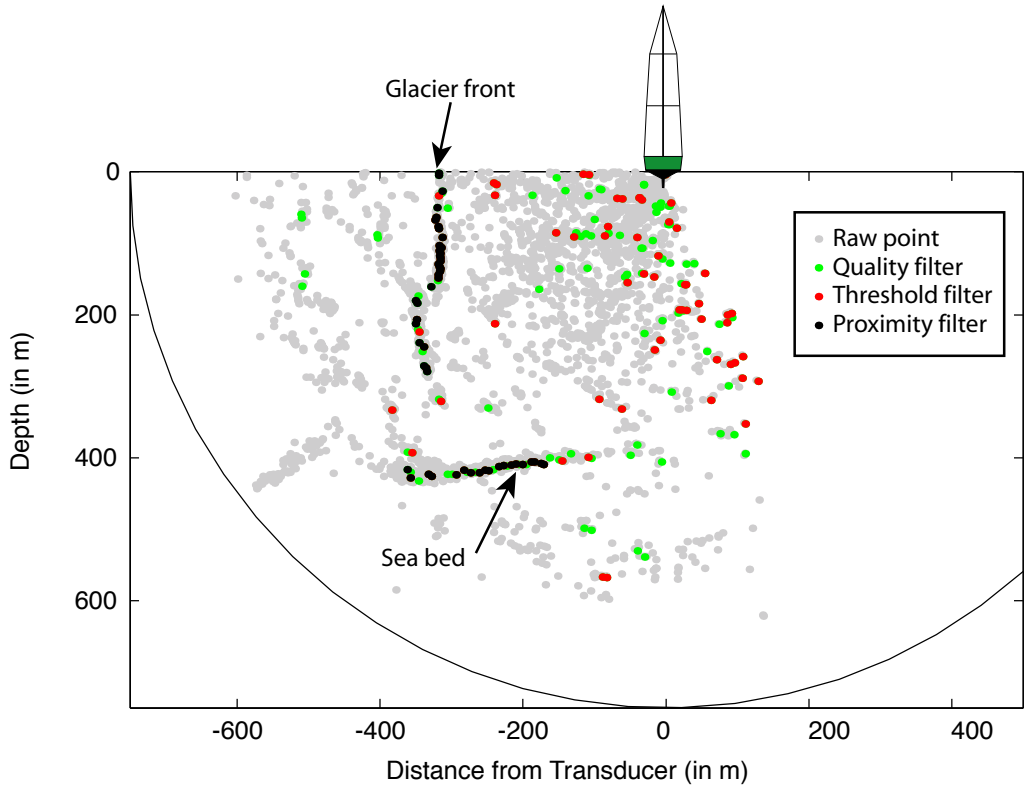

Manual filtering: Once filtered within each ping, the points are displayed in fixed coordinate system, where manual filtering is performed to remove outliers and separate the seabed from the glacier front.

Isobath filtering: After the ping coordinate system and manual filters have been applied the general shape of the ice front is clearly visible. However the multiple sources of error in geo-referencing (i.e. GPS positioning, heading, roll, duration of the ping, variation in speed of sound due to salinity changes...) produce a thick surface instead of a skin surface (i.e. with no thickness), which is necessary to compare two surveys of the ice-front.

The thick point cloud is thus filtered to obtain a skin surface that best represents the glacier front. The complex shape of the front, with bays and headlands associated to a large point cloud (up to 10 million points) render the filtering difficult and computationally demanding. In order to simplify the extraction of the skin surface, we assume that at a given z depth the ice front can be considered as a single continuous curve. This assumption is validated by the absence of upward opening caves or submarine pinnacle-like structures. Cavities in the ice front have been observed in places, but due to the shadow of the upper edge on the ice front below it is not possible to determine if the cavity is a downward opening cave or a horizontal roof-like overhang. We therefore assume that cavities in the ice front are horizontal roof-like overhangs, hence respect the continuity assumption.

For a horizontal layer 20 m high, the ice front is unfolded using a curvilinear transformation based on the general horizontal shape of the whole glacier front. This conversion is performed in order to simplify the evaluation of the ice-front skin surface using an explicit curve $y = f(x)$ instead of a parametric curve $x = f_1(t); y = f_2(t)$, which is otherwise necessary when multiple y values exist for a single x, as in the case of bays or headlands with acute angles. It is assumed that the ice front at a given depth is the curvilinear

smoothed curve (i.e. isobath) determined by a penalised least square method (Garcia, 2010) of all the data points within this horizontal layer. All isobaths are then converted back into the fixed coordinate system by reversing the curvilinear transformation.

8.3.2 Glacier coordinate system and gridding

In the Earth coordinate system $R = (E, N, z)$, each survey determines the position of the glacier front $F_{(R)}$, with E and N the eastern and northern coordinates of the universal transverse Mercator (UTM) for the zone 22W and z the depth positive downward ($z = 0$ at mean sea level). For calculation of the ice advection and the submarine melting it is convenient to transform the front position F into two other coordinate systems as described below:

The glacier coordinate system $y = G(x, z)$: is colinear to the general flowing direction of the glacier, with x the distance perpendicular to the ice flow from the south margin and y the distance parallel to the main ice flow of the glacier, with positive value downstream. This coordinate system enables ice advection to be easily estimated between two surveys of the ice front (Figure 8.4).

The ice front coordinate system $n = I(s, z)$: follows the shape of the front, with s and n the distance along, and orthogonal, to the general horizontal shape of the glacier front. This coordinate system facilitates the estimation of the normal distance between two surveys of the ice front, hence the action submarine melting (Figure 8.4).

For the coordinate system $G\ (I)$, a grid is applied along the $x\ (s)$ and z coordinates, with a resolution of 20×20 m. The $y\ (n)$ value of the gridded $G\ (I)$ is the average of all $y\ (n)$ raw values contained in a grid point.

Figure 8.4: a) Map of Store Glacier, with the transect (orange line) used in the G coordinate system, and the position of the fjord temperature profile concomitant with the scans. b) Schematics of the coordinate system used in the chapter. c) Schematic of how the submarine melt and calving rates are estimated from two successive front positions

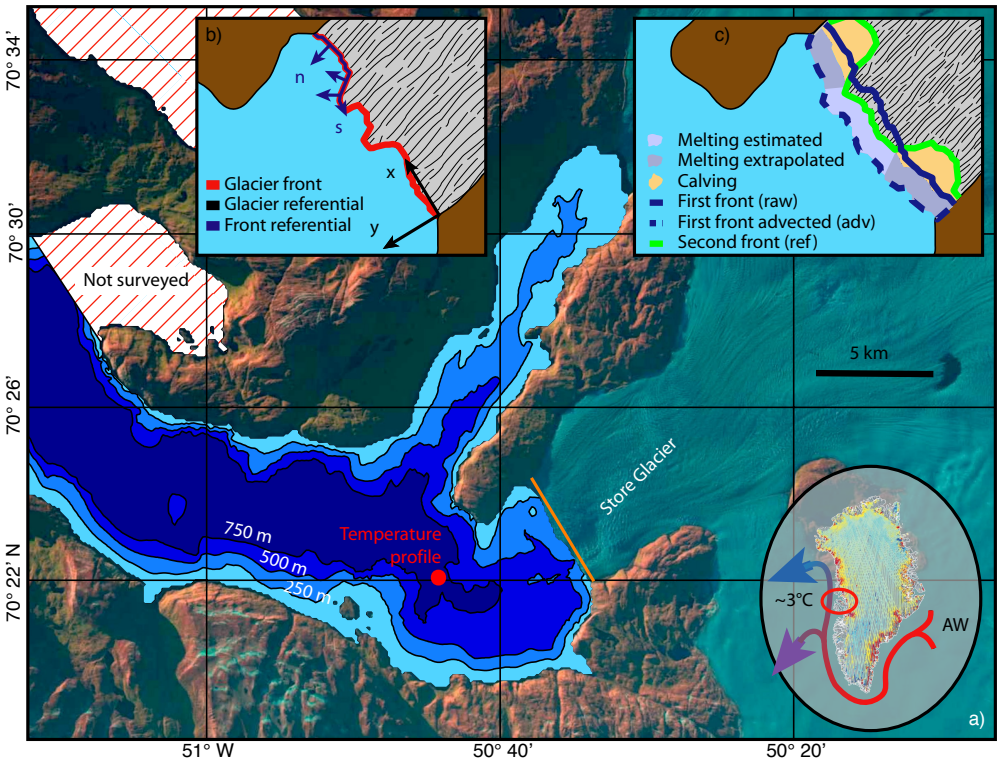

8.3.3 Glacier front area

Two types of area can be defined for the glacier front: (1) the area of a section perpendicular to the ice flow through which the glacier is advected (hereafter,

$S_{section}$); and (2) the surface area of the ice-ocean interface (hereafter, S_{front}), taking into account the geometry of the ice front, which represent the surface area where submarine melting acts. $S_{section}$ is estimated using the bathymetry along x at $y = 0$ Similarly, S_{front} is estimated using the bathymetry, following the reference path along s at $n = 0$

8.3.4 Glacier front dynamics

Three major processes affects the ice position on the submarine part of the glacier front: (1) advection related to the specific glacier dynamics, (2) iceberg calving, and (3) submarine melting.

We can then make the assumption that, on average, the advance or retreat of the glacier front is defined as:

$$\Delta A = (V - C - SBM)\Delta t \tag{8.1}$$

where ΔA the observed movement of the front; V the glacier velocity; C the calving rate; SBM the submarine melting rate and Δt the lapse of time between two measurements of the front.

8.3.5 Glacier velocity estimation

To quantify the submarine melt and calving rates it is necessary to estimate the glacier velocity V at any point of the front. As in Equation (8.1) the calving

and submarine melting rates are strictly positive (i.e. $C \geq 0$ and $SBM \geq 0$), the impact of the velocity V on each part of the glacier front is at a minimum greater than the observed advance ΔA, such as:

$$\begin{aligned} V(x,z) \geq & \frac{\Delta A(x,z)}{\Delta t} \\ \geq & \frac{G_2(x,z) - G_1(x,z)}{t_2 - t_1} \end{aligned} \tag{8.2}$$

where $V(x,z)$ the velocity of the ice front at any given point, and G the position of the front F in the glacier coordinate system (Section 8.3.2).

Estimation of Store Glacier front velocity has been performed using repeated photogrammetry from an unmanned autonomous vehicle (UAV) in July 2013. This produced a maximum velocity of $V \simeq 16\,\mathrm{m\,d^{-1}}$ at the middle of the glacier front and followed a power law function from the edge of the glacier toward the centre (Ryan and others, 2014). However, between our surveys we observed an advection $\Delta A/\Delta t$ up to $\sim 20\,\mathrm{m\,d^{-1}}$ near the center of the glacier, therefore the velocity relation deduced by Ryan and others (2014) cannot be used directly. Indeed it would contradict Equation (8.2) as $V(x) < \Delta A(x)/\Delta t$ and results in Equation (8.1) of either a negative calving or submarine rate (i.e. accretion of ice), which is not possible in positive temperature water.

When no major calving events occur between two surveys of the ice front, it is deduced from Equation (8.1) that:

$$V(x,z) = \frac{\Delta A(x,z)}{\Delta t} + SBM(x,z) \tag{8.3}$$

Then if we assume that (1) Store Glacier has a plug flow dynamic (i.e. no variation of velocity with depth – Rignot, 2006), and (2) at any x point of the glacier front there is a depth z where $SBM \simeq 0$, it follows from Equations (8.2) and (8.3):

$$V(x,z) \simeq max \left\{ \frac{\Delta A(x, \forall z)}{\Delta t} \right\} \tag{8.4}$$

In the case where the submarine melting is not null at any given depth, Equation (8.4) will underestimate the actual velocity of the glacier front, which consequently will produce conservative submarine melt and calving rates in Equation (8.1).

The occurrence of a calving event between the two surveys used to estimate the glacier velocity will produce a local underestimation of the glacier velocity. Therefore to limit the potential impact of small calving events on the estimation of $V(x,z)$, we determine an idealised velocity profile $V_i(x,z)$ at each point of the ice front, such that:

$$\begin{cases} V_i(x,z) & = \alpha x + \beta \text{ per segments} \\ V_i(x,z) & \geq V(x, \forall z) \end{cases} \tag{8.5}$$

Finally we assume that the idealised velocity of the glacier V_i is representative of the average velocity of the glacier between each survey (Figure 8.6).

8.3.6 Correction of the glacier velocity

To quantify and isolate the impact of SBM and C between two positions of the glacier front (hereafter, the earliest scan is referred as: F^{raw} and the latter as: F^{ref}) it is necessary to compensate the effect of glacier velocity (Equation (8.1)). On the glacier coordinate system where $y = G(x, z)$, the earlier scan $F^{raw}_{(G)}$ is advected downstream using the idealised velocity profile $V_i(x, z)$ to obtain the advected profile $F^{adv}_{(G)}$, such that:

$$F^{adv}_{(G)}(x, z) = F^{raw}_{(G)}(x, z) + V_i(x, z)\Delta t \tag{8.6}$$

In the following sections, all comparisons between two fronts position are performed using a front of reference F^{ref} and a front corrected for the advection F^{adv}

8.3.7 Front ablation processes

Observation of time-lapse photographs shows that at Store Glacier major calving events (i.e. affecting a substantial part of the glacier front) are location-specific and episodic. Thus, the front of the glacier undergoes periods without any major calving event, during which only submarine melting is responsible for the difference in position between the front corrected for advection $F^{adv}_{(G)}$ and the front of reference $F^{ref}_{(G)}$.

Submarine melt rate

For simplification, we suppose the submarine melting (SBM) to act along the normal vector of any part of the ice face. In the ice front coordinate system I

the distance along the normal vector to the ice front F^{ref} can be described as $n = F_{(I)}(s, z)$, therefore the SBM corresponds to:

$$SBM(s, z) = \frac{F^{ref}_{(I)}(s, z) - F^{adv}_{(I)}(s, z)}{\Delta t} \tag{8.7}$$

8.3.8 Uncertainty evaluation

The horizontal resolution of the scan is a direct function of the distance travelled by the survey boat between pings, hence 2D slices. At a survey velocity of 0.5 – 1 m s^{-1} this produces a horizontal resolution of 0.5 – 1 m for a surveying range of 750 m. The typical error in positioning the survey boat using the post-processed GPS is <0.1 m, while any error on the heading is amplified by the lever effect of the surveying range of the Bathyswath. Indeed with a heading error of 0.1 (i.e. the typical error with the Crescent vector GPS) at a range of 500 m, the horizontal error is 0.9 m. The horizontal resolution is finally estimated as 0.5 – 1±1 m. Another source of uncertainty concerns the evaluation of the distance between the sonar transducer and the ice-front and the inability to determine if a return signal comes from the start or the end of a pulse, therefore giving an uncertainty equal to the pulse length (Bathyswath, user manual). During all surveys the measurements were collected using a pulse length equivalent to 2 m. As a result of the front being surveyed mostly perpendicular to the ice face, we assume that the pulse induced error can be attributed to the uncertainty in y for a front in the glacier coordinate system $F_{(G)}$. Thus, the uncertainty on Δy, the

distance separating two fronts, is equivalent to the squared sum of the uncertainty in position:

$$e\Delta y = \sqrt{2^2 + 2^2} \tag{8.8}$$

$$= 2.8\, m \tag{8.9}$$

The estimation of the uncertainty in the velocity of the glacier eV depends on the uncertainty of the distance $e\Delta y$ between the two fronts used to determine V and the lapse of time Δt between these two measurements:

$$eV = \frac{e\Delta y}{\Delta t} \tag{8.10}$$

Similarly, the uncertainty related to the submarine melting $eSBM$ is a function of the uncertainties $e\Delta y$ and Δt:

$$eSBM = \frac{e\Delta y}{\Delta t} \tag{8.11}$$

Finally, the uncertainty on the calving rate eC is based on the uncertainties of the glacier velocity eV, the submarine melting $eSBM$ and the distance $e\Delta y$ between the two fronts considered:

$$eC = \sqrt{(eVS_{section})^2 + (eSBMS_{front})^2 + (e\Delta yS_{section})^2} \tag{8.12}$$

8.4 Results

8.4.1 Repeated scan

Estimating the submarine melting on an active calving front like Store Glacier contain a certain aspect of serendipity. Indeed, the resolution of the Bathyswath system used of 2.8 m is in the same order of magnitude than the daily submarine melt rate that we are trying to measure (i.e. $1-4\,\mathrm{m\,d^{-1}}$). Thus, as observed in Equation (8.11), to reduce the uncertainty on the submarine melt rate estimation, it is necessary to increase the time between two surveys of the glacier front. However, if any major calving event occurs during this interval it will not be possible to differentiate the ablation caused by the submarine melt from the calving. To add to this already complex situation, the glacier front is not always accessible for surveying as the presence of brash-ice and icebergs, often clustering for period of time along the glacier front, limits the maneuverability of the boat and make either the survey impossible or very dangerous. It is thus a matter of observation of the glacier front, personal judgement and speculation between the relatively unpredictable character of a calving event, which usually happen on a multi-day period, the accessibility of the glacier front, and the necessity to increase the time between the surveys in order to improve the submarine melt estimation. Yet, if two surveys of the front are taken without a calving event occurring meanwhile, it is possible to obtain

During the summer 2012, the relatively clear conditions of Store Glacier front allowed regular access for surveying. Hence, three scans of almost the whole glacier front were collected on the 3^{rd}, 12^{th}, and 17^{th} of July 2012 (Hereafter, $F3$ $F12$

and $F17$) (Figures 8.5 and 8.6). The presence of a thick band of brash-ice and icebergs at the margin of the main plume (Chapter 5) on July 17th, precluded from surveying approximately 800 m of the glacier front situated beneath the main surface plume. Moreover, the presence of brash-ice near the transducer head and the high turbidity at the surface of the fjord impeded the measurement of the upper 100 m of the glacier front in all three scans.

8.4.2 Glacier description

The plan view shape of the glacier front appears to be constrained by the bathymetry of the fjord. Indeed, most of the glacier front appears to be standing at the edge of steep down-sloping ridges. The center section of the glacier front stands at the edge of a 2 km wide plateau, at ∼500 m depth overlooking the head of a basin leading to the deepest part of the fjord (Figure 8.5). Similarly, on the north and south margin the glacier front is perched at the top of almost vertical cliffs.

In all surveys most of the width of front the glacier is grounded to the seabed, although a section 800 m wide on the south section of the glacier front is clearly detached from the bottom and could possibly be floating, as suggested by Ryan and others (2014). Due to the limited extend of the ungrounded section of the glacier front, it is unlikely that this section is freely-floating. This large cave, extending from the seabed approximately 170 m upward, is situated below the main upwelling plume visible at the surface (Figure 8.5 and chapters 5 and 6). Moreover, this cave is at the head of a ∼600 m deep trough, which could then enhance the access of the warm Atlantic water into the plume (Chapters 3, 5 and 6, Xu and others, 2013). Similarly, near the center of the glacier front, where a deep

plume was identified (Chapter 6) another cave, although narrower, is observed with approximately 200 m width and 200 m height (Figure 8.5).

Figure 8.5: Store Glacier front. a) The three positions of the glacier as on the 3rd (red), 12th (blue) and 17th (green) of July. Zoom on 17th July survey of the caves observed in all survey along the seabed and beneath (b) the deep plume, and (c) the surface plume (Chapters 5 and 6). Land and glacier topography are extracted from the Greenland Ice Mask Project (GIMP) with Formosat-2 satellite image from 28th June 2008 overlaid on the glacier. Vertical height is exaggerated 2 times (a) and at scale (b and c). Note the deep trough leading to the main plume on the south side.

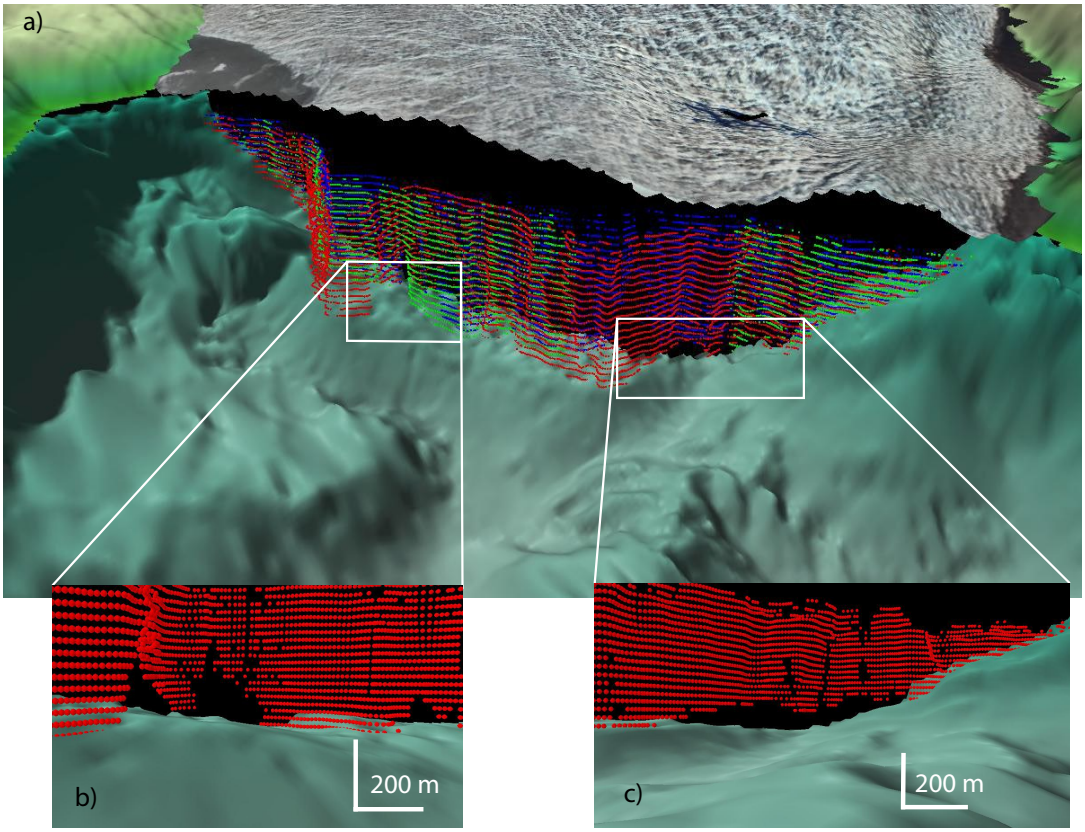

The $F3$ and $F12$ scans exhibit the presence of a cavity at the base of the glacier in the southern part of the front, and below the plume observed at the surface, which could possibly be the main portals for the subglacial fresh water discharge (Chapters 3, 5 and 6).

The time-lapse photographs recorded the calving of the two headlands visible on $F3$, which calved through two sets of major calving events on the 4^{th} and 11^{th} of July (Figure 8.6). However, between the 12^{th} and 17^{th} of July calving only occurred near the glacier margins, leaving the centre of the front intact. The submarine area of the cross-section, $S_{section}$ is estimated to be $1.9 \times 10^6\,\text{m}^2$, while the surface area of the ocean-glacier interface S_{front}, which is affected by the geometry of the glacier front, was estimated using the scan $F12$ to be $2.2 \times 10^6\,\text{m}^2$

8.4.3 Glacier Velocity

An estimated velocity profile of the glacier is achieved using scans $F12$ and $F17$ since no major calving events occurred between these scans. Using Equation (8.2) gives the observed velocity $V(x,z)$ of $21 \pm 2.8\,\text{m}\,\text{d}^{-1}$ at the center of the glacier (Figure 8.6). Local negative velocity reflects the effect of medium size calving events, while localised artefacts with strong positive or negative velocities result from filtering or error in the geo-referencing (amplified where the glacier front becomes almost parallel to the y axis). The idealised velocity profile $V_i(x,z)$ is thus determined using Equation (8.4), without taking into account artefacts or calving events, along four segments. The velocity $V_i(x,z)$ is linearly interpolated between the observed velocities $V(x,z)$ at the apex of each segment (Figure 8.6).

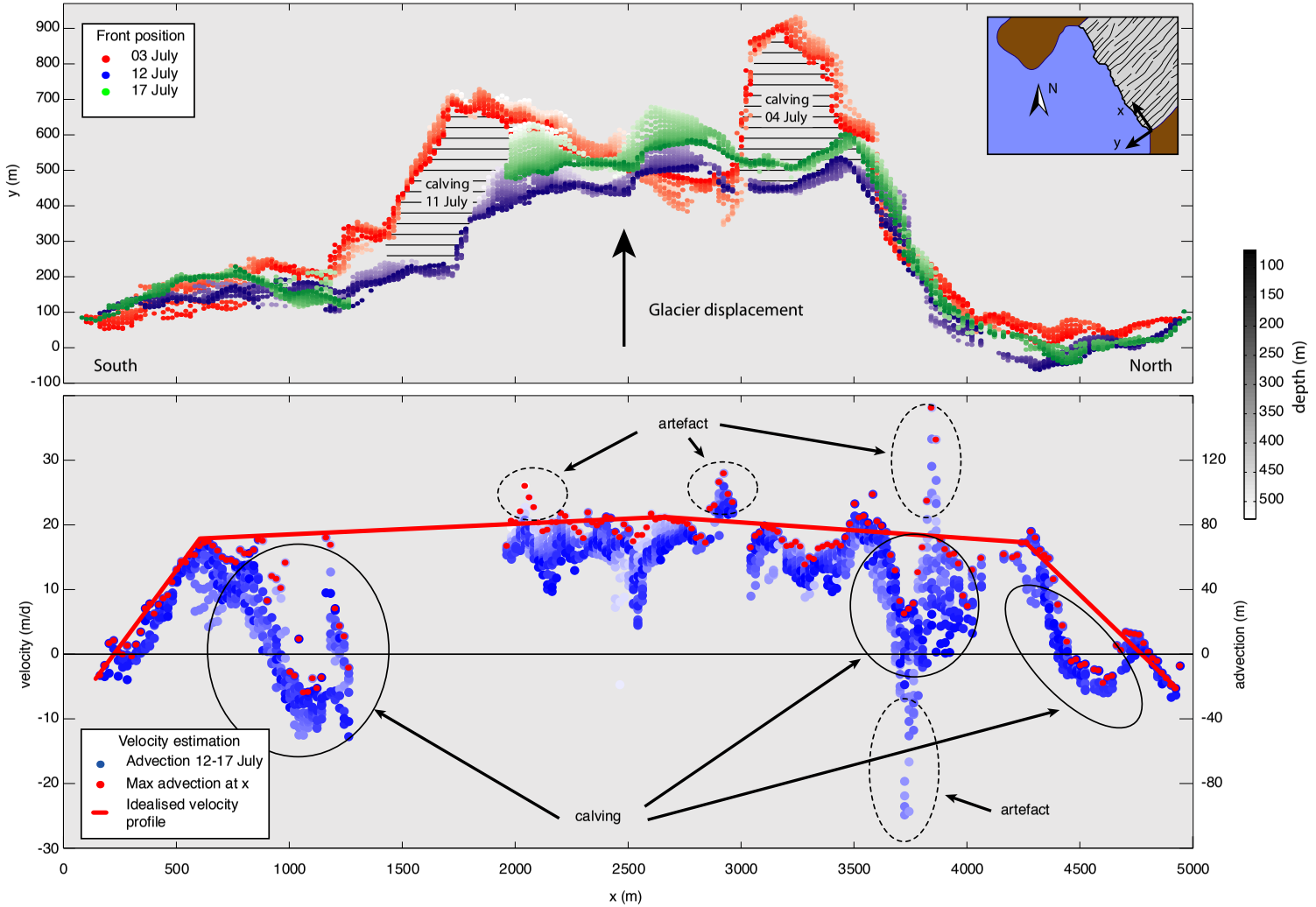

Figure 8.6: Top - Position of the front for the three surveys. Inset shows the type of coordinate system used: Glacier coordinate system (Figure 8.4). Bottom - Glacier velocity profile (red line) deduced from observed advection (blue). The red dots show where the advection is maximal for a given x value.

8.4.4 Submarine melting

As well as estimating the velocity profile, scans $F12$ and $F17$ are used to quantify the SBM, by applying Equation (8.7). The local submarine melting impact is thus obtained for each part of the glacier front surveyed in both $F12$ and $F17$ (Figures 8.5 and 8.7). Near the northern and southern margins two areas have melt rates higher than the glacier velocity itself. These are artefacts related to the calving events previously described.

Thus, to estimate the spatial distribution of SBM, without biases due to the calving events, only the central area from s=1750 m to s= 3500 m is considered (Figure 8.7).

The average per depth shows that the submarine melting is near $0\,\mathrm{m\,d^{-1}}$ at 500 m depth, (i.e. the toe of the glacier), gradually increasing to $3\,\mathrm{m\,d^{-1}}$ at around 400 m depth and reaching $4\,\mathrm{m\,d^{-1}}$ at 100 m depth (Figure 8.7). No direct measurement are available for the upper 100 m of the glacier front.

The average per vertical strip along the front shows a higher melt inside the bay than at the tips of the headlands (Figure 8.8). Due to the lack of measurement during $F17$ over the section of the glacier front corresponding to the main plume (Chapters 5 and 6), it was not possible to evaluate the submarine melt inside the upwelling plume.

The average submarine melting rate over the whole central area is $\overline{SBM} = 3.4 \pm 0.7\,\mathrm{m\,d^{-1}}$

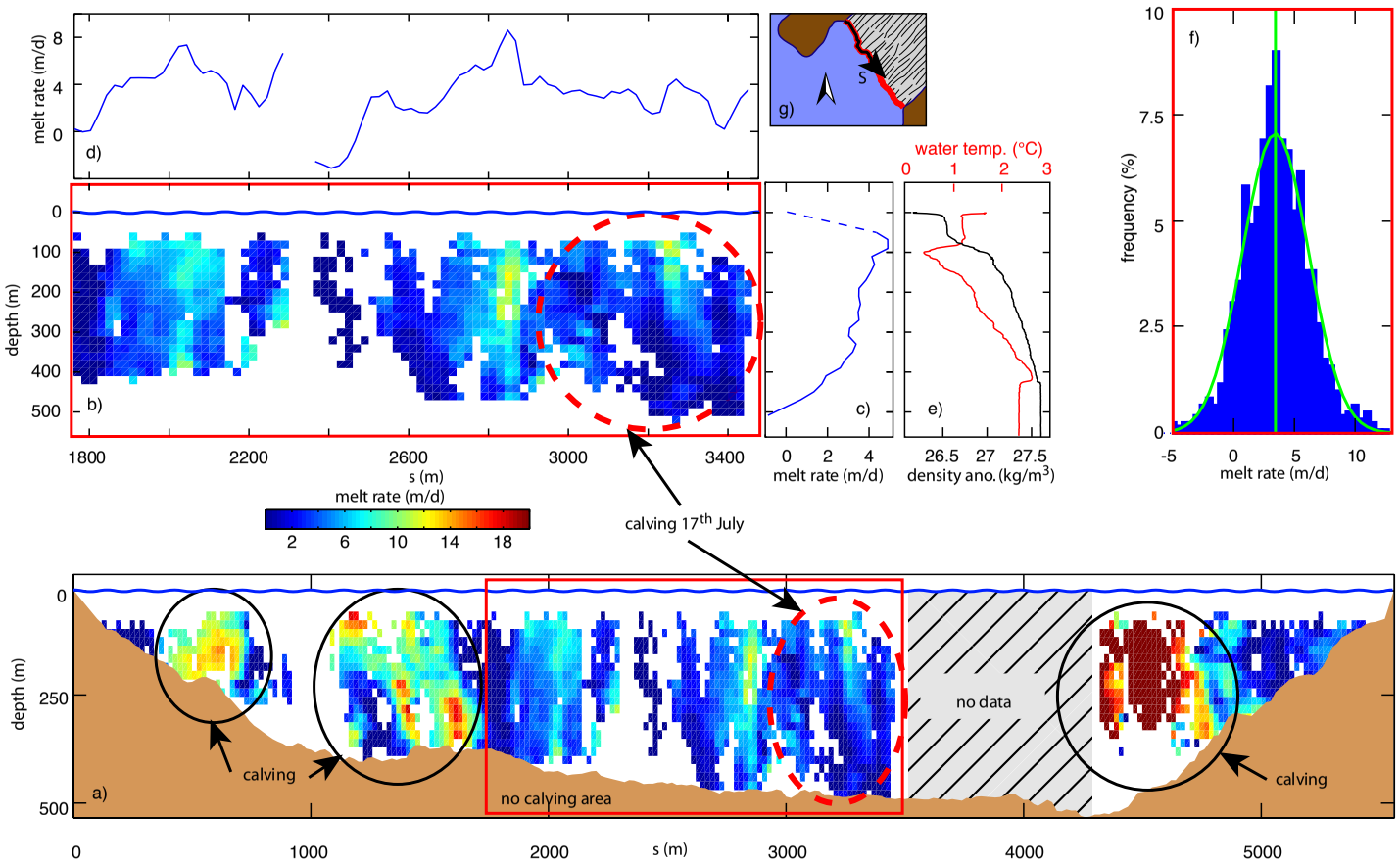

Figure 8.7: Melt rate estimation from scan on 12$^{\text{th}}$ and 17$^{\text{th}}$ of July, a) on the whole glacier front, b) on the extracted area. c) Depth averaged, and d) along front averaged melt rate. e) Concomitant temperature and density profile. f) melt rate distribution on the extracted area and the average melt rate used in the paper (green vertical line). The gaussian curve (green) has similar mean and σ than the melt rate distribution. g) the coordinate system used in this graph: Front coordinate system (Figure 8.4). Position of calving events are marked as well as the approximate position of the iceberg reconstructed in Chapter 7.

Figure 8.8: Submarine melt estimation (colorcoded) draped on $F17$ ice front. Color-mapping is similar to Figure 8.7

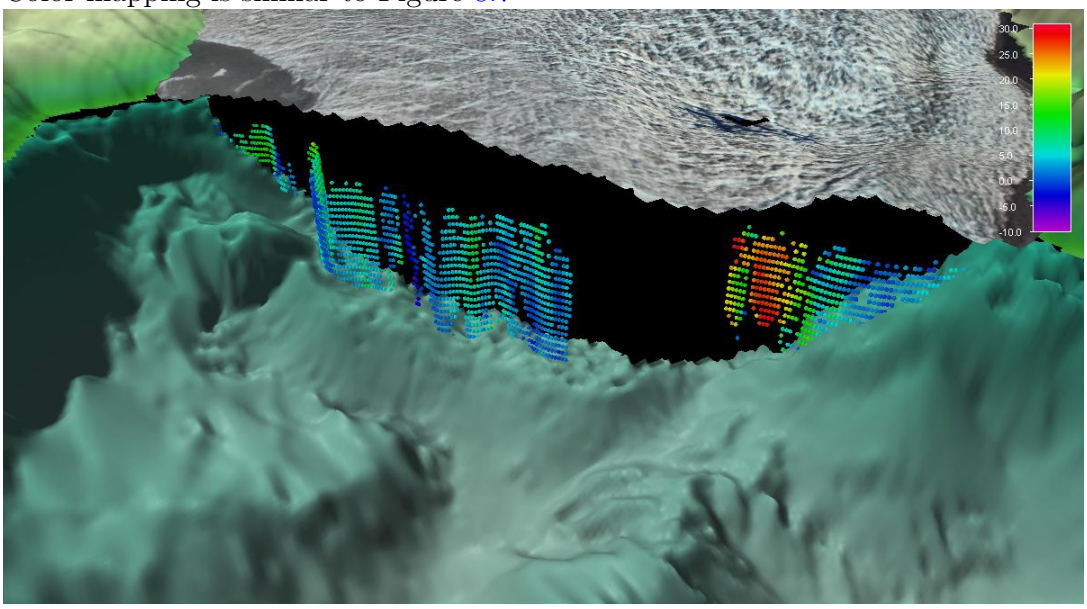

8.5 Discussion

8.5.1 Velocity profile

The maximum flow rate of $21 \pm 0.7\,\mathrm{m\,d^{-1}}$ estimated at Store is ~40% higher than previous estimates of about 15-16 $\mathrm{m\,d^{-1}}$ (Ahn and Box, 2010; Ryan and others, 2014). This could potentially be the result of a faster glacier during the record breaking 2012 melt-season (Nghiem and others, 2012; Tedesco and others, 2013). Using the area $S_{section}$ of the cross-glacier section and the idealised velocity profile $V_i(x)$, deduced from the observed advance of the glacier, produces a submarine ice-discharge of $29.9 \times 10^6\,\mathrm{m^3\,d^{-1}}$ ($9.8\,\mathrm{Gt\,yr^{-1}}$).

8.5.2 Submarine melting

The average $\overline{SBM}$ of $3.4 \pm 0.7\,\mathrm{m\,d^{-1}}$, observed in the central part of the glacier, confirms the magnitude of previous indirect estimates of $2-3\,\mathrm{m\,d^{-1}}$ for Store Glacier in August 2010 from oceanographic observations (Xu and others, 2013) and using the Motyka model (Chapter 4) as well as numerical simulation estimates of $0.7-2\,\mathrm{m\,d^{-1}}$ (O'Leary, 2011; Xu and others, 2013, 2012).

Assuming that the average $\overline{SBM}$ represents the impact of submarine melt over the entire surface area of the glacier front (S_{front}), submarine melt would thus contribute to $\sim$25$\pm$5% of the submarine ablation of the glacier during summer months, while the rest would be due to iceberg calving (note that above sea-level it is aerial melting and calving which will ablate the ice front). This value is consistent with an initial estimate for Store Glacier which assesses the annual (i.e. including the winter months) submarine contribution at $\sim$14% (Chapter 4).

The histogram of the submarine melt rate measurements, in the central area reveals a distribution similar to a Gaussian curve with identical mean and σ (Figure 8.7, f), Moreover, a statistical test of Kolmogorov-Smirnov (whose null hypothesis is that the distribution is Gaussian) validates the null hypothesis with a p-value = 43.6% We thus assume that a part of the variability in the submarine melting measurements is associated with independent random errors.

The submarine melt vertical profile is in good agreement with the submarine melt impact deduced from the reconstruction of a recently calved iceberg (Chapter 7), thus it is hypothesised that over the upper 100 m, where the lack of sonar measurement prevented us from measuring the glacier front evolution, the melt rate diminishes from $\sim 4\,\mathrm{m\,d^{-1}}$ at 100 m depth to near $0\,\mathrm{m\,d^{-1}}$ at the surface (Fig-

ure 8.7). These observations associated with the estimation of the submarine melting rate confirm the predictions using numerical simulation (Kimura and others, 2014; O'Leary, 2011; Xu and others, 2013, 2012).

The comparison of the fjord temperature profile with the submarine melting profile shows that the maximum melting occurs at the depth of the minimum of temperature at 100 m depth (Figure 8.7). This apparent contradiction can be explained by the free-forced buoyancy entrainment resulting from melting ice in seawater which (1) transports the deep warm water upward along the ice face (Huppert and Josberger, 1980; Josberger and Martin, 1981; Sciascia and others, 2013), and (2) enhances the submarine melt rate by increasing the velocity-dependent turbulent transfer coefficients of salt and heat at the ice face (Sciascia and others, 2013). Indeed, at the base of the glacier front, the warm Atlantic Water reaching up to 2.5°C (Figure 8.7) is the main fuel for the melting, but the limited vertical circulation impedes the melt rate (Jenkins, 1991, 2011; Kimura and others, 2014; O'Leary, 2011; Xu and others, 2013, 2012). As the water gains more vertical velocity as it rises along the front (Kimura and others, 2014; Sciascia and others, 2013) the melt rate increases despite the ambient temperatures decreasing. Finally the presence of minimum temperature near 100 m depth, associated with a pycnocline (Figure 8.7), both reduces the submarine melt fuel and the vertical circulation, resulting in a reduction of melting toward the surface.

8.6 Conclusion

Using a cutting-edge method of repeated 3D submarine scanning of a major outlet glacier front permits the first direct measurements of the submarine melt rate over

a section $\sim$2 km wide and 500 m high. We observed negligible submarine melt rate at the base of the ice face, gradually increasing to $\sim$3 m d^{-1} at 250 m depth, reaching its maximum with $\sim$4 m d^{-1} at 100 m depth before decreasing toward the sea surface. The vertical profile of melting and rate is in accordance with prediction from numerical simulation.

On average, the summer submarine melt rate on Store Glacier was 3.4 ± 0.7 m d^{-1} which correspond to $\sim$25$\pm$5% of the frontal ablation.

Chapter 9

Synthesis

This thesis has focused on the ocean-glacier and provides insight into the interaction processes impacting glacier fronts and the controls that govern them. The following chapter draws upon the results of recent publications to place the four experiments presented in Chapters 3 to 8 into a broader context, before suggesting directions for future research.

9.1 The state of knowledge before 2011

Melting of vertical ice-faces in the ocean and their consequences on the ocean circulation was first studied around 1980 with different field measurements in the Arctic and laboratory experiments (Gade, 1993). However, these studies were motivated by the impact of melting on the upwelling of nutrients as a stimulus to the biological activity (Greisman, 1979; Horne, 1985).

Around 1990, submarine melting was first considered as an important factor influencing glacier stability, yet only for Antarctic ice shelves (Holland and Jenkins, 1999; Jenkins, 1991, 1999). It was only by the start of the millennium that the case of significant submarine melting was considered important for vertical ice fronts of Arctic glaciers (Motyka and others, 2003). The forcing of subglacial fresh water injected at depth into the fjord and entraining the fjord bottom water is thus proposed as the main driver of the melt rate. Over the last decade, and around Greenland, this led to a succession of field measurement and modelling studies emphasising the potentially strong impact of the warming Atlantic water, found around Greenlnad, on the glacier stability (Holland and others, 2008; Rignot, 2006; Straneo and others, 2010).

9.2 Progress between 2011 and 2014

Since these initial observations (1979 – 2011), our knowledge of the dynamics of ocean-glacier interface around the Greenland Ice Sheet has developed significantly. The following sections discuss recent developments (2011-2014) relevant to the main research in this thesis.

9.2.1 ocean-glacier interaction processes

The presence and structure of the ocean-glacier interaction processes at Store and Rink glaciers are consistent with observations from other fjord systems around Greenland characterised by a multi-layers fjord system: (1) the bottom layers, from the base of the glacier to approximately 200 m depth, exhibit only the action

of submarine melting by the warm Atlantic water; (2) the upper layer from 200 m to the fjord surface layer is a mixture of submarine melt and subglacial fresh water (Figures 3.2 and 3.3, Johnson and Munchow, 2011; Mortensen and others, 2013; Straneo and Cenedese, 2013; Straneo and others, 2012) and (3) the surface layer is a complex combination of ocean-atmosphere interaction, iceberg melting, river and ocean-mixing (Bendtsen and others, 2014; Mortensen and others, 2013, 2011). Chapter 3 emphasised that the general ocean-glacier interaction pattern, of the upper layer, can vary significantly with the discharge of subglacial fresh water (Figure 3.7), from one fjord to another (Mortensen and others, 2011; Straneo and others, 2012) or seasonally (Mortensen and others, 2013).

The multilayer structure and its variability is known to have an impact on the the fjord circulation (Sciascia and others, 2013, 2014; Sole and others, 2012; Sutherland, 2012) and the heat source available at the glacier front for melting the ice (Jackson and Sutherland, 2014; Sole and others, 2012).

In Store Fjord, a strong variability in direction and velocity of the current has been observed during the winter (Figure 4.5). Similar observations exist from the east coast of Greenland and are suggested to be driven by wind events on the continental shelf producing an oscillating intermediary circulation inside the fjord. The intermediary circulation is thought to drive variations of temperature and depth of the Atlantic water (Jackson and Sutherland, 2014; Straneo and others, 2010; Sutherland, 2012). In contrast, at Store the intermediary circulation was not associated with variations in temperature of the Atlantic water (Figures 4.3 and 4.5) suggesting that the depth of the entrance sill as well as the water present in the vicinity of the continental shelf also influences the impact of the intermediary circulation on the water column structure at glacier front. Moreover, the annual

presence of the warm Atlantic water near the glacier front (Figures 3.2 and 4.5) can contribute to an important heat source, driving submarine melt at the glacier front (Jackson and Sutherland, 2014; Mortensen and others, 2013; Straneo and others, 2011; Xu and others, 2013).

The depth of sills at the entrances to fjords was identified as having an important role in terms of controlling the water present at the glacier front as well as the fjord circulation (Chapters 3 and 4, Mortensen and others, 2011; Straneo and Cenedese, 2013; Straneo and others, 2012). In Store Fjord the only sill present is on the continental shelf at 450 m depth, meaning there is a direct route for the warm Atlantic water to reach Store Glacier (Chapter 2).

During winter months, the upper layer of the fjord containing a combination of submarine melting and runoff mixing (Figures 3.2 and 4.5, Mortensen and others, 2013; Straneo and Cenedese, 2013) is replaced by cold polar water (Figures 3.2 and 4.5, Straneo and others, 2012), when the discharge of subglacial fresh water decreases. Despite that change, in Chapter 4 we showed that the limited, yet continuous, subglacial discharge of basal melt water was sufficient to produce a significant submarine melting throughout the winter (Figure 4.6, Christoffersen and others, 2012) contrary to the common assumption of negligible winter submarine melt (Nick and others, 2013; Sciascia and others, 2014; Sole and others, 2012; Todd and Christoffersen, 2014).

9.2.2 Submarine melting: rate and seasonal evolution

The summer submarine melt rate of $3.4 \pm 0.7\,\mathrm{m\,d^{-1}}$ measured from repeated scans of the glacier front (Chapter 8) confirmed and refined previous estimates of 2–

$4\,\mathrm{m\,d^{-1}}$ for similar glaciers around Greenland (Enderlin and Howat, 2013; Rignot and others, 2010; Sutherland, 2012; Xu and others, 2013). Such melting has a significant impact on the dynamics of major outlets like Store; submarine melting contributes to ∼25% of the summer ablation.

The measured and observed vertical profile of the submarine melt rate at Store is in good agreement with numerical modelling of this process at a vertical ice front (Figures 7.3 and 8.7, Kimura and others, 2014; O'Leary, 2011; Sciascia and others, 2013; Xu and others, 2012).

The vertical distribution of submarine melting ranges from almost null at the glacier foot (i.e. 500 m depth), gradually increasing to $3\,\mathrm{m\,d^{-1}}$ around 300 m depth and reaching up to $4\,\mathrm{m\,d^{-1}}$ at 100 m depth before decreasing again toward the surface(Figure 8.7).

Features observed on a recently calved iceberg demonstrate that the submarine melting also affects the shape of the glacier front and, in particular, produces vertical runnels which by increasing the surface area of contact between the glacier and the ocean likely enhances the impact of submarine melting (Figures 7.4 and 7.5).

Strong melting is commonly hypothesised to be driven by the discharge at depth of supraglacial runoff, on the order of $200-500\,\mathrm{m^3\,s^{-1}}$ during the melt season (i.e. June-August – Kimura and others, 2014; Rignot and others, 2010; Sole and others, 2012; Xu and others, 2013, 2012). In consequence, submarine melting is usually supposed to be negligible (i.e. $<0.4\,\mathrm{m\,d^{-1}}$ – Sciascia and others, 2013; Xu and others, 2013, 2012) during the rest of the year (Sciascia and others, 2013; Sole and others, 2012; Xu and others, 2013). However, we have shown from the first-ever winter observations of the submarine melt in Greenland (Chapter 4)

that a significant and sustained submarine melt rate of $1.9 \pm 0.5\,\mathrm{m\,d^{-1}}$ (55% of the summer submarine melt) occurs throughout the winter (Figure 4.6). This winter-time melting is driven by the limited, yet continuous, discharge of subglacial fresh water originating from basal melting of the glacier (Christoffersen and others, 2012).

Modelling experiments suggest a square or cubit-root relation between the discharge of subglacial runoff and submarine melt rate (Sciascia and others, 2013; Xu and others, 2013, 2012). Therefore, glacier acceleration, should increase basal melting (Bougamont and others, 2011), and thus results in a higher submarine melting (particularly during winter months) than an increase of the already strong supraglacial-melting of the glacier.

In Chapters 4 and 8, we estimate that the present annual submarine melt at Store Glacier account for $\sim 1.5\,\mathrm{Gt\,yr^{-1}}$ or 14% of the total glacier front discharge. This amount is comparable to summer surface ablation.

9.2.3 Impact of the upwelling plume on the glacier front

Glacier upwelling-plumes forced, on a vertical ice front, by the discharge of subglacial fresh water at depth has been modelled (Jenkins, 1991, 2011; Kimura and others, 2014; Mugford and Dowdeswell, 2011; O'Leary, 2011; Sciascia and others, 2013; Sole and others, 2012; Xu and others, 2013, 2012). However, the lack of direct measurements from within and around active plumes precluded vigorous test of the numerical models. In Chapters 5 and 6, we observed the circulation and characteristics of water within two plumes (Figures 6.3 and 6.4). As predicted by the numerical models, some plumes do not reach the surface and outflow directly

at depth, while others reach the surface before sinking back to their hydrostatic equilibrium depth (Figure 6.4, Sciascia and others, 2013; Xu and others, 2013, 2012).

The upwelling plume is the ocean-glacier process captivating most of the interest as its presence generates a buoyancy driven convective circulation near the glacier front, entraining the warm Atlantic water in contact with the ice and producing an enhanced submarine melt rate. In Chapter 6, we showed that for the two plume, observed at Store, the fresh water (both subglacial and submarine meltwater) dilution into the ambient water is of ∼16.5‰ and ∼ 5.5‰, for the surface plume and the deep plume, respectively. These results are in good agreement with the numerically modelled plume at Store where the dilution is estimated to ∼20‰ and ∼8‰ for a surface and bottom plume, respectively (figures 2-a and 2-b of Xu and others, 2013). Furthermore we estimated the submarine melt induced by the plume to $\sim 100\,m^3\,s^{-1}$ and $\sim 20\,m^3\,s^{-1}$ for a runoff discharge of $\sim 95\,m^3\,s^{-1}$ and $\sim 35\,m^3\,s^{-1}$ for the surface and the deep plume, respectively. Both of these upwelling plumes appear on the glacier front section area where $200-800\,m$ large caves are visible on the glacier (Chapter 8).

Due to the narrowness of the glaciated fjords compared to their length, the lateral circulation induced by the upwelling plume is generally considered negligible (Sciascia and others, 2013; Sole and others, 2012; Xu and others, 2012) or only acting on a limited distance (Kimura and others, 2014; Xu and others, 2013). Although the assumption of a predominantly along-fjord circulation is probably valid away from the glacier front, in Chapter 5 the observation of a lateral circulation on the whole glacier front of 5-10 $cm\,s^{-1}$ and correlated to the plume activity (Figures 5.3

and 5.7), highlights the need for modelling the entire glacier width in order to correctly evaluate the impact of the plume on the terminus.

During the periods of low plume activity the lateral circulation is affected by unidentified external factors which could potentially be the intermediary circulation driven by wind events on the continental shelf (Sciascia and others, 2014; Straneo and others, 2010; Sutherland, 2012).

9.3 Direction for future research

The attention that marine-terminating glaciers receives from the scientific community has rapidly increased over the past decade in response to the need for further understanding of the contribution of marine outlet glaciers to Greenland Ice Sheet dynamics and sea level rise. Despite this interest, the very limited number of field observations, largely due to the logistical and safety challenges which are associated to any field campaign in Greenland, have limited the ability to answer many key questions. Thus, we anticipate that more research will be undertaken over the coming years and in particular to evaluate the dynamic response of the front of a marine-terminating glacier in a warming climate.

Future studies should be directed at understanding the relationship between glacier acceleration and submarine melt rate and any potential feedback which might exist. Chapter 4 addressed this issue, although more observation is necessary. Time-series observations of submarine melt rate and evaluation of the basal meltwater runoff would help quantify the interaction.

The partitioning of the ice loss between the processes acting at the glacier front is essential if we are to estimate which process(es) will be more sensitive to variation, in particular, the impact of submarine melting and plume activity on the calving behaviour. Such partitioning can be achieved by estimating the calving rate during periods of intense or low plume/submarine melt activity to then deduce the impact of these processes on the calving rate (Chapter 4). Another approach would be to use a 3D interface model of the ocean-glacier area with an actively evolving ice front (advance, calving, submarine melting), which would allow for sensitivity tests of each of process (i.e. upwelling plume, iceberg calving, submarine melting) to the dynamics of the ice front and thus potentially to the glacier as a whole.

It would also be valuable to continue to evaluate the pattern of the submarine melt impacts as started in Chapter 8. Using underwater sensors with longer range could allow for scanning the glacier front even when brash-ice precludes easy access to the terminus. Another solution will be to equip a submarine-based platform to perform the scanning of the glacier front by navigating a few meters below the surface of the fjord, hence avoiding most of the brash-ice. Such solution could also be applicable during winter months when the fjord is frozen. An important challenge will be to accurately position the submarine-platform during the survey.

The used of recently calved and capsized icebergs to yield information regarding the submerged part of the glacier front is also an interesting path to explore (Chapter 7). The possibility to observe the texture of the reconstructed iceberg using the structure-from-motion method is a valuable advantage to observe small to large scale impact of submarine melting. The high cost associated with the use of a helicopter to survey an iceberg as in Chapter 7 could easily be mitigated by the

use of an unmanned aerial vehicle (UAV), which would offer even more flexibility than the helicopter.

Is it also critical to evaluate at the scale of Greenland the submarine melt rate which is sustained by the marine-terminating glaciers and the controls that govern it (e.g. depth of the glacier, presence of the Atlantic warm water, activity of the plume). This work was started by Enderlin and Howat (2013) for floating termini. However, because their method is not applicable for the submarine melting occurring on vertical ice fronts (most Greenland glaciers) further development will be necessary. The use of the Gade and Motyka models (Chapter 4) combined with oceanographic measurements from around Greenland could be a way to access this information on a large scale.

The main limitation of Gade and Motyka models, i.e. the necessity to evaluate the average fjord circulation, can be assessed using current profilers installed on moorings (Jackson and Sutherland, 2014). However, the presence of deep icebergs drifting in the fjord are a hazard to expensive equipment (Sutherland, 2012). An alternative approach would be to use time-lapse cameras overlooking the fjord and tracking icebergs of different size. Due to the difference in the draft of the bigger and the smaller icebergs it should be possible using a range of iceberg sizes to evaluate fjord currents for individual layers.

Another option to estimate the submarine melt rate is to repetitively evaluate the iceberg discharge through a section near the glacier front. Combined with an accurate glacier discharge at the glacier front (Joughin and Smith, 2013; Moon and others, 2012; Ryan and others, 2014), it should be possible to produce a time-series of the calving discharge and deduce the mean submarine melt sustained by the glacier. An advantage of this approach is that it could potentially be based on

satellite imagery as for Enderlin and Hamilton (2014); Enderlin and Howat (2013) but also on relatively straightforward-to-acquire stereo photography time-lapse cameras or UAV surveys (Ryan and others, 2014).

As discussed by Straneo and Cenedese (2013) the presence of sills and the impact of the intermediary circulation on the characteristics of the water in contact with a glacier front can have a significant impact on the ocean-glacier interaction. It is thus imperative to improve the number of oceanographic surveys (bathymetry and hydrography) from around Greenland, starting with the north-west and south-east coasts where most glacier accelerations were observed over the last decade (Joughin and others, 2010; Moon and others, 2012).

Field based observation as in Chapter 6 should be undertaken to confirm and validate model results concerning the upwelling plume structure and dynamic. In particular, evaluation of the subglacial outlet distribution, geometry and discharge is fundamental because it appears to largely contribute to plume dynamics and induced submarine melt rate (Kimura and others, 2014; Xu and others, 2013). Such observation could be performed using a combination of the technology applied in Chapter 8 to detect the subglacial outlet geometry associated to a acoustic current profiler as in Chapter 6 to determine jet velocity. Moreover measurement of the plume-water characteristics and the associated current from within the core of the plume will help understand the entrainment parameters and internal dynamics. The use of a remote controlled or autonomous platform to conduct the measurements is necessary due to the high risk associated with approaching the ice front. Multiple tracers in addition to the temperature and salinity such as the dissolved oxygen or nutrient concentration could also contribute to help partitioning the

different mixing occurring inside the plume and to quantify the submarine melt occuring in the core of the plume.

Further evaluation of the plumes impact on the full width of the glacier front is necessary. Chapter 5 revealed that plume activity was inducing an horizontal circulation on the whole glacier front. Yet, the submarine melt impact induced by the plume on the glacier front external to the plume, has not been evaluated. More systematic quantification of the plume activity is necessary, especially the horizontal circulation induced by the plume, the impact of the plume position/activity on the front geometry and calving rate. As discussed in Chapter 5, the use of high frequency time-lapse imagery and associated tracking of icebergs could provide such quantitative information.

Chapter 10

General conclusions

A cutting-edge method to measure directly the submarine melt rate of a vertical ice-front, was developed using repeated 3D scanning of the submerged part of a tidewater glacier front. This method successfully provided the first direct measurement of the submarine melt rate over 2 km of the glacier front at high spatial resolution (i.e. 20×20 m). The resulting dataset was used to estimate an average submarine melt rate of $3.4\pm0.7\,\mathrm{m\,d^{-1}}$ at Store Glacier during the summer 2012 with a vertical pattern having a maximum of $3-4\,\mathrm{m\,d^{-1}}$ between 100 – 400 m depth reducing to almost no-melt toward both the surface and the bottom of the fjord.

The collection of oceanographic measurements during the winter 2012–2013 applied to refined versions of the Gade and Motyka models permitted the first evaluation from observation of the winter submarine melt rate for a vertical ice-front glacier in Greenland. An intense submarine melt rate of $1.9\pm0.5\,\mathrm{m\,d^{-1}}$ was observed throughout the winter. The winter submarine melt rate is 3 – 5 times larger

than numerical predictions and corresponds to 55% of the summer submarine melt. This ground-breaking result invalidates the common assumption that submarine melt can be neglected during non-summer months. Such significant submarine melt is fuelled by the presence throughout the year of a 2.8°C Atlantic water at the base of the glacier front and driven by the limited, but continuous, subglacial runoff of basal melt water, which is itself a function of ice velocity. The recent acceleration of the Greenland Ice Sheet would thus have resulted in both an increased discharge at the ice front and an increased submarine melt, particularly during winter months.

The evaluation of the submarine melt rate during both summer and winter months allowed us to determine the contribution of this process as 14% of the annual ice discharge at the glacier front. During July 2012 the submarine melt contributed to ∼25% of the front ablation. The partitioning of the different forcings on the annual submarine melt stressed the significant importance of the basal runoff which account for ∼60% of this melt, while the surface runoff contributed to 25% and the free-forced submarine melting accounted for the remaining 15%.

Comparison of the ocean-glacier interaction pattern at two major outlet glaciers of Uummannaq Bay (Rink and Store) during two contrasting melt-seasons (2009 and 2010), yielded similarities and differences, particularly over the upper 200 m of the water column, which are thought to be driven by the discharge of subglacial runoff.

A novel method to evaluate fjord circulation and upwelling-plume activity at the glacier front with a high spatial (<20 m) and temporal (4 min) resolution was developed using a time-lapse camera overlooking the ice front. The tracking of the icebergs between the frames revealed a significant lateral circulation along the

glacier front forced by the upwelling-plume as well as unidentified external forcing. The lateral circulation induced by the plume along the glacier front outside to the plume is neglected in common numerical simulations. However, with velocities on the order of $5-10\,\mathrm{cm\,s^{-1}}$ over the whole glacier front external to the plume, plume-induced circulation will have a significant submarine melt impact which might exceed the strong but spatially limited impact internal to the plume itself.

Vertical runnels with width varying form 0.5-10 m, and with a fractal like pattern, is expected to enhance the submarine melt impact by increasing the surface of contact between the glacier and the ocean.

Bibliography

Aagaard, Knut and Eddy Carmack, 1981. On the halocline of the Arctic Ocean, *Deep Sea Research Part A. Oceanographic Research Papers*, **28**(6), 529–545.

Ahlstrøm, Andreas P, S B Andersen, Morten L Andersen, H Machguth, Faezeh M Nick, Ian Joughin, C H Reijmer, R S W van de Wal, J P Merryman Boncori, Jason E Box, M Citterio, D van As, R S Fausto and Alun L Hubbard, 2013. Seasonal velocities of eight major marine-terminating outlet glaciers of the Greenland ice sheet from continuous in situ GPS instruments, *Earth System Science Data Discussions*, **6**(1), 27–57.

Ahn, Yushin and Jason E Box, 2010. Glacier velocities from time-lapse photos: technique development and first results from the Extreme Ice Survey (EIS) in Greenland, *Journal of Glaciology*, **56**(198), 723–734.

Amundson, Jason M, Mark Fahnestock, Martin Truffer, J Brown, M P Lüthi and Roman J Motyka, 2010. Ice mélange dynamics and implications for terminus stability, Jakobshavn Isbræ, Greenland, *Journal of Geophysical Research*, **115**(F1), F01005.

Andersen, Morten L, T B Larsen, M Nettles, P Elosegui, D van As, G S Hamilton, L A Stearns, J L Davis, Andreas P Ahlstrøm, J de Juan, G Ekström, L Stenseng, S A Khan, R Forsberg and Dorthe Dahl-Jensen, 2010. Spatial and temporal melt variability at Helheim Glacier, East Greenland, and its effect on ice dynamics, *Journal of Geophysical Research*, **115**(F4).

Arneborg, Lars and Bengt Liljebladh, 2001. The internal seiches in Gullmar Fjord. Part I: dynamics, *Journal of Physical Oceanography*, **31**(9), 2549–2566.

van As, D, Alun L Hubbard, Bent Hasholt, A B Mikkelsen, Michiel van den Broeke and R S Fausto, 2012. Large surface meltwater discharge from the Kangerlussuaq sector of the Greenland ice sheet during the record-warm year 2010 explained by detailed energy balance observations, *The Cryosphere*, **6**(1), 199–209.

Azetsu-Scott, Kumiko, Brian Petrie, Philip Yeats and Craig Lee, 2012. Composition and fluxes of freshwater through Davis Strait using multiple chemical tracers, *Journal of Geophysical Research*, **117**(C12), C12011.

Bamber, Jonathan L, J A Griggs, Ruud Hurkmans, J A Dowdeswell, S P Gogineni, Ian M Howat, J Mouginot, J Paden, Eric Rignot and D Steinhage, 2013. A new bed elevation dataset for Greenland, *The Cryosphere*, **7**(2), 499–510.

Bartholomew, Ian, Peter Nienow, Andrew Sole, Douglas Mair, Thomas Cowton and Jemma Wadham, 2011. Supraglacial forcing of subglacial drainage in the ablation zone of the Greenland ice sheet, *Geophysical Research Letters*, **38**(8), L08502.

Beem, L H, Slawek M Tulaczyk, M A King, Marion Bougamont, H A Fricker and Poul Christoffersen, 2014. Variable deceleration of Whillans Ice Stream, West Antarctica, *Journal of Geophysical Research: Earth Surface*, **119**(2), 212–224.

Bendtsen, Jørgen, John Mortensen and Soren Rysgaard, 2014. Seasonal surface layer dynamics and sensitivity to runoff in a high Arctic fjord (Young Sound/Tyrolerfjord, 74 °N), *Journal of Geophysical Research: Oceans*, **119**(9), 6461–6478.

Benn, Douglas I, Charles R Warren and Ruth H Mottram, 2007. Calving processes and the dynamics of calving glaciers, *Earth-Science Reviews*, **82**(3-4), 143–179.

Bigg, Grant R, Martin R Wadley, David P Stevens and John A Johnson, 1997. Modelling the dynamics and thermodynamics of icebergs, *Cold Regions Science and Technology*, **26**(2), 113–135.

Bindschadler, Robert A, Sophie Nowicki, Ayako Abe-Ouchi, Andy Aschwanden, Hyeungu Choi, Jim Fastook, Glen Granzow, Ralf Greve, Gail Gutowski, Ute Herzfeld, Charles Jackson, Jesse Johnson, Constantine Khroulev, Anders Levermann, William H Lipscomb, Maria A Martin, Mathieu Morlighem, Byron R

Parizek, David Pollard, Stephen F Price, Diandong Ren, Fuyuki Saito, Tatsuru Sato, Hakime Seddik, Helene Seroussi, Kunio Takahashi, Ryan Walker and Wei Li Wang, 2013. Ice-sheet model sensitivities to environmental forcing and their use in projecting future sea level (the SeaRISE project), *Journal of Glaciology*, **59**(214), 195–224.

Bougamont, Marion, S Price, Poul Christoffersen and Antony J Payne, 2011. Dynamic patterns of ice stream flow in a 3-D higher-order ice sheet model with plastic bed and simplified hydrology, *Journal of Geophysical Research*, **116**(F4), F04018.

Box, Jason E, 2013. Greenland Ice Sheet Mass Balance Reconstruction. Part II: Surface Mass Balance (1840–2010), *Journal of Climate*, **26**(18), 6974–6989.

Box, Jason E, JC Stroeve, DK Hall and Konrad Steffen, 2012. Greenland ice sheet albedo feedback: thermodynamics and atmospheric drivers, *The Cryosphere*, **6**(4), 821–839.

van den Broeke, Michiel, J Bamber, J Ettema, Eric Rignot, E Schrama, Willem Jan van de Berg, E van Meijgaard, I Velicogna and B Wouters, 2009. Partitioning Recent Greenland Mass Loss, *Science*, **326**(5955), 984–986.

Chandler, Dave M, J L Wadham, G P Lis, Thomas Cowton, A Sole, Ian Bartholomew, J Telling, Peter Nienow, E B Bagshaw, Douglas Mair, S Vinen and Alun L Hubbard, 2013. Evolution of the subglacial drainage system beneath the Greenland Ice Sheet revealed by tracers, *Nature Geoscience*, **6**(3), 195–198.

Chauché, Nolwenn, Alun L Hubbard, J C Gascard, Jason E Box, R Bates, M Koppes, A Sole, Poul Christoffersen and H Patton, 2014. Ice–ocean interaction and calving front morphology at two west Greenland tidewater outlet glaciers, *The Cryosphere*, **8**(4), 1457–1468.

Christoffersen, Poul, Marion Bougamont, Sasha P Carter, Helen A Fricker and Slawek M Tulaczyk, 2014. Significant groundwater contribution to Antarctic ice streams hydrologic budget, *Geophysical Research Letters*, **41**(6), 2003–2010.

Christoffersen, Poul, Martin O'Leary, Jan H Van Angelen and Michiel van den Broeke, 2012. Partitioning effects from ocean and atmosphere on the calving

stability of Kangerdlugssuaq Glacier, East Greenland, *Annals of Glaciology*, **53**(60), 249–256.

Chu, Vena W, Laurence C Smith, Asa K Rennermalm, Richard R Forster, Jason E Box and Niels Reehy, 2009. Sediment plume response to surface melting and supraglacial lake drainages on the Greenland ice sheet, *Journal of Glaciology*, **55**(194), 1072–1082.

Cowton, Thomas, Peter Nienow, Andrew Sole, Jemma Wadham, G P Lis, Ian Bartholomew, Douglas Mair and Dave M Chandler, 2013. Evolution of drainage system morphology at a land-terminating Greenlandic outlet glacier, *Journal of Geophysical Research: Earth Surface*, **118**(1), 29–41.

Dowdeswell, J A, K.A. Hogan, C. Ó Cofaigh, E.M.G. Fugelli, J. Evans and R. Noormets, 2014. Late Quaternary ice flow in a West Greenland fjord and cross-shelf trough system: submarine landforms from Rink Isbrae to Uummannaq shelf and slope, *Quaternary Science Reviews*, **92**, 292–309.

Dutrieux, Pierre, Craig Stewart, Adrian Jenkins, Keith W Nicholls, H F J Corr, Eric Rignot and Konrad Steffen, 2014. Basal terraces on melting ice shelves, *Geophysical Research Letters*, **41**(15), 5506–5513.

Enderlin, E M and G S Hamilton, 2014. Estimates of iceberg submarine melting from high-resolution digital elevation models: application to Sermilik Fjord, East Greenland, *Journal of Glaciology*, **60**(224), 1084–1092.

Enderlin, Ellyn M and Ian M Howat, 2013. Submarine melt rate estimates for floating termini of Greenland outlet glaciers (2000–2010), *Journal of Glaciology*, **59**(213), 67–75.

Fofonoff, Nick P and Robert C Millard, 1983. Algorithms for computation of fundamental properties of seawater, *Unesco technical papers in marine science*, **44**.

Gade, Herman G, 1979. Melting of ice in sea water: A primitive model with application to the Antarctic ice shelf and icebergs, *Journal of Physical Oceanography*, **9**(1), 189–198.

Gade, Herman G, 1993. When ice melts in sea water: A review, *Atmosphere-Ocean*, **31**(1), 139–165.

Garcia, Damien, 2010. Robust smoothing of gridded data in one and higher dimensions with missing values, *Computational Statistics and Data Analysis*, **54**(4), 1167–1178.

Greisman, Paul, 1979. On upwelling driven by the melt of ice shelves and tidewater glaciers, *Deep Sea Research Part A. Oceanographic Research Papers*, **26**(9), 1051–1065.

Hanna, Edward, Philippe Huybrechts, Konrad Steffen, John Cappelen, Russell Huff, Christopher Shuman, Tristram Irvine-Fynn, Stephen Wise and Michael Griffiths, 2008. Increased runoff from melt from the Greenland Ice Sheet: a response to global warming, *Journal of Climate*, **21**(2), 331–341.

Hock, Regine, 2005. Glacier melt: a review of processes and their modelling, *Progress in Physical Geography*, **29**(3), 362–391.

Holland, David M and Adrian Jenkins, 1999. Modeling thermodynamic ice-ocean interactions at the base of an ice shelf, *Journal of Physical Oceanography*, **29**(8), 1787–1800.

Holland, David M, Robert H Thomas, Brad de Young, Mads H Ribergaard and Bjarne Lyberth, 2008. Acceleration of Jakobshavn Isbrae triggered by warm subsurface ocean waters, *Nature Geoscience*, **1**(10), 659–664.

Hopkins, Tom Sawyer, 1991. The GIN Sea—A synthesis of its physical oceanography and literature review 1972–1985, *Earth-Science Reviews*, **30**(3), 175–318.

Horne, Edward P W, 1985. Ice-induced vertical circulation in an Arctic fiord, *Journal of Geophysical Research: Oceans (1978–2012)*, **90**(C1), 1078–1086.

Howat, Ian M, A Negrete and Ben E Smith, 2014. The Greenland Ice Mapping Project (GIMP) land classification and surface elevation data sets, *The Cryosphere*, **8**(4), 1509–1518.

Hubbard, Alun L, 2011. The Times Atlas and actual Greenland ice loss, *Geology Today*, **27**(6), 212–215.

Hudson, B, I Overeem, D McGrath, J P M Syvitski, A Mikkelsen and Bent Hasholt, 2014. MODIS observed increase in duration and spatial extent of sediment plumes in Greenland fjords, *The Cryosphere*, **8**(4), 1161–1176.

Huppert, Herbert E and Edward G Josberger, 1980. The melting of ice in cold stratified water, *J. Phys. Oceanogr*, **10**(6), 953–960.

Huppert, Herbert E and J Stewart Turner, 1980. Ice blocks melting into a salinity gradient, *Journal of Fluid Mechanics*, **100**(02), 367–384.

Jackson, Rebecca H and David A Sutherland, 2014. Externally forced fluctuations in ocean temperature at Greenland glaciers in non-summer months, *Nature Geoscience*, **7**(7), 503–508.

Jakobsson, Martin, Larry Mayer, Bernard Coakley, Julian A Dowdeswell, Steve Forbes, Boris Fridman, Hanne Hodnesdal, Riko Noormets, Richard Pedersen, Michele Rebesco, Hans Werner Schenke, Yulia Zarayskaya, Daniela Accettella, Andrew Armstrong, Robert M Anderson, Paul Bienhoff, Angelo Camerlenghi, Ian Church, Margo Edwards, James V Gardner, John K Hall, Benjamin Hell, Ole Hestvik, Yngve Kristoffersen, Christian Marcussen, Rezwan Mohammad, David Mosher, Son V Nghiem, Maria Teresa Pedrosa, Paola G Travaglini and Pauline Weatherall, 2012. The International Bathymetric Chart of the Arctic Ocean (IBCAO) Version 3.0, *Geophysical Research Letters*, **39**(12), L12609.

Jenkins, Adrian, 1991. A one-dimensional model of ice shelf-ocean interaction, *Journal of Geophysical Research*, **96**(C11), 20671–20,677.

Jenkins, Adrian, 1999. The impact of melting ice on ocean waters, *Journal of Physical Oceanography*, **29**(9), 2370–2381.

Jenkins, Adrian, 2011. Convection-Driven Melting near the Grounding Lines of Ice Shelves and Tidewater Glaciers, *Journal of Physical Oceanography*, **41**(12), 2279–2294.

Jenkins, Adrian, Pierre Dutrieux, Stanley S. Jacobs, Stephen D McPhail, James R Perrett, Andrew T Webb and David White, 2010. Observations beneath Pine Island Glacier in West Antarctica and implications for its retreat, *Nature Geoscience*, **3**(7), 468–472.

Johnson, Helen L and A Munchow, 2011. Ocean circulation and properties in Petermann Fjord, Greenland, *Journal of Geophysical Research: Oceans (1978–2012)*, **116**(C1), C01003.

Josberger, Edward G and Seelye Martin, 1981. A laboratory and theoretical study of the boundary layer adjacent to a vertical melting ice wall in salt water., *Journal of Fluid Mechanics*, **111**, 439–473.

Joughin, Ian and Ben E Smith, 2013. Further summer speedup of Jakobshavn Isbræ, *The Cryosphere Discussions*, **7**(6), 5461–5473.

Joughin, Ian, Ben E Smith, Ian M Howat, Dana Floricioiu, Richard B Alley, Martin Truffer and Mark Fahnestock, 2012. Seasonal to decadal scale variations in the surface velocity of Jakobshavn Isbrae, Greenland: Observation and model-based analysis, *Journal of Geophysical Research*, **117**(F2), F02030.

Joughin, Ian, Ben E Smith, Ian M Howat, Ted Scambos and Twila Moon, 2010. Greenland flow variability from ice-sheet-wide velocity mapping, *Journal of Glaciology*, **56**(197), 415–430.

Kimura, Satoshi, Adam S Candy, Paul R Holland, Matthew D Piggott and Adrian Jenkins, 2013. Adaptation of an unstructured-mesh, finite-element ocean model to the simulation of ocean circulation beneath ice shelves, *Ocean Modelling*, **67**(C), 39–51.

Kimura, Satoshi, Paul R Holland, Adrian Jenkins and Matthew Piggott, 2014. The Effect of Meltwater Plumes on the Melting of a Vertical Glacier Face, *J. Phys. Oceanogr.*

Kjær, Kurt H., Shfaqat A Khan, Niels J Korsgaard, John Wahr, Jonathan L Bamber, Ruud Hurkmans, Michiel van den Broeke, Lars H Timm, Kristian K Kjeldsen and Anders A Bjørk, 2012. Aerial Photographs Reveal Late–20th-Century Dynamic Ice Loss in Northwestern Greenland, *Science*, **337**(6094), 569–573.

McFadden, Ellyn M, Ian M Howat, Ian Joughin, Ben E Smith and Yushin Ahn, 2011. Changes in the dynamics of marine terminating outlet glaciers in west Greenland (2000–2009), *Journal of Geophysical Research*, **116**(F2), F02022.

Moon, T, Ian Joughin, B Smith and Ian M Howat, 2012. 21st-Century Evolution of Greenland Outlet Glacier Velocities, *Science*, **336**(6081), 576–578.

Mortensen, John, Jørgen Bendtsen, Roman J Motyka, K Lennert, Martin Truffer, Mark Fahnestock and Soren Rysgaard, 2013. On the seasonal freshwater strati-

fication in the proximity of fast-flowing tidewater outlet glaciers in a sub-Arctic sill fjord, *Journal of Geophysical Research: Oceans*, **118**(3), 1382–1395.

Mortensen, John, K Lennert, Jørgen Bendtsen and Soren Rysgaard, 2011. Heat sources for glacial melt in a sub-Arctic fjord (Godthåbsfjord) in contact with the Greenland Ice Sheet, *Journal of Geophysical Research: Oceans (1978–2012)*, **116**(C1), C01013.

Motyka, Roman J, William P Dryer, Jason M Amundson, Martin Truffer and Mark Fahnestock, 2013. Rapid submarine melting driven by subglacial discharge, LeConte Glacier, Alaska, *Geophysical Research Letters*, **40**(19), 5153–5158.

Motyka, Roman J, Lewis Hunter, Keith A Echelmeyer and Cathy Connor, 2003. Submarine melting at the terminus of a temperate tidewater glacier, LeConte Glacier, Alaska, USA, *Annals of Glaciology*, **36**(1), 57–65.

Motyka, Roman J, Martin Truffer, Mark Fahnestock, John Mortensen, Soren Rysgaard and Ian M Howat, 2011. Submarine melting of the 1985 Jakobshavn Isbræ floating tongue and the triggering of the current retreat, *Journal of Geophysical Research*, **116**(F1), F01007.

Mugford, RI and J A Dowdeswell, 2011. Modeling glacial meltwater plume dynamics and sedimentation in high-latitude fjords, *Journal of Geophysical Research: Oceans (1978–2012)*, **116**(F1), F01023.

Myers, Paul G, Nilgun Kulan and Mads H Ribergaard, 2007. Irminger Water variability in the West Greenland Current, *Geophysical Research Letters*, **34**(17).

Nghiem, S V, D K Hall, T L Mote, M Tedesco, M R Albert, K Keegan, C A Shuman, N E DiGirolamo and G Neumann, 2012. The extreme melt across the Greenland ice sheet in 2012, *Geophysical Research Letters*, **39**(20), L20502.

Nicholls, K W, E P Abrahamsen, J J H Buck, P A Dodd, C Goldblatt, G Griffiths, K J Heywood, N E Hughes, A Kaletzky, G F Lane-Serff, S D McPhail, N W Millard, K I C Oliver, J Perrett, M R Price, C J Pudsey, K Saw, K Stansfield, M J Stott, P Wadhams, A T Webb and J P Wilkinson, 2006. Measurements beneath an Antarctic ice shelf using an autonomous underwater vehicle, *Geophysical Research Letters*, **33**(8), L08612.

Nick, Faezeh M, Alun L Hubbard, Kees Van der Veen and Andreas Vieli, 2010a. Role of ice-ocean interaction on glacier instability applied to Petermann galcier, *Geophyscal Research Abstracts*, **12**, 11533.

Nick, Faezeh M, Cornelis J Van der Veen, Andreas Vieli and Douglas I Benn, 2010b. A physically based calving model applied to marine outlet glaciers and implications for the glacier dynamics, *Journal of Glaciology*, **56**, 1–14.

Nick, Faezeh M, Andreas Vieli, Morten Langer Andersen, Ian Joughin, Antony Payne, Tamsin L. Edwards, Frank Pattyn and Roderik S. W. van de Wal, 2013. Future sea-level rise from Greenland/'s main outlet glaciers in a warming climate, *Nature*, **497**(7448), 235–238.

O'Leary, Martin, 2011. Frontal processes on tidewater glaciers, (PhD thesis), Cambridge.

O'Leary, Martin and Poul Christoffersen, 2013. Calving on tidewater glaciers amplified by submarine frontal melting, *The Cryosphere*, **7**(1), 119–128.

Padman, L and S Erofeeva, 2004. A barotropic inverse tidal model for the Arctic Ocean, *Geophysical Research Letters*, **31**(2).

Pfeffer, W. T., 2007. A simple mechanism for irreversible tidewater glacier retreat, *Journal of Geophysical Research: Oceans (1978–2012)*, **112**(F3), F03S25.

Powell, R D, 1990. Glacimarine processes at grounding-line fans and their growth to ice-contact deltas, *Geological Society, London, Special Publications*, **53**(1), 53–73.

Price, Stephen F, Antony J Payne, Ian M Howat and Ben E Smith, 2011. Committed sea-level rise for the next century from Greenland ice sheet dynamics during the past decade, *Proceedings of the National Academy of Sciences*, **108**(22), 8978–8983.

Pritchard, Hamish D, Robert J Arthern, David G Vaughan and Laura A Edwards, 2009. Extensive dynamic thinning on the margins of the Greenland and Antarctic ice sheets, *Nature*, **461**(7266), 971–975.

Rennermalm, A K, L C Smith, Vena W Chu, Jason E Box, R R Forster, Michiel van den Broeke, D van As and S E Moustafa, 2013. Evidence of meltwater retention within the Greenland ice sheet, *The Cryosphere*, **7**(5), 1433–1445.

Ribergaard, Mads Hvid, 2009. Oceanographic Investigations off West Greenland, *Danish Metrological Institute (DMI) Centre for Ocean and Ice*.

Rignot, Eric, 1996. Tidal motion, ice velocity and melt rate of Petermann Gletscher, Greenland, measured from radar interferometry, *Journal of Glaciology*, **42**(142), 476–485.

Rignot, Eric, 2006. Changes in the Velocity Structure of the Greenland Ice Sheet, *Science*, **311**(5763), 986–990.

Rignot, Eric, Michele Koppes and Isabella Velicogna, 2010. Rapid submarine melting of the calving faces of West Greenland glaciers, *Nature Geoscience*, **3**(3), 187–191.

Rignot, Eric and J Mouginot, 2012. Ice flow in Greenland for the International Polar Year 2008-2009, *Geophysical Research Letters*, **39**(11), L11501.

Rignot, Eric and Konrad Steffen, 2008. Channelized bottom melting and stability of floating ice shelves, *Geophysical Research Letters*, **35**(2), L02503.

Ryan, J C, Alun L Hubbard, J Todd, J R Carr, Jason E Box, Poul Christoffersen, T O Holt and N Snooke, 2014. Repeat UAV photogrammetry to assess calving front dynamics at a large outlet glacier draining the Greenland Ice Sheet, *The Cryosphere Discussions*, **8**(2), 2243–2275.

Salcedo-Castro, Julio, Daniel Bourgault and Brad deYoung, 2011. Circulation induced by subglacial discharge in glacial fjords: Results from idealized numerical simulations, *Continental Shelf Research*, **31**(13), 1396–1406.

Schild, Kristin M, 2013. Seasonal variations of outlet glacier terminus position in Greenland, *Journal of Glaciology*, **59**(216), 759–770.

Schoof, Christian, 2010. Ice-sheet acceleration driven by melt supply variability, *Nature*, **468**(7325), 803–806.

Sciascia, Roberta, Claudia Cenedese and Patrick Heimbach, 2013. Seasonal variability of submarine melt rate and circulation in an East Greenland fjord, *Journal of Geophysical Research: Oceans*, **118**(5), 2492–2506.

Sciascia, Roberta, Claudia Cenedese and D Nicolì, 2014. Impact of periodic intermediary flows on submarine melting of a Greenland glacier, *Journal of Geophysical Research: Oceans*, **119**.

Shepherd, A, E R Ivins, G A, V R Barletta, M J Bentley, S Bettadpur, K H Briggs, D H Bromwich, R Forsberg, N Galin, M Horwath, S Jacobs, Ian Joughin, M A King, J T M Lenaerts, J Li, S R M Ligtenberg, A Luckman, S B Luthcke, M McMillan, R Meister, G Milne, J Mouginot, A Muir, J P Nicolas, J Paden, Antony J Payne, H Pritchard, Eric Rignot, H Rott, L S Sorensen, T A Scambos, B Scheuchl, E J O Schrama, B Smith, A V Sundal, J H van Angelen, Willem Jan van de Berg, Michiel van den Broeke, D G Vaughan, I Velicogna, J Wahr, P L Whitehouse, D J Wingham, D Yi, D Young and H J Zwally, 2012. A Reconciled Estimate of Ice-Sheet Mass Balance, *Science*, **338**(6111), 1183–1189.

Sole, Andrew, Antony J Payne, Peter Nienow, Poul Christoffersen, Finlo R Cottier and M E Inall, 2012. Increased glacier runoff enhances the penetration of warm Atlantic water into a large Greenland fjord, *The Cryosphere Discussions*, **6**(6), 4861–4896.

Stearns, Leigh A and Gordon S Hamilton, 2007. Rapid volume loss from two East Greenland outlet glaciers quantified using repeat stereo satellite imagery, *Geophysical Research Letters*, **34**(5), L05503.

Steffen, Konrad, Jason E Box and Waleed Abdalati, 1996. Greenland climate network: GC-Net, *US Army Cold Regions Reattach and Engineering (CRREL), CRREL Special Report*, 98–103.

Stocker, Thomas F, Dahe Qin, Gian-Kasper Plattner, M Tignor, Simon K Allen, Judith Boschung, Alexander Nauels, Yu Xia, Vincent Bex and Pauline M Midgley, 2013. Climate change 2013: The physical science basis, *Intergovernmental Panel on Climate Change, Working Group I Contribution to the IPCC Fifth Assessment Report (AR5)(Cambridge Univ Press, New York)*.

Straneo, Fiammetta and Claudia Cenedese, 2013. The Dynamics of Greenland's Glacial Fjords and Their Role in Climate, *Annual Review of Marine Science*, **7**(2015), 7.1–7.25.

Straneo, Fiammetta, Ruth Curry, David A Sutherland, Gordon S Hamilton, Claudia Cenedese, Kjetil Våge and Leigh A Stearns, 2011. Impact of fjord dynamics and glacial runoff on the circulation near Helheim Glacier, *Nature Geoscience*, **4**(5), 322–327.

Straneo, Fiammetta, Gordon S Hamilton, David A Sutherland, Leigh A Stearns, Fraser J M Davidson, Mike O Hammill, Garry B Stenson and Aqqalu Rosing-Asvid, 2010. Rapid circulation of warm subtropical waters in a major glacial fjord in East Greenland, *Nature Geoscience*, **3**(3), 182–186.

Straneo, Fiammetta and Patrick Heimbach, 2013. North Atlantic warming and the retreat of Greenland's outlet glaciers, *Nature*, **504**(7478), 36–43.

Straneo, Fiammetta, Patrick Heimbach, Olga Sergienko, Gordon Hamilton, Ginny Catania, Stephen Griffies, Robert Hallberg, Adrian Jenkins, Ian Joughin, Roman Motyka, W Tad Pfeffer, Stephen F Price, Eric Rignot, Ted Scambos, Martin Truffer and Andreas Vieli, 2013. Challenges to Understanding the Dynamic Response of Greenland's Marine Terminating Glaciers to Oceanic and Atmospheric Forcing, *Bulletin of the American Meteorological Society*, **94**(8), 1131–1144.

Straneo, Fiammetta, David A Sutherland, David Holland, Carl Gladish, Gordon S Hamilton, Helen L Johnson, Eric Rignot, Yun Xu and Michele Koppes, 2012. Characteristics of ocean waters reaching Greenland's glaciers, *Annals of Glaciology*, **53**(60), 202–210.

Sutherland, David A, 2012. Estimating ocean heat transports and submarine melt rates in Sermilik Fjord, Greenland, using lowered acoustic Doppler current profiler (LADCP) velocity profiles, *Annals of Glaciology*, **53**(60), 50–58.

Sutherland, David A and Robert S Pickart, 2008. The East Greenland Coastal Current: Structure, variability, and forcing, *Progress in Oceanography*, **78**(1), 58–77.

Sutherland, David A, Garry B Stenson, Fraser J M Davidson, Mike O Hammill and Aqqalu Rosing-Asvid, 2013. Atlantic water variability on the SE Greenland continental shelf and its relationship to SST and bathymetry, *Journal of Geophysical Research: Oceans*, **118**(2), 847–855.

Syvitski, James PM, 1989. On the deposition of sediment within glacier-influenced fjords: oceanographic controls, *Marine Geology*, **85**(2), 301–329.

Tedesco, Marco, Xavier Fettweis, Michiel van den Broeke, R S W van de Wal, CJPP Smeets, Willem Jan van de Berg, MC Serreze and Jason E Box, 2011. The role of albedo and accumulation in the 2010 melting record in Greenland, *Environmental Research Letters*, **6**(1), 014005.

Tedesco, M, X Fettweis, T Mote, J Wahr, P M Alexander, Jason E Box and B Wouters, 2013. Evidence and analysis of 2012 Greenland records from spaceborne observations, a regional climate model and reanalysis data, *The Cryosphere*, **7**(2), 615–630.

Thomas, Robert H, 2004. Force-perturbation analysis of recent thinning and acceleration of Jakobshavn Isbrae, Greenland, *Journal of Glaciology*, **50**(168), 57–66.

Todd, J and Poul Christoffersen, 2014. Are seasonal calving dynamics forced by buttressing from ice mélange or undercutting by melting? Outcomes from full-Stokes simulations of Store Gletscher, West Greenland, *The Cryosphere Discussions*, **8**(4), 3525–3561.

van de Wal, R S W, W Boot, Michiel van den Broeke, C H Reijmer, J J A Donker and J Oerlemans, 2008. Large and rapid melt-induced velocity changes in the ablation zone of the Greenland ice sheet, *Science*, **321**(5885), 111–113.

van de Wal, R S W, W Boot, H Snellen, Michiel van den Broeke and J Oerlemans, 2012. Twenty-one years of mass balance observations along the K-transect, West Greenland, *ESSD*, **4**(1), 31–35.

Weidick, Anker and Ole Bennike, 2007. Quaternary glaciation history and glaciology of Jakobshavn Isbræ and the Disko Bugt region, West Greenland: a review, *Geol. Surv. Den. Green. Bull.*, **14**, 1–78.

Wessel, Pål and Walter HF Smith, 1996. A global, self-consistent, hierarchical, high-resolution shoreline database, *Journal of Geophysical Research: Oceans (1978–2012)*, **101**(B4), 8741–8743.

Xu, Yun, Eric Rignot, Ian Fenty, Dimitris Menemenlis and M. Mar Flexas, 2013. Subaqueous melting of Store Glacier, west Greenland from three-dimensional, high-resolution numerical modeling and ocean observations, *Geophysical Research Letters*, **40**(17), 4648–4653.

Xu, Yun, Eric Rignot and Dimitris Menemenlis, 2012. Numerical experiments on subaqueous melting of Greenland tidewater glaciers in response to ocean warming and enhanced subglacial discharge, *Annals of Glaciology*, **53**(60), 229–234.

Appendix A

Publication

The following article was published during the course of the study. It is based on chapter 3 and is included below.

Chauché, Nolwenn, Alun L Hubbard, J C Gascard, Jason E Box, R Bates, M Koppes, A Sole, Poul Christoffersen and H Patton, 2014. Ice–ocean interaction and calving front morphology at two west Greenland tidewater outlet glaciers, *The Cryosphere*, **8**(4), 1457–1468

The Cryosphere, 8, 1457–1468, 2014
www.the-cryosphere.net/8/1457/2014/
doi:10.5194/tc-8-1457-2014

The Cryosphere Open Access

Ice–ocean interaction and calving front morphology at two west Greenland tidewater outlet glaciers

N. Chauché[1], A. Hubbard[1], J.-C. Gascard[2], J. E. Box[3,4], R. Bates[5], M. Koppes[6], A. Sole[7], P. Christoffersen[8], and H. Patton[1]

[1]Department of Geography and Earth Science, Aberystwyth University, Aberystwyth, UK
[2]Laboratoroire d'Océanographie et du Climat, Expérimentation et approche Numérique, Université Pierre et Marie Curie, Paris, France
[3]Byrd Polar Research Center, The Ohio State University, Columbus, Ohio, USA
[4]Geological Survey of Denmark and Greenland, Copenhagen, Denmark
[5]School of Geography and Geosciences, St-Andrews University, St-Andrews, UK
[6]Department of Geography, University of British Columbia, Vancouver, Canada
[7]Department of Geography, University of Sheffield, Sheffield, UK
[8]Scott Polar Research Institute, University of Cambridge, Cambridge, UK

Correspondence to: N. Chauché (noc3@aber.ac.uk)

Received: 5 October 2013 – Published in The Cryosphere Discuss.: 20 November 2013
Revised: 24 May 2014 – Accepted: 12 June 2014 – Published: 8 August 2014

Abstract. Warm, subtropical-originating Atlantic water (AW) has been identified as a primary driver of mass loss across the marine sectors of the Greenland Ice Sheet (GrIS), yet the specific processes by which this water mass interacts with and erodes the calving front of tidewater glaciers is frequently modelled and much speculated upon but remains largely unobserved. We present a suite of fjord salinity, temperature, turbidity versus depth casts along with glacial runoff estimation from Rink and Store glaciers, two major marine outlets draining the western sector of the GrIS during 2009 and 2010. We characterise the main water bodies present and interpret their interaction with their respective calving fronts. We identify two distinct processes of ice–ocean interaction which have distinct spatial and temporal footprints: (1) homogenous free convective melting which occurs across the calving front where AW is in direct contact with the ice mass, and (2) localised upwelling-driven melt by turbulent subglacial runoff mixing with fjord water which occurs at distinct injection points across the calving front. Throughout the study, AW at $2.8 \pm 0.2\,^{\circ}C$ was consistently observed in contact with both glaciers below 450 m depth, yielding homogenous, free convective submarine melting up to ~ 200 m depth. Above this bottom layer, multiple interactions are identified, primarily controlled by the rate of subglacial fresh-water discharge which results in localised and discrete upwelling plumes. In the record melt year of 2010, the Store Glacier calving face was dominated by these runoff-driven plumes which led to a highly crenulated frontal geometry characterised by large embayments at the subglacial portals separated by headlands which are dominated by calving. Rink Glacier, which is significantly deeper than Store has a larger proportion of its submerged calving face exposed to AW, which results in a uniform, relatively flat overall frontal geometry.

1 Introduction and background

The west Greenland current advects deep (> 400 m), warm (> 3 °C) and saline (> 34.8 PSU – practical salinity units) Atlantic water around the south coast of Greenland, transferring large fluxes of thermal energy of a subtropical origin into this sensitive polar environment (Christoffersen et al., 2012; Holland et al., 2008; Kjær et al., 2012; Mortensen et al., 2011; Ribergaard, 2007; Sutherland et al., 2013). The frontal dynamics of tidewater outlet glaciers draining the Greenland Ice Sheet (GrIS) can be profoundly influenced by Atlantic water (AW), which has the potential to directly access their

calving fronts via over-deepened glacial troughs cut through the continental shelf, thereby controlling their energy and mass balance (Hanna et al., 2014; Pfeffer, 2007; Rignot et al., 2010). For example, in west Greenland the sustained attrition of Jakobshavn Isbræ, observed since 1998 (Joughin et al., 2012), has been attributed to warming of subsurface water in Disko Bay and adjacent coastal seas (Holland et al., 2008). Similarly, AW was identified circulating within Sermilik and Kangerdlugssuaq fjords in east Greenland and is implicated in the retreat of Helheim and Kangerdlugssuaq glaciers over the last decade (Straneo et al., 2010, 2011). In NW Greenland, two distinct phases of dynamic ice loss (1985–1990 and 2005–2010) across the Melville Coast have been attributed to oceanic rather than atmospheric forcing (Kjær et al., 2012). An implicit assumption in these studies is that warm AW comes into direct contact with the marine termini of large tidewater outlet glaciers draining the ice sheet (Holland et al., 2008; Kjær et al., 2012; Motyka et al., 2011; Rignot et al., 2010; Straneo et al., 2012). Yet to date few observational studies have been focused on the actual ice–ocean interface, in particular on the specific controls governing submarine melt rates and the concomitant mass and energy exchanges which determine outlet glacier and fjord dynamics alike (Hubbard, 2011).

To date, several processes of interaction between fjord water and tidewater calving fronts have been observed, modelled and/or speculated upon including forced convection caused by buoyant subglacial fresh water (SgFW) discharged at depth and entraining AW as it rises (Jenkins, 2011; Mugford and Dowdeswell, 2011; Salcedo-Castro et al., 2011; Sciascia et al., 2013; Sole et al., 2012; Xu et al., 2012, 2013) as well as wind stress and tide-driven fjord circulation (Mortensen et al., 2011; Sole et al., 2012; Straneo et al., 2010; Sutherland and Straneo, 2012). Furthermore, it is emerging that circulation in Greenland's deep fjords is more complex than the single convective cell (estuarine-like) circulation model that has been assumed previously in energy-mass balance calculations (Motyka et al., 2003; Rignot et al., 2010). For instance, a vertical superposition of convective cells was observed (Straneo et al., 2011; Sutherland and Straneo, 2012) and more recently modelled (Sciascia et al., 2013; Sole et al., 2012) within fjords in east Greenland.

In this study we observe and document the interaction between fjord waters and the calving front at two major outlets – Rink and Store – that drain the western GrIS over two successive, but contrasting, melt years in August 2009 and 2010. The processes of AW-driven submarine melting and subglacial fresh-water-driven upwelling plumes are observed in both fjords. Differences and similarities in the spatial and temporal patterns of these processes are identified and highlighted, demonstrating significant impact and control of subglacial fresh-water runoff and discharge on calving front dynamics and geometry.

2 Field site

Uummannaq Bay is unique on the west coast of Greenland insofar as it has an over-deepened glacial trough to at least ~ 450 m depth, which extends uninterrupted to the continental shelf break (Jakobsson et al., 2012). It thereby provides a direct route for AW from Baffin Bay to enter its inner fjord basins and access over a dozen marine-terminating outlet glaciers which drain this sector of the GrIS (Fig. 1). The existence of two large marine-terminating outlet glaciers, Rink and Store, which drain this sector into Uummannaq Bay, make it a useful target to isolate and compare individual tidewater glacier responses to similar atmospheric and oceanic forcing but with contrasting bed, fjord and frontal geometries and geological controls. Rink and Store glaciers are the second and third largest outlets in west Greenland after Jakobshavn Isbræ, with an estimated discharge of 11–17 $\mathrm{km^3\,year^{-1}}$ and 14–18 $\mathrm{km^3\,year^{-1}}$ respectively (Weidick and Bennike, 2007). This corresponds to 7 and 8 % of the total annual discharge for the western GrIS (Rignot et al., 2008). A recent aerial study of Store Glacier's terminus calculates the mass flux through the calving front of Store Glacier to be 11.5 $\mathrm{km^3\,year^{-1}}$ (Ryan et al., 2014). Both glaciers and fjords are over 5 km wide and at least 100 km long with catchment sizes of 45 000 $\mathrm{km^2}$ for Rink and 34 000 $\mathrm{km^2}$ for Store (Rignot et al., 2008). Despite this, Store has a larger ablation area due to its lower-lying hypsometric profile. Bathymetric mapping reveals that both fjords have an inner basin deeper than 1000 m and that the maximum depth of the calving front of Rink Glacier is ~ 750 m, and at Store Glacier it is ~ 500 m. At Rink Fjord a transverse sill is located 50 km from the ice front with a minimum depth of ~ 400 m (Dowdeswell et al., 2014) whist Store Fjord has no such sill or obstruction to the outer trough (Fig. 1).

3 Methods

3.1 Data collection

Two hydrographic surveys were conducted in August 2009 and 2010 comprising of 5 and 7 conductivity, temperature, turbidity and depth (hereafter called CTD) casts at Rink Fjord and 12 and 11 casts at Store Fjord respectively. The CTD casts were taken along and across each fjord, at a distance of between 200 m and 20 km from their respective calving fronts (Figs. 1 and 2) and to a maximum depth of 750 m. The hydrographic instrument used was a MIDAS Valeport 2000 conductivity–temperature–depth profiler, equipped with a Seapoint turbidity sensor (Table 1). Measurements were logged at a sampling rate of 4 Hz with a descent rate of 1–2 $\mathrm{m\,s^{-1}}$, yielding 10 to 20 samples for every 5 m of vertical profile. The instrument also logged on recovery, which at a slower ascent rate of 0.3–0.5 $\mathrm{m\,s^{-1}}$ provided ~ 40 samples per 5 m vertical interval. Data were filtered by remov-

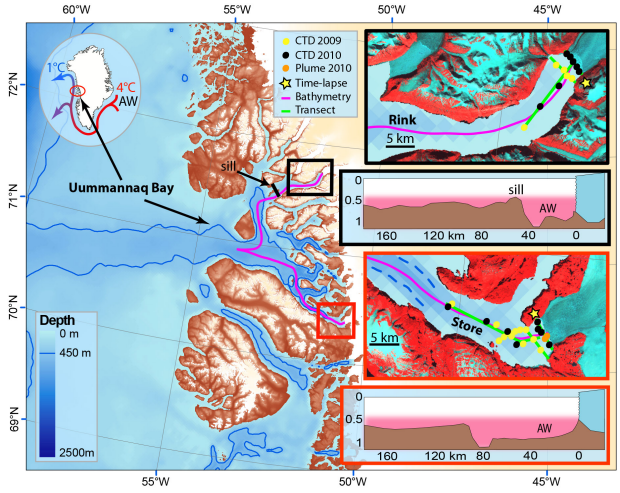

Figure 1. Map of the study area. The yellow and black dots represent the CTD sections in 2009 and 2010 respectively. In the International Bathymetry Chart of the Arctic Ocean (IBCAO), the 450 m contour has been highlighted in blue to indicate the trough across the continental shelf allowing the AW to enter the fjord. Bathymetry of the centre line of Store and Rink fjords are shown for each fjord and correspond approximately to the purple line on the maps. Position of the shallowest sill in Rink Fjord is shown as a thick black line. Orange dots show the position of Store 2010 profiles inside and outside the surface plume. Note that although the IBCAO bathymetry appears to be correct for the outer part of the fjord, that of the inner fjords is inaccurate, as depths of up to 800 and 1100 m are observed near Store and Rink fronts, respectively. A false colour Landsat mosaic from August 2010 is used for the inset maps, superimposed over land and glaciers. Topography (brown shade) and ice mask (off-white) are taken from Greenland Ice Map Project (GIMP).

ing points of more than one standard deviation from the unweighted moving average window ($n = 16$) to yield a statistically significant result. The filtered data were then averaged into 5 m vertical bins. Both the ascent and descent data were used to improve error estimation. The standard deviation provides an indication of measurement uncertainty and corresponds to ±0.023 °C for potential temperature, ±0.025 PSU for salinity and ±1.4 nephelometric turbidity unit (NTU) for the turbidity. Potential temperature (θ) and salinity (S) were calculated according to the equations of state of seawater published by UNESCO 1983 (Fofonoff and Millard, 1983) and used to identify specific water bodies and mixing processes.

The turbidity in the fjord was used to trace the sediment-loaded subglacial fresh water (Bartholomew et al., 2011; Motyka et al., 2003). Turbidity estimates are, however, based on backscattering on light, depending of both sediment concentration and type (lithology and size) of particles, which can vary from one fjord to another. To compare the extent of fresh-water-induced buoyant upwelling plumes, we expressed the turbidity as a percentage of the maximum value recorded in each fjord (i.e. within the plumes).

3.2 Water-body identification

When plotted in potential temperature–salinity (θ–S) space, two types of water body can be differentiated: (a) Water types are defined by thick, homogenous layers, in excess of 50 m within the water profile, which share similar temperature and salinity ($\Delta\theta < 0.2$ °C and $\Delta S < 0.2$ PSU). Such water types can be identified by dense clustering on a θ–S diagrams; (b) Mixed water masses are defined as a layer within the water column combining two water types and are characterised by the line joining the two water types on the θ–S diagram. We define a mixed water mass when its thickness exceeds 50 m, its $\delta\theta/\delta S$ gradient is constant and when there is sufficient difference ($\Delta\theta > 0.5$ °C and/or $\Delta S > 0.5$ PSU) between the top and the bottom of the layer.

3.3 Identification of interaction processes

To isolate which water body is driving subaqueous melt, we calculate the temperature and salinity loss due to the melting of glacier ice with reference to the Gade-slope (Gade, 1979; Holland and Jenkins, 1999; Mortensen et al., 2013; Straneo et al., 2011, 2012). Given a potential temperature for glacier ice (θ_i) at the front, we define an effective potential temperature (θ_{eff}) of the corresponding virtual water type by calculating the energy required to melt a unit weight of ice as follows:

$$\theta_{eff} = \theta_f - \frac{L_i - C_i(\theta_f - \theta_i)}{C_{sw}}, \quad (1)$$

where θ_f is the pressure-corrected melting point of ice, L_i ($337\,kJ\,kg^{-1}$) is the latent heat of fusion, C_i ($2.1\,kJ\,kg^{-1}\,K^{-1}$) the specific heat capacity of ice and C_{sw} ($3.9\,kJ\,kg^{-1}\,K^{-1}$) the specific heat capacity of seawater. In the θ–S diagram, the mixed water mass resulting from submarine melting of the glacier will fall on the Gade-slope joining the water, driving the melt and the virtual water type with characteristics $\theta = \theta_{eff}$ and $S = 0$. A similar identification procedure can be applied to track runoff mixing and resulting mixed water mass as it will follow a line joining the ambient water and the fresh runoff water ($\theta = 0$ °C; $S = 0$ °C) (Mortensen et al., 2013; Straneo et al., 2011, 2012) (hereafter called the runoff slope). If both submarine melting and runoff mixing are affecting the same water parcel, the resulting mixed water mass will have a θ–S gradient proportional to the theoretical slope of each process (Mortensen et al., 2013).

3.4 Interpolation of oceanic measurements

Temperature, salinity and turbidity were interpolated across and along Rink and Store fjords. The cross profile was interpolated immediately adjacent to each ice front (~ 200 m)

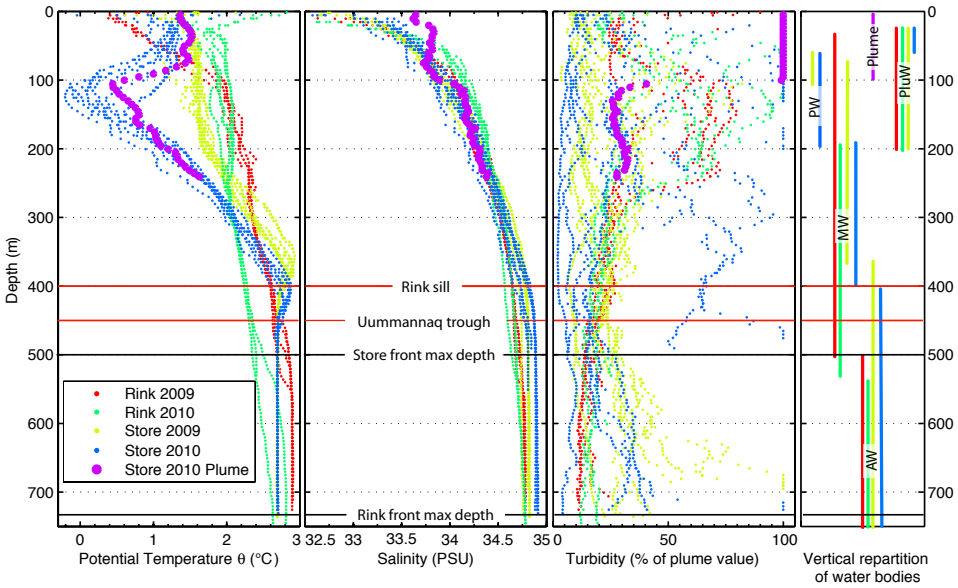

Figure 2. Potential temperature, salinity and turbidity vs. depth for all profiles. On the right-hand side panel, each water-body vertical extent is represented for each survey. The estimated maximal depth of each glacier front is shown with a continuous horizontal black line. The depth of Uummannaq Trough and Rink Sill are shown as horizontal red lines. The turbidity has been converted to a percentage of the maximum value measured inside the plume of each fjord. For Store in 2010, the profile inside the plume (ST 16) is shown in purple.

Table 1. Profiler's sensors (CTD) specifications, MIDAS Valeport 2000.

Sensor	Pressure	Conductivity	Temperature	Turbidity
Type	Strain gauge	Valeport inductive coils	Fast-response platinum thermometer	Seapoint
Accuracy	0.2 Bar	0.01 mS cm^{-1}	0.01 °C	15 NTU

and the long-profile section tracks the midpoint of each fjord (Fig. 1).

3.5 Runoff discharge estimation

In addition to synoptic meteorological conditions, surface glacier meltwater runoff is dependent upon the ablation area, its hypsometry and the seasonal distribution of snow/ice and its concomitant albedo. Monthly mean values of surface melt for each glacier were estimated following Box (2013) using a positive degree-day/melt-rate model applied to glacier catchment. The catchment of each glacier was determined from the GIMP digital elevation model (DEM) of the ice sheet (Bamber et al., 2013). For the purposes of this study we assume an efficient, fully developed drainage system as would be expected in the latter half of the melt season where the bulk of surface meltwater runoff drains and is discharged directly into the fjord as subglacial fresh water (Chandler et al., 2013; Schoof, 2010).

4 Results

4.1 Water types present at the glacier front

Compiled θ–S plots reveal that the distinct water bodies observed within both Rink and Store fjords (Figs. 2 and 3, Table 2) interact with their respective calving fronts (Sect. 4.2). Except for polar water (PW) described below, all the other water bodies observed were directly adjacent ($\sim$ 200 m) to each glacier and can be assumed to be in direct contact with the submerged calving face. Four distinct water types were observed:

1. Surface water (SW) is the uppermost layer of the fjord and is strongly affected by solar insolation, atmospheric forcing, brash-ice melt as well other external processes including river runoff and vertical mixing (Mortensen et al., 2011). In this study, the pycnocline at the lower interface of the SW appears to act as a barrier to buoyant upwelling waters (Sect. 4.4) often constraining them below the SW. Throughout our surveys, SW was limited to the upper 15 m of the water column with temperatures ranging from 0 to 10 °C and in salinity from 28

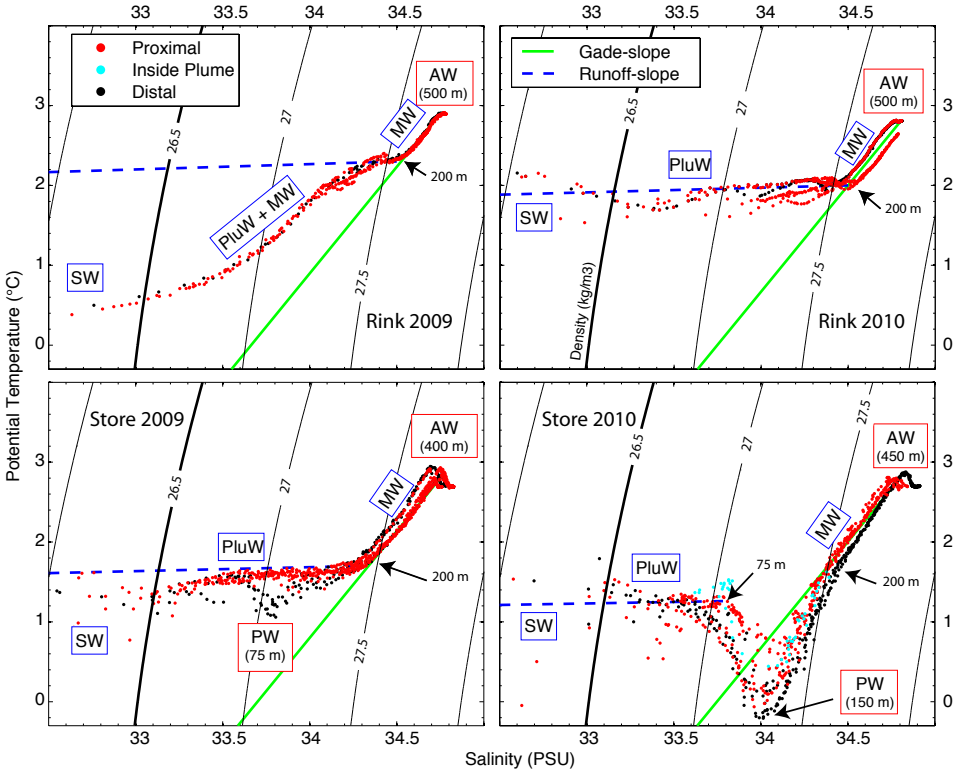

Figure 3. Potential temperature–salinity diagram of the CTD stations in 2009 and 2010 for Rink and Store fjords. The distal (∼ 20–30 km) and proximal (∼ 0.2–1 km) profiles are in black and red, respectively. The labels and the depth of the water types are outlined in red whilst the mixed water masses are in blue. Isopycnals are in black with $\sigma = 26.5\,\mathrm{kg\,m^{-3}}$ highlighted in bold to represent the lower limit of the surface water. Green continuous and blue dashed lines represent the theoretical Gade-slope and runoff slope, respectively.

to 33 PSU. We define the limit of the SW by its density ($\sigma_\theta < 26.5\,\mathrm{kg\,m^{-3}}$) as it is above this value that most of the variability appears.

2. Atlantic water (AW) (Straneo et al., 2012), also known as subpolar mode water (Mortensen et al., 2011) or intermediate Irminger water (Ribergaard, 2007), is the deepest and warmest water body present in the fjord. This water type is advected along the coast by the west Greenland Current (Mortensen et al., 2011, 2013; Ribergaard, 2007; Straneo and Heimbach, 2013; Straneo et al., 2012), entering the fjord via the Uummannaq Bay trough carved across the continental shelf. Throughout our surveys, AW was always present below 400 to 500 m depth and had highly consistent temperature and salinity characteristics ($\theta = 2.8 \pm 0.2\,^\circ\mathrm{C}$ and $S = 34.8 \pm 0.1$ PSU) for both fjords over both years.

3. Polar water (PW), which was only observed in Store Fjord, is the coldest water body (Figs. 2 and 3). PW originates from the Arctic Ocean (Hopkins, 1991) and is present along the west coast of Greenland at 50 to 150 m depth (Ribergaard, 2007) where it would be able to advect into Uummannaq Bay. In 2010 at Store, PW was observed at 50 to 200 m depth, separating SW and AW, and had a minimum temperature of $\theta \sim = 0\,^\circ\mathrm{C}$ and $S = 34$ PSU at ~ 150 m. Remnant traces of PW were visible at Store in 2009 for the most distal CTD cast (~ 10 km from the glacier) but were not observed any nearer or in direct contact with the calving front (Fig. 4). PW was not observed in Rink Fjord in either year.

4. Subglacial fresh water (SgFW) includes basal as well as surface runoff and is injected into the fjords at distinct portals at depth in the calving front. SgFW is very difficult to measure in its original state due to the vigorous mixing which occurs on its injection from the portal (Salcedo-Castro et al., 2011; Xu et al., 2012, 2013). Hence, SgFW is reasonably assumed to have the basic characteristics of $\theta = 0\,^\circ\mathrm{C}$ and $S = 0$ PSU (Mortensen et al., 2013; Straneo et al., 2012).

4.2 Mixed water masses and inferred processes

4.2.1 Submarine melting

Applying Eq. (1) and assuming a temperature for glacier ice of $\theta_\mathrm{i} = -10\,^\circ\mathrm{C}$ (taken from Jakobshavn Isbræ; Thomas,

Table 2. Characteristics of the water types and mixed waters observed during the surveys.

	Water types			Mixed water masses		
	AW	PW	SgFW	MW	PluW	SW
[θ(°C);S(PSU)] or [δ(°C)/δS(PSU)]	[2.8; 34.8]	[0; 34]	[0; 0]	(2.5)	(0.05)	NA
Origin	Subpolar gyre	Arctic Ocean	Surface/basal glacier melt	Resulting from submarine melting	Resulting from runoff mixing	River mixing, solar insolation
Transport	Advected by WGC	Advected by WGC	Local formation	Local formation	Local formation	Local formation
Depth range	400 m bottom	∼ 50–200 m	∼ 500 m (Store) ∼ 750 m (Rink)	200– ∼ 400 m	15–200 m or 15–75 m	0–15 m

2004) and a salinity (S_i) of 0 PSU at the base of Store calving front yields a virtual water-type temperature of $\theta_{eff} = -89.8$ °C. Note that θ_{eff} is not sensitive to the assumed values of θ_i. Hence, meltwater (MW) driven by AW ($S = 34.8$ PSU and $\theta = 2.8$ °C) will follow a Gade-slope of ~ 2.7 °C PSU^{-1}. MW was found in all surveys above the AW and below SW (or PW if present). The gradient derived from our observations of MW of ~ 2.5 °C PSU^{-1} is in good agreement with the theoretical Gade-slope (Fig. 3). MW was observed from 100 to 250 m from the base of the calving front up to 200 m from the surface (Fig. 2). Rink Fjord in 2009 was an exception when MW was present along with plume water (see below) from 200 m to 15 m depth (Fig. 3). The presence of MW below the outer sill depth at Rink Fjord (Fig. 2) indicates that it is formed locally by interaction with the calving front and is not merely advected in from Baffin Bay.

4.2.2 Runoff mixing

Following Straneo et al. (2011, 2012), the horizontal inflection in the θ–S diagram is used to define the second apex of the runoff slope (Fig. 3) and gives a theoretical value of ~ 0.05 °C PSU^{-1} and 0.04 °C PSU^{-1} respectively. Plume water (PluW) is produced by the mixing of SgFW with ambient fjord water at depth and is sometimes referred to as subglacial water (Mortensen et al., 2011). In our surveys, PluW has a runoff slope of ~ 0.07 °C PSU^{-1} (Fig. 3) and was found below the SW and above a depth of either 200 m (Rink 2009–2010 and Store 2009) or 75 m (Store 2010) depth.

Mixing of MW and PluW with similar proportions to each other was only observed in 2009 at Rink within the upper layer.

Due to the lack of direct observation of plume processes (within tens of metres of the ice front), the inflection in the θ–S diagram (Fig. 3) reflects the depth at which the PluW outflows horizontally and not the depth of injection of the SgFW into the fjord.

4.3 SgFW discharge estimation

The surveys were conducted in August of 2009 and 2010 during two contrasting melt seasons with very different glacier meltwater runoff characteristics. In 2009, air temperatures and glacial melt were normal and approximate the 2000 to 2010 mean, whereas temperature, extent and magnitude of surface melt were record-setting in 2010 (Tedesco et al., 2011; van As et al., 2012). In the absence of precipitation during both sets of surveys we assume that the monthly variations in the discharge of SgFW are predominantly driven by glacier surface melt. Surface melt runoff modelling yields a predicted SgFW discharge at Rink of 1000 ± 300 m^3 s^{-1} in 2009 and 1500 ± 450 m^3 s^{-1} in 2010. At Store, the SgFW discharge is estimated at 1500 ± 450 m^3 s^{-1} in 2009 and 2000 ± 600 m^3 s^{-1} in 2010. Uncertainties are defined by the 30 % standard error derived from comparisons between modelled (Box, 2013) and measured (van de Wal et al., 2012) runoff at the Kangerlussuaq transect, some 300 km to the south of our study site. Given that Rink and Store catchments are within the same fjord system, it can be noted that any bias in the runoff model should affect both glaciers consistently and hence the relative variation in discharge of SgFW for the two glaciers can be compared directly. The SgFW discharge of Store Glacier in 2009 was ∼ 50 % greater than that for Rink, due to the latter's reduced ablation area. Driven by very high air temperatures in August 2010, SgFW discharge at both glaciers is amplified by ∼ 50 % compared to 2009.

4.4 Turbidity analysis and plume observation

At Store, a variable turbid plume was visible at the water surface adjacent to the calving front in time-lapse imagery acquired in July 2009 (http://vimeo.com/2638166) (Ahn and Box, 2010), but was not visible in August. In contrast, in August 2010, a large, dominant turbid plume extended ∼ 1 km away from the ice front. Logging of the time-lapse imagery indicates that the forced convection associated with

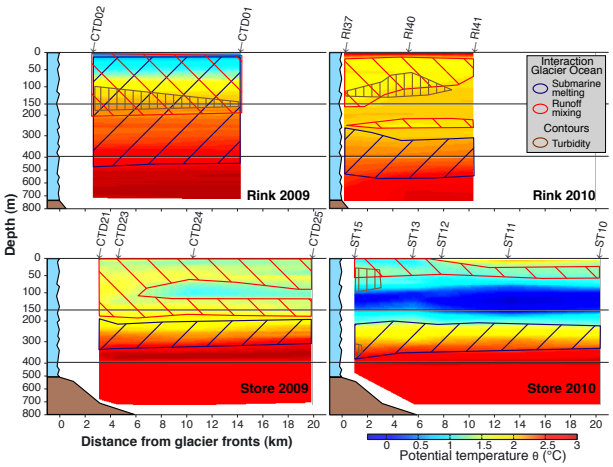

Figure 4. Potential temperature along fjord section (parallel to the fjord main axis), with the glacier front to the left and the open ocean to the right. Dashed areas show waters resulting from submarine melting (blue) and runoff mixing (red). The brown dashed area corresponds to a turbidity > 80 % of the maximum recorded in the plume. The estimated bottom profile is depicted as a solid brown area.

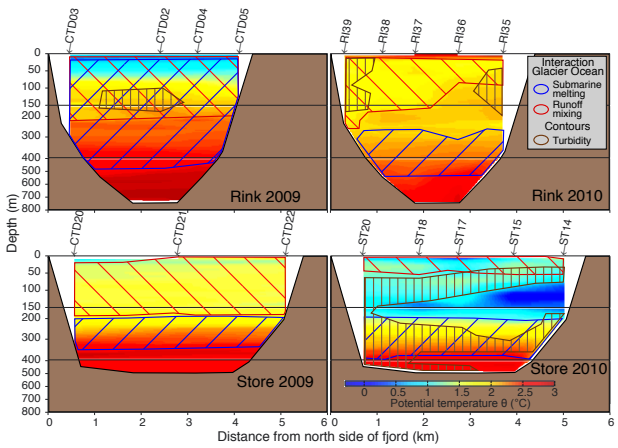

Figure 5. Same as Fig. 4, but with the across-fjord section (parallel to the front at ∼ 200–1000 m distance). The north side of the fjord is on the left and it is facing the ice front.

the plume was attaining the surface from June until the end of August 2010. Horizontal surface outflow from this plume attained speeds up to $\sim 1.5\,\mathrm{m\,s^{-1}}$, sufficient to force brash ice or mélange out from the embayment (Fig. 8). A distinct boundary was observed at the outer limit of the plume, visible by a marked change in water turbidity (Fig. 8). The outflow of PluW is observed at 50–100 m depth (Fig. 5) and extends up to 3 km away from the front (Fig. 4). A layer of intense turbidity was also observed from 300 m depth to the bottom (Figs. 4, 5 and 7) at Store in 2010 (Fig. 5). Turbidity measurements within and just outside of the surface plume (visually defined by the contrast in water colour), indicate that PluW sinks below the pycnocline of the SW after attaining the surface (Fig. 7), an observation that is in agreement with plume modelling at Store (Xu et al., 2013).

In contrast to Store, there was very little surface plume activity observed at Rink. Logging of time-lapse photography of Rink (http://vimeo.com/6038577) (Ahn and Box, 2010) reveals just one surface plume on its southern margin in July 2009 and 2010, which had, however, disappeared completely by early August. Despite this apparent absence of surface plume activity, turbid waters were observed just below SW, suggesting that the plume was still present but was not attaining the surface. In August 2009, a submarine turbid water jet was present in the middle of the cross section between 100 and 200 m depth and spreading up to 10 km down the fjord (Fig. 4). In August 2010, two turbid jets are present, one along the north side of the fjord and one along the south side with the strongest jet measured beneath the pycnocline of the SW at 15 m depth (Fig. 5).

5 Discussion

5.1 Ocean–glacier interaction

The hydrographic surveys at Rink and Store provide four snapshots of glacier–ocean interaction during the latter half of the melt season when SgFW discharge should be most pronounced. Direct observation of these interactions and their repartitioning within the water column shows marked similarities and differences between both years and the fjords from which we identify key suites of processes significantly and simultaneously impacting a water parcel (hereafter called states). Below 200 m depth, free convective submarine melting is the only process which is consistently identified (Figs. 4 and 5), whereas three different states can be distinguished within the upper layers of the water column (0–200 m depth): state (1) – submarine melting interlaced with runoff mixing both of similar magnitude (Rink 2009); state (2) – significant runoff mixing (Store 2009 and Rink 2010); state (3) – similar to state 2 but with a shallower (< 75 m depth) outflow (Store 2010).

Comparison of these observed states with calculated SgFW discharge suggests that the interaction processes in the upper layer are potentially influenced by glacier meltwater runoff rates. Indeed, when the SgFW discharge increases at Store, the PluW outflow becomes shallower and evolves from state 2 to state 3 (Fig. 6), an observation which resonates with recent modelling (Sciascia et al., 2013; Xu et al., 2013).

At Rink, in 2009, both PluW and MW were observed in similar proportions in the upper layer. By contrast, in 2010 PluW was the only water to contribute significantly to the upper layer. As both the temperature and depth of the AW as well as the vertical extent of submarine melting remained the same in the 2009 and 2010 surveys, we infer that the 50 %

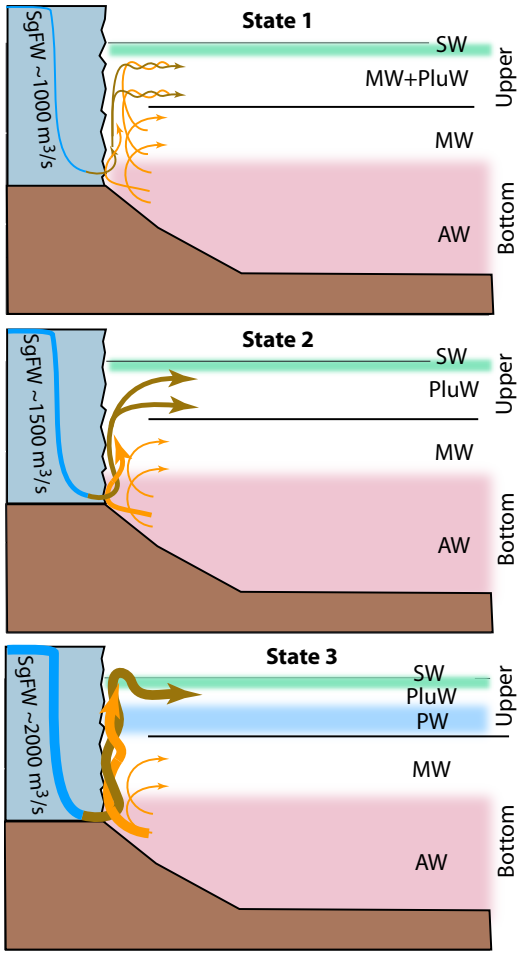

Figure 6. Simplified schematic of the three states of interaction identified (Sect. 5.1), the associated SgFW discharge and the circulation induced at the glacier front. The arrow thicknesses represent an approximate magnitude, and the colours represent the different processes of interaction with the following: SgFW (blue), runoff mixing (brown) and submarine melting (orange). The upper and bottom layers are represented above and below 200 m depth. Each water body observed in the water column is labelled as in the text (Sects. 4.1 and 4.2)

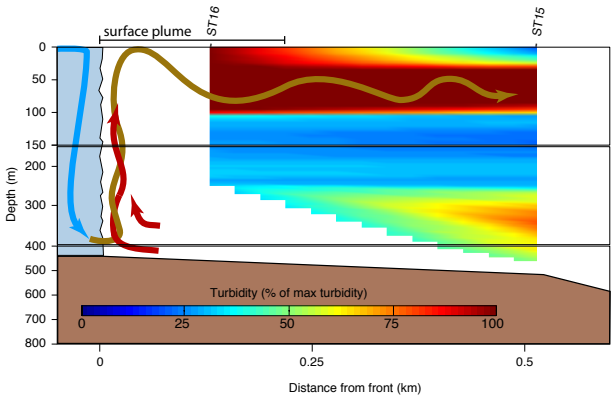

Figure 7. Turbidity section across the boundary of the surface plume at Store in 2010 (Fig. 8). The turbidity is shown as a percentage of the maximum turbidity recorded in the plume. The profile ST15 was done ~ 200 m outside the turbid plume where the surface of the sea was a normal blue colour and no significant surface current was observed. The profile ST16 was done ~ 100 m inside the surface plume, the colour of the surface was dark brown and a strong turbulent current flowing away from the glacier was observed. ST16 was not lowered to the bottom of the fjord for safety reasons, therefore interpolation below 250 m is not realistic. The arrows show a schematics circulation in the plume with SgFW in blue, AW in red and PluW in brown.

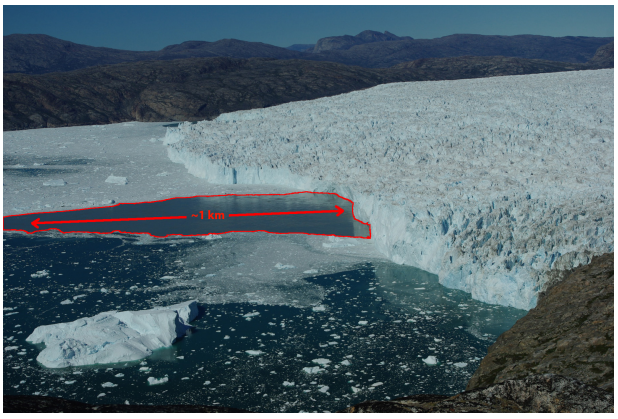

Figure 8. Picture taken from the southern side of Store Glacier in 2012 (looking north). The red line shows the boundary of the turbid surface plume observed from June to September and its approximate extent.

stronger SgFW discharge in 2010 is responsible for a more pronounced runoff-mixing impact and hence PluW contribution.

A simplified schematic of the three observed states of ocean–glacier interaction and the associated circulation patterns are presented (Fig. 6). Excluded from this schematic are external factors such as wind-driven circulation (Straneo et al., 2010; Sutherland and Straneo, 2012), tides (Mortensen et al., 2011) and seasonality of the forcing cycle (Mortensen et al., 2013), all of which will influence the circulation patterns as well.

Despite these limitations, the circulation induced by the runoff mixing and submarine melting, and its evolution, must significantly contribute to the general circulation across and along the glacier front. Indeed, both processes produce vertical entrainment of ambient AW water in direct contact with the ice front, which is a major driver of enhanced melting at the calving front (Jenkins, 1991, 2011; Josberger and Martin, 1981; Xu et al., 2012, 2013).

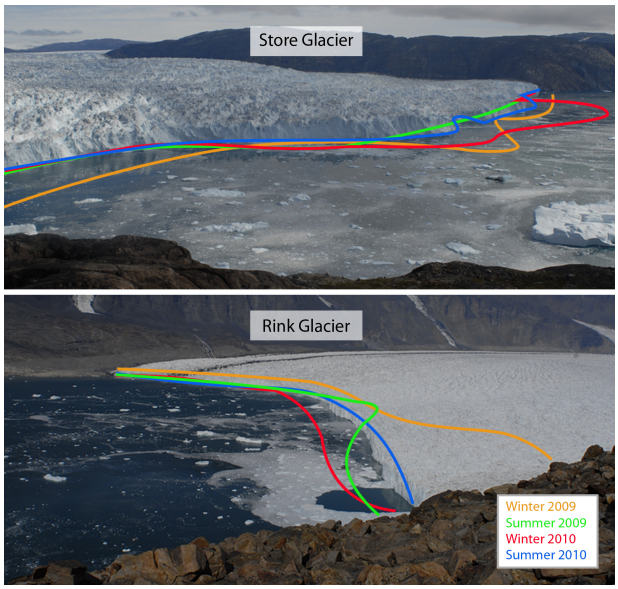

Figure 9. Time-lapse photographs of Store and Rink glacier termini in August 2010. The general shape and position of each glacier front for the winter preceding each survey and the summer of the survey have been outlined in orange (winter 2009), green (summer 2009), red (winter 2010) and blue (summer 2010).

5.2 SgFW-driven upwelling: spatial spreading and glacier impact

Glacier buoyant upwelling plumes, producing PluW, are commonly associated with enhanced submarine melting through the entrainment of warm water along the ice front (Jenkins, 2011; Motyka et al., 2003, 2011; Rignot et al., 2010; Sciascia et al., 2013; Sole et al., 2012; Xu et al., 2012, 2013). The scale of the subglacial channels allowing SgFW to enter the fjord is, to date, not well defined (Jenkins, 2011; Sciascia et al., 2013; Xu et al., 2013). It has been hypothesised that emerging SgFW is channelised and hence injected through discrete portals (Jenkins, 2011; Mugford and Dowdeswell, 2011) rather than being evenly injected all along the front (Sciascia et al., 2013; Sole et al., 2012; Xu et al., 2012; 2013). This is in agreement with the well-defined surface plume observed at Store (Fig. 8) and elsewhere (Mortensen et al., 2013; Motyka et al., 2003; Rignot et al., 2010; Xu et al., 2013), which indicates a point source injection at depth, and with the presence of turbid jets at Rink (Fig. 5) which also have a distinct spatial footprint. In all surveys, the layer of PluW was, nevertheless, present uniformly across the fjord near the glacier and fading downstream (Figs. 4 and 5), suggesting that despite the potential localised injection point, PluW rapidly spreads across as well as along the fjord at its depth of hydrostatic equilibrium.

5.3 Oceanic and bathymetric influence on glacier front behaviour

The presence of sills in Uummannaq Bay has a strong impact on how water is transported into the deeper fjords and toward each of the glaciers' calving fronts. The trough on the continental shelf near Uummannaq entrance provides access for all water above 450 m to penetrate as far as Store. At Rink, the presence of an additional sill at 400 m depth and 50 km down the fjord (Dowdeswell et al., 2014) further affects the temperature of water found at Rink's calving front. Indeed, we found the bottom water at Rink to have the characteristics of the AW found at Store at 400 m depth (i.e. the depth of Rink sill) (Fig. 2).

At Rink Glacier, mass loss (i.e. calving and submarine melt combined), logged by time-lapse photography, appears to be relatively homogeneous across the entire ice front with maximum losses at the central sector, coincident with the deepest part of the fjord and fastest ice flow. At Store Glacier, frontal mass loss during both summers is greater on the southern flank, where a large embayment between two headlands coincides with an upwelling plume visible at the surface. These observations suggest that in addition to the fjord geometrical control on the glacier calving processes (McFadden et al., 2011; Schild and Hamilton, 2013), the presence of warm, subpolar-originating water bodies at the glacier front, along with the presence of sills and inner basins in the fjord, also has a considerable impact on the calving dynamics, and thus on the shape of the calving front. We hypothesise that deep tidewater glaciers, such as Rink ($\sim$ 750 m), which are exposed significantly to warm AW at their base ($\sim$ 75 % at Rink), will be influenced by widespread, submarine melting, which would favour a relatively flat calving face (Fig. 9). For glaciers such as Store, which have a shallower ice front (< 500 m), the impact of SgFW discharge on the upper layer (0–200 m) may be the primary factor driving frontal geometry and dynamics. We suggest that notch cutting and the resulting headlands along the ice front are related to the presence of localised plume-induced melting of the ice front where SgFW is released from subglacial portals (Figs. 8 and 9). The local undercutting of the calving face will, in this case, create a crenulated ice front characterised by a series of embayments and separated by headlands where calving processes will dominate.

6 Conclusions

Hydrographic surveys in Uummannaq Bay in August 2009 and 2010 reveal that warm ($2.8 \pm 0.2\,^{\circ}$C) and deep Atlantic water (AW) was present below 450 m and driving free convective submarine melting of Rink and Store, two fast-flowing outlets of west Greenland. Subglacial fresh water (SgFW) injected at depth was also observed to force buoyant plumes where runoff mixing is the main process involved,

yielding a turbid outflow of plume water (PluW). Turbidity transects across the upwelling plumes show that, after attaining the surface, the plume sinks below surface water (SW) and replaces any water present at its level of outflow along and across the fjord. The plumes do not necessarily surface in the fjords, as revealed by jets of turbid water, observed at depths of 50 to 100 m. Two layers can be distinguished in the fjord structure. The upper layer (0–200 m) experiences the greatest differences in between the fjords and surveys, with three different states of interaction observed: submarine melting and runoff mixing (state 1), runoff mixing alone (state 2) and runoff mixing alone at shallower depth (75 m) (state 3). The evolution of the upper layer structure from state 1 to state 3 is hypothesised to be primarily controlled by the increase of SgFW discharge. The bottom layer below 200 m depth has similar characteristics in all surveys, with free convective submarine melting being the only process involved. At Rink Glacier, which is 750 m deep, $\sim$ 75 % of the ice front is affected by submarine melting which favours a relatively flat calving front. In contrast, at Store, which is up to 500 m deep, SgFW discharge and buoyancy-driven plumes affect over 40 % of the calving front, leading to a crenulated terminus characterised by a series of notches separated by headlands which are exposed to mechanical failure and calving.

Acknowledgements. We wish to acknowledge fieldwork support from NERC Grant NE/G010595/1, the Aberystwyth University Research Fund and the Royal Geographical Society. N. Chauché is supported by an Aberystwyth University Research Studentship and wishes to acknowledge the support of LOCEAN (University of Pierre and Marie Curie, UPMC). J. E. Box was supported by The Ohio State University's Climate Water and Carbon initiative managed by D. Alsdorf and the Geological Survey of Denmark and Greenland. J.-C. Gascard acknowledges the support of Arctic Climate Change, Economy and Society (ACCESS). We are indebted to the tireless crew of S/V *Gambo* and all those who have supported this project, particularly the Uummannaq Polar Institute and Children's Home.

Edited by: E. Larour

References

Ahn, Y. and Box, J. E.: Glacier velocities from time-lapse photos: technique development and first results from the Extreme Ice Survey (EIS) in Greenland, J. Glaciol., 56, 723–734, 2010.

Bamber, J. L., Griggs, J. A., Hurkmans, R. T. W. L., Dowdeswell, J. A., Gogineni, S. P., Howat, I., Mouginot, J., Paden, J., Palmer, S., Rignot, E., and Steinhage, D.: A new bed elevation dataset for Greenland, The Cryosphere, 7, 499–510, doi:10.5194/tc-7-499-2013, 2013.

Bartholomew, I., Nienow, P., Sole, A., Mair, D., Cowton, T., Palmer, S., and Wadham, J.: Supraglacial forcing of subglacial drainage in the ablation zone of the Greenland ice sheet, Geophys. Res. Lett., 38, doi:10.1029/2011GL047063, 2011.

Box, J. E.: Greenland Ice Sheet Mass Balance Reconstruction. Part II: Surface Mass Balance (1840–2010), J. Climate, 26, 6974–6989, doi:10.1175/JCLI-D-12-00518.1, 2013.

Chandler, D. M., Wadham, J. L., Lis, G. P., Cowton, T., Sole, A., Bartholomew, I., Telling, J., Nienow, P., Bagshaw, E. B., Mair, D., Vinen, S., and Hubbard, A.: Evolution of the subglacial drainage system beneath the Greenland Ice Sheet revealed by tracers, Nat. Geosci., 6, 195–198, doi:10.1038/ngeo1737, 2013.

Christoffersen, P., O'Leary, M., Van Angelen, J. H., and van den Broeke, M.: Partitioning effects from ocean and atmosphere on the calving stability of Kangerdlugssuaq Glacier, East Greenland, Ann. Glaciol., 53, 249–256, doi:10.3189/2012AoG60A087, 2012.

Dowdeswell, J. A., Hogan, K. A., Ó Cofaigh, C., Fugelli, E. M. G., Evans, J., and Noormets, R.: Late Quaternary ice flow in a West Greenland fjord and cross-shelf trough system: submarine landforms from Rink Isbrae to Uummannaq shelf and slope, Quaternary Sci. Rev., 92, 292–309, doi:10.1016/j.quascirev.2013.09.007, 2014.

Fofonoff, N. and Millard, R. C.: Algorithms for Computation of Fundamental Properties of Seawater. Endorsed by Unesco/SCOR/ICES/IAPSO Joint Panel on Oceanographic Tables and Standards and SCOR Working Group 51. Unesco Technical Papers in Marine Science, No. 44., 1983.

Gade, H. G.: Melting of ice in sea water: A primitive model with application to the Antarctic ice shelf and icebergs, J. Phys. Oceanogr., 9, 189–198, 1979.

Hanna, E., Huybrechts, P., Steffen, K., Cappelen, J., Huff, R., Shuman, C., Irvine-Fynn, T., Wise, S., and Griffiths, M.: Increased Runoff from Melt from the Greenland Ice Sheet: A Response to Global Warming, J. Climate, 21, 331–341, doi:10.1175/2007JCLI1964.1, 2014.

Holland, D. M. and Jenkins, A.: Modeling thermodynamic ice-ocean interactions at the base of an ice shelf, J. Phys. Oceanogr., 29, 1787–1800, 1999.

Holland, D. M., Thomas, R. H., de Young, B., Ribergaard, M. H., and Lyberth, B.: Acceleration of Jakobshavn Isbrae triggered by warm subsurface ocean waters, Nat. Geosci., 1, 659–664, 2008.

Hopkins, T. S.: The GIN Sea – A synthesis of its physical oceanography and literature review 1972–1985, Earth-Sci. Rev., 30, 175–318, 1991.

Hubbard, A. L.: The Times Atlas and actual Greenland ice loss, Geology Today, 27, 212–215, doi:10.1111/j.1365-2451.2011.00812.x, 2011.

Jakobsson, M., Mayer, L., Coakley, B., Dowdeswell, J. A., Forbes, S., Fridman, B., Hodnesdal, H., Noormets, R., Pedersen, R., Rebesco, M., Schenke, H. W., Zarayskaya, Y., Accettella, D., Armstrong, A., Anderson, R. M., Bienhoff, P., Camerlenghi, A., Church, I., Edwards, M., Gardner, J. V., Hall, J. K., Hell, B., Hestvik, O., Kristoffersen, Y., Marcussen, C., Mohammad, R., Mosher, D., Nghiem, S. V., Pedrosa, M. T., Travaglini, P. G., and Weatherall, P.: The International Bathymetric Chart of the Arctic Ocean (IBCAO) Version 3.0, Geophys. Res. Lett., 39, L12609, doi:10.1029/2012GL052219, 2012.

Jenkins, A.: A one-dimensional model of ice shelf-ocean interaction, J. Geophys. Res., 96, 20671–20677, 1991.

Jenkins, A.: Convection-Driven Melting near the Grounding Lines of Ice Shelves and Tidewater Glaciers, J. Phys. Oceanogr., 41, 2279–2294, doi:10.1175/JPO-D-11-03.1, 2011.

Josberger, E. G. and Martin, S.: A laboratory and theoretical study of the boundary layer adjacent to a vertical melting ice wall in salt water, Journal of Fluid Mechanics, 111, 439–473, 1981.

Joughin, I., Smith, B. E., Howat, I. M., Floricioiu, D., Alley, R. B., Truffer, M., and Fahnestock, M.: Seasonal to decadal scale variations in the surface velocity of Jakobshavn Isbrae, Greenland: Observation and model-based analysis, J. Geophys. Res., 117, F02030, doi:10.1029/2011JF002110, 2012.

Kjær, K. H., Khan, S. A., Korsgaard, N. J., Wahr, J., Bamber, J. L., Hurkmans, R., van den Broeke, M., Timm, L. H., Kjeldsen, K. K., and Bjørk, A. A.: Aerial Photographs Reveal Late–20th-Century Dynamic Ice Loss in Northwestern Greenland, Science, 337, 569–573, 2012.

McFadden, E. M., Howat, I. M., Joughin, I., Smith, B. E., and Ahn, Y.: Changes in the dynamics of marine terminating outlet glaciers in west Greenland (2000–2009), J. Geophys. Res., 116, F02022, doi:10.1029/2010JF001757, 2011.

Mortensen, J., Lennert, K., and Bendtsen, J.: Heat sources for glacial melt in a sub-Arctic fjord (Godthåbsfjord) in contact with the Greenland Ice Sheet, J. Geophys. Res., 116, C01013, doi:10.1029/2010JC006528, 2011.

Mortensen, J., Bendtsen, J., Motyka, R. J., Lennert, K., Truffer, M., Fahnestock, M., and Rysgaard, S.: On the seasonal freshwater stratification in the proximity of fast-flowing tidewater outlet glaciers in a sub-Arctic sill fjord, J. Geophys. Res-Oceans, 118, 1382–1395, doi:10.1002/jgrc.20134, 2013.

Motyka, R. J., Hunter, L., Echelmeyer, K. A., and Connor, C.: Submarine melting at the terminus of a temperate tidewater glacier, LeConte Glacier, Alaska, USA, Ann. Glaciol., 36, 57–65, 2003.

Motyka, R. J., Truffer, M., Fahnestock, M., Mortensen, J., Rysgaard, S., and Howat, I. M.: Submarine melting of the 1985 Jakobshavn Isbræ floating tongue and the triggering of the current retreat, J. Geophys. Res., 116, F01007, doi:10.1029/2009JF001632, 2011.

Mugford, R. and Dowdeswell, J. A.: Modeling glacial meltwater plume dynamics and sedimentation in high-latitude fjords, J. Geophys. Res., 116, F01023, doi:10.1029/2010JF001735, 2011.

Pfeffer, W. T.: A simple mechanism for irreversible tidewater glacier retreat, J. Geophys. Res., 112, F03S25, doi:10.1029/2006JF000590, 2007.

Ribergaard, M. H.: Oceanographic Investigations off West Greenland, Danish Metrological Institute Centre for Ocean and Ice (DMI), Copenhagen, 2007.

Rignot, E., Box, J. E., and Hanna, E.: Mass balance of the Greenland ice sheet form 1958 to 2007, Geophys. Res. Lett., 1–5, L20502, doi:10.1029/2008GL035417, 2008.

Rignot, E., Koppes, M., and Velicogna, I.: Rapid submarine melting of the calving faces of West Greenland glaciers, Nat. Geosci., 3, 187–191, 2010.

Ryan, J. C., Hubbard, A. L., Todd, J., Carr, J. R., Box, J. E., Christoffersen, P., Holt, T. O., and Snooke, N.: Repeat UAV photogrammetry to assess calving front dynamics at a large outlet glacier draining the Greenland Ice Sheet, The Cryosphere Discuss., 8, 2243–2275, doi:10.5194/tcd-8-2243-2014, 2014.

Salcedo-Castro, J., Bourgault, D., and deYoung, B.: Circulation induced by subglacial discharge in glacial fjords: Results from idealized numerical simulations, Cont. Shelf Res., 31, 1396–1406, 2011.

Schild, K. M. and Hamilton, G. S.: Seasonal variations of outlet glacier terminus position in Greenland, J. Glaciol., 59, 759–770, doi:10.3189/2013JoG12J238, 2013.

Schoof, C.: Ice-sheet acceleration driven by melt supply variability, Nature, 468, 803–806, doi:10.1038/nature09618, 2010.

Sciascia, R., Straneo, F., Cenedese, C., and Heimbach, P.: Seasonal variability of submarine melt rate and circulation in an East Greenland fjord, J. Geophys. Res. Oceans, 118, 2492–2506, doi:10.1002/jgrc.20142, 2013.

Sole, A. J., Payne, A. J., Nienow, P. W., Christoffersen, P., Cottier, F. R., and Inall, M. E.: Increased glacier runoff enhances the penetration of warm Atlantic water into a large Greenland fjord, The Cryosphere Discuss., 6, 4861–4896, doi:10.5194/tcd-6-4861-2012, 2012.

Straneo, F. and Heimbach, P.: North Atlantic warming and the retreat of Greenland's outlet glaciers, Nature, 504, 36–43, doi:10.1038/nature12854, 2013.

Straneo, F., Hamilton, G. S., Sutherland, D. A., Stearns, L. A., Davidson, F., Hammill, M. O., Stenson, G. B., and Rosing-Asvid, A.: Rapid circulation of warm subtropical waters in a major glacial fjord in East Greenland, Nat. Geosci., 3, 182–186, 2010.

Straneo, F., Curry, R., Sutherland, D. A., Hamilton, G. S., Cenedese, C., Våge, K., and Stearns, L. A.: Impact of ocean stratification on submarine melting of a major Greenland outlet glacier, Nature Precedings, 2011.

Straneo, F., Sutherland, D. A., Holland, D. M., Gladish, C., Hamilton, G. S., Johnson, H. L., Rignot, E., Xu, Y., and Koppes, M.: Characteristics of ocean waters reaching Greenland's glaciers, Ann. Glaciol., 53, 202–210, doi:10.3189/2012AoG60A059, 2012.

Sutherland, D. A. and Straneo, F.: Estimating ocean heat transports and submarine melt rates in Sermilik Fjord, Greenland, using lowered acoustic Doppler current profiler (LADCP) velocity profiles, Ann. Glaciology, 53, 50–58, doi:10.3189/2012AoG60A050, 2012.

Sutherland, D. A., Straneo, F., Stenson, G. B., Davidson, F. J. M., Hammill, M. O., and Rosing-Asvid, A.: Atlantic water variability on the SE Greenland continental shelf and its relationship to SST and bathymetry, J. Geophys. Res.-Oceans, 118, 847–855, doi:10.1029/2012JC008354, 2013.

Tedesco, M., Fettweis, X., van den Broeke, M., van de Wal, R. S. W., Smeets, C. J. P. P., van de Berg, W. J., Serreze, M. C., and Box, J. E.: The role of albedo and accumulation in the 2010 melting record in Greenland, Environ. Res. Lett., 6, 014005, doi:10.1088/1748-9326/6/1/014005, 2011.

Thomas, R. H.: Force-perturbation analysis of recent thinning and acceleration of Jakobshavn Isbrae, Greenland, J. Glaciol., 50, 57–66, 2004.

van As, D., Hubbard, A. L., Hasholt, B., Mikkelsen, A. B., van den Broeke, M. R., and Fausto, R. S.: Large surface meltwater discharge from the Kangerlussuaq sector of the Greenland ice sheet during the record-warm year 2010 explained by detailed energy balance observations, The Cryosphere, 6, 199–209, doi:10.5194/tc-6-199-2012, 2012.

van de Wal, R. S. W., Boot, W., Smeets, C. J. P. P., Snellen, H., van den Broeke, M. R., and Oerlemans, J.: Twenty-one years of mass balance observations along the K-transect, West Greenland, Earth Syst. Sci. Data, 4, 31–35, doi:10.5194/essd-4-31-2012, 2012.

Weidick, A. and Bennike, O.: Quaternary glaciation history and glaciology of Jakobshavn Isbræ and the Disko Bugt region, West Greenland: a review, Geological Survey of Denmark and Greenland, 2007.

Xu, Y., Rignot, E., Fenty, I., Menemenlis, D., and Flexas, M. M.: Subaqueous melting of Store Glacier, west Greenland from three-dimensional, high-resolution numerical modeling and ocean observations, Geophys. Res. Lett., 40, 4648–4653, doi:10.1002/grl.50825, 2013.

Xu, Y., Rignot, E., Menemenlis, D., and Koppes, M.: Numerical experiments on subaqueous melting of Greenland tidewater glaciers in response to ocean warming and enhanced subglacial discharge, Ann. Glaciol., 53, 229–234, doi:10.3189/2012AoG60A139, 2012.